

A SEARCH FOR SUPERSYMMETRY IN EVENTS WITH A Z BOSON,  
JETS, AND MISSING TRANSVERSE ENERGY IN  $p - p$  COLLISIONS  
WITH  $\sqrt{s}=13$  TEV WITH THE ATLAS DETECTOR

TOVA RAY HOLMES



Physics Department  
University of California, Berkeley

August 2016 – version 1.0

Tova Ray Holmes: *A Search for Supersymmetry in Events with a Z Boson, Jets, and Missing Transverse Energy in  $p - p$  Collisions with  $\sqrt{s}=13$  TeV with the ATLAS Detector*, © August 2016





## ABSTRACT

---

A search for new phenomena in final states containing a Z boson decaying to electrons or muons, jets, and large missing transverse momentum is presented. This search uses proton–proton collision data collected during 2015 and 2016 at a center of mass energy  $\sqrt{s} = 13$  TeV by the ATLAS detector at the Large Hadron Collider, which correspond to an integrated luminosity of  $3.3 \text{ fb}^{-1}$ . The search targets the pair production of supersymmetric particles, squarks or gluinos, which decay via jets and a Z boson to the lightest Supersymmetric particle, which does not interact with the ATLAS detector. Results are interpreted in simplified models of gluino-pair (squark-pair) production, and provide sensitivity to gluinos (squarks) with masses as large as 1.3 (1.0) TeV.



## PUBLICATIONS

---

Some results and ideas presented have previously appeared in the following publications:

[this\_paper]



## ACKNOWLEDGEMENTS

---

Put your acknowledgements here.



## CONTENTS

---

<b>I</b>	<b>INTRODUCTION</b>	<b>1</b>
1	INTRODUCTION	3
<b>II</b>	<b>THEORY AND MOTIVATION</b>	<b>7</b>
2	THEORY AND MOTIVATION	9
2.1	The Standard Model . . . . .	9
2.1.1	Matter . . . . .	9
2.1.2	Forces . . . . .	11
2.1.3	Phenomenology of Proton-Proton Collisions . . . . .	20
2.1.4	Problems in the Standard Model . . . . .	22
2.2	Supersymmetry . . . . .	24
2.2.1	The Minimal Supersymmetric Standard Model . . . . .	25
2.2.2	Solutions to Standard Model Problems . . . . .	27
2.2.3	Simplified Models of Supersymmetry . . . . .	28
2.3	Monte Carlo Event Generation . . . . .	30
<b>III</b>	<b>THE EXPERIMENT</b>	<b>37</b>
3	THE LARGE HADRON COLLIDER	39
3.1	The Injector Complex . . . . .	40
3.2	Operation of the Large Hadron Collider . . . . .	41
3.3	Luminosity . . . . .	43
3.4	Pile-up in proton-proton Collisions . . . . .	43
4	THE ATLAS DETECTOR	47
4.1	Coordinate System Used in the ATLAS Detector . . . . .	47
4.2	The Inner Detector . . . . .	48
4.2.1	The Pixel Detector . . . . .	48
4.2.2	The Silicon Microstrip Tracker . . . . .	50
4.2.3	The Transition Radiation Tracker . . . . .	50
4.3	The Calorimeters . . . . .	51
4.4	The Muon Spectrometer . . . . .	52
4.5	The Magnet System . . . . .	55
4.6	The Trigger System and Data Acquisition . . . . .	56
5	OBJECT RECONSTRUCTION IN THE ATLAS DETECTOR	61
5.1	Electrons . . . . .	61
5.2	Photons . . . . .	64
5.3	Muons . . . . .	66
5.4	Jets . . . . .	68
5.5	Overlap Removal . . . . .	71
5.6	Missing Transverse Momentum . . . . .	73
6	APPLICATION OF A NEURAL NETWORK TO PIXEL CLUSTERING	77
6.1	Clustering in the Pixel Detector . . . . .	77
6.1.1	Charge Interpolation Method . . . . .	78

6.1.2	Improving Measurement with Neural Networks . . . . .	78
6.2	Impact of the Neural Network . . . . .	79
6.2.1	The Neural Network in 13 TeV Data . . . . .	80
<b>IV</b>	<b>SEARCHING FOR SUPERSYMMETRY</b>	<b>85</b>
7	<b>BACKGROUND PROCESSES</b>	<b>87</b>
7.1	Data and Monte Carlo Samples . . . . .	89
8	<b>OBJECT IDENTIFICATION AND SELECTION</b>	<b>91</b>
8.1	Electrons . . . . .	91
8.2	Muons . . . . .	92
8.3	Jets . . . . .	92
8.4	Photons . . . . .	93
9	<b>EVENT SELECTION</b>	<b>95</b>
9.1	Trigger Strategy . . . . .	96
9.2	Signal Efficiency and Contamination . . . . .	98
10	<b>BACKGROUND ESTIMATION</b>	<b>101</b>
10.1	Flavor Symmetric Processes . . . . .	101
10.1.1	Flavor Symmetry Method . . . . .	101
10.1.2	Sideband Fit Method . . . . .	103
10.2	$Z/\gamma^*$ + jets Background . . . . .	105
10.2.1	Photon and $Z$ Event Selection . . . . .	107
10.2.2	Smearing of Photon Events . . . . .	108
10.2.3	$p_T$ Reweighting of Photon Events . . . . .	110
10.2.4	Determining $H_T$ and $m_{\ell\ell}$ . . . . .	111
10.2.5	Subtraction of $V\gamma$ Events . . . . .	113
10.2.6	Validation in Data . . . . .	115
10.3	Fake and Non-Prompt Leptons . . . . .	117
10.4	Diboson and Rare Top Processes . . . . .	118
11	<b>SYSTEMATIC UNCERTAINTIES</b>	<b>125</b>
11.1	Uncertainties on Data-Driven Backgrounds . . . . .	125
11.1.1	Uncertainties on the Flavor Symmetry Method . . . . .	125
11.1.2	Uncertainties on the $\gamma$ + jets Method . . . . .	129
11.1.3	Uncertainties on the Fakes Background . . . . .	132
11.2	Theoretical and Experimental Uncertainties . . . . .	133
11.3	Impact of Uncertainties on the Signal Region . . . . .	134
12	<b>RESULTS</b>	<b>139</b>
13	<b>INTERPRETATIONS</b>	<b>145</b>
<b>V</b>	<b>CONCLUSIONS</b>	<b>149</b>
14	<b>CONCLUSIONS AND OUTLOOK</b>	<b>151</b>
	<b>BIBLIOGRAPHY</b>	<b>153</b>

## LIST OF FIGURES

---

Figure 1	The Standard Model of particle physics, containing all known bosons and fermions, with the addition of the hypothetical graviton. [7] . . . . .	10
Figure 2	Gluon self coupling Feynman diagrams involving 3- and 4-gluon interactions. . . . .	14
Figure 3	Quark couplings to the different types of gauge bosons. The $q_{u,d}$ labels represent any up- or down-type quarks. . . . .	14
Figure 4	The running of the strong coupling constant, $\alpha_s$ . [14] . . . . .	15
Figure 5	Feynman diagrams of trilinear gauge couplings in the Standard Model (SM). . . . .	17
Figure 6	Feynman diagrams of weak couplings to leptons in the SM. . . . .	18
Figure 7	Feynman diagrams demonstrating Higgs couplings to the weak gauge bosons in the SM. . . . .	19
Figure 8	Feynman diagrams showing Higgs couplings to fermions in the SM. . . . .	20
Figure 9	2008 MSTW Parton Distribution Functions (PDFs) for various particle types given as a function of $x$ and $Q^2$ , the square of the parton-parton momentum transfer. [15] . . . . .	21
Figure 10	Cross-sections for many SM processes at the Tevatron and Large Hadron Collider (LHC) [16]. . . . .	22
Figure 11	Galactic rotation curve of velocity as a function of radius in NGC 3198. Included is the observed data, as well as the expected velocity distribution from a disk-shaped galaxy corresponding to the expected density from electromagnetic observations. Another curve corresponding to a halo-shaped matter distribution is superimposed, and the halo and disk are summed and fit to the data. [20] . . . . .	23
Figure 12	Two example vertices allowed by the Minimal Supersymmetric Standard Model (MSSM). . . . .	26
Figure 13	Running of the strong, weak, and electromagnetic coupling constants for the SM (left) and MSSM (right). [27] . . . . .	27
Figure 14	Feynman diagram of the decay considered in the simplified models used in the analysis presented in Part iv. . . . .	29
Figure 15	$13\text{ TeV}$ production cross-sections for sparticles, as a function of sparticle mass [32]. . . . .	30

Figure 16	Results of an 8 TeV search performed by the ATLAS collaboration in a signal region targeting events like those in Figure 14. The events in the signal region are displayed as a function of $m_{\ell\ell}$ , the invariant mass of the event's leading leptons. The SM backgrounds are shown with their full uncertainties based on data-driven background estimations, and two signals are superimposed on the distribution. The observed datapoints are higher than the expected background, with a total excess of $3.0\sigma$ [1]. . . . .	31
Figure 17	Results of an 8 TeV search performed by the Compact Muon Solenoid (CMS) collaboration in a signal region including a broad range of $m_{\ell\ell}$ . A $2.4\sigma$ local excess is seen in the low $m_{\ell\ell}$ region, and no excess of events is seen in the region with $m_{\ell\ell}$ consistent with an on-shell Z boson. The data is fit based on a data driven estimate of the flavor symmetric background (FS) and the Drell-Yan background (DY), with an additional component for the signal [34]. . . . .	32
Figure 18	Preliminary results from a 13 TeV search targeting the same signal region as Figure 16, performed on $3.2 \text{ fb}^{-1}$ of 2015 data. The events in the signal region are displayed as a function of $m_{\ell\ell}$ , the invariant mass of the event's leading leptons. Flavor symmetric and $Z/\gamma^* + \text{jets}$ backgrounds are taken from data-driven methods, while the other backgrounds are taken from Monte Carlo simulation (MC). They are compared to the data, which shows a $2.2\sigma$ excess of events. Distributions from two signal points are superimposed [2]. . . . .	33
Figure 19	Number of secondary vertices in a module in the first layer of the pixel detector in data (top) and MC (bottom). There are more events in the data than the MC [45]. . . . .	35
Figure 20	The LHC main collider ring and pre-accelerator Super Proton Synchrotron (SPS) overlaid on a map of Switzerland and France, with the four main LHC experiments identified. . . . .	39
Figure 21	The pre-accelerators of the LHC. . . . .	40
Figure 22	Bunch structure in the Proton Synchrotron (PS), SPS, and LHC. . . . .	41
Figure 23	Cross-section of a cryodipole magnet in the LHC. . .	
Figure 24	Beam spot in the ATLAS detector for one run in 2015. Distributions show only the highest $p_T$ vertex per event. Left is the $x - y$ distribution of vertices, while the right plot shows the $x - z$ distribution. . .	42

Figure 25	Instantaneous luminosity of one fill of 7 TeV data in 2011. . . . .	44
Figure 26	ATLAS luminosity for Run 1 and Run 2, as of September 2016. . . . .	44
Figure 27	Average number of interactions per crossing shown for 2015 and 2016 separately, as well as the sum of the two years. . . . .	45
Figure 28	Diagram of the ATLAS detector, with subsystems and magnets identified. . . . .	47
Figure 29	Diagram of the ATLAS Inner Detector, containing the Pixel, SCT, and TRT subsystems. . . . .	49
Figure 30	Diagram of one-quarter of the ATLAS Inner Detector in the $R - z$ plane, with lines drawn to indicate various $\eta$ locations. . . . .	50
Figure 31	The calorimeter system of the ATLAS detector. . . . .	51
Figure 32	Layout of the LAr calorimeter module at central $\eta$ [48]. . . . .	52
Figure 33	An $x$ - $y$ view of the Muon Spectrometer (MS). In it, the three barrel layers are visible, as well as the overlapping, differently sized chambers. The outer layer of the MS is about 20m in diameter. . . . .	53
Figure 34	An $r$ - $z$ view of the MS. The three layers of the barrel and endcap MS are visible, and all muons at $ \eta  < 2.7$ should traverse three detectors, assuming they propagate in an approximately straight line from the interaction point. . . . .	54
Figure 35	The magnet system of the ATLAS detector. The inner cylinder shows the solenoid which gives a uniform magnetic field in the Inner Detector (ID). Outside of that are the barrel and endcap toroids, which provide a non-uniform magnetic field for the MS. . . . .	55
Figure 36	Plots of the magnetic field within the ATLAS detector. Top is the field (broken into its $R$ and $z$ components) as a function of $z$ for several different values of $R$ . Bottom is the field integral through the Monitored Drift Tubes (MDTs) as a function of $ \eta $ for two different $\phi$ values. . . . .	57
Figure 37	Level One ( $L_1$ ) trigger rates for a run in July 2016 as a function of luminosity block, an approximately 60-second long period of data-taking. The total rate is lower than the combined stack because of overlapping triggers. . . . .	58
Figure 38	High Level Trigger (HLT) trigger rates for a run in July 2016 as a function of luminosity block, an approximately 60-second long period of data-taking. The total rate is lower than the combined stack because of overlapping triggers. . . . .	59

Figure 39	Trigger efficiencies as a function of $E_T$ for data and MC. Efficiencies are given for offline selected loose electrons. . . . .	59
Figure 40	Identification efficiencies from MC samples for Loose, Medium, and Tight working points. Left is the efficiency for identification of true electrons taken from $Z \rightarrow ee$ MC, and right is the efficiency for misidentification of jets as electrons taken from dijet MC [54]. . . . .	62
Figure 41	Combined electron reconstruction and identification efficiencies measured as a function of $\eta$ for data (using the tag-and-probe method on $Z \rightarrow ee$ events) and $Z \rightarrow ee$ MC. Distributions include all electrons with $E_T > 15$ GeV. [54]. . . . .	63
Figure 42	Comparison of Tight identification efficiency measurements from data and $Z \rightarrow \ell\ell\gamma$ MC for unconverted (left) and converted (right) photons, with an inclusive $\eta$ selection. The bottom of each figure shows the ratio of data and MC efficiencies. [57]. . . . .	65
Figure 43	Muon reconstruction efficiency for the Medium and (for small $ \eta $ ) Loose working points measured with $Z \rightarrow \mu\mu$ events in data using the tag-and-probe method and in MC as a function of $\eta$ . The ratio between the two is shown at the bottom. [59] . . . . .	67
Figure 44	Muon reconstruction efficiency for the High- $p_T$ working point measured with $Z \rightarrow \mu\mu$ events in data using the tag-and-probe method and in MC as a function of $\eta$ . The ratio between the two is shown at the bottom. [59] . . . . .	68
Figure 45	Distribution of event $p_T$ density, $\rho$ , taken from MC dijets for different numbers of primary vertices. [61]	70
Figure 46	Energy response as a function of energy and $\eta$ for Electromagnetic (EM) jets in dijet MC. [61] . . . . .	70
Figure 47	Dijet MC distributions of the number of pile-up jets passing the Jet Vertex Tagger (JVT) and Jet Vertex Fraction (JVF) cuts (left) and the efficiency for jets from the primary vertex (right) as a function of number of primary vertices in the event [62]. . . . .	71
Figure 48	Distribution of MV2c20 output for $b$ -jets, $c$ -jets, and light-flavor jets in $t\bar{t}$ MC [63]. . . . .	72
Figure 49	Distributions of the resolution of the $x$ and $y$ components of Track Soft Term (TST) $E_T^{\text{miss}}$ in $Z \rightarrow \mu\mu$ events in data and MC [65]. . . . .	73

Figure 50	Distributions of the jet term (top left), muon term (top right), and <b>TST</b> (bottom) $E_T^{\text{miss}}$ in $Z \rightarrow \mu\mu$ events in data and <b>MC</b> . In the jet term distribution, the feature at zero is due to events with no jets, and the spike at 20 GeV corresponds to the minimum jet $p_T$ considered for the analysis [65]. . . . .	75
Figure 51	A few possible types of clusters in the Pixel Detector. (a) shows a single particle passing through a layer of the detector, (b) shows two particles passing through the detector, creating a single merged cluster, and (b) shows a single particle emitting a $\delta$ -ray as it passes through the detector [66]. . . . .	77
Figure 52	One example of a two-particle cluster and its truth information compared with the output of the Neural Networks ( <b>NNs</b> ). The boxes represent pixels, with a color scale indicating Time Over Threshold ( <b>ToT</b> ). At top, the $p(N = i)$ values give the output of the Number <b>NN</b> , the probabilities that the cluster contains 1, 2, and 3 particles. Given the highest probability is for $N = 2$ , the other <b>NNs</b> predict the position and errors of the two particles (in white). The black arrows and squares represent the truth information from the cluster, and the black dot and dotted line show the position measurement for the un-split cluster [66]. . . . .	80
Figure 53	$x$ resolutions for clusters with 3 (top) and 4 (bottom) pixels in the $x$ direction in 7 TeV data for Connected Component Analysis ( <b>CCA</b> ) (using only charge interpolation to determine position) and <b>NN</b> clustering taken from <b>MC</b> [66]. . . . .	81
Figure 54	Performance of the pixel neural network used to identify clusters created by multiple charged particles, as a function of constant coherent scaling of the charge in each pixel in the cluster. The top figure shows the rate at which the neural network wrongly identifies clusters with one generated particle as clusters with multiple particles. The bottom figure shows the rate at which the neural network correctly identifies clusters generated by multiple particles as such. . . . .	83
Figure 55	Fraction of cluster classes as a function of the distance between tracks for IBL (top) and 2nd pixel layer (bottom). . . . .	84
Figure 56	An example Feynman diagram of $t\bar{t}$ production and decay. . . . .	87
Figure 57	An example Feynman diagram of the production and decay of a WZ event. . . . .	88

Figure 58	An example Feynman diagram of the production and decay of a $Z/\gamma^* + \text{jets}$ event. . . . .	88
Figure 59	Schematic diagrams of the control, validation and signal regions for the on-shell $Z$ (top) and edge (bottom) searches. For the on-shell $Z$ search the various regions are shown in the $m_{\ell\ell} - E_T^{\text{miss}}$ plane, whereas in the case of the edge search the signal and validation regions are depicted in the $H_T - E_T^{\text{miss}}$ plane. . . . .	96
Figure 60	Signal region acceptance (left) and efficiency (right) in SRZ for the simplified model with gluino pair production with $\tilde{\chi}_2^0$ decays to $\tilde{\chi}_1^0$ and an on-shell $Z$ boson with 1GeV neutralino LSP. Acceptance is calculated by applying the signal-region kinematic requirements to truth objects in MC, which do not suffer from identification inefficiencies or measurement resolutions. . . . .	98
Figure 61	Expected signal contamination in CRT (left) and CR-FS (right) for the signal model with gluino pair production, where the gluinos decay to quarks and a neutralino, with the neutralino subsequently decaying to a $Z$ boson and a 1GeV neutralino LSP. . . . .	99
Figure 62	Expected signal contamination in VRS (left) and VRT (right) for the signal model with gluino pair production, where the gluinos decay to quarks and a neutralino, with the neutralino subsequently decaying to a $Z$ boson and a 1GeV neutralino LSP. . . . .	99
Figure 63	Comparison of data and MC in a selection like SRZ, without the $E_T^{\text{miss}}$ cut. . . . .	105
Figure 64	MC comparison of boson $p_T$ in a selection of photon and $Z \rightarrow \ell\ell$ events with $H_T > 600$ GeV. . . . .	107
Figure 65	$E_{T,\parallel}^{\text{miss}}$ distributions in MC for $Z+\text{jets}$ ee (left) and $\mu\mu$ (right) channels compared to $\gamma + \text{jets}$ in an inclusive region with $H_T > 600$ GeV. . . . .	109
Figure 66	$E_{T,\parallel}^{\text{miss}}$ distributions in MC for $Z+\text{jets}$ ee (left) and $\mu\mu$ (right) channels compared to $\gamma + \text{jets}$ in an inclusive region with $H_T > 600$ GeV after the smearing procedure has been performed. These distributions have also been $p_T$ reweighted, as described in Section 10.2.3. . . . .	110
Figure 67	Photon reweighting factors for the ee (left) and $\mu\mu$ (right) channels derived from data and MC. . . . .	111
Figure 68	$E_T^{\text{miss}}$ distribution comparing MC distributions of photon and $Z$ events before any smearing is applied (top), with only $p_T$ reweighting applied (bottom left), and after $p_T$ reweighting and smearing have both been applied (bottom right) in the ee channel of 2016 data. . . . .	112

Figure 69	$E_T^{\text{miss}}$ distribution comparing MC distributions of photon and Z events before any smearing is applied (top), with only $p_T$ reweighting applied (bottom left), and after $p_T$ reweighting and smearing have both been applied (bottom right) in the $\mu\mu$ channel of 2016 data. . . . .	113
Figure 70	$Z/\gamma^* + \text{jets}$ MC $m_{\ell\ell}$ distribution compared to the prediction from $\gamma + \text{jets}$ method performed on MC (left) and the prediction from $\gamma + \text{jets}$ method performed on data (right). . . . .	114
Figure 71	Comparison of data and MC in CR- $\gamma$ without any $H_T$ cut, including the contributions from various $V\gamma$ processes. . . . .	114
Figure 72	Total $\gamma + \text{jets}$ data prediction in SRZ (excluding the $E_T^{\text{miss}}$ cut) and the prediction after the $V\gamma$ subtraction. . . . .	115
Figure 73	$E_T^{\text{miss}}$ distribution in VRZ $ee$ (left) and $\mu\mu$ (right) with total data yield compared to the sum of the prediction from the $\gamma + \text{jets}$ method, the prediction from the flavor symmetry method, the prediction from the fake background estimation (included under “other”), and the remaining backgrounds taken from MC. . . . .	116
Figure 74	$\Delta\phi(\text{jet}, p_T^{\text{miss}})$ distribution in for the leading jet (left) and the subleading jet (right). The comparison is performed in VRZ with the cut on $\Delta\phi(\text{jet}_{12}, p_T^{\text{miss}})$ removed. The total data yield is compared to the sum of the prediction from the $\gamma + \text{jets}$ method, the prediction from the flavor symmetry method, the prediction from the fake background estimation (included under “other”), and the remaining backgrounds taken from MC. . . . .	116
Figure 75	Sub-leading lepton $p_T$ for $ee$ (left) and $\mu\mu$ (right) events in the tight-tight region used to measure the real-lepton efficiency for 2016. . . . .	118
Figure 76	Sub-leading lepton $p_T$ for $\mu e$ (left) and $\mu\mu$ (right) events in the tight-tight region used to measure the fake-lepton efficiency for 2016. . . . .	119
Figure 77	Same sign validation regions in the $ee$ (top left), $\mu\mu$ (top right), $e\mu$ (bottom left) and $\mu e$ (bottom right) channels combining 2015+2016 data. Uncertainty bands include both statistical and systematic uncertainties. . . . .	119
Figure 78	Distribtuions of data and MC in VR-WZ. Reconstructed transverse mass of the W (top) and mass of the Z (bottom). . . . .	121
Figure 79	Distribtuions of data and MC in VR-WZ. $p_T$ of the W (top) and Z (bottom). . . . .	122

Figure 80	Distribtuions in VR-WZ. On the top, mass of the Z bosons in the event, and on the bottom, $p_T$ of the Z bosons. . . . .	123
Figure 81	<b>MC</b> closure plots of VRS (top) and SRZ (bottom). The number of events from MC (black points) is compared to the number of events predicted from the flavor symmetry method (yellow histogram). The comparison is performed before the expanded $m_{\ell\ell}$ window is used to predict the on-Z bin, but because the shape is taken from the same <b>MC</b> , the result is identical. . . . .	126
Figure 82	Measurements of $k$ , the ratio of electron to muon events, in bins of $p_T$ and $\eta$ . On the top is the measurements indexed by the leading lepton, while the measurements indexed by the subleading lepton are on the bottom. These efficiencies are for the 2016 dataset. . . . .	127
Figure 83	$\alpha$ , the trigger efficiency ratio, calculated as a function of $E_T^{\text{miss}}$ from three different sources: data (blue), the usual skimmed $t\bar{t}$ <b>MC</b> (red), and an unskimmed $t\bar{t}$ <b>MC</b> (green). . . . .	129
Figure 84	Plots of the fraction of on-Z events with a VR-FS-like selection as a function of $H_T$ . The top figure shows 2015 data and <b>MC</b> while the bottom figure shows the same for 2016. . . . .	130
Figure 85	$E_T^{\text{miss}}$ distributions for $\gamma + \text{jets}$ predictions using different reweighting variables, as well as distributions with the nominal reweighting but with smearing functions taken from data and from <b>MC</b> in a $\geq 2$ -jet region. . . . .	131
Figure 86	<b>MC</b> closure of the $\gamma + \text{jets}$ method as a function of $E_T^{\text{miss}}$ comparing the <b>MC</b> prediction of the Z background with the $\gamma + \text{jets}$ method performed on $\gamma + \text{jets}$ <b>MC</b> . The uncertainty band includes both statistical and reweighting uncertainties. . . . .	132
Figure 87	Distributions of $m_T(\ell, E_T^{\text{miss}})$ , the transverse mass of the lepton and the $E_T^{\text{miss}}$ in a Validation Region ( <b>VR</b> ) designed to target $W\gamma$ processes. Top is the distribution with a $E_T^{\text{miss}}$ cut at 100 GeV, and bottom is the same distribution with a $E_T^{\text{miss}}$ cut of 200 GeV. . . . .	137

Figure 88	Comparison of background predictions and data yields in four validation regions, as well as the signal region. Definitions of all regions can be found in <a href="#">Table 7</a> , with both rare top and fake backgrounds grouped together under the “other” label. The uncertainty band includes all statistical and systematic uncertainties. Below is a panel of the one-sided statistical significances of the deviations between the predicted and observed quantities for each region. . . . .	<a href="#">139</a>
Figure 89	Comparisons as a function of $m_{\ell\ell}$ of background predictions with observed data in an SRZ-like region, with the $m_{\ell\ell}$ cut removed. Left is the same-flavor channel, where all background shapes are taken from <a href="#">MC</a> and scaled to their SRZ predictions, except for the $Z/\gamma^* + \text{jets}$ background, which is taken entirely from the data-driven background. Right is the different-flavor channel, in which the backgrounds are taken directly from <a href="#">MC</a> , except for $t\bar{t}$ , which is scaled to match the total data yield. . . . .	<a href="#">141</a>
Figure 90	Distributions of observed data, background predictions, and simulated signals are shown in SRZ as a function of $m_{\ell\ell}$ , $p_T^{\ell\ell}$ , $E_T^{\text{miss}}$ , $H_T$ , number of jets, and number of $b$ -jets. The two example signals have $(m(\tilde{g}), m(\tilde{\chi}_2^0)) = (1095, 205)$ GeV. All background shapes are taken from <a href="#">MC</a> , and in the case of flavor symmetric and $Z/\gamma^* + \text{jets}$ backgrounds, their yields are scaled to match the data-driven predictions. Uncertainties include statistical and systematic components. . . . .	<a href="#">142</a>
Figure 91	Comparisons as a function of $\Delta\phi(\text{jet}_{12}, p_T^{\text{miss}})$ of background predictions with observed data in an SRZ-like (left) and VRS-like (right) region, with the $\Delta\phi(\text{jet}_{12}, p_T^{\text{miss}})$ cut removed. All background shapes are taken from <a href="#">MC</a> and scaled to their SRZ predictions, except for the $Z/\gamma^* + \text{jets}$ background, which is taken entirely from the data-driven background. . . . .	<a href="#">144</a>

Figure 92	Expected and observed exclusion contours derived from the results in SRZ for the (top) $\tilde{g}-\tilde{\chi}_2^0$ on-shell grid and (bottom) $\tilde{q}-\tilde{\chi}_2^0$ on-shell grid. The dashed blue line indicates the expected limits at 95% CL and the yellow band shows the $1\sigma$ variation of the expected limit as a consequence of the uncertainties in the background prediction and the experimental uncertainties in the signal ( $\pm 1\sigma_{\text{exp}}$ ). The observed limits are shown by the solid red line, with the dotted red lines indicating the variation resulting from changing the signal cross section within its uncertainty ( $\pm 1\sigma_{\text{theory}}^{\text{SUSY}}$ ). . . . .	<a href="#">146</a>
Figure 93	Expected and observed exclusion contours derived from the results in SRZ for the $\tilde{g}-\tilde{\chi}_1^0$ on-shell grid. The dashed blue line indicates the expected limits at 95% CL and the yellow band shows the $1\sigma$ variation of the expected limit as a consequence of the uncertainties in the background prediction and the experimental uncertainties in the signal ( $\pm 1\sigma_{\text{exp}}$ ). The observed limits are shown by the solid red line, with the dotted red lines indicating the variation resulting from changing the signal cross section within its uncertainty ( $\pm 1\sigma_{\text{theory}}^{\text{SUSY}}$ ). . . . .	<a href="#">147</a>
Figure 94	Expected 95% Confidence Level (CL) exclusion contours (dashed) and $5\sigma$ discovery contours (solid) for $L_{\text{int}} = 300^{-1}$ (black) and $3000^{-1}$ (red) for gluino pair-production, with $1\sigma$ bands representing the uncertainty on the production cross-section. Superimposed is the observed 8 TeV exclusion for similar models. [105] . . . . .	<a href="#">152</a>

## LIST OF TABLES

---

Table 1	Supermultiplets of supersymmetric and SM particles. Sfermions, on the first five rows, are all spin-0. Higgsinos and gauginos are all spin-1/2. Three sets of each fermion’s supermultiplet exist, one for each generation. [25] . . . . .	25
Table 2	Simulated background event samples used in this analysis with the corresponding matrix element and parton shower generators, cross-section order in $\alpha_s$ used to normalise the event yield, underlying-event tune and PDF set. . . . .	90
Table 3	Summary of the electron selection criteria. The signal selection requirements are applied on top of the baseline selection. . . . .	91
Table 4	Summary of the muon selection criteria. The signal selection requirements are applied on top of the baseline selection. . . . .	92
Table 5	Summary of the jet and $b$ -jet selection criteria. The signal selection requirements are applied on top of the baseline requirements. . . . .	93
Table 6	Summary of the photon selection criteria. . . . .	94
Table 7	Overview of all signal, control and validation regions used in the on-shell Z search. More details are given in the text. The flavour combination of the dilepton pair is denoted as either “SF” for same-flavour or “DF” for different flavour. All regions require at least two leptons, unless otherwise indicated. In the case of CR $\gamma$ , VR-WZ, VR-ZZ, and VR-3L the number of leptons, rather than a specific flavour configuration, is indicated. The main requirements that distinguish the control and validation regions from the signal region are indicated in bold. Most of the kinematic quantities used to define these regions are discussed in the text. The quantity $m_T(\ell_3, E_T^{\text{miss}})$ indicates the transverse mass formed by the $E_T^{\text{miss}}$ and the lepton which is not assigned to either of the Z-decay leptons. . . . .	97
Table 8	Lepton trigger requirements used for the analysis in different regions of lepton- $p_T$ phase space. . . . .	98

Table 9	Yields in signal and validation regions for the flavor symmetric background. Errors include statistical uncertainty, uncertainty from MC closure, uncertainty from the $k$ and $\alpha$ factors, uncertainty due to deriving triggers efficiencies from a DAOD, and uncertainty on the MC shape used to correct for the $m_{\ell\ell}$ expansion. . . . .	103
Table 10	Background fit results from the sideband fit method. The $t\bar{t}$ MC's normalization is taken as a free parameter in the fit to data in CRT, then that normalization factor is applied in SRZ. The results are shown here both divided between the $ee$ and $\mu\mu$ channels and summed together. All other backgrounds are taken from MC in CRT, while in SRZ, the $Z/\gamma^* + \text{jets}$ contribution is taken from the $\gamma + \text{jets}$ method. The uncertainties quoted include both statistical and systematic components. . . . .	104
Table 11	Summary of the $t\bar{t}$ normalization factors calculated by the sideband fit to CRT and VRT for the 2015+2016 data. . . . .	105
Table 12	Comparison of Flavor Symmetric (FS) background predictions from the nominal method, the flavor symmetry method, and the cross-check, the sideband fit method. Uncertainties include statistical and systematic uncertainties in both cases. . . . .	106
Table 13	List of triggers used to collect photon events in 2015 and 2016 data-taking. . . . .	108
Table 14	Control regions used to measure efficiencies of real and fake leptons. The flavour combination of the dilepton pair is denoted as either "SF" for same-flavour or "DF" for different flavour. The charge combination of the leading lepton pairs are given as "SS" for same-sign or "OS" for opposite-sign. . . . .	118
Table 15	Yields in validation regions. In VRS, data-driven background estimates are used for $Z/\gamma^* + \text{jets}$ , fakes, and FS processes. All other backgrounds are taken from MC, including all backgrounds in the multi-lepton VRS. Uncertainties include statistical and systematic components. . . . .	120

Table 16	Uncertainties in the on-Z signal and validation regions. Nominal predictions are given with statistical uncertainty (including uncertainty from subtracted backgrounds), MC Closure uncertainty, uncertainty on the prediction from varying $k$ and $\alpha$ by their statistical uncertainties, comparing the efficiencies from AODs to that of DAODs, and on the $m_{\ell\ell}$ widening, which includes MC statistics and a data/MC comparison in a loosened region. . . . .	<a href="#">125</a>
Table 17	Uncertainty breakdown for the $\gamma + \text{jets}$ method in SRZ. Uncertainties considered are the impact of MC uncertainty on $V\gamma$ backgrounds, MC closure, uncertainty on $m_{\ell\ell}$ shape (also determined via MC closure), reweighting uncertainties, smearing uncertainties, and statistical uncertainty on the $\gamma + \text{jets}$ events used in the method. . . . .	<a href="#">133</a>
Table 18	Systematic uncertainties on the fake-lepton background for on-Z regions for 2015+2016 yields. The nominal yield includes statistical uncertainty from the baseline selection in a given region. The following rows indicate the results of varying the real and fake lepton efficiencies up and down by by their statistical uncertainty. Real cont. gives an uncertainty on the the contamination of real leptons in the fake lepton efficiency. $b$ -jet and no $b$ -jet indicate the impact of requiring or vetoing $b$ -tagged jets in the regions used to measure the fake efficiency. . . . .	<a href="#">133</a>
Table 19	Fractional uncertainties of dibosons in signal and validation regions from Sherpa scale variations. . .	<a href="#">135</a>
Table 20	Comparison of yields in on-Z and off-Z regions in Sherpa and Powheg diboson MC at $14.7 \text{ fb}^{-1}$ . . .	<a href="#">135</a>
Table 21	Overview of the dominant sources of systematic uncertainty on the total background estimate in the signal regions. The values shown are relative to the total background estimate, shown in %. . . . .	<a href="#">136</a>
Table 22	Number of events expected and observed in the $ee$ , $\mu\mu$ , and combined channels. Expected predictions include all systematic and statistical uncertainties discussed in <a href="#">Chapter 11</a> . Also shown is the discovery $p$ -value for zero signal strength ( $p(s = 0)$ ) [99], Gaussian significance, 95% CL observed and expected upper limits on the number of signal events ( $S^{95}$ ), and the corresponding observed upper limit on the visible cross section ( $\langle e\sigma \rangle_{\text{obs}}^{95}$ ). . . . .	<a href="#">140</a>

## LISTINGS

---

## ACRONYMS

---

- IBL Insertable B-Layer  
MS Muon Spectrometer  
ID Inner Detector  
SCT Silicon Microstrip Tracker  
TRT Transition Radiation Tracker  
NN Neural Network  
CCA Connected Component Analysis  
ToT Time Over Threshold  
MDT Monitored Drift Tube  
CSC Cathode-Strip Chamber  
RPC Resistive Plate Chamber  
TGC Thin Gap Chamber  
L<sub>1</sub> Level One  
HLT High Level Trigger  
L<sub>1</sub>Calo L<sub>1</sub> Calorimeter Trigger  
L<sub>1</sub>Topo L<sub>1</sub> Topological Trigger  
CTP Central Trigger Processor  
TTC Trigger Timing and Control  
ROB Read Out Board  
RoI Region of Interest  
LHC Large Hadron Collider  
LEP Large Electron-Positron  
SPS Super Proton Synchrotron  
CMS Compact Muon Solenoid  
ALICE A Large Ion Collider Experiment  
LHCb Large Hadron Collider beauty  
RF Radiofrequency

PSB	Proton Synchrotron Booster
PS	Proton Synchrotron
OR	Overlap Removal
EM	Electromagnetic
LCW	Local Cluster Weighting
JES	Jet Energy Scale
JER	Jet Energy Resolution
JVT	Jet Vertex Tagger
JVF	Jet Vertex Fraction
CST	Calorimeter Soft Term
TST	Track Soft Term
MC	Monte Carlo simulation
SM	Standard Model
BSM	Beyond the Standard Model
SUSY	Supersymmetry
QCD	Quantum Chromodynamics
PDF	Parton Distribution Function
DM	Dark Matter
LO	Leading Order
NLO	Next to Leading Order
NLO+NLL	Next-to-Leading-Logarithmic Accuracy
SUSY	Supersymmetry
MSSM	Minimal Supersymmetric Standard Model
LSP	Lightest Supersymmetric Particle
AOD	Analysis Object Data
dAOD	derived AOD
SR	Signal Region
VR	Validation Region
CR	Control Region
FS	Flavor Symmetric

CL Confidence Level

HL-LHC High Luminosity Large Hadron Collider



<sup>1</sup>

## Part I

<sup>2</sup>

### INTRODUCTION

<sup>3</sup>



4

5 INTRODUCTION

---

6 In 2010, the LHC began colliding protons in its 27 km ring, taking its place  
7 as the most powerful in a long line of accelerators aimed at uncovering the  
8 fundamental rules that govern particle physics. Its primary goal was to  
9 complete the Standard Model of particle physics by discovering the Higgs  
10 boson, the last remaining particle that physicists felt sure must exist. With  
11 its presence, the Standard Model would be consistent, explaining every ob-  
12 served interaction of known particles, with a complete mathematic frame-  
13 work to describe each feature. However, even with a Higgs boson, the  
14 Standard Model contained hints that it might be incomplete, suspicious  
15 features that suggested that at a higher energy, there might be something  
16 more.

17 In 2012, the ATLAS and CMS Experiments discovered the Higgs boson,  
18 leaving the LHC physics community without a single primary goal, but  
19 rather a host of theories to explore, each extending the Standard Model  
20 in a different way. Each theory attempts to solve one of the mysteries left  
21 by the Standard Model, providing an explanation for Dark Matter, sug-  
22 gesting a mechanism that could explain Gravity's weakness, or explain-  
23 ing the Higgs boson's mass. For decades, the most popular of these has  
24 been Supersymmetry, which proposes a fermionic symmetry and requires  
25 a menagerie of new Supersymmetric particles, none of which has yet been  
26 observed.

27 Supersymmetry simultaneously solves more of the Standard Model's  
28 problems than any other, making it appealing to theorists and experimen-  
29 talists alike. But in order to do this, Supersymmetric particles must appear  
30 with masses of approximately 1 TeV, precisely the range of energies the  
31 LHC is capable of exploring. In 2015, after a three-year shutdown, the LHC  
32 nearly doubled the energy of its collisions, opening up new territory to  
33 be explored by analyzers, and providing data that could either discover or  
34 exclude many Supersymmetric models.

35 The analysis presented in this thesis searches for Supersymmetry, seek-  
36 ing to identify events in which Supersymmetric particles are produced in  
37 proton-proton collisions, then decay via a Z boson to a chargeless Super-  
38 symmetric particle which escapes ATLAS without detection. A similar AT-  
39 LAS search, performed with data from the lower-energy collisions 2012,  
40 observed a  $3\sigma$  excess of events over the expected Standard Model back-  
41 ground [1].

42 The excess generated a great deal of interest in this channel, and re-  
43 investigating it became a top priority when the upgraded LHC turned back  
44 on in 2015. A preliminary search, performed using the 2015 data only, was  
45 released at the end of that year. Again an excess was observed, this time  
46 with a significance of  $2.2\sigma$  [2].

47 This thesis describes a search for Supersymmetry performed in this  
48 channel using data taken by the ATLAS detector in 2015 and 2016, includ-  
49 ing an explanation of the theory and motivation behind the search, and a  
50 description of the LHC and the ATLAS detector. The remaining chapters  
51 are laid out as follows:

52 CHAPTER 2 outlines the Standard Model of Particle Physics and the  
53 benefits of extending it to include Supersymmetry, then continues on to  
54 introduce the specific models used in the search presented in later chapters.  
55 It also provides an overview of the process of generating MC for use in the  
56 ATLAS experiment.

57 CHAPTER 3 describes the LHC and its operation, including the magnet  
58 system, the preaccelerator complex, and some of the phenomenology of  
59 collisions at 13 TeV.

60 CHAPTER 4 contains descriptions of the many pieces of the ATLAS de-  
61 tector, and how they serve to detect particles coming from LHC collisions.  
62 ATLAS’s magnet and trigger systems are also discussed.

63 CHAPTER 5 details the process of reconstruction, the procedure by which  
64 the electric signals in the ATLAS detector are interpreted as particles to be  
65 used for analysis.

66 CHAPTER 6 presents a neural network designed to improve tracking in  
67 the ATLAS Pixel Detector, and describes the benefits of its implementation.

68 CHAPTER 7 lists the main backgrounds for the Supersymmetry search  
69 described in this thesis, and provides general ideas of how they can be  
70 reduced.

71 CHAPTER 8 outlines how objects are identified and selected for this anal-  
72 ysis, referencing many of the working points defined in Chapter 5.

73 CHAPTER 9 explains the analysis’s search strategy, defining signal, con-  
74 trol, and validation regions, and briefly describing how each contributes  
75 to the search.

76 CHAPTER 10 describes, for each of the backgrounds described in Chap-  
77 ter 7, how estimates of the Standard Model contributions to the signal  
78 region are performed.

79 CHAPTER 11 builds off of Chapter 11, and continues to detail how the  
80 uncertainties on each estimate are assessed.

81 CHAPTER 12 shows the results of the analysis, comparing expectations  
82 based on background estimates to the observed data.

<sup>83</sup> CHAPTER 13 provides interpretations of the results, and explains the  
<sup>84</sup> statistical procedure used to define exclusions on Supersymmetric models.

<sup>85</sup> CHAPTER 14 concludes with a summary of the results, and an outlook  
<sup>86</sup> for future searches.



87

## Part II

88

### THEORY AND MOTIVATION

89

This section describes the theoretical foundation for the analysis presented in [Part iv](#). It includes an overview of the Standard Model, including its phenomenology in a  $pp$  collider. The theory of Supersymmetry is explained, and the motivation for extending the Standard Model to include it is presented. In addition, this section includes an explanation of Monte Carlo generators and details about the specific form of Supersymmetry searched for in this analysis.

90

91

92

93

94

95

96



97

98 THEORY AND MOTIVATION

---

99 The Standard Model ([SM](#)) of particle physics represents all particles and in-  
100 teractions currently known. It is formulated using the principles of Quan-  
101 tum Field Theory, with the constraints of several symmetries and physical  
102 requirements to determine the rules for allowed interactions [3]. Devel-  
103 oped in the 1960s and 70s [4–6], it has been immensely successful at pre-  
104 dicting the existence of particles before their discovery, and has held up  
105 to many high-precision tests. Despite this success, it has several shortcom-  
106 ings. Though the [SM](#) is likely correct at the energies thus far probed, it  
107 may be missing key components that become more important at higher  
108 energies. Models supplementing the [SM](#) with additional particles and in-  
109 teractions are referred to as Beyond the Standard Model ([BSM](#)) theories.

110 One possible extension of the [SM](#) is Supersymmetry ([SUSY](#)), a theory  
111 which postulates an additional symmetry between bosons and fermions  
112 to the [SM](#), creating a spectrum of [SUSY](#) particles (sparticles) which interact  
113 with the particles of the [SM](#). This theory motivates the search performed  
114 in [Part iv](#) of this thesis, and its theoretical appeals are discussed in this  
115 section, along with specific models considered in the search.

## 116 2.1 THE STANDARD MODEL

117 The [SM](#) of particle physics describes the interactions of all of the particles  
118 currently known to exist, and consists of matter particles and force carriers,  
119 as well as the Higgs boson, which fits into neither category. This model has  
120 been unprecedentedly successful in predicting new particles and phenom-  
121 ena, including the prediction of the Higgs boson almost 50 years before its  
122 discovery in 2012, which completed the [SM](#).

123 The particles of the [SM](#) are divided into two categories: fermions and  
124 bosons [3]. The fermions comprise all the matter described by the [SM](#), and  
125 are spin- $\frac{1}{2}$  particles. The bosons are integer spin-particles, most of which  
126 are spin-1. These particles provide a mechanism to explain three of the four  
127 forces known to physics, with gravity still lacking a quantum formulation.  
128 The Higgs boson, the only spin-0 particle in the [SM](#), provides a mechanism  
129 for giving mass to the other particles. The full [SM](#), with the addition of the  
130 hypothetical graviton, is presented in [Figure 1](#).

131 2.1.1 *Matter*

132 The matter described by the [SM](#) is made up of fermions, spin- $\frac{1}{2}$  particles  
133 which can be broken into two groups, quarks and leptons. The leptons all  
134 interact weakly, while the quarks additionally interact strongly. Half the  
135 leptons as well as all quarks are electromagnetically charged.

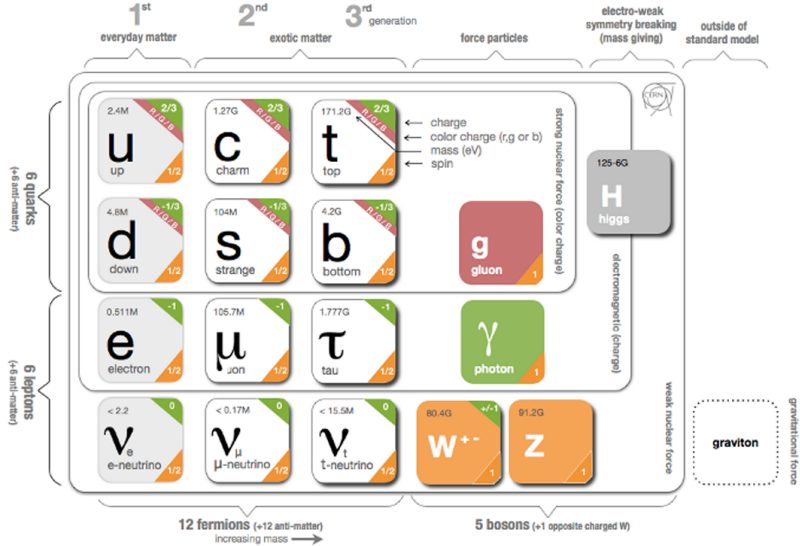


Figure 1: The Standard Model of particle physics, containing all known bosons and fermions, with the addition of the hypothetical graviton. [7]

### 136 2.1.1.1 Leptons

137 Leptons, as seen in the bottom left of Figure 1, exist in three generations,  
 138 each labeled by a flavor: electron, muon, and tau. In the case of the massive  
 139 leptons, these flavors are mass eigenstates, and the generations are placed  
 140 in an order based on increasing mass. Each massive lepton is negatively  
 141 electromagnetically charged and has a positively charged anti-particle.

142 The three neutrinos exist in the same flavors as the massive leptons, but  
 143 these flavor eigenstates do not correspond exactly to mass eigenstates [8].  
 144 As a consequence, neutrinos oscillate between flavors as they propagate  
 145 through space. These oscillations are the only evidence of neutrino mass,  
 146 which is bound from below by the mass splittings determined from the  
 147 oscillation and bound from above by cosmological limits on the universe's  
 148 mass density [9]. Though it is still uncertain if the masses of the neutrinos  
 149 follow the same hierarchy as the massive leptons, that expected ordering  
 150 is slightly experimentally preferred over the inverted hierarchy [10].

151 Unlike the massive leptons, the neutrinos are not electrically charged,  
 152 and it is not yet known whether each neutrino has a separate anti-particle,  
 153 or if it is its own antiparticle. Because they are not electromagnetically  
 154 charged, they can only interact weakly, making them extremely difficult  
 155 to detect. As a consequence of their ability to evade detection, neutrinos'  
 156 properties are nearly impossible to study with general purpose particle  
 157 detectors.

158 The SM conserves lepton number,  $L$ , which is defined as the number  
 159 of leptons minus the number of anti-leptons in a state, and can also be  
 160 defined for each lepton flavor. Though there are anomalies that appear in  
 161 second order SM interactions which could provide very small violations  
 162 of this conservation, it holds to great precision in experiment.  $\mu \rightarrow e\gamma$

163 branching ratios, for example, have been constrained to  $10^{-13}$  [11]. As a  
164 consequence of this conservation, the lightest massive lepton, the electron,  
165 is stable.

166 2.1.1.2 *Quarks*

167 Quarks, as seen in the top left of [Figure 1](#), are also electromagnetically  
168 charged particles that interact weakly, but are differentiated from the leptons by their strong interactions. They are also organized in three genera-  
169 tions ordered by mass, and come in pairs of *up*-type and *down*-type quarks,  
170 named after the lightest generation. Though the up quark is lighter than  
171 the down, that rule is reversed in the subsequent two generations. Up-type  
172 quarks are electromagnetically charged  $+\frac{2}{3}$ , while the down-type quarks  
173 are charged  $-\frac{1}{3}$ . Quarks are also charged under the strong interaction,  
174 whose three charges are often characterized by colors: red, green, and blue.  
175 Each quark has an anti-particle with the opposite charges.

176 These fractional charges and individual colors are never seen in nature  
177 because of the requirement (discussed further in [Section 2.1.2.2](#)) that stable  
178 particle states be color-neutral. To accomplish this, quarks can create two-  
179 particle bound states called *mesons* consisting of one quark and one anti-  
180 quark with the same color charge, or three-particle bound states of quarks  
181 or anti-quarks with the three different color charges, which are called  
182 *baryons*. The lightest color neutral state containing only quarks, the pro-  
183 ton (*uud*), is stable. Extremely unstable bound states consisting of higher  
184 numbers of quarks can also exist, such as the pentaquark discovered in  
185 2015 at the [LHC](#). [12] Collectively, these multi-quark bound states are called  
186 *hadrons*.

187 Like leptons, the number of quarks in a state is conserved, up to very  
188 small anomalies. However, because quarks cannot exist in an isolated state,  
189 that conservation is described in terms of baryon number ( $B$ ) defined simi-  
190 larly to lepton number. Baryons are defined with  $B = 1$ , while anti-baryons  
191 have the quantum number  $B = -1$ . Mesons have  $B = 0$ .

193 2.1.2 *Forces*

194 The fermions in the previous section interact via the electromagnetic, weak,  
195 and strong forces. In a perturbative quantum field theory, interactions via  
196 these forces are represented by mediating bosons. These force carriers in-  
197 teract only with particles charged with their force's quantum numbers.  
198 The photon, for example, interacts only with electromagnetically charged  
199 particles. Gluons, mediators of the strong force, interact only with color  
200 charged particles, quarks and gluons. All fermions are weakly charged  
201 and interact with the weak force's mediators, the  $W$  and  $Z$  bosons.

202 The formulation for each of these forces is developed by requiring that  
203 the [SM](#) Lagrangian be locally gauge invariant [8]. This can be accomplished  
204 by adding gauge fields to the Lagrangian, whose behavior under gauge  
205 transformations cancels out the gauge dependence of the free Lagrangian.

206 However, adding a mass term for these fields reintroduces gauge dependence,  
 207 so this mechanism only creates forces mediated by massless gauge  
 208 bosons. The addition of the Higgs field provides mass terms for the weak  
 209 gauge bosons (as well as other particles) without interfering with the  
 210 gauge invariance.

211 The total gauged symmetry group for the SM is  $SU_C(3) \times SU_L(2) \times$   
 212  $U_Y(1)$ , where C stands for color, the charge of the strong force, L stands  
 213 for left, because the weak force is left-handed, and Y is the hypercharge  
 214 quantum number, the charge of the unified electroweak force.

215 2.1.2.1 *The Electromagnetic Force*

216 Electromagnetism provides the simplest example of a requirement of local  
 217 gauge invariance generating a Lagrangian description of a force. Electromagnetism  
 218 has one massless mediator, the photon, which interacts with  
 219 all electromagnetically charged particles. What follows is a brief description  
 220 of how enforcing this invariance generates a Lagrangian of the same  
 221 form as the classical electromagnetic Lagrangian, which can be easily incor-  
 222 porated into the SM.

223 The particles in Section 2.1.1 are fermions, and so the Lagrangian de-  
 224 scribing their free propagation are Dirac Lagrangians and all follow the  
 225 form

$$\mathcal{L} = i\bar{\psi}\gamma^\mu\partial_\mu\psi - m\bar{\psi}\psi. \quad (1)$$

226 Requiring that the free Lagrangians for these particles be invariant un-  
 227 der a  $U(1)$  local gauge transformation,  $e^{iq\lambda(x)}$ , can be accomplished by  
 228 adding a term to the Lagrangian which cancels the derivative term arising  
 229 from  $\lambda$ 's dependence on  $x$ :

$$\mathcal{L} = i\bar{\psi}\gamma^\mu\partial_\mu\psi - m\bar{\psi}\psi - (q\bar{\psi}\gamma^\mu\psi)A_\mu \quad (2)$$

230 where  $A_\mu$  is a “gauge field” that transforms according to

$$A_\mu \rightarrow A_\mu + \partial_\mu\lambda. \quad (3)$$

231 This vector field must also come with a free term,

$$\mathcal{L} = -\frac{1}{16\pi}F^{\mu\nu}F_{\mu\nu} + \frac{1}{8\pi}m_A^2A^\nu A_\nu. \quad (4)$$

232 The mass term for this field would not itself be invariant under the  
 233 transformation, but the field can simply be made massless to avoid this  
 234 problem. The final Lagrangian, then, is

$$\mathcal{L} = i\bar{\psi}\gamma^\mu\partial_\mu\psi - m\bar{\psi}\psi - \frac{1}{16\pi}F^{\mu\nu}F_{\mu\nu} - (q\bar{\psi}\gamma^\mu\psi)A_\mu \quad (5)$$

which is precisely the original Lagrangian with the addition of terms replicating the form of the Maxwell Lagrangian. In a quantized interpretation, it describes a field that interacts with particles with non-zero electromagnetic charge  $q$  via interactions with a massless spin-1 boson, the photon. In the quantum formulation, this charge is dependent on the energy scale of the interaction, and the strength of the interaction is more typically described by the electromagnetic coupling constant

$$\alpha_{EM}(\mu) = q(\mu)^2 / 4\pi. \quad (6)$$

For the purpose of succinct notation, this Lagrangian is often rewritten in terms of the *covariant derivative*

$$D_\mu = \partial_\mu + iq\lambda A_\mu \quad (7)$$

which immediately cancels the gauge dependent term created by the transformation. This mechanism is mathematically simple in the  $U(1)$  case, but can be replicated for more complicated gauge transformations with perturbative approximations.

#### 2.1.2.2 The Strong Force

The strong force is generated by a similar process of requiring local gauge invariance, but in this case, for a  $SU(3)$  transformation. The interactions of the strong force are described by the theory of quantum chromodynamics, which is given by the Lagrangian

$$\mathcal{L}_{strong} = -\frac{1}{4}G_{\mu\nu}^\alpha G^{\alpha\mu\nu} - \frac{1}{2}\bar{Q}_m D Q_m \quad (8)$$

where the  $\alpha$  index runs from 1 to 8 and represents the eight force carriers of the strong force, the gluons.  $m$  indexes the three quark generations, and  $G_{\mu\nu}^\alpha$  is the field strength tensor, defined as

$$G_{\mu\nu}^\alpha = \partial_\mu G_\nu^\alpha - \partial_\nu G_\mu^\alpha + g_s f_{\beta\gamma}^\alpha G_\mu^\beta G_\nu^\gamma \quad (9)$$

where  $g_s$  is a function of the energy scale of the interaction  $\mu$ , and is related to the strong coupling constant by

$$\alpha_s(\mu) = g_s(\mu)^2 / 4\pi. \quad (10)$$

The first term of the Lagrangian gives the gluon self-coupling interactions, with terms involving 2, 3, and 4 gluon field terms. The 2-field portion is simply the field strength tensor, but the other terms give gluon self-interaction terms that can be described by the Feynman diagrams in [Figure 2](#). Unlike photons, gluons are charged by the force they carry, making self-interaction possible.

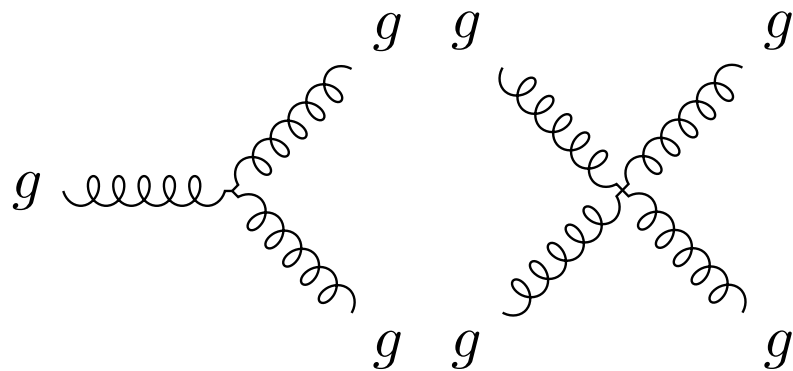


Figure 2: Gluon self coupling Feynman diagrams involving 3- and 4-gluon interactions.

264 In the second term,  $\not{D}Q_m$  is the covariant derivative acting on the quark  
 265 field. The quarks are in fact charged under all three forces, strong, electro-  
 266 magnetic, and weak, so the covariant derivative includes terms to make  
 267 each of the force's Lagrangians gauge invariant. Thus this term introduces  
 268 quark-boson interactions of four types, seen in [Figure 3](#). The quarks' cou-  
 269 ppling to the gluon is the strongest, with the other couplings happening at  
 270 lower rates. The couplings to the  $W$  and  $Z$  bosons are described in [Sec-](#)  
 271 [tion 2.1.2.3](#).

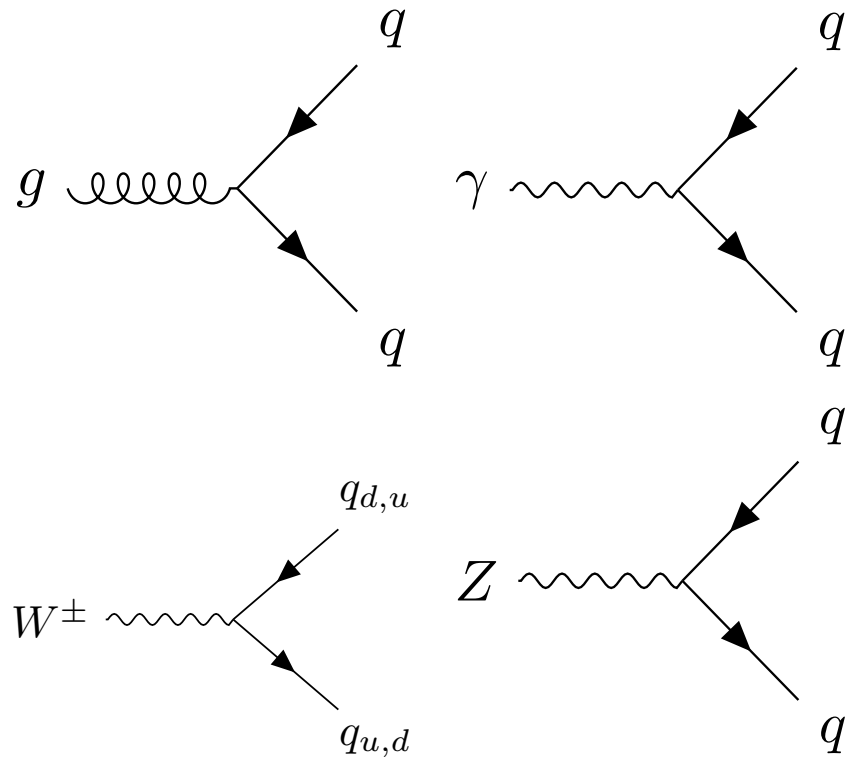


Figure 3: Quark couplings to the different types of gauge bosons. The  $q_{u,d}$  labels represent any up- or down-type quarks.

Quantum Field Theory assumes that particles are essentially *free*, propagating without interaction, and considers all interactions as perturbations on a free theory. So long as multiple interactions are much less likely than a single interaction, or put another way, so long as the coupling constants for each force are much less than one, this perturbative approximation is essentially correct. However, the strong coupling constant,  $\alpha_s$ , this assumption is not always valid.  $\alpha_s$  changes as a function of the energy of an interaction according to its renormalization group equation

$$\mu_R^2 \frac{d\alpha_s}{d\mu_R^2} = \beta(\alpha_s) = -(b_0\alpha_s^2 + b_1\alpha_s^3 + b_2\alpha_s^4 + \dots) \quad (11)$$

where  $\mu_R^2$  gives the renormalization scale, and each  $b_n$  gives a correction to the  $\beta$ -function based on diagrams with  $n$  loops [13]. The overall negative sign produces the unique energy dependence of  $\alpha_s$ , which becomes very small at high energy scales and asymptotically increases at low energies. Figure 4 shows this effect translated to distance scales, demonstrating that  $\alpha_s \ll 1$  and can be considered perturbatively at small distance scales, but at large distance scales  $\alpha_s$  approaches 1, and a perturbative approximation can no longer be used. Instead, for distances larger than  $10^{-16}$ , the colorless hadrons introduced in Section 2.1.1.2 must be used to describe strong interactions.

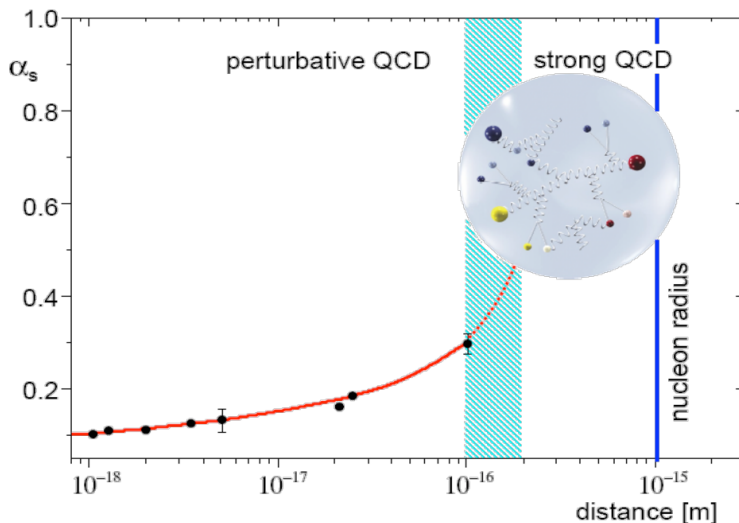


Figure 4: The running of the strong coupling constant,  $\alpha_s$ . [14]

The boundary between these regimes is referred to as  $\Lambda_{QCD}$  and differentiates energies at which Quantum Chromodynamics (QCD) can be considered perturbatively and those at which it cannot. The LHC is capable of producing individual high-energy quarks in its hard scatterings, but they lose energy as they radiate gluons, eventually entering the energy regime below  $\Lambda_{QCD}$ . The transition between these two regimes is complex,

296 and dictates the way that strongly charged particles appear in the ATLAS  
 297 detector. This is described in more detail in [Section 2.1.3.1](#).

298 **2.1.2.3 The Electroweak Force**

299 A similar process, using an  $SU(2)$  gauge transformation, can produce a  
 300 Lagrangian that would suffice to describe the  $W$  and  $Z$  bosons of the **SM**, if  
 301 only they were massless. However, they are not, so an alternate mechanism  
 302 is needed to generate massive force carriers.

303 Before a mechanism for their masses was understood, and before they  
 304 were discovered, the large masses of the  $W$  and  $Z$  bosons were proposed  
 305 in order to unify the electromagnetic and weak forces into the electroweak  
 306 force [8]. The large masses were crucial to explain the discrepancy in the  
 307 strength of the two forces.

308 The unified electroweak force is generated by a symmetry group written  
 309 as  $SU(2)_L \times U(1)_Y$ , where  $L$  refers to left-handed fields, and  $Y$  is the  
 310 quantum number for *hypercharge*. This new quantum number is defined as

$$Y = 2(Q - T_3) \quad (12)$$

311 where  $Q$  is the electromagnetic charge and  $T_3$  is the third component  
 312 of weak isospin  $\mathbf{T}$ , the quantum number relating to the weak interaction.  
 313 In the unified theory, quark and lepton singlets interact according to their  
 314 hypercharge, and left-handed quarks and leptons, grouped according to  
 315 their generation, interact as doublets.

316 The gauge bosons resulting from this unified theory include a triplet,  $\mathbf{W}$ ,  
 317 with coupling  $g_W$ , and a singlet field  $B$ , with coupling  $g'/2$ . However, the  
 318 electroweak symmetry is broken, and mixing between these states occurs.  
 319 Rewritten in their mass basis, the standard electroweak force carriers are  
 320 produced:  $W^\pm$ , two states with identical coupling resulting from the first  
 321 two states of the  $\mathbf{W}$  triplet, the  $Z$  and the photon field  $A$  resulting from  
 322 the mixing of the last  $\mathbf{W}$  state and  $B$ .

323 The electroweak Lagrangian is much more complicated than the strong  
 324 Lagrangian, and can be divided into several terms:

$$\mathcal{L}_{\text{electroweak}} = \mathcal{L}_{\text{gauge}} + \mathcal{L}_{\text{fermions}} + \mathcal{L}_{\text{Higgs}} + \mathcal{L}_{\text{Yukawa}}. \quad (13)$$

325 The first term can be written as follows

$$\mathcal{L}_{\text{gauge}} = -\frac{1}{4}W^{a\mu\nu}W^a_{\mu\nu} - \frac{1}{4}B^{\mu\nu}B^{\mu\nu} \quad (14)$$

326 where the  $a$  indices are numbered 1 through 3 and indicate the genera-  
 327 tors of  $SU(2)$  which are written

$$W^a_{\mu\nu} = \partial_\mu W^a_\nu - \partial_\nu W^a_\mu + g_2 \epsilon_{abc} W^b_\mu W^c_\nu \quad (15)$$

328 The gauge portion of the Lagrangian then generates interaction terms  
 329 of between the gauge fields, which when rewritten in terms of the mass-  
 330 eigenstate basis, generates interactions between three gauge bosons, like  
 331 the ones in [Figure 5](#), as well as interactions between four gauge bosons.

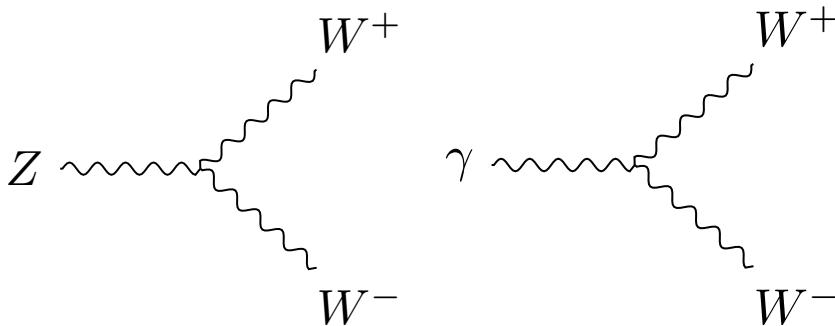


Figure 5: Feynman diagrams of trilinear gauge couplings in the [SM](#).

332 The fermion portion of the Lagrangian is written as

$$\begin{aligned} \mathcal{L}_{fermion} = & -\frac{1}{2}\bar{L}_m D \not{D} L_m - \frac{1}{2}\bar{Q}_m D \not{D} Q_m \\ & -\frac{1}{2}\bar{U}_m D \not{D} U_m - \frac{1}{2}\bar{D}_m D \not{D} D_m \\ & -\frac{1}{2}\bar{E}_m D \not{D} E_m \end{aligned} \quad (16)$$

333 where  $L$  is the left-handed lepton doublet,  $Q$  is the left-handed quark  
 334 doublet,  $U$  is the right-handed singlet for up-type quarks,  $D$  is the same for  
 335 down-type quarks, and  $E$  is the right-handed singlet for electrons, muons  
 336 and taus. Each of these fields has an implicit index running from 1 to 3  
 337 to represent the three generations. The covariant derivative in each term  
 338 includes terms including all the gauge fields the fermion is charged under.  
 339 Unlike the other forces, the weak force treats left- and right-handed  
 340 fermion fields differently; it only interacts with the left-handed fields, so  
 341 only the first two terms' covariant derivatives include  $W$  terms. The first  
 342 term in this Lagrangian, for example, produces weak interactions depicted  
 343 in [Figure 6](#). The  $Z$  bosons, because they represent a mixing between the  
 344  $W$  and  $B$  fields, can interact with right-handed leptons and quarks, but  
 345 do so with different strengths than left-handed particles.

346 No right-handed term appears for the neutrino field, because only left-  
 347 handed neutrinos and right-handed anti-neutrinos have been observed.  
 348 However, because neutrinos have non-zero mass, their chirality can change  
 349 with frame boosts, which complicates any claim that right-handed neutrinos  
 350 do not exist [3]. It is possible that neutrinos are their own antiparticle,  
 351 making the right-handed anti-neutrino the solution to this problem. It's  
 352 also possible that very massive right-handed neutrinos do exist, and sim-  
 353 ply haven't been discovered yet.

354 The remaining two terms of the electroweak Lagrangian are related to  
 355 the Higgs field, which is the source of electroweak symmetry breaking.

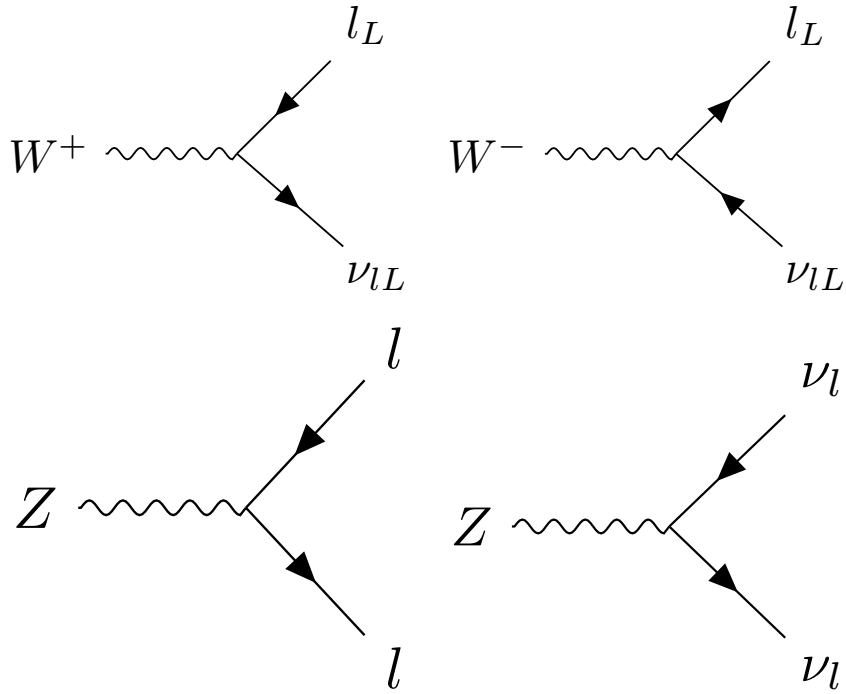


Figure 6: Feynman diagrams of weak couplings to leptons in the SM.

#### 356 2.1.2.4 The Higgs Mechanism

357 The Higgs mechanism presents a way to generate a mass term for the  
 358 electroweak gauge bosons. It is a scalar field, with a Lagrangian

$$\mathcal{L}_{Higgs} = \frac{1}{2}(\partial_\mu\phi)^*(\partial^\mu\phi) + \frac{1}{2}\mu^2\phi^*\phi - \frac{1}{4}\lambda^4(\phi^*\phi)^2 \quad (17)$$

359 where  $\phi$  is a complex scalar field,  $\phi = \phi_1 + i\phi_2$ . This looks very similar to  
 360 a standard scalar field Lagrangian, but the signs on the mass and interac-  
 361 tion terms are reversed, implying an imaginary mass term. However, this  
 362 isn't a good interpretation of the Lagrangian, because it differs from all  
 363 previously considered Lagrangians in one important way: its ground state  
 364 does not occur at  $\phi = 0$ . Because quantum field theory is perturbative, its  
 365 validity only holds when expanded around a ground state, which, when  
 366 calculated for this Higgs Lagrangian, must satisfy

$$\phi_1^2 + \phi_2^2 = \frac{\mu^2}{\lambda^4}. \quad (18)$$

367 The original Lagrangian can then be rewritten in terms of a field  $v +$   
 368  $H(x)$  centered around the ground state with energy called the vacuum  
 369 expectation value defined as.

$$v = \frac{\mu}{\lambda^2}. \quad (19)$$

This rewriting produces a Lagrangian with a non-imaginary mass. However, in an effect called *spontaneous symmetry breaking*, the original  $SO(2)$  rotational symmetry of the Lagrangian is lost, resulting only in a  $U(1)$  rotational symmetry; the Lagrangian is invariant under a phase transformation.

As in [Section 2.1.2.1](#), it is possible to make the Lagrangian invariant under a local  $U(1)$  transformation,  $\phi \rightarrow e^{i\theta(x)}\phi$  by adding a massless gauge field  $A^\mu$  and using the covariant derivative. Due to the many cross terms from the non-zero ground state, terms for the mass of one of the scalar bosons as well as the gauge field appear, leaving only one massless scalar boson. This massless boson, it turns out, can be completely removed from the theory via local  $U(1)$  transformations, ultimately producing a theory with one massive scalar (the Higgs) and a massive gauge field ( $W$ ).

The Higgs interaction with the weak gauge bosons also creates couplings between the particles, which can be seen in [Figure 7](#). There are also Higgs self-interaction terms included in the Lagrangian, producing vertices describing 3- and 4-Higgs interactions.

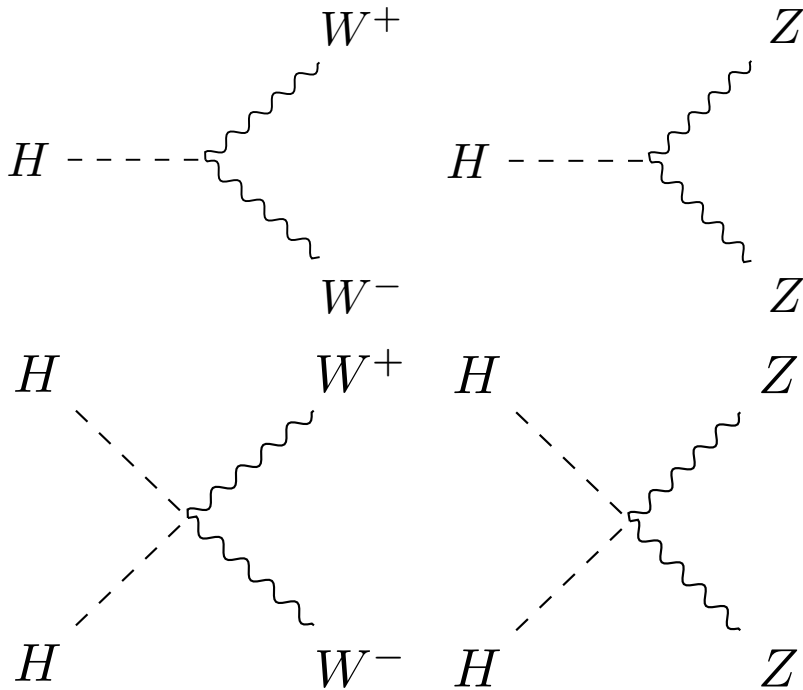


[Figure 7](#): Feynman diagrams demonstrating Higgs couplings to the weak gauge bosons in the [SM](#).

The remaining piece of the Lagrangian,  $\mathcal{L}_{Yukawa}$  describes the Higgs field's interactions with the fermions of the [SM](#), and can be written as

$$\mathcal{L}_{Yukawa} = -\Gamma_{mn}^e \bar{L}_m \phi E_n - \Gamma_{mn}^u \bar{Q}_m \phi U_n - \Gamma_{mn}^d \bar{Q}_m \phi D_n + h.c. \quad (20)$$

where *h.c.* is the hermitian conjugate term, and the  $\Gamma$  matrices are indexed by generation, and, when diagonalized, are proportional to the

391 masses of the fermions. The Higgs field's vacuum expectation value pro-  
 392 duces terms that look like fermion mass terms. Additionally, terms that  
 393 couple the fermions to the Higgs field are produced, with each fermion's  
 394 coupling proportional to its mass, according to

$$g_f = \sqrt{2} \frac{m_f}{v} \quad (21)$$

395 where  $m_f$  is the mass of the fermion. Feynman diagrams for lepton and  
 396 quark terms can be seen in [Figure 8](#).

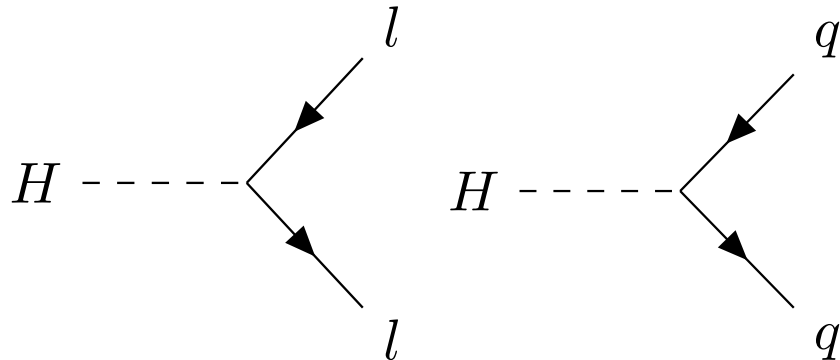


Figure 8: Feynman diagrams showing Higgs couplings to fermions in the [SM](#).

### 397 2.1.3 Phenomenology of Proton-Proton Collisions

398 As discussed in [Chapter 3](#), the [LHC](#) collides bunches of high-energy pro-  
 399 tons, and the interactions of these protons' constituent quarks produce the  
 400 wide array of particles seen in the ATLAS detector. The [LHC](#) typically cites  
 401 its energy in terms of  $\sqrt{s}$ , the center of mass energy of protons in the two  
 402 colliding beams, which in Run 2 is 13 TeV. However, because the proton is  
 403 not fundamental, this energy is divided among many particles that make  
 404 up the proton.

405 To first order, a proton consists of three quarks: two up quarks and one  
 406 down quark, held together by gluons. However, a real quantum mechani-  
 407 cal system is much more chaotic; in addition to these three quarks, called  
 408 *valence* quarks, there are many others popping into and out of existence.  
 409 These additional quarks are called *sea* quarks and can also carry fractions  
 410 of the proton's energy.

411 The particles inside the proton can have a wide range of energies de-  
 412 pending on the internal dynamics at the moment of the collision. These  
 413 cannot be predicted exactly, but probabilistic models called Parton Distri-  
 414 bution Functions ([PDFs](#)) describe the likelihood of any given configuration.  
 415 These functions are determined using data from hard scattering experi-  
 416 ments and give probabilistic estimates for how often a given type of parti-  
 417 cle appears with a fraction  $x$  of the total proton energy, as seen in [Figure 9](#).

418 A classical proton model would suggest that each valence quark carries  
 419 about one-third of the total proton energy. In practice, they each typically

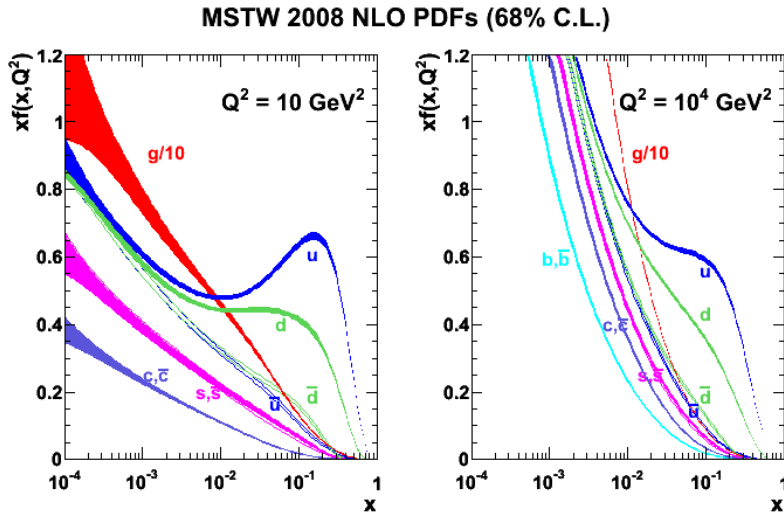


Figure 9: 2008 MSTW PDFs for various particle types given as a function of  $x$  and  $Q^2$ , the square of the parton-parton momentum transfer. [15]

account for less than a third of the total energy, with the remaining energy divided among the many sea quarks and gluons. Thus, in a proton-proton collision, the initial particles rarely have more than a third of the beam energy, and often have a much lower energy resulting from the interaction of sea quarks.

These PDFs are used at the LHC to calculate the probability for a given process to occur, or its *cross-section*. The cross-section for a process to occur with a two-proton initial state is given by

$$\sigma(P_1, P_2 \rightarrow X) = \sum_{i,j} \int_0^1 dx_1 dx_2 f_i(x_1, Q^2) f_j(x_2, Q^2) \hat{\sigma}(x_1 P_1, x_2 P_2, Q^2) \quad (22)$$

where  $i$  and  $j$  are indices representing the partons within proton 1 and 2 respectively,  $x_{i,j}$  gives these partons' momentum fraction, and  $f_{i,j}$  gives their PDFs.  $\hat{\sigma}$  gives the cross-section for a process going from partons to  $X$ , also referred to as the *matrix element*, and  $Q^2$  gives the energy scale of this hard scattering of partons.

Figure 10 shows cross-sections for many SM processes as a function of energy, demonstrating how processes involving high-mass objects have increasingly large cross-sections as the energy of the collider increases. In the analysis discussed in Part iv, the most important SM backgrounds are from top quarks, Z bosons, and diboson processes (ZZ, WW, and WZ). Though Z boson production has the highest cross-section of those processes, it contributes the least to the background of the search because of the specific requirements made on events designed to reduce SM backgrounds. Details on these backgrounds and how they can appear as signal-like events are given in Chapter 7.

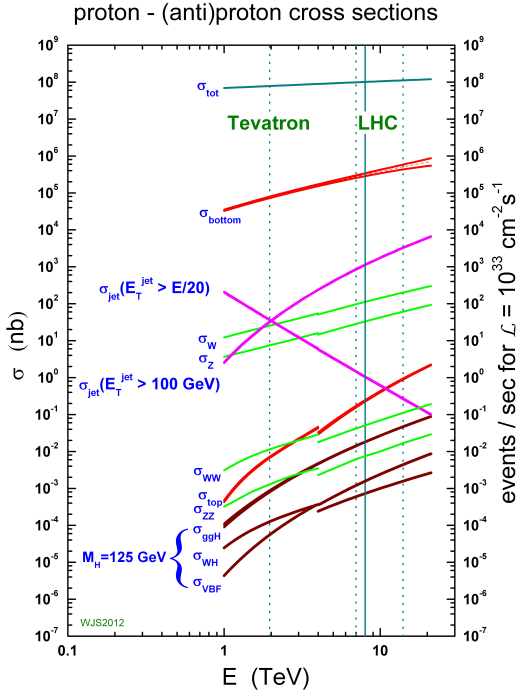


Figure 10: Cross-sections for many SM processes at the Tevatron and LHC [16].

443 2.1.3.1 *Production of Jets in the ATLAS Detector*

444 For most particles, the output of the hard scattering process is similar to  
 445 the objects observed by a detector; electrons, photons, and muons emerging  
 446 from final states are all observed as they pass through sensitive materi-  
 447 als, albeit with some radiation and conversion. For color-charged particles,  
 448 however, this is not the case.

449 As discussed in Section 2.1.2.2, quarks and gluons are strongly charged,  
 450 and the coupling constant of the strong force increases asymptotically at  
 451 large distance scales. As a consequence, rather than continuing to exist as  
 452 a colored state, it is energetically preferable for high energy quarks and  
 453 gluons produced in hard scatterings to radiate additional colored parti-  
 454 cles and form colorless bound states. This process is called *hadronization*,  
 455 and in it, a single colored particle is transformed into a spray of hadrons.  
 456 The process continues until the hadrons no longer have enough energy to  
 457 produce new hadrons, at about 1 GeV.

458 The resulting spray of particles is called a *jet*, and it is jets, rather than in-  
 459 dividual quarks or gluons, that are observed by a detector. Grouping these  
 460 particles into a jet is a non-trivial process, and is discussed in Section 5.4.

461 2.1.4 *Problems in the Standard Model*

462 Although the SM is a self-consistent theory that describes to great accuracy  
 463 all of the particles and forces it includes, it does have certain shortcomings.  
 464 The most glaring is the omission of gravity. Though the force is well un-

derstood at large scales via the theory of General Relativity, no satisfying quantum description of gravity has been accepted, much less proven. The Planck scale, the energy scale at which gravitational interactions become large enough that no sound theory can ignore gravity, is at about  $10^{19}$  GeV, 16 orders of magnitude above the electroweak scale, so the exclusion of gravity from the SM is unlikely to directly affect LHC physics.

Another clear omission of the SM is Dark Matter (DM), so named for its lack of electromagnetic interactions. This type of matter was first identified in 1933 through the observation of galactic rotation curves [17]. The speed of rotation indicated both that there was more mass in the system than could be accounted for by observations made directly of the galaxy, and that this additional matter was distributed in a halo, not a disk like the typical luminous matter. This effect can be seen in Figure 11, which demonstrates that the observed galactic density as a function of radius does not match the expected density from the luminous galactic disk. Since then, evidence for DM has been observed in colliding clusters [18], measurements of the cosmic microwave background [19], and in many more rotational curves, but the particles that form DM have never been directly detected or seen at a particle accelerator. As a consequence, very few details are known about the nature of this matter, only its density throughout the universe and that it does not interact strongly or electromagnetically.

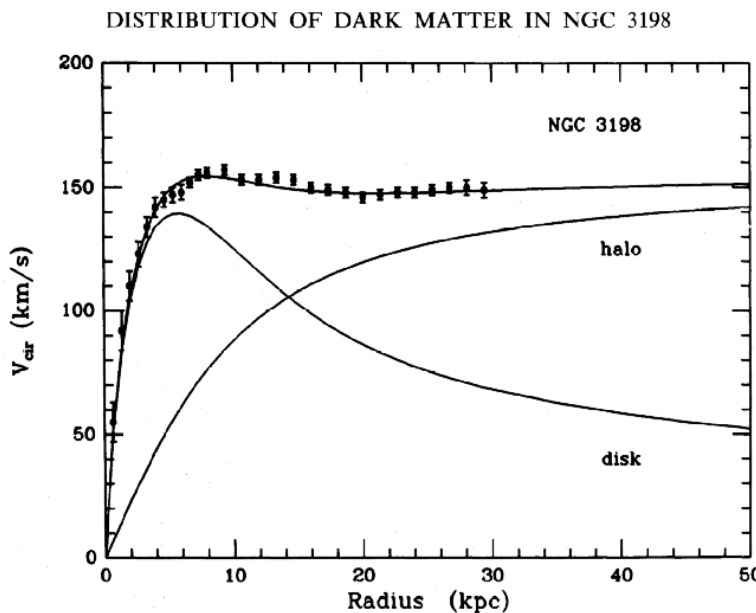


Figure 11: Galactic rotation curve of velocity as a function of radius in NGC 3198. Included is the observed data, as well as the expected velocity distribution from a disk-shaped galaxy corresponding to the expected density from electromagnetic observations. Another curve corresponding to a halo-shaped matter distribution is superimposed, and the halo and disk are summed and fit to the data. [20]

Beyond the omissions of gravity and DM, there are several aesthetic problems with the SM - ones that could have no solution, but seem to suggest

488 that the current SM are missing some pieces. The first is the sheer number  
 489 of parameters in the SM. There are 26 independent parameters determin-  
 490 ing the mass of the particles and all the couplings between them. Besides  
 491 the rough grouping of fermions into generations, there seems to be no or-  
 492 der to masses of particles, and no way to predict many of the masses or  
 493 couplings.

494 In the past, large numbers of seemingly unrelated parameters have indi-  
 495 cated that a theory has a more fundamental form at shorter distance scales.  
 496 The large number of elements, it turned out, could be explained by differ-  
 497 ent groupings of three particles, the proton, neutron, and electron. Later,  
 498 the menagerie of hadrons became so large that a similar re-imagining of  
 499 what was fundamental took place, and the theory of quarks gave an or-  
 500 der to the many mesons and baryons [21]. This pattern leaves physicists  
 501 suspicious of any theory with too many particles and free parameters, sug-  
 502 gesting that perhaps, at a higher energy, there is a simpler model that can  
 503 unify many of the seemingly disparate elements of the SM.

504 In addition, some of these seemingly independent parameters have sus-  
 505 picious symmetry. The Higgs mass, for example, has been measured to be  
 506  $125.7 \pm 0.4$  GeV[13]. This mass is the sum of the bare mass, the one that ap-  
 507 pears in the Lagrangian, and quantum corrections from interactions with  
 508 other particles, which are proportional to the square of the particles' mass.  
 509 Since new physics must exist at the Planck scale to account for gravity,  
 510 these corrections could be up to 35 orders of magnitude larger than the  
 511 Higgs mass. Though the bare mass could theoretically cancel out this mas-  
 512 sive correction, these parameters should be independent, and the odds  
 513 that they would be precisely the same to 35 places are very, very small.  
 514 This near-exact canceling is often called *fine-tuning*, an undesirable trait in  
 515 a theory which suggests that some more fundamental symmetry has been  
 516 missed. A *natural* solution, one free of this fine-tuning, is sought to resolve  
 517 this SM problem.

## 518 2.2 SUPERSYMMETRY

519 Supersymmetry (SUSY) was proposed and developed in the 1970s to give  
 520 solutions to many of these SM shortcomings [22–24]. The theory works  
 521 by introducing a fermionic symmetry to the SM, in addition to the usual  
 522 spacetime symmetries of translations, rotations, and changes of Lorentz  
 523 frame. The combination of the usual spacetime with this fermionic dimen-  
 524 sion is called a *superspace*. Rotations in this dimension result in a particle's  
 525 spin changing by  $1/2$ , turning a spin- $1/2$  fermion into a spin-0 particle,  
 526 for example. As a consequence, this symmetry requires the existence of  
 527 many new particles - a bosonic *sfermion* for each fermion of the SM and a  
 528 fermionic *gaugino* for each of the gauge bosons. These superpartners of SM  
 529 particles should have identical quantum numbers to the original particle,  
 530 except for their spins. Table 1 shows the SM particles and their superpart-  
 531 ners.

Names	sparticles	particles	$SU(3)_C, SU(2)_L, U(1)_Y$
squarks, quarks	$Q$	$(\tilde{u}_L \tilde{d}_L)$	$(u_L d_L)$
	$\tilde{u}$	$\tilde{u}_R^*$	$u_R^\dagger$
	$\tilde{d}$	$\tilde{d}_R^*$	$d_R^\dagger$
sleptons, leptons	$L$	$(\tilde{\nu} \tilde{e}_L)$	$(\nu e_L)$
	$\tilde{e}$	$\tilde{e}_R^*$	$e_R^\dagger$
Higgs, higgsinos	$H_u$	$(\tilde{H}_u^+ \tilde{H}_u^0)$	$(H_u^+ H_u^0)$
	$H_d$	$(\tilde{H}_d^0 \tilde{H}_d^-)$	$(H_d^0 H_d^-)$
gluino, gluon	$\tilde{g}$	$g$	$(8, 1, 0)$
winos, $W$ bosons	$\tilde{W}^\pm \tilde{W}^0$	$W^\pm W^0$	$(1, 3, 0)$
bino, $B$ boson	$\tilde{B}^0$	$B^0$	$(1, 1, 0)$

Table 1: Supermultiplets of supersymmetric and SM particles. Sfermions, on the first five rows, are all spin-0. Higgsinos and gauginos are all spin-1/2. Three sets of each fermion's supermultiplet exist, one for each generation. [25]

If the theory is symmetric under these fermionic rotations, these particle-sparticle pairs can be described by a single *superfield*, which simultaneously describes the behavior of both SM and SUSY particles in the super-space. However, this completely symmetric behavior is untenable given basic observations of matter in the universe. For example, if there were a *selectron* (the superpartner of the electron,  $\tilde{e}$ ), with identical mass to the electron, it would have been detected long ago. In fact, such a particle would fundamentally change atomic structure, with the bosonic selectrons capable of piling into the ground state of an atom, and removing all the interesting valence-shell interactions of electrons that determine molecular structure. Thus, if SUSY does exist, the symmetry must be broken, so that the superpartners have much higher masses than the original SM particles.

### 2.2.1 The Minimal Supersymmetric Standard Model

The Minimal Supersymmetric Standard Model (MSSM) was designed to be the simplest supersymmetric extension of the SM that remains self consistent, and it results in the particles seen in Table 1[25]. The formulation of the MSSM begins by introducing a second Higgs doublet to account for the different masses of the sparticles. As with the SM Higgs, electroweak symmetry breaking results in the loss of degrees of freedom, and only five of the original eight states remain, the lightest of which,  $h^0$ , can be interpreted as the SM Higgs already discovered. There are two remaining neutral states,  $A^0$  and  $H^0$ , as well as two charged Higgses,  $H^\pm$ .

The neutral Higgs states mix with the neutral gauge bosons, while the charged Higgs states mix with the charged gauge bosons, producing a series of states labeled only by their charge and the order of their masses.

557 The neutral states, collectively called the neutralinos, are identified from  
 558 lightest to heaviest,  $\tilde{\chi}_1^0, \tilde{\chi}_2^0, \tilde{\chi}_3^0$ , and  $\tilde{\chi}_4^0$ . The charged states, referred to as  
 559 charginos, are similarly called  $\tilde{\chi}_1^\pm$  and  $\tilde{\chi}_2^\pm$ .

560 The [MSSM](#) introduces many new interactions between [SM](#) particles and  
 561 sparticles. Though these don't represent all possible interactions, a gen-  
 562 eral rule is that any [SM](#) vertex can have two interacting particles replaced  
 563 with their sparticle equivalents, and this vertex will be part of the [MSSM](#).  
 564 [Figure 12](#) gives two examples of such vertices.

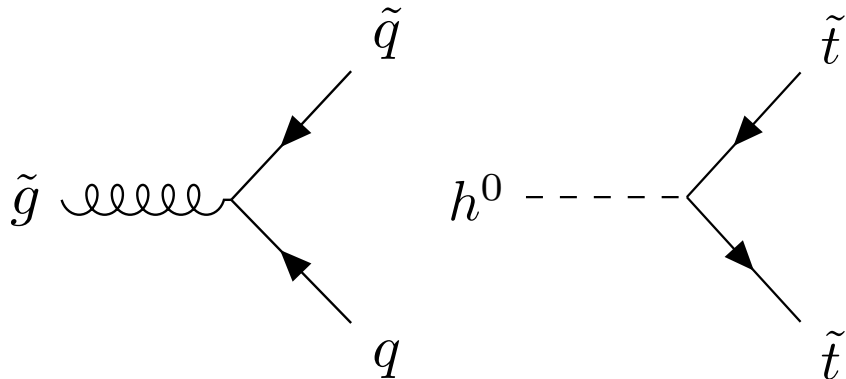


Figure 12: Two example vertices allowed by the [MSSM](#).

565 In addition to these interactions, there are several terms that appear in  
 566 the [MSSM](#) Lagrangian that violate the  $B$  and  $L$  conservation observed in  
 567 the [SM](#). In fact, these terms violate  $B - L$ , which, unlike  $B$  and  $L$  conser-  
 568 vation individually, does not have even small violations in the [SM](#). These  
 569 superpotential terms appear as follows

$$W_{\Delta L=1} = \frac{1}{2} \lambda^{ijk} L_i L_j \bar{e}_k + \lambda''^{ijk} L_i Q_j \bar{d}_k + \mu'^i L_i H_u \quad (23)$$

$$W_{\Delta B=1} = \frac{1}{2} \lambda''^{ijk} \bar{u}_i \bar{d}_j \bar{d}_k. \quad (24)$$

570 Because there are very strong limits on non-conservation of  $B - L$  from  
 571 proton decay experiments, these terms present a challenge for the [MSSM](#). It  
 572 would be possible, of course, to simply tune the  $\lambda$  parameters to be small  
 573 enough to fit within experimental constraints, but these terms can also be  
 574 eliminated by introducing a new conserved quantity,  $R$ -parity. It is defined  
 575 by

$$P_R = -1^{3(B-L)+2s} \quad (25)$$

576 where  $s$  is the spin of the particle. Requiring that all terms in the La-  
 577 grangian have a multiplicative  $P_R$  of 1 excludes the terms in [Equation 24](#),  
 578 removing the interactions that would lead to proton decay. All [SM](#) parti-  
 579 cles are  $R$ -parity even, while the sparticles are  $R$ -parity odd, so the con-  
 580 servation of  $R$ -parity can translate into a conservation of number of par-  
 581 ticles and sparticles. As a consequence, massive sparticles typically decay  
 582 through a chain of lighter sparticles, emitting [SM](#) particles along the way.

## 583 2.2.2 Solutions to Standard Model Problems

584 Perhaps the most compelling consequence of SUSY comes from *R*-parity,  
 585 which, through the formation of a new quantum number unique to sparti-  
 586 cles, requires the Lightest Supersymmetric Particle (LSP) to be stable. This  
 587 stable particle, if it is not electromagnetically charged charged, provides  
 588 an excellent candidate DM particle. The lightest neutralino, for example,  
 589 is a viable DM candidate because it does not interact electromagnetically  
 590 or strongly, a constraint required due to measurements of the relic den-  
 591 sity of DM in the universe. An interaction cross-section higher than what's  
 592 expected for weak interactions would have led the DM particle and its anti-  
 593 particle to annihilate at lower densities, leaving a much smaller amount of  
 594 DM in the universe than what is observed today [26].

595 Many believe that a complete SM should include a unification of the  
 596 three forces, as electromagnetism and the weak force have already been  
 597 unified. This requires that at some higher energy, the coupling constants  
 598 of all three forces merge. However, in the SM, the coupling constants come  
 599 close to aligning, but don't perfectly cross. With the addition of MSSM  
 600 particles with masses at the TeV scale, the alignment is near perfect, as  
 601 shown in Figure 13. This may be a mathematical coincidence, but it's very  
 602 compelling to those physicists who believe that *grand unified theory* must  
 603 exist.

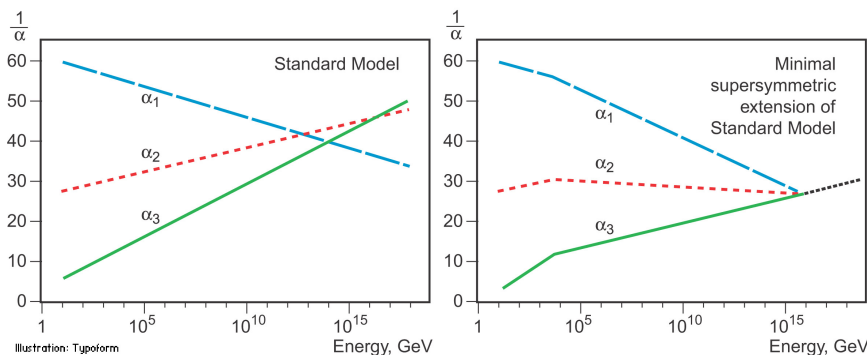


Figure 13: Running of the strong, weak, and electromagnetic coupling constants for the SM (left) and MSSM (right). [27]

604 SUSY also has the potential to solve the naturalness problem in the SM.  
 605 In the SM, the massive amounts of fine tuning are required to cancel the  
 606 quadratic corrections to the Higgs mass that result from loops involving,  
 607 most importantly, the top quark. In the MSSM, an similar loop involving  
 608 the stop quark (the vertex for which is depicted in Figure 12) contributes  
 609 to the Higgs mass with the opposite sign, making it possible to naturally  
 610 cancel the corrections without fine tuning. However, the larger the mass  
 611 difference between the top quark and stop quark, the larger the remaining  
 612 correction when the two terms cancel. Consequentially, to preserve a rea-  
 613 sonable degree of naturalness (and here the definition of "reasonable" is  
 614 subject to some debate), the stop quark should appear at masses not too  
 615 much larger than the top's, at approximately the TeV scale.

616 This naturalness mass limit, as well as the unification of couplings, make  
 617 the argument for searching for SUSY at the LHC particularly compelling, as  
 618 the LHC is the first collider capable of producing particles at the TeV scale.  
 619 As new exclusions on SUSY are set, the remaining phase space becomes  
 620 slightly less natural. But there is no shortage new SUSY models with un-  
 621 excluded parameters, which are continually proposed as new limits are  
 622 created.

623 *2.2.3 Simplified Models of Supersymmetry*

624 There are many different theorized models of SUSY, with different mecha-  
 625 nisms for breaking the symmetry. The MSSM has 120 free parameters, with  
 626 complex interactions that determine the mass hierarchy and interaction  
 627 rates of the sparticles. From an experimental point of view, the details of  
 628 these theories and the exact way the hierarchies are generated are less  
 629 relevant to a search than their outputs.

630 Simplified models, which are typically inspired by more complete theo-  
 631 ries, are used to tune the observables of a model more directly. These mod-  
 632 els each consist of one production and decay diagram, with the masses  
 633 and branching ratios of the particles free to be tuned directly. In a more  
 634 complete theory, it is instead necessary to modify more fundamental pa-  
 635 rameters like the symmetry breaking scale. A change like this impacts the  
 636 properties of all the sparticles, but the details of its impact are model de-  
 637 pendent. The simplified models allow for relatively model independent  
 638 interpretations that can be reinterpreted in the context of a more complete  
 639 SUSY theory [28].

640 In the analysis presented in Part iv, a simplified model is used which  
 641 produces the decay depicted in Figure 14 with a 100% branching ratio.  
 642 This decay chain begins with the pair production of gluinos, which decay  
 643 via a pair of quarks to the second lightest neutralino, which then decay via  
 644 a Z boson to the lightest neutralino. Only events in which the Z boson de-  
 645 cays to pairs of electrons or muons are considered, with all-hadronic final  
 646 states left to other searches [29]. The quarks emitted in the gluon decay are  
 647 allowed to have flavors  $u$ ,  $d$ ,  $c$ , and  $s$ , each with a 25% probability. A similar  
 648 model involving squark pair production is also considered, with the same  
 649 breakdown of flavors. In this simplified model, the lightest neutralino is  
 650 the LSP, and is stable.

651 Using this simplified model, the masses of the particles can be set di-  
 652 rectly. This is very helpful for the generation of MC, discussed in Sec-  
 653 tion 2.3, because a grid of different mass values of the important sparticles  
 654 involved in the decay can be generated. Cross-sections calculations are  
 655 performed for each point on these grids [30]. This grid allows analyzers to  
 656 make predictions of likely signals, and to exclude the simplified models  
 657 as a function of the mass of the sparticles in the case that no discrepancies  
 658 between predictions and observations are seen.

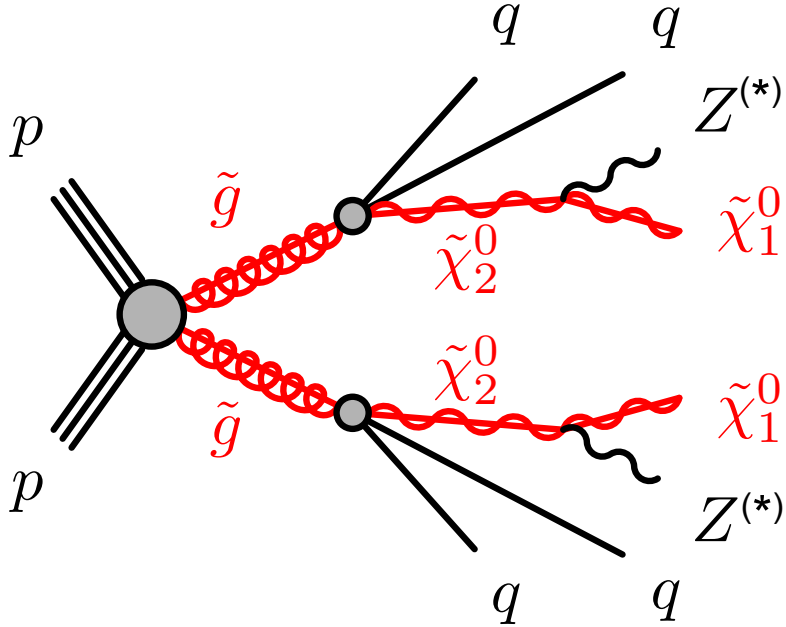


Figure 14: Feynman diagram of the decay considered in the simplified models used in the analysis presented in Part iv.

659 2.2.3.1 *Context and Motivation*

660 This channel is well motivated from a theoretical perspective. Production  
 661 of strongly charged sparticles, shown in Figure 15, is hypothesized to oc-  
 662 cur at much larger rates than the production of other particles, due to the  
 663 difference in coupling constants. The specific decay considered in these  
 664 simplified models does not have the largest branching ratio of all possi-  
 665 ble decays; even considering only changes to the SM decays involved, a  
 666  $Z \rightarrow qq$  decay is roughly seven times more likely than  $Z \rightarrow \ell\ell$ . However,  
 667 processes with higher branching ratios, like those producing an all-jet final  
 668 state, often have much higher SM backgrounds, making them difficult to  
 669 identify, even if they occur more frequently. This final state balances SM  
 670 backgrounds and branching ratios, and when compared to other searches  
 671 performed by the ATLAS collaboration, has competitive expected sensitiv-  
 672 ity to SUSY [31].

673 Processes similar to the one described by Figure 14 have been the target  
 674 of previous LHC searches. Both CMS and ATLAS performed searches for  
 675 SUSY in the two lepton channel with the 8 TeV data collected in 2012. The  
 676 ATLAS search saw a  $3\sigma$  excess, shown in Figure 16 [1]. The CMS search  
 677 saw no excess in a similarly motivated signal region, albeit with different  
 678 kinematic cuts than ATLAS's, following up on a 7 TeV search that saw no  
 679 excess [33, 34].

680 Both searches also identified events with two leptons that weren't con-  
 681 sistent with an on-shell  $Z$  decay, and in this region, an excess with a local  
 682 significance of  $2.4\sigma$  was observed by CMS, shown in Figure 17. No excess

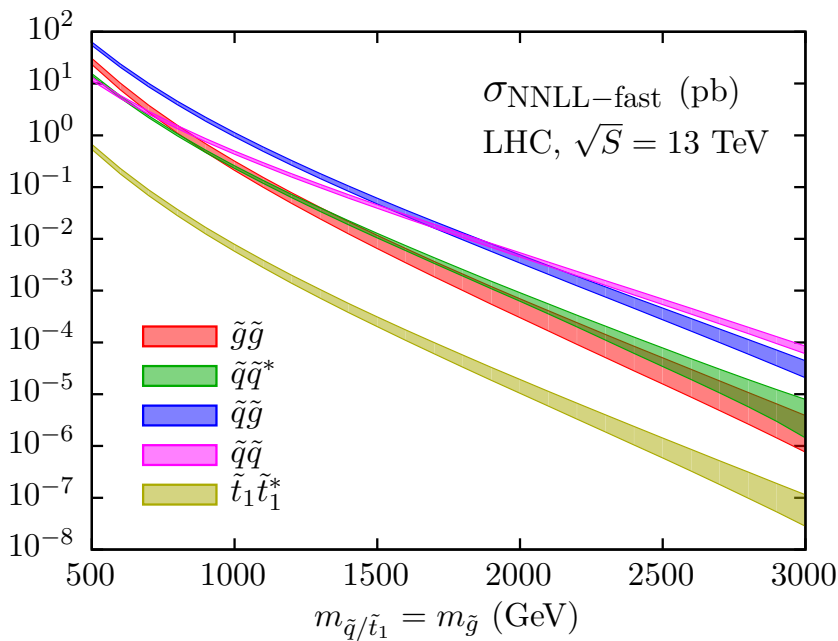


Figure 15: 13 TeV production cross-sections for sparticles, as a function of sparticle mass [32].

683 was observed by the ATLAS collaboration in a signal region with identical  
 684 kinematic cuts [1].

685 These two excesses generated significant interest in the two lepton chan-  
 686 nel, and both CMS and ATLAS produced preliminary results in December  
 687 2015 with the first  $3.2 \text{ fb}^{-1}$  of 13 TeV data. ATLAS again reported an excess  
 688 on the Z mass peak [2], shown in Figure 18, while CMS saw no excesses [35].  
 689 An all-hadronic ATLAS SUSY search released in 2016 which was sensitive  
 690 to the same models also saw no significant excess [29].

### 691 2.3 MONTE CARLO EVENT GENERATION

692 The complex events of the LHC are difficult to model, but modeling them  
 693 is crucial to analyzers' understanding of SM backgrounds and potential  
 694 signals. To simplify the modeling process, particle interactions are broken  
 695 down into very small steps, each with associated probabilities of various  
 696 outcomes. This modeling method is called Monte Carlo simulation (MC),  
 697 and, at the LHC it is broken into several larger steps which are each han-  
 698 dled by different software.

699 The first step, discussed in Section 2.1.3, is to determine the energies  
 700 of the initial particles in a collision, which are provided by several differ-  
 701 ent PDF sets. These distributions come from experimental measurements,  
 702 though there is some variation between different sets. Three different sets  
 703 are used in this analysis: NNPDF2.3LO [36] and NLO CT10 [37] for back-  
 704 ground and signal processes, and MSTW 2008 [15] for pile-up events, dis-  
 705 cussed more in Section 3.4.

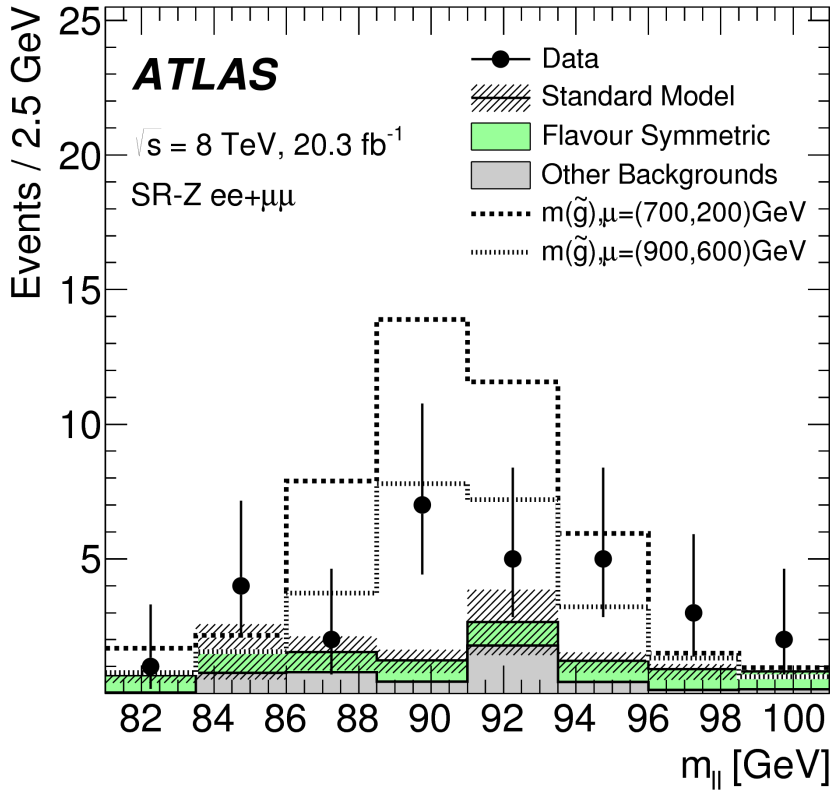


Figure 16: Results of an 8 TeV search performed by the ATLAS collaboration in a signal region targeting events like those in Figure 14. The events in the signal region are displayed as a function of  $m_{\ell\ell}$ , the invariant mass of the event's leading leptons. The SM backgrounds are shown with their full uncertainties based on data-driven background estimations, and two signals are superimposed on the distribution. The observed data-points are higher than the expected background, with a total excess of  $3.0\sigma$  [1].

With the initial states of the constituents of the protons described by these probabilistic models, the next step is to model the hard scattering process resulting from the interaction of two of these particles. This is accomplished by a generator, which calculates the cross-sections of the Feynman diagrams of a given process. In particular, these generators typically produce *matrix elements*, which describe the probability to go from an initial to final state via a hard scattering, including the kinematics of the output. The generator uses these matrix elements to assign one of these hard scattering final states to each event. These hard scattering outputs are then passed to the next step, where parton showering, fragmentation, final and initial state radiation, and hadronization can occur.

The calculation of these diagrams can become very complicated when more and more loops are allowed. The simplest calculations, which include diagrams without any loops, are referred to as Leading Order (LO), while calculations including diagrams with one loop are called Next to Leading Order (NLO), and additional Ns can be added to describe more

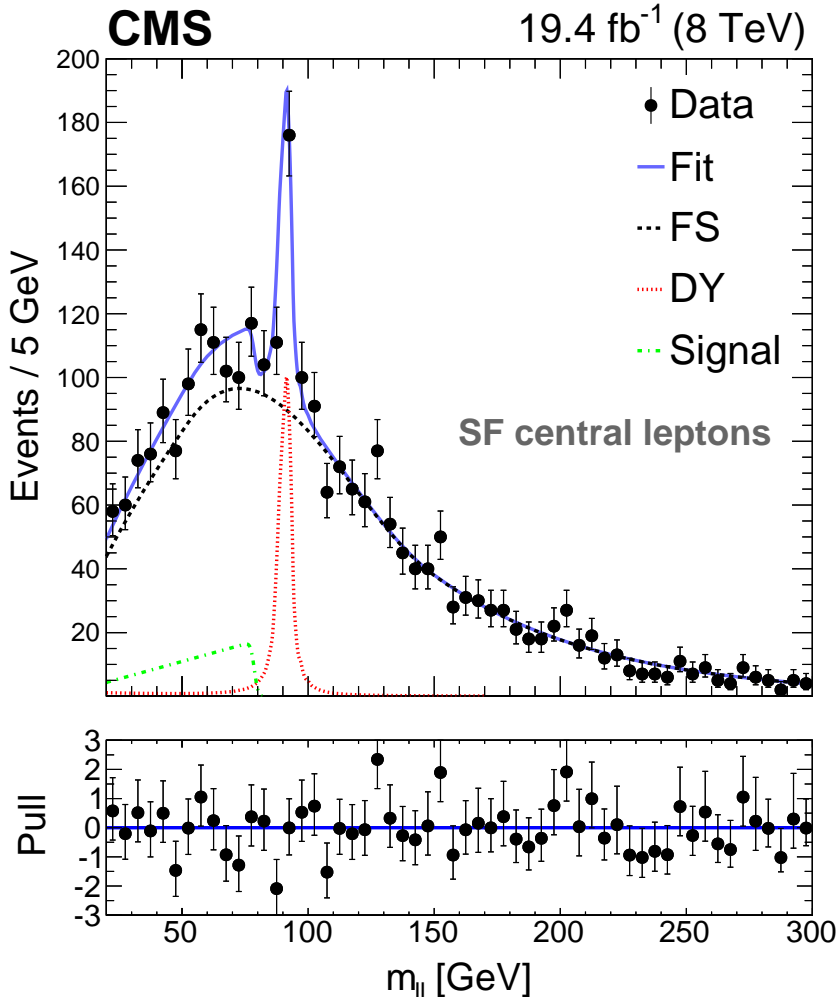


Figure 17: Results of an 8 TeV search performed by the CMS collaboration in a signal region including a broad range of  $m_{\ell\ell}$ . A  $2.4\sigma$  local excess is seen in the low  $m_{\ell\ell}$  region, and no excess of events is seen in the region with  $m_{\ell\ell}$  consistent with an on-shell Z boson. The data is fit based on a data driven estimate of the flavor symmetric background (FS) and the Drell-Yan background (DY), with an additional component for the signal [34].

722 complex calculations. In addition, the total cross-section for a given pro-  
 723 cess can be calculated at a higher order and used to scale the overall num-  
 724 ber of events generated for the process.

725 These calculations can also be tuned, varying parameters in the genera-  
 726 tion to create outputs that most closely match experimental data. In some  
 727 cases, this can mean that a tune might include values for certain physi-  
 728 cal quantities that are different from their measured values because this  
 729 configuration ultimately produces a result more similar to data.

730 Examples of generators include MADGRAPH5\_AMC@NLO [38], POWHEG  
 731 Box [39–41], and SHERPA [42]. Each has different strengths and is used  
 732 to describe processes that best match those strengths. POWHEG Box, for  
 733 example, cannot perform its own parton showering, and must be inter-

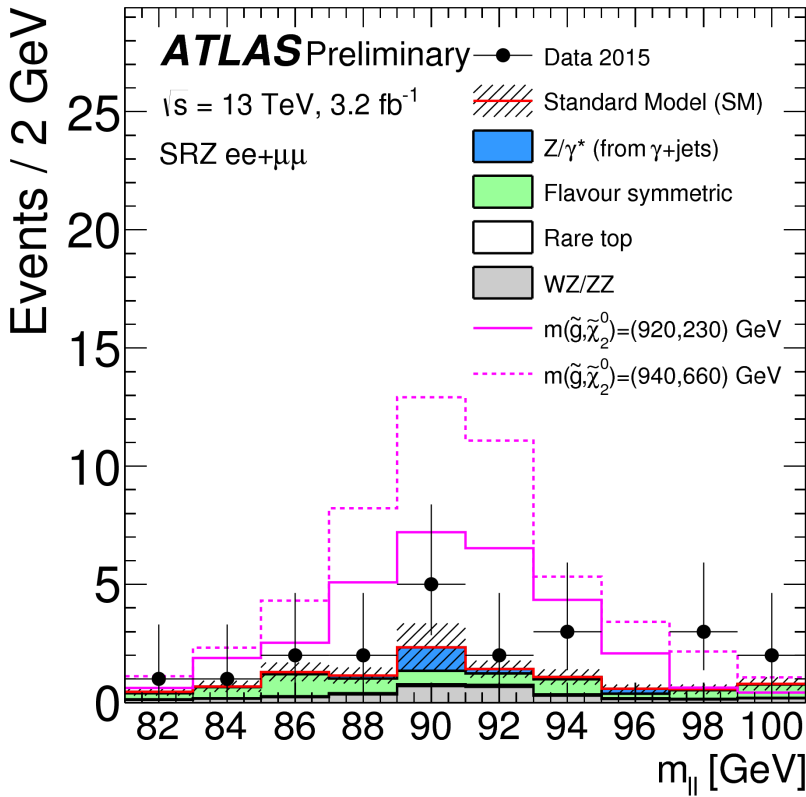


Figure 18: Preliminary results from a 13 TeV search targeting the same signal region as Figure 16, performed on  $3.2 \text{ fb}^{-1}$  of 2015 data. The events in the signal region are displayed as a function of  $m_{\ell\ell}$ , the invariant mass of the event's leading leptons. Flavor symmetric and  $Z/\gamma^*$  + jets backgrounds are taken from data-driven methods, while the other backgrounds are taken from MC. They are compared to the data, which shows a  $2.2\sigma$  excess of events. Distributions from two signal points are superimposed [2].

faced with another generator, typically Pythia [43], in order to describe any physics processes beyond the hard scattering, which can cause discontinuities in its predictions for large numbers of partons. However, it can calculate matrix elements at NLO, giving it an advantage in calculating some complex processes. SHERPA performs its own parton showering, but in most cases calculates its matrix elements at LO. The main advantage MADGRAPH5\_AMC@NLO, which must also be interfaced with another generator perform parton showering, is its simple user interface. This makes it popular for producing SUSY signal samples, which must be done by each analysis team searching for a different SUSY process.

Once the final state particles of the hard interaction and showering have been calculated, the pile-up of the LHC (described in Section 3.4) must be accounted for. Events called *minimum bias* are generated to match the overall production of the LHC collisions, with no preselection. These events are overlaid on the original hard scatter to produce a more realistic repre-

749 sentation of the many simultaneous interactions observed in the ATLAS  
750 detector.

751 This collection of particles must then be translated into signals in the  
752 detector. Their trajectories in the magnetic fields of the detector, their inter-  
753 actions in each layer, and the way these interactions deposit charge in each  
754 subdetector are modeled in software called GEANT4 [44]. In this software,  
755 every piece of the ATLAS detector is modeled, including the magnetic  
756 field and the many different materials. Particles then follow trajectories  
757 through the simulated detector and interact with the different materials  
758 based on several preprogrammed options for each material. For example  
759 a photon traveling through a material could continue along its trajectory,  
760 convert into a positron-electron pair, or deposit energy. As it crosses into  
761 a new material, a new set of options opens up for interactions. The parti-  
762 cle is tracked until all of its energy is lost or it exits the geometry of the  
763 simulation.

764 The model of the detector used for this process is iteratively perfected  
765 by comparing data to MC. Figure 19 shows an example of a discrepancy  
766 between the simulation and observed data in the number of secondary  
767 vertices in a pixel module, which should correspond to the amount of  
768 material in the area. Observations of discrepancies like this can be used to  
769 correct the materials in the simulation.

770 Custom ATLAS code converts the energy deposited in active sensors  
771 into signals that resemble the expected detector response. These responses  
772 are typically very complicated with many parameters, and are frequently  
773 iterated on to best match the data. Electronic noise must also be added to  
774 correctly approximate the operating conditions of the detector. Additional  
775 alterations to this signal translation, including dead sensors and misalign-  
776 ments of the detector, can also be added at this stage.

777 Once the simulated particles have been converted into detector signals,  
778 the same reconstruction software used on data can be used on the MC,  
779 converting the detector signals back into particle interpretations. This re-  
780 construction process is described in Chapter 5. The original information  
781 about the particles from the generator, referred to as *truth* information, is  
782 also kept, and can be compared to the reconstruction output to study its  
783 efficacy.

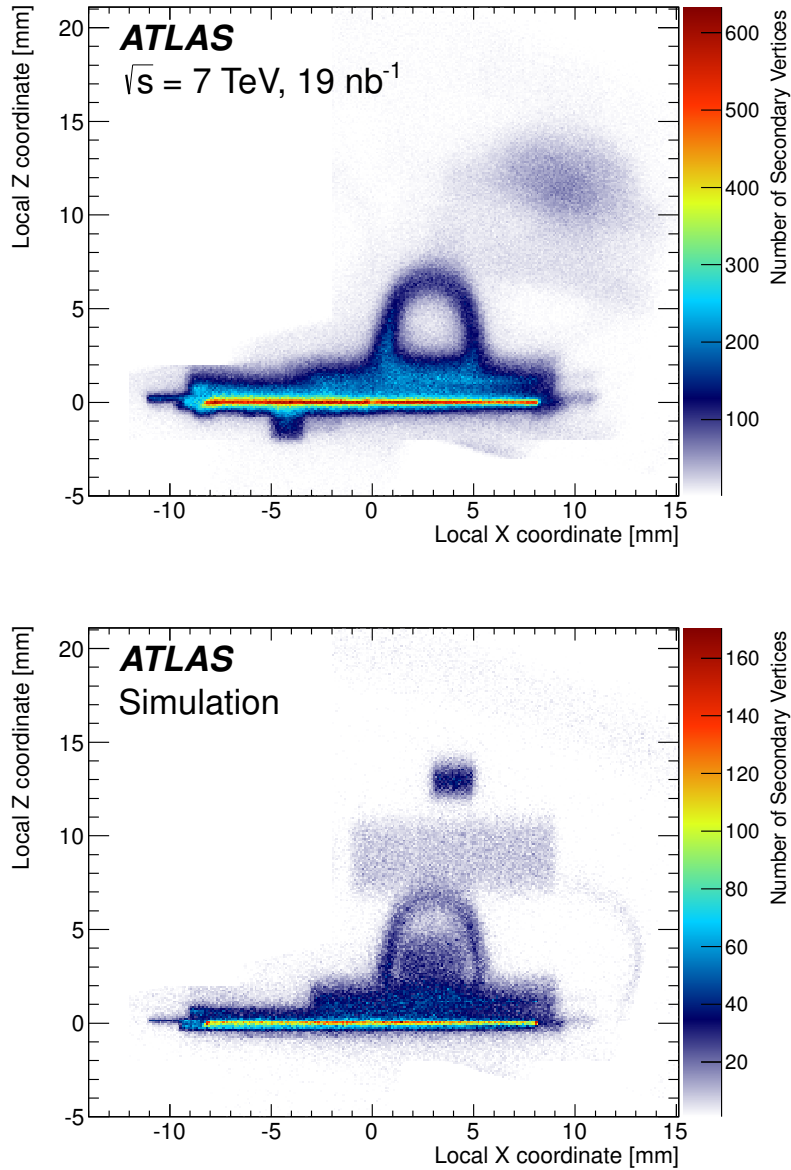


Figure 19: Number of secondary vertices in a module in the first layer of the pixel detector in data (top) and MC (bottom). There are more events in the data than the MC [45].



784                              **Part III**

785                              **THE EXPERIMENT**

786     This section describes the LHC and the ATLAS detector, which  
787     collectively provide the physical environment and the data col-  
788     lection for the analysis discussed in Part iv. Reconstruction of  
789     events in the ATLAS detector is also explained, with an empha-  
790     sis on the reconstruction of tracks in the innermost part of the  
791     detector.



# 3

792

## 793 THE LARGE HADRON COLLIDER

794 The LHC is unique in the world, producing proton-proton collisions at en-  
795 ergies an order of magnitude higher than any accelerator before [46]. It  
796 provides unique environments at its collision points where massive, unsta-  
797 ble particles can exist for an instant, then decay to the ordinary material of  
798 the universe. It is the goal of the ATLAS experiment to identify these short-  
799 lived particles, but the LHC's work of producing them is equally complex.

800 The LHC sits in a 26.7 km circular tunnel that straddles the French-Swiss  
801 border outside of Geneva, originally built in 1989 for the Large Electron-  
802 Positron (LEP) collider [47]. In the LHC, two beams of protons are accel-  
803 erated to 6.5 TeV, then focused and collided at four points around the  
804 ring, which can be seen in Figure 20. These points are each encased by  
805 particle detectors, which can examine the outputs of the collisions, and  
806 have different strengths and goals. The two multipurpose detectors are AT-  
807 LAS and CMS, which have very complex detectors aimed and measuring  
808 as many SM particles as possible and discovering new processes [48, 49].  
809 Large Hadron Collider beauty (LHCb) examines processes related to the  $b$   
810 quark [50]. Meanwhile, A Large Ion Collider Experiment (ALICE) focuses  
811 on special runs of the LHC which collide lead ions instead of protons, and  
812 seeks to understand the high energy densities resulting from the collisions  
813 of such massive, complex particles [51].

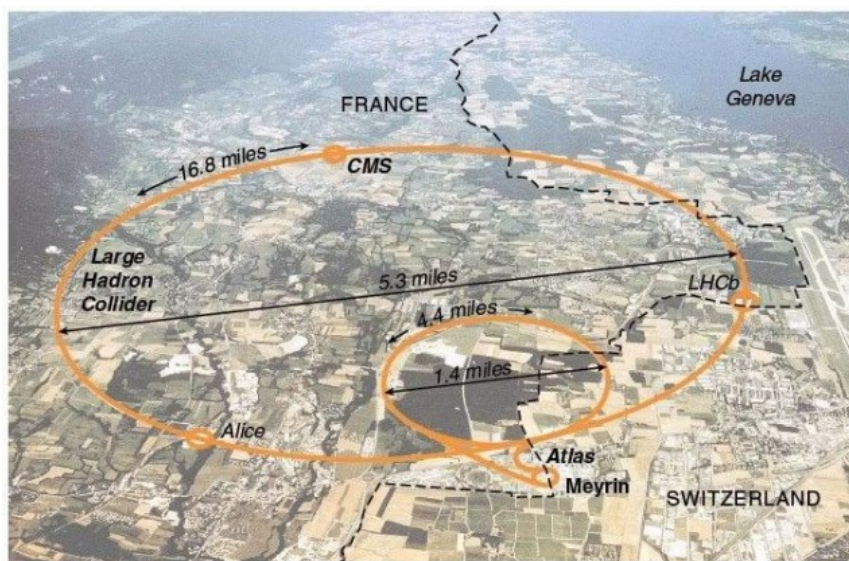


Figure 20: The LHC main collider ring and pre-accelerator SPS overlaid on a map of Switzerland and France, with the four main LHC experiments identified.

## 814 3.1 THE INJECTOR COMPLEX

815 The goal of the LHC is to provide high luminosity proton-proton collisions  
 816 at 13 TeV. To achieve this, it must be capable of rapidly accelerating large  
 817 numbers of protons and holding them at a constant energy, and organizing  
 818 them into bunches which can be focused and collided at precise points  
 819 and times. To do this, a complex system of pre-accelerators is required, as  
 820 well as a precisely engineered system of magnets within the LHC. The full  
 821 system of pre-accelerators is shown in Figure 21.

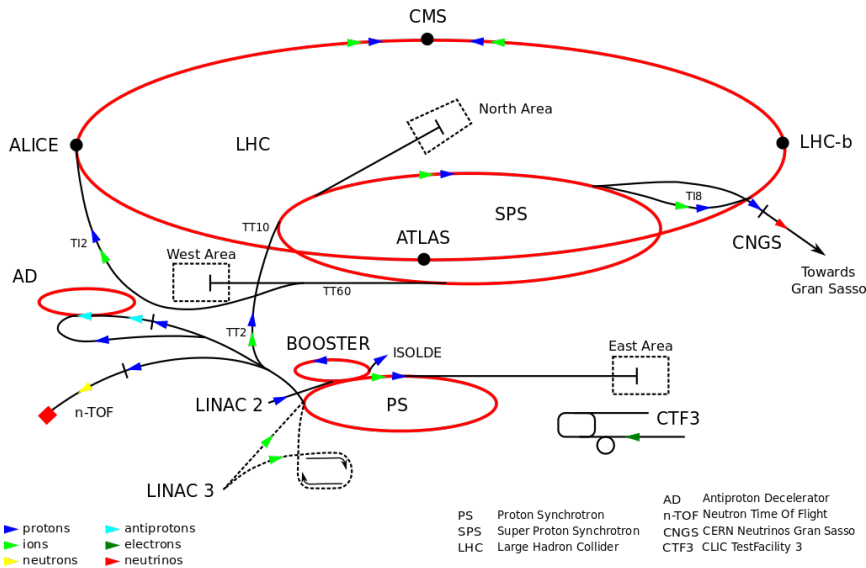


Figure 21: The pre-accelerators of the LHC.

822 The chain begins with when hydrogen gas is stripped of its electrons  
 823 and injected in short pulses into Linac2, a linear accelerator which uses  
 824 Radiofrequency (RF) cavities, which use alternating positive and negative  
 825 electric fields to simultaneously push and pull particles forward through  
 826 the accelerator. This RF behavoir keeps the bunches of protons resulting  
 827 from the original pulses separated, beginning the formation of the bunch  
 828 structure used for collisions. Quadropole magnets along the accelerator  
 829 keep the beam focused. By the end of the accelerator, protons have reached  
 830 50 MeV.

831 The proton beam is then injected into the Proton Synchrotron Booster  
 832 (PSB), the first circular accelerator in the pre-accelerator chain. It increases  
 833 its magnetic field as the protons increase in speed, ultimately accelerating  
 834 them to 1.4 GeV.

835 At this point the proton beam moves on to the PS, a 600 m long circular  
 836 accelerator that consists of 277 electromagnets that accelerate the protons  
 837 up to 25 GeV, and 100 additional dipole magnets to bend the beam.

838 The last accelerator before injection into the LHC is the SPS, a 7 km long  
 839 ring which, long before the LHC tunnel was built, was responsible for the  
 840 discovery of the W and Z bosons. The SPS accelerates particles up to 450  
 841 GeV before they are launched into the LHC.

842 Proton bunches are structured for ease of acceleration, with distinct  
 843 features resulting from each of the pre-accelerators. The PS produces 72  
 844 bunches separated by 25 ns, which are injected into the SPS, as seen in Fig-  
 845 ure 22. However, as the magnetic field directing these protons out of the  
 846 PS loop is turned on, there must be a gap in the bunch structure. Without  
 847 this gap, called the injection kicker rise time, the changing magnetic field  
 848 would direct particles out of the accelerator and produce high amounts  
 849 of unsafe radiation around the PS. A similar gap in bunch structure is  
 850 required for the injection from the SPS to the LHC. The injection process  
 851 is repeated until the LHC is completely filled with around 2000 bunches,  
 852 which takes about three minutes.

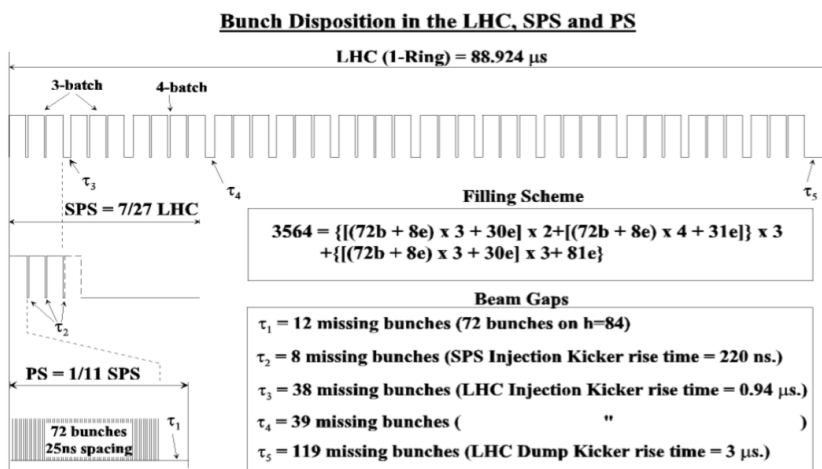


Figure 22: Bunch structure in the PS, SPS, and LHC.

### 853 3.2 OPERATION OF THE LARGE HADRON COLLIDER

854 The LHC consists of eight straight sections each connected by an arc. In  
 855 each straigh section, RF cavities accelerate protons, ultimately bringing  
 856 them up to 6.5 GeV. Between these straight sections, 8.4 T dipole mag-  
 857 nets bend the beams to maintain the approximately circular path. How-  
 858 ever, because the LHC is a proton-proton collider as opposed to a proton-  
 859 antiproton collider, the two counter-rotating beams must be housed in  
 860 separate rings and be accelerated separately. To achieve this, twin-bore su-  
 861 perconducting magnets, one example of which can be seen in Figure 23,  
 862 surround the two rings and accelerate them both. Quadropole magnets are  
 863 used at the four collision points to focus the beams, which cross at an inter-  
 864 action point at the center of a detector. In total there are 1232 main dipole  
 865 magnets over 5000 additional magnets, which are all are superconducting  
 866 and kept below their critical temperatures by liquid helium cooling.

867 When first injected into the LHC, the protons must be accelerated over  
 868 many turns through the machine, with the magentic field from the dipoles  
 869 increasing with each pass to apply more force with which to bend the  
 870 beam. Once the protons have reached a maximum energy, a process called

### LHC DIPOLE : STANDARD CROSS-SECTION

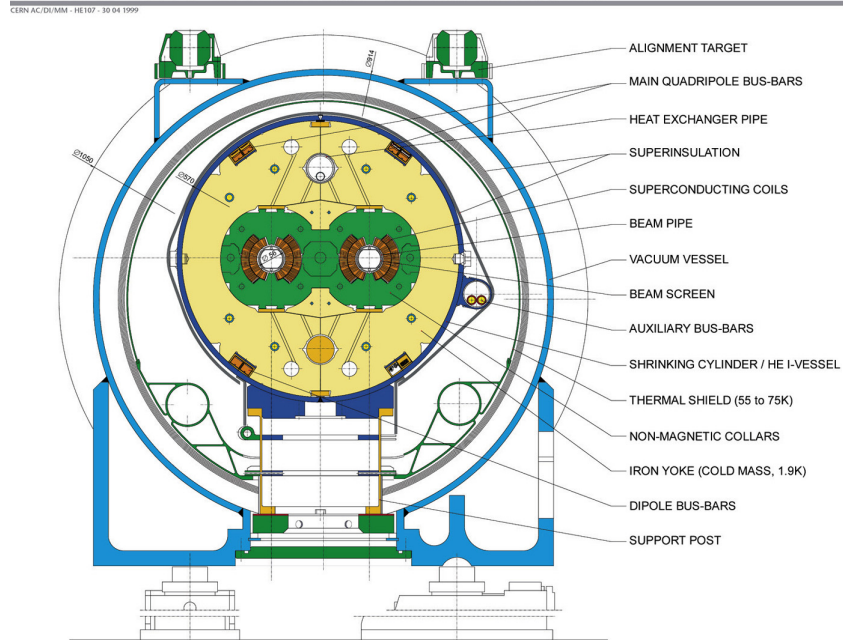


Figure 23: Cross-section of a cryodipole magnet in the LHC.

“squeezing” occurs, in which the total transverse area of the beam is reduced and bunches are elongated slightly. The shape produced by this process determines the “beam spot” for the ATLAS detector, the measurement of the area in which collisions occur within the detector. As shown in Figure 24, the collisions all occur very close together in the  $x - y$  plane, but have a long spread in the  $z$  direction<sup>1</sup>.

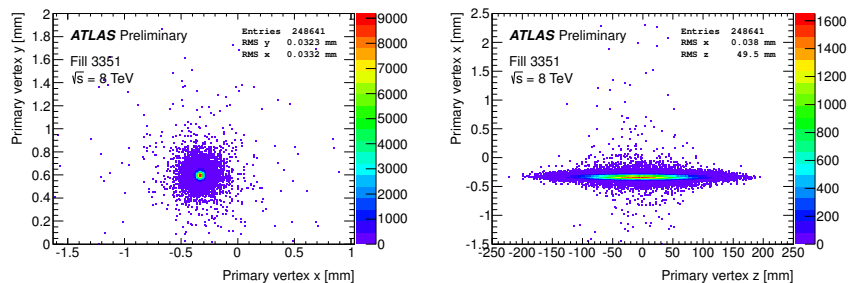


Figure 24: Beam spot in the ATLAS detector for one run in 2015. Distributions show only the highest  $p_T$  vertex per event. Left is the  $x - y$  distribution of vertices, while the right plot shows the  $x - z$  distribution.

Once the beams are at a stable energy and have been squeezed, the LHC indicates that it is physics-ready to the experiments around the ring, and, after some additional checks by each experiment, data-taking can begin. As collisions occur, the beam is depleted, and when it is sufficiently depleted to require a new fill, or if any instability occurs, the beam is dumped into a cavern filled with steel and concrete, which absorbs the energy.

<sup>1</sup> The coordinate system used here is discussed in Section 4.1.

## 884 3.3 LUMINOSITY

885 The goal of the collisions provided by the LHC is to produce SM and BSM  
 886 particles, which can be observed by the detectors. How frequently a given  
 887 process could occur was a crucial consideration in its design. The number  
 888 of events of a given type is given by

$$889 N_{event} = L\sigma_{event} \quad (26)$$

890 where  $L$  is the luminosity delivered by the LHC and  $\sigma_{event}$  is the cross-  
 891 section of the process in question. These cross-sections vary over many or-  
 892 ders of magnitude for different processes, as shown in Figure 10, a plot of  
 893 many different SM cross-sections. As a consequence, a very large amount  
 894 of luminosity is required to produce the more rare events, and to have  
 895 enough statistical power to differentiate them from other much more com-  
 mon events.

896 The instantaneous luminosity at the LHC is given by

$$897 L = \frac{N_b^2 n_b f_{rev} \gamma_r}{4\pi \epsilon_n \beta^*} F \quad (27)$$

898 where  $N_b$  is the number of protons per bunch ( $\sim 10^{11}$ ),  $n_b$  is the number  
 899 of bunches in each beam ( $\sim 10^3$ ),  $f_{rev}$  is the number of times per second  
 900 that the beam travels around the ring,  $\gamma_r$  is the relativistic gamma factor,  
 901  $\epsilon_n$  is the normalized transverse beam emittance, and  $\beta^*$  is the  $\beta$ -function  
 902 at the collision point, which describes the transverse displacement of par-  
 903 ticles in the beam.  $F$  gives the reduction factor due to the geometry of the  
 beam crossings, and is given by

$$904 F = \left(1 + \left(\frac{\theta_c \sigma_z}{2\sigma^*}\right)^2\right)^{-1/2} \quad (28)$$

905 where  $\theta_c$  is the crossing angle of the beams,  $\sigma_z$  is the RMS of the bunch  
 length in the  $z$  direction, and  $\sigma^*$  is the same in the transverse direction.

906 As the proton beams circulate and collide,  $N_b$  decreases, producing a  
 907 falling instantaneous luminosity, as seen in a Run 1 example in Figure 25.  
 908 In Run 2, peak instantaneous luminosity was brought up to  $10^{34} \text{ cm}^{-2}\text{s}^{-1}$ .  
 909 This high instantaneous luminosity and consistent running resulted in  
 910 much faster data collection than in Run 1, which is depicted in Figure 26.

## 911 3.4 PILE-UP IN PROTON-PROTON COLLISIONS

912 One consequence of the high instantaneous luminosity is “pile-up”, or  
 913 multiple simultaneously interactions. Because each bunch has on order  
 914 100 billion protons, it is very likely that multiple protons will collide in  
 915 the same bunch crossing. In fact, the average number of simultaneous  
 916 interactions in 13 TeV data, shown in Figure 27, is about twenty.

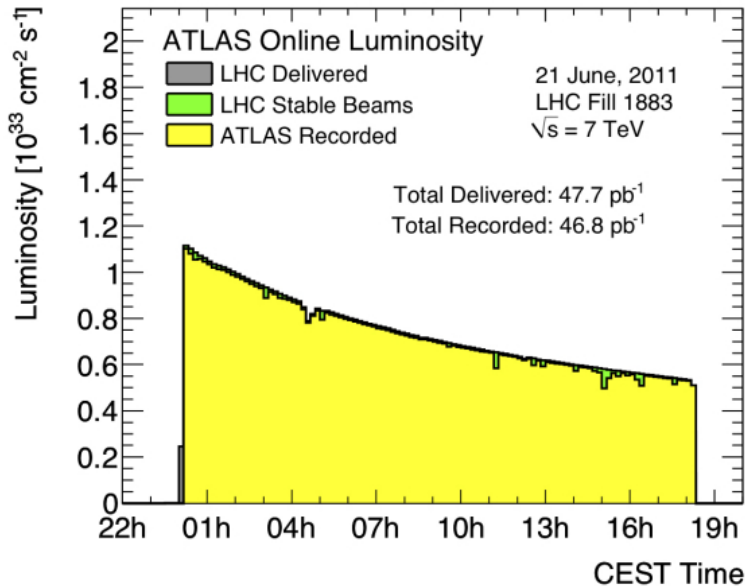


Figure 25: Instantaneous luminosity of one fill of 7 TeV data in 2011.

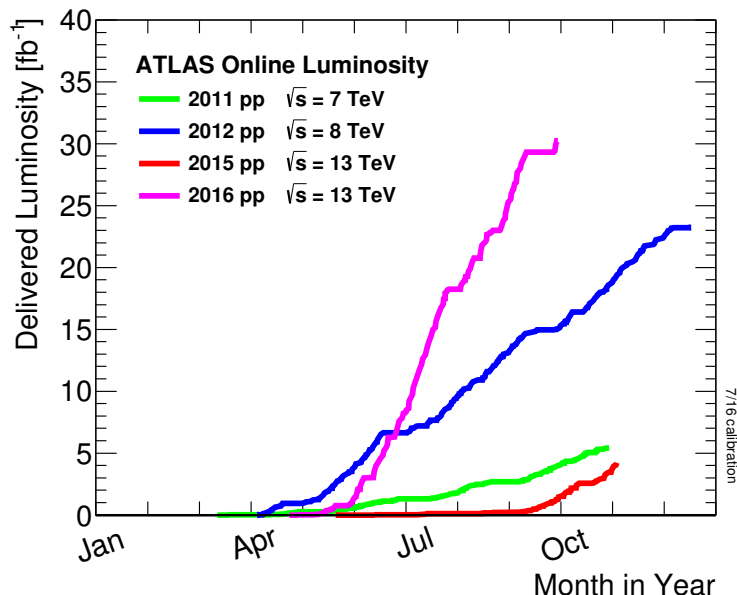


Figure 26: ATLAS luminosity for Run 1 and Run 2, as of September 2016.

917 Pile-up can be a difficult challenge for the ATLAS collaboration because  
 918 it typically results in additional jets in an event, and can increase SM back-  
 919 grounds for analyses seeking to identify events with jets. It can also add  
 920 to the overall hadronic energy of an event, and that energy can be mis-  
 921 assigned to other objects. Fortunately, it is typically possible to resolve the  
 922 different vertices that each proton-proton collision makes, and so pile-up  
 923 jets can be identified and rejected.

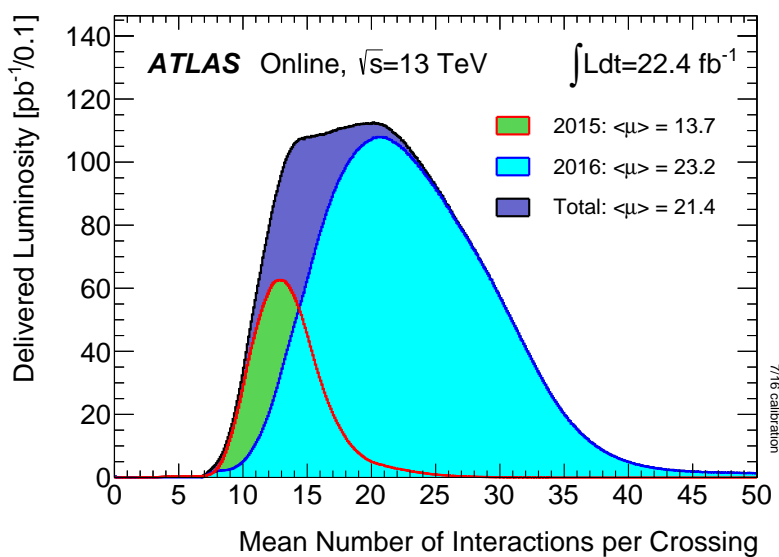


Figure 27: Average number of interactions per crossing shown for 2015 and 2016 separately, as well as the sum of the two years.



924

## 925 THE ATLAS DETECTOR

926 The ATLAS detector circumscribes the LHC’s beam pipe, enclosing the col-  
 927 lision point with a series of particle detecting layers, aimed at making as  
 928 many measurements of the particles leaving the collision point as possible.  
 929 Its goal is to get a precise measurement of all the stable or semi-stable par-  
 930 ticles flying from proton-proton collisions at its center, allowing analyzers  
 931 to fully reconstruct the kinematics of the underlying processes.

932 The ATLAS detector is the largest detector of its kind, measuring 44  
 933 m in length and 25 m in height, as seen in Figure 28. The size is mainly  
 934 determined by the constraints of the MS, discussed in Section 4.4, which is  
 935 the largest and outermost subsystem. The MS is submerged in a spatially  
 936 varying magnetic field provided by three toroidal magnets, while the ID  
 937 (Section 4.2) is encased by a superconducting solenoid, which provides a  
 938 uniform 2 T field throughout its volume [48].

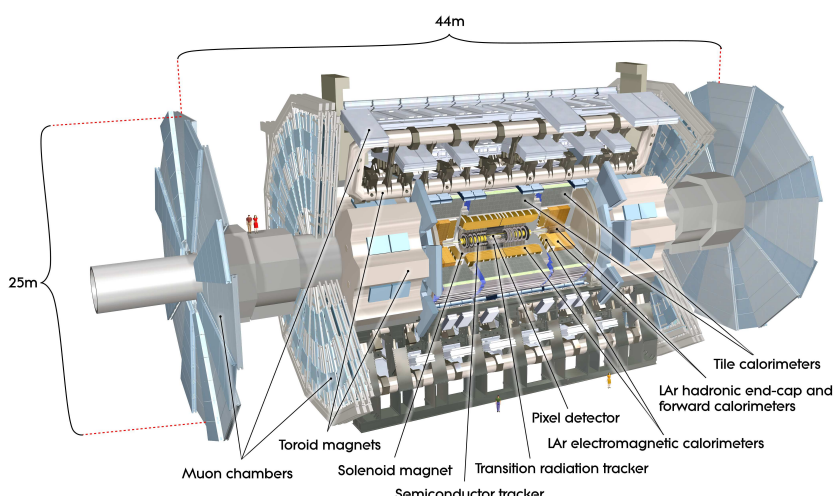


Figure 28: Diagram of the ATLAS detector, with subsystems and magnets identified.

## 939 4.1 COORDINATE SYSTEM USED IN THE ATLAS DETECTOR

940 The ATLAS detector is centered around the  $p - p$  collision point, and is  
 941 built radially out from the beam pipe, maintaining as much rotational  
 942 symmetry around the beam pipe as possible. It is also symmetric in the  
 943 forward-backward directions. A coordinate system using the collision point  
 944 as the origin is used, with the beam line defining the  $z$ -axis. The positive  
 945  $x$  direction is defined as pointing to the center of the LHC ring, while the  
 946 positive  $y$  direction points upwards. For ease of reference, the side of the

947 detector in the positive- $z$  direction is referred to as the A side, and the  
 948 other side is referred to as the C side.

949 Because of the cylindrical design of the detector, angular coordinates are  
 950 often used. The azimuthal angle  $\phi$  defines the angle around the beam pipe  
 951 and the polar angle  $\theta$  defines the angle from the beam axis ( $z$ ). However, a  
 952 transformation of the polar angle called pseudorapidity ( $\eta$ ) is used more  
 953 often, and is defined as

$$\eta = -\ln[\tan \frac{\theta}{2}]. \quad (29)$$

954  $\eta$  is used because the particle distribution from LHC collisions is roughly  
 955 uniform in this variable. Building on this definition, angular distance be-  
 956 tween objects is typically defined as

$$\Delta R = \sqrt{\Delta\eta^2 + \Delta\phi^2}. \quad (30)$$

957 Often variables are defined purely in the transverse plane, which is in-  
 958 dicated by a subscripted  $T$ , as in  $p_T$ , which gives an object's transverse  
 959 momentum.

## 960 4.2 THE INNER DETECTOR

961 The Inner Detector (**ID**) is responsible for the production of tracks, esti-  
 962 mates of the paths charged particles take as they travel through the detec-  
 963 tor. Collisions in the detector can produce about 1000 particles, so identi-  
 964 fying and differentiating all the tracks resulting from a collision is both a  
 965 hardware and a computational challenge.

966 The **ID** consists of three separate subdetectors, each of which has mul-  
 967 tiple layers capable of producing an electrical signal, called a *hit*, when a  
 968 charged particle travels through its active material. ATLAS tracking soft-  
 969 ware considers all these hits and forms tracks, with the goal of minimizing  
 970 fake tracks due to random noise and maximizing the efficiency of identi-  
 971 fying a real particle. Some details of this procedure are discussed in [Chapter 6](#). The full **ID** can be seen in [Figure 29](#), while a schematic in [Figure 30](#)  
 972 shows more detail on the placement of each layer.  
 973

### 974 4.2.1 *The Pixel Detector*

975 The pixel detector lies closest to the beam pipe of the LHC, and has four lay-  
 976 ers comprising 92 million pixels. There are three standard layers, referred  
 977 to as Layers 0-2 (L0, L1, L2), and an additional layer added for the 2015  
 978 data-taking, called the Insertable B-Layer (**IBL**).

#### 979 4.2.1.1 *The Original Pixel Detector*

980 The Pixel Detector consists of high-precision silicon chip pixel modules,  
 981 with 1744 in total, and each module is made up of 16 sensors each with

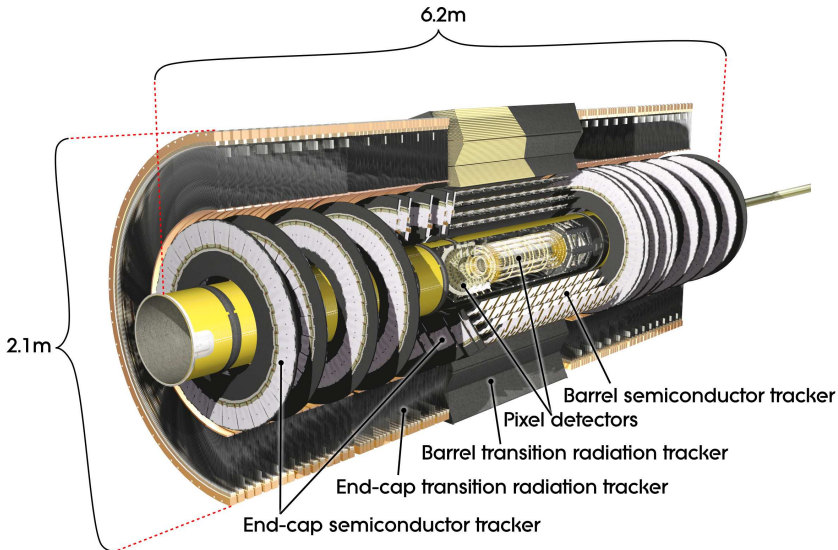


Figure 29: Diagram of the ATLAS Inner Detector, containing the Pixel, SCT, and TRT subsystems.

982 its own read-out system. Each sensor is identical, containing 47232 pixels,  
 983 which are typically each  $50 \times 400 \mu\text{m}^2$ , though pixels at the edges of the  
 984 sensors are slightly longer, at  $50 \times 600 \mu\text{m}^2$ .

985 As shown in Figure 30, the central  $\eta$  region (barrel) is covered by three  
 986 concentric cylindrical layers of sensors, while the higher  $\eta$  region (end-cap)  
 987 is covered by a series of three disks positioned in the  $x - y$  plane. Together,  
 988 they give complete coverage out to  $|\eta| = 2.5$ , and a particle coming from  
 989 the collision point will typically produce hits in three layers.

990 The sensors are n-type silicon wafers with a voltage applied, and a pass-  
 991 ing charged particle produces thousands of electron-hole pairs inside the  
 992 material, which drift in the electric field towards the mounted read-out  
 993 system. A hit occurs when the resulting current becomes large enough to  
 994 pass a threshold designed to suppress noise. A larger total charge deposit  
 995 will result in the signal remaining over the threshold for a longer period  
 996 of time. The initial timing of the hit, and the Time Over Threshold (ToT)  
 997 are both recorded. This measurement is spatially accurate in the barrel  
 998 (endcap) to  $10 \mu\text{m}$  in the  $R - \phi$  direction and  $115 \mu\text{m}$  in the  $z (R)$  direction.

#### 999 4.2.1.2 Addition of the IBL

1000 In 2014, the IBL was added to the pixel detector. This layer sits on top  
 1001 of the beam pipe, inside barrel Lo, providing a measurement of particles  
 1002 only about 3 cm away from the interaction point. Its addition provides  
 1003 greater precision for all track measurements, but it is especially useful for  
 1004 the detection of  $B$  mesons, whose non-trivial lifetimes lead to secondary  
 1005 vertices in ATLAS events. The location of the IBL gives a measurement  
 1006 closer to these secondary vertices, and its increased pixel density increases  
 1007 the probability that these vertices can be resolved.

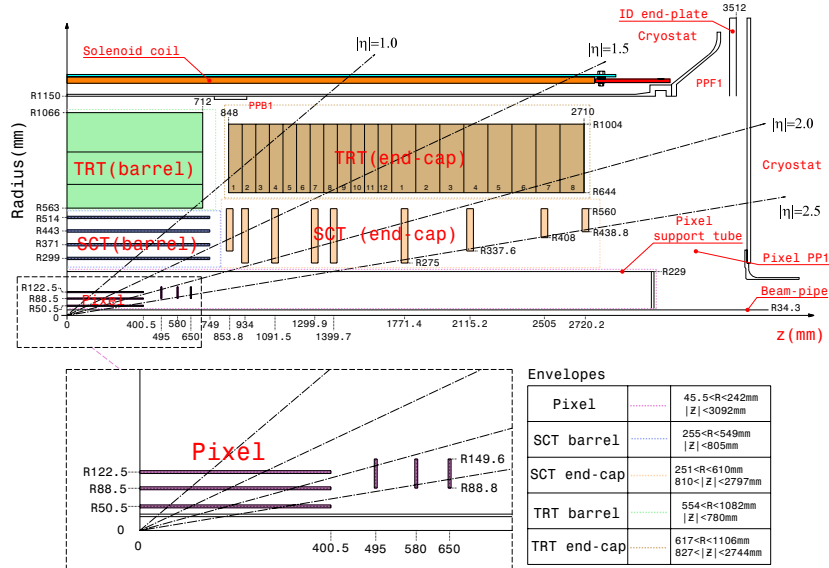


Figure 30: Diagram of one-quarter of the ATLAS Inner Detector in the  $R - z$  plane, with lines drawn to indicate various  $\eta$  locations.

#### 1008 4.2.2 The Silicon Microstrip Tracker

1009 The Silicon Microstrip Tracker (**SCT**) employs a similar technology to the  
 1010 Pixel Detector, with 15912 sensors and 6.3 million readout channels. Its  
 1011 difference from the Pixel Detector is in the readout, which is performed  
 1012 by a series of 12 cm long strips with a width of  $80\text{ }\mu\text{m}$ . These layers are  
 1013 paired, placed on top of one another at a small (40 mrad) angle to allow for  
 1014 position determination in both directions, giving 4 spatial measurements  
 1015 for each particle passing through the **SCT**. In the barrel, these strips run  
 1016 parallel to the beam pipe, while in the endcap, they are arranged radially.  
 1017 These strips have a resolution in the barrel (endcap) of  $17\text{ }\mu\text{m}$  in the  $R - \phi$   
 1018 direction and  $580\text{ }\mu\text{m}$  in the  $z$  ( $R$ ) direction.

#### 1019 4.2.3 The Transition Radiation Tracker

1020 The Transition Radiation Tracker (**TRT**) uses 4 mm diameter gas-filled tubes,  
 1021 each with a high voltage wire suspended along the center of the tube. The  
 1022 tubes run the length of the barrel, with a separate wire in the positive and  
 1023 negative  $z$  direction. In the endcap, the tubes are arranged radially. In total,  
 1024 there are about 351,000 readout channels in the **TRT**. This detector makes  
 1025 measurements only in the  $R - \phi$  direction, where the resolution of each  
 1026 measurement is  $130\text{ }\mu\text{m}$ , and coverage extends to  $|\eta| = 2.0$ . Each particle  
 1027 typically creates about 36 hits as it passes through the **TRT**.

1028 Particles passing through the gas mixture of the **TRT** ionize the gas, pro-  
 1029 ducing electrons which drift towards the wire due to a potential difference  
 1030 applied between it and the tube. The **TRT** also responds to low-energy trans-  
 1031 sition radiation photons, which produce a much larger signal than charged

1032 particles passing through the detector. Because of this strong difference in  
 1033 signals, hits from the [TRT](#) are used to help differentiate between electrons  
 1034 and photons in the detector.

1035 4.3 THE CALORIMETERS

1036 Unlike the tracking detectors, which aim to take measurements of a parti-  
 1037 cle with minimal alterations of its trajectory, the calorimeters measure the  
 1038 energy of objects by stopping them entirely. The calorimeters, which can be  
 1039 seen in [Figure 31](#), provide coverage out to  $|\eta| < 4.9$ . High granularity elec-  
 1040 tronagnetic measurements are made within  $|\eta| < 2.5$  to complement the  
 1041 [ID](#)'s tracking capability. In this range, high  $p_T$  electrons and photons have  
 1042 nearly straight tracks, making momentum measurement through track cur-  
 1043 vature difficult, leaving the calorimeter as the primary energy measure-  
 1044 ment. The hadronic calorimeters, as well as the higher  $|\eta|$  electromag-  
 1045 netic calorimeters, have a coarser granularity.

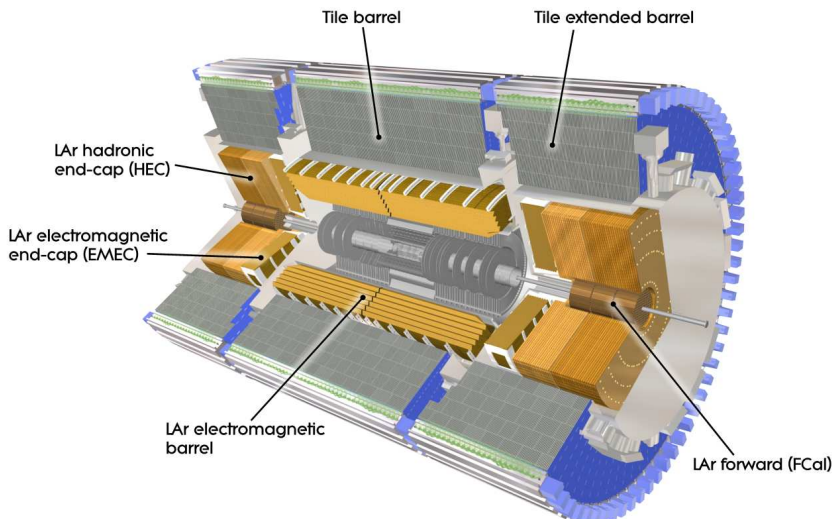


Figure 31: The calorimeter system of the ATLAS detector.

1046 Besides measuring the energy of passing particles, another task of the  
 1047 calorimeter system is to limit punch-through to the [MS](#), described in [Sec-](#)  
 1048 [tion 4.4](#). All other particles must be fully stopped by the calorimeters to  
 1049 allow for clean signals from muons, and to measure the total energy of the  
 1050 particle. This requirement sets a minimum number of interaction lengths  
 1051 for each of the calorimeters.

1052 **THE LAR ELECTROMAGNETIC CALORIMETER** uses liquid argon as its  
 1053 active detector medium alternating with layers of lead acting as the ab-  
 1054 sorber. The layers are shaped like accordions, which allows for complete  
 1055 coverage with multiple layers of active material, three in central  $\eta$  ( $0 <$   
 1056  $|\eta| < 2.5$ ) and two at higher  $\eta$  ( $2.5 < |\eta| < 3.2$ ). [Figure 32](#) shows the layout  
 1057 of a central  $\eta$  module, including this accordion-like layering. At  $|\eta| < 1.8$ ,

1058 an instrumented liquid argon presampler provides a measurement of en-  
 1059 ergy lost prior to reaching the calorimeters. The total energy resolution for  
 1060 this detector is about 10%.

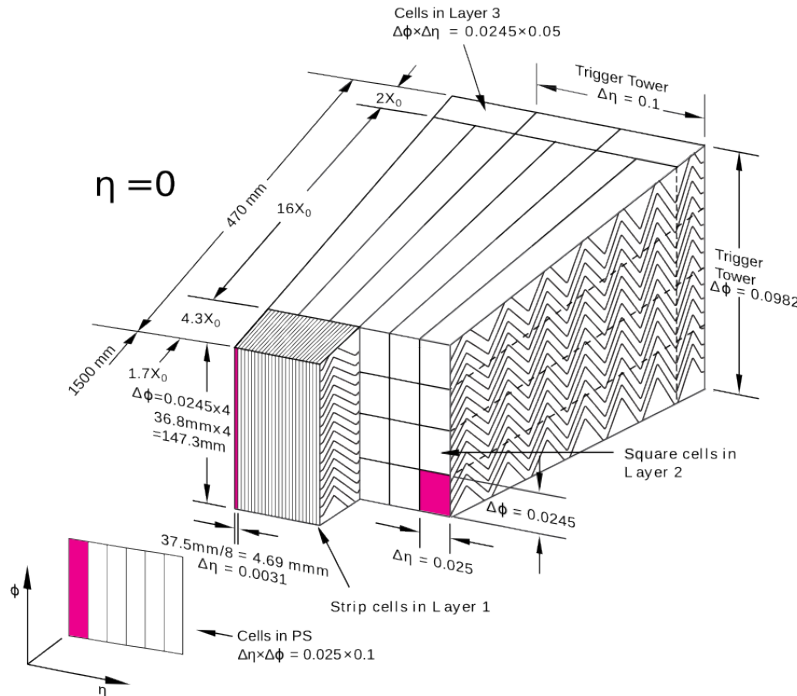


Figure 32: Layout of the LAr calorimeter module at central  $\eta$  [48].

1061 **THE TILE CALORIMETER** is a hadronic calorimeter which surrounds  
 1062 the LAr Calorimeter. It uses layers of steel as its absorber with scintillating  
 1063 tiles as the active material between them, which are read out by photomul-  
 1064 tiplier tubes. The Tile Calorimeter covers  $|\eta| < 1.7$  with a typical energy  
 1065 resolution of about 50%.

1066 **THE LAR HADRONIC ENDCAP CALORIMETER** covers the hadronic calorime-  
 1067 try for higher  $\eta$ . It uses liquid argon active material and copper plate  
 1068 absorbers, resulting in an energy resolution of approximately 50%. This  
 1069 calorimeter covers  $1.5 < |\eta| < 3.2$ , overlapping with the hadronic calorime-  
 1070 ters in either direction of its  $\eta$  range.

1071 **THE FCAL** or forward calorimeter provides electromagnetic and hadronic  
 1072 coverage at very high  $\eta$  ( $3.1 < |\eta| < 4.9$ ). This calorimeter also uses liquid  
 1073 argon as its active material, and uses copper-tungsten as the absorber. Its  
 1074 energy resolution is about 100%.

#### 1075 4.4 THE MUON SPECTROMETER

1076 The Muon Spectrometer ([MS](#)) measures charged particles that penetrate the  
 1077 calorimeter system. Because the calorimeters are designed to completely

absorb electrons, photons, and hadrons, the [MS](#) mainly detects muons, which pass through the calorimeter with very little loss of energy. The goal of the [MS](#) is to give a high-precision measurement of these muons, and also to be able to quickly identify events with muons for the sake of triggering, discussed in [Section 4.6](#). The layout of the [MS](#) can be seen in Figures 33 and 34. Muons can be measured for all  $|\eta| < 2.7$ , and they can be triggered on for  $|\eta| < 2.4$ . The entire system is about 24 m tall and 40 m long.

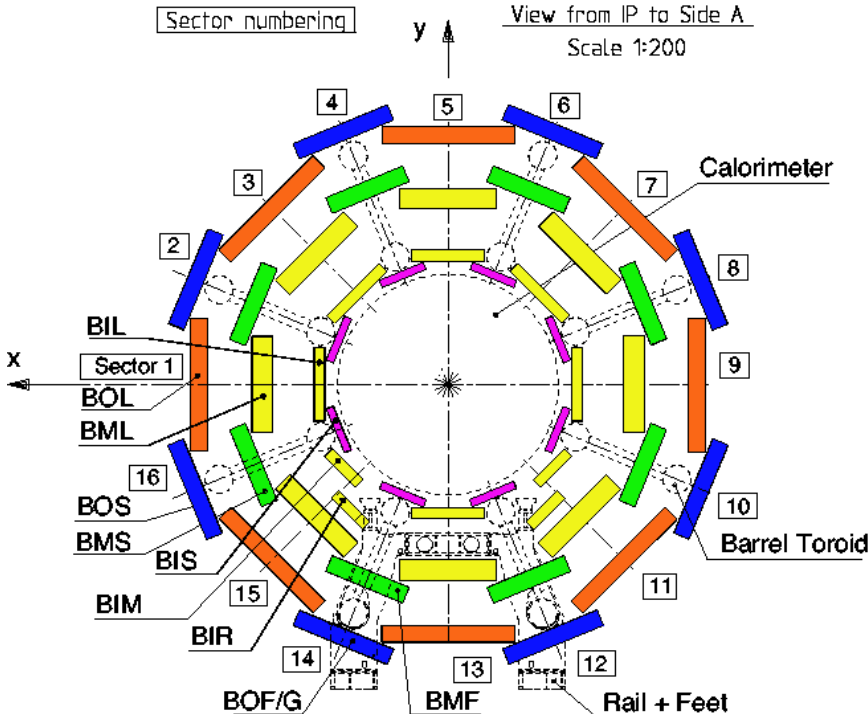


Figure 33: An  $x$ - $y$  view of the [MS](#). In it, the three barrel layers are visible, as well as the overlapping, differently sized chambers. The outer layer of the [MS](#) is about 20m in diameter.

To achieve these goals, the [MS](#) has several subsystems. The system responsible for precision measurement is called the Monitored Drift Tubes ([MDTs](#)). This subdetector consists of chambers of three to eight layers of tubes, with three layers of chambers covering both the barrel and end-cap regions. In the barrel, these chambers are arranged in layers concentric cylinders with small overlaps between adjacent chambers. The chambers are oriented such that the drift tubes are parallel to the beam line. In the endcap, the chambers form disks with drift tubes approximately aligned in the  $R$  direction.

The tubes each contain an Ar/CO<sub>2</sub> gas mixture and a single high voltage wire which runs at its center along its length. Charged particles excite the gas as they pass through it, producing electrons which drift towards the high voltage wire. The resulting electric signal is read out, and the magnitude and timing of the signals are both used to differentiate particle traces from noise.

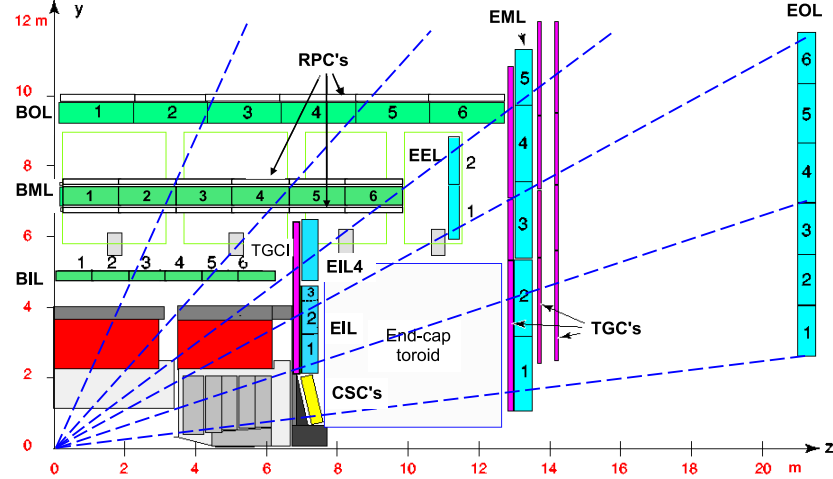


Figure 34: An  $r$ - $z$  view of the MS. The three layers of the barrel and endcap MS are visible, and all muons at  $|\eta|<2.7$  should traverse three detectors, assuming they propagate in an approximately straight line from the interaction point.

Though very effective at giving a precise measurement, the MDTs have two shortcomings. The first is that the measurement is only precise in the direction perpendicular to the tubes; in the direction parallel to them, the resolution is not much better than the length of the drift tube, which are typically several meters long. The resolution in the perpendicular direction is about  $35\ \mu\text{m}$  with the combined measurement of all the tubes in a chamber. The second major shortcoming is that the MDTs are slow, with a maximum drift time of about 700 ns.

The slow drift time means that muons from sequential collisions can appear in the same event, and that the signals from the MDTs are received too late to be used for triggering. To solve the former problem, another detector called the Cathode-Strip Chambers (CSCs) is used in high-rate regions of the MS. This detector consists of multi-wire proportional chambers which have cathode strips on either side of the anode in orthogonal directions, providing a  $40\ \mu\text{m}$  resolution in one direction and 5mm resolution in the other. Their drift times are much shorter than those of the MDTs, at about 40 ns. They are placed in the forward region of the detector ( $2<|\eta|<2.7$ ) where the incident particle rates are highest.

To achieve responses fast enough to be used for triggering, Resistive Plate Chambers (RPCs) and Thin Gap Chambers (TGCs) are used. These chambers both take less than 25 ns to produce a signal. The RPCs are used in the barrel and are made up of two high-resistance plastic plates with a gas mixture under an electric field between them. Passing particles ionize this gas, and the resulting signal is read out via metallic strips mounted to the plastic plates. The TGCs used in the endcap are a form of multi-wire proportional chambers, like the CSCs. Unlike the CSCs, the cathode is placed extremely close to the wires, speeding up its operation.

1128 The massive **MS** is subject to deformations due to gravity and the mag-  
 1129 netic field. To achieve a high precision alignment, these deformations are  
 1130 constantly monitored in each **MDT** chamber with a set of four optical align-  
 1131 ment rays, which give alignment information at the precision of  $<30\ \mu\text{m}$ .  
 1132 In addition, a sag-adjustment system can use this information to re-align  
 1133 any wires that droop under gravity's pull. Lastly, the **MS** can be aligned  
 1134 using the tracks made from hits it measures, discussed more in [Section 5.3](#).

1135 4.5 THE MAGNET SYSTEM

1136 The ATLAS magnet system consists of four superconducting magnets: an  
 1137 inner solenoid, a barrel toroid, and two endcap toroids. Collectively, they  
 1138 are 22m in diameter and 26m long, and their basic layout can be seen in  
 1139 [Figure 35](#).

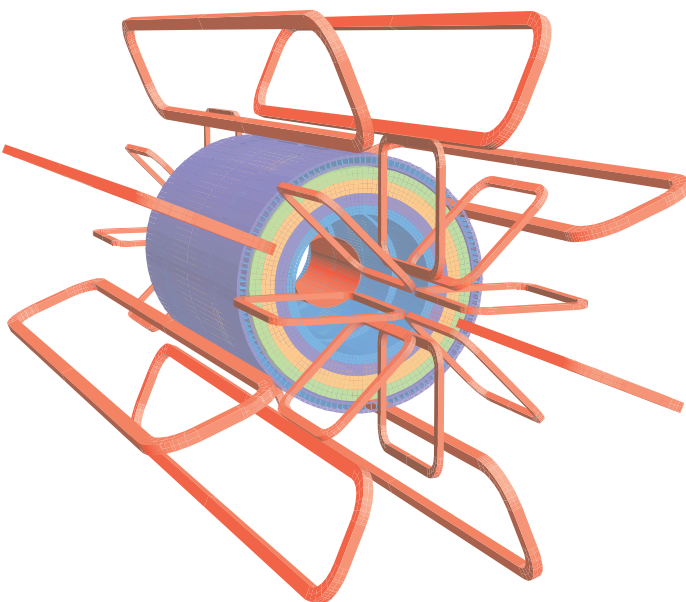


Figure 35: The magnet system of the ATLAS detector. The inner cylinder shows the solenoid which gives a uniform magnetic field in the **ID**. Outside of that are the barrel and endcap toroids, which provide a non-uniform magnetic field for the **MS**.

1140 The solenoid is inside the calorimeter volume and provides a uniform  
 1141 2T magnetic field for particles traveling through the **ID**. This axial field  
 1142 causes the trajectories of charged particles to bend in the  $x - y$  plane, and  
 1143 measurements of the curvature of these trajectories give the most accurate  
 1144  $p_{\text{T}}$  measurement for many particles according to the equation

$$p_{\text{T}} = qB\rho \quad (31)$$

1145 where  $q$  is the charge of the particle,  $B$  is the magnetic field in the  $z$   
 1146 direction, and  $\rho$  is the radius of curvature.

Because the solenoid is placed between the tracking system and the calorimeter, it is important that it interfere minimally with particles in order to allow the calorimeter to measure their full energies. The solenoid is placed inside the same vacuum chamber as the LAr calorimeter and is made of Al-stabilized NbTi superconductor with aluminum casing, giving it a total thickness of about 0.66 radiation lengths.

The barrel toroid is outside the calorimeters and provides the magnetic field for the barrel [MS](#), which varies from 0.2–2.5T. The endcap toroids have a magnetic field range of 0.2–3.5T. All three toroid magnets are made with Al-stabilized Nb/Ti/Cu superconducting coils supported by Al-alloy struts.

The magnets are cooled with liquid helium, and take up to a month to be brought down to operating temperatures. All magnets have cold masses surrounding them to absorb heat in the event of a quench.

The  $B$ -field resulting from this magnet system can be seen in [Figure 36](#). The plot on top demonstrates the relatively constant field rate within the barrel which drops steeply at  $|z|=2$ . The bottom plot shows the field integral in the [MDTs](#) as a function of  $|\eta|$ , demonstrating the good coverage out to  $|\eta|<2.6$  excluding a transition region between the barrel and endcap, where the field changes rapidly, making precise  $p_T$  construction difficult.

#### 4.6 THE TRIGGER SYSTEM AND DATA ACQUISITION

The [LHC](#) provides proton bunch crossings every 25 ns, and each of these events contains about one MB of data, corresponding to 40 TB/s, a completely unmanageable amount of data. In addition to this concern, many of ATLAS’s subdetectors like the pixel detector and [MDTs](#) take much longer than 25 ns to read out, making keeping up with the bunch crossing rate impossible. To reduce the total data read out and allow for selective reading out of the slower detectors, a triggering system is used.

The trigger system uses fast detectors to get a coarse picture of an event’s topology, which is then compared to a trigger menu, which lists the types of events that are interesting enough to keep. Overall, the trigger system reduces the 40 million events a second to about 1000 to be fully read out from the ATLAS detector.

This filtering of events is done in two steps: the [L<sub>1</sub>](#) trigger is implemented in hardware and reduces the initial 40MHz to 100kHz, while the [HLT](#) is implemented in software, further reducing the rate to 1kHz [[52](#)]. The [L<sub>1</sub>](#) trigger uses coarse granularity information from the fast read-out subdetectors: the calorimeters, the [RPCs](#) and [TGCs](#).

The coarse grained calorimeter information used for the [L<sub>1</sub>](#) trigger decision is referred to as L<sub>1</sub> Calorimeter Trigger ([L<sub>1</sub>Calo](#)) and uses information from all calorimeter systems. [L<sub>1</sub>Calo](#) is responsible for all triggers excluding muons, meaning it must be capable of identifying a large number of different objects and event topologies, including high- $p_T$  objects,  $E_T^{\text{miss}}$ , and large amounts of hadronic energy. The trigger can also identify isolated

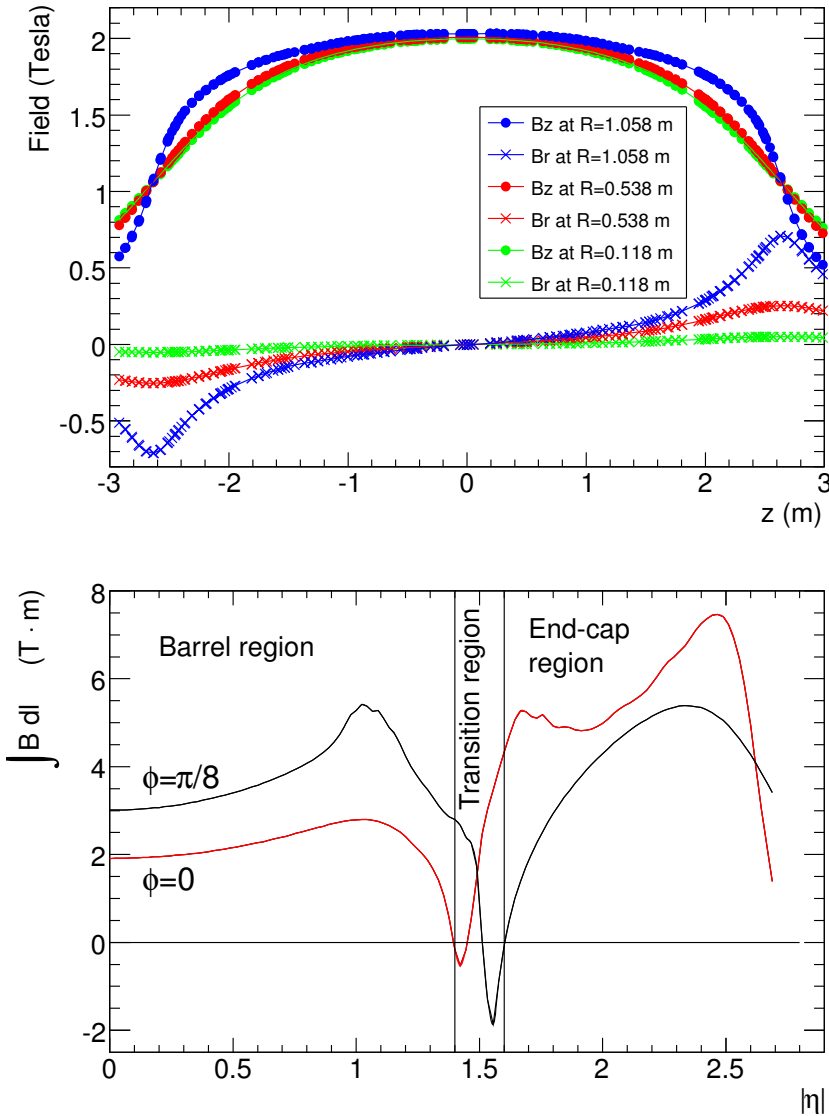


Figure 36: Plots of the magnetic field within the ATLAS detector. Top is the field (broken into its  $R$  and  $z$  components) as a function of  $z$  for several different values of  $R$ . Bottom is the field integral through the MDTs as a function of  $|\eta|$  for two different  $\phi$  values.

1191 objects, objects with very few calorimeter deposits from other objects near  
 1192 them.

1193 For muon triggers, the trigger algorithm looks for patterns of hits from  
 1194 the RPC and TGC that are consistent with high- $p_T$  muons with origins at  
 1195 the interaction point.

1196 An example of the L1 trigger rates for different types of events can be  
 1197 seen in Figure 37 for one run in July 2016. The common features to all rates  
 1198 are due to LHC luminosity changes, deadtimes due to detector inefficiency,  
 1199 and adjustment of prescales to optimize trigger bandwidth.

1200 All of this information is analyzed by the Central Trigger Processor  
 1201 (CTP), which uses a trigger menu identifying all types of events to be kept

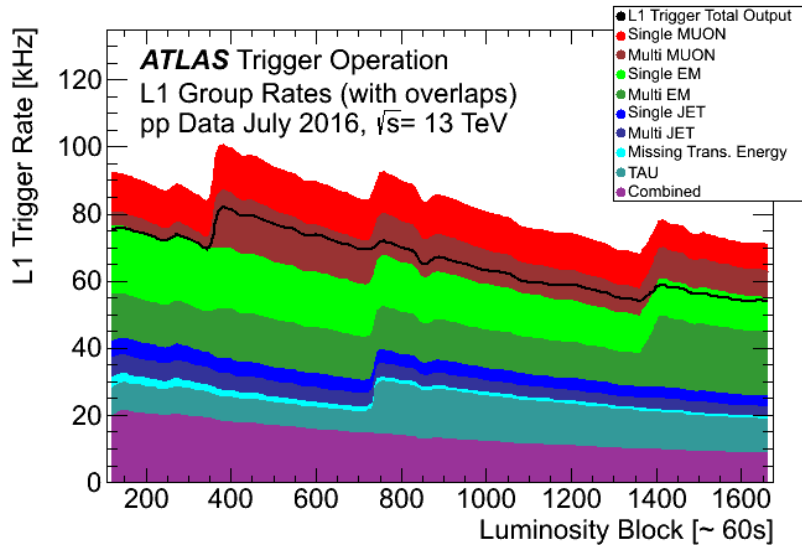


Figure 37:  $\text{L}_1$  trigger rates for a run in July 2016 as a function of luminosity block, an approximately 60-second long period of data-taking. The total rate is lower than the combined stack because of overlapping triggers.

to return a trigger decision. The event must be processed in about 2.5  $\mu\text{s}$  so that the remaining event information not yet read out is still available on the subdetectors when the trigger decision is made. This decision is passed to the Trigger Timing and Control (TTC), which communicates with all subdetectors. Upon receiving a  $\text{L}_1$  trigger, the subdetectors read out all the information they've stored about the event and place it on their Read Out Boards ( $\text{ROBs}$ ).

The  $\text{HLT}$  takes the data from particular Region of Interests ( $\text{RoIs}$ ), areas containing interesting objects that caused the  $\text{L}_1$  trigger, and analyzes this much more complete picture of the region to decide whether or not the event is still interesting enough to keep. This process has its own trigger menu with dedicated  $\text{L}_1$  seeds for each item.  $\text{HLT}$  triggers typically have slightly higher thresholds than their corresponding  $\text{L}_1$  triggers to ensure that events that would pass the  $\text{HLT}$  requirements are very likely to have passed the  $\text{L}_1$  requirements. Figure 38 shows the  $\text{HLT}$  rates for the same run in July. In addition to the event types seen in Figure 37, the  $\text{HLT}$  can also identify events with  $b$ -jets, differentiate between electrons and photons, and identify events interesting for B-physics.

Events passing the  $\text{HLT}$  trigger are written to disk to be analyzed. An example of the total trigger efficiency for single electron triggers is shown in Figure 39. Trigger efficiencies can be taken directly from  $\text{MC}$ , and are measured in data via a method called tag-and-probe, the main principles of which are discussed in Section 10.3.

Events types that occur very frequently, such that it would require too much of the total trigger bandwidth to record all events passing a given threshold, are prescaled. Events passing these triggers are only recorded a

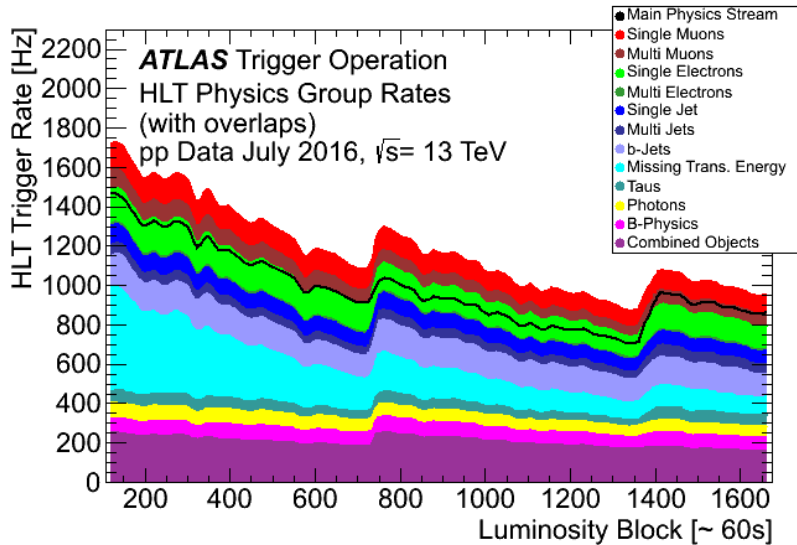


Figure 38: HLT trigger rates for a run in July 2016 as a function of luminosity block, an approximately 60-second long period of data-taking. The total rate is lower than the combined stack because of overlapping triggers.

fraction of the time, and these prescaling rates are used to adjust the final data to account for the limited rate. For example, the lowest unprescaled single electron trigger in 2016 data-taking required an electron with 60 GeV  $p_T$ . A trigger requiring electrons with only 10 GeV  $p_T$  also exists, but is prescaled by approximately a factor of ten.

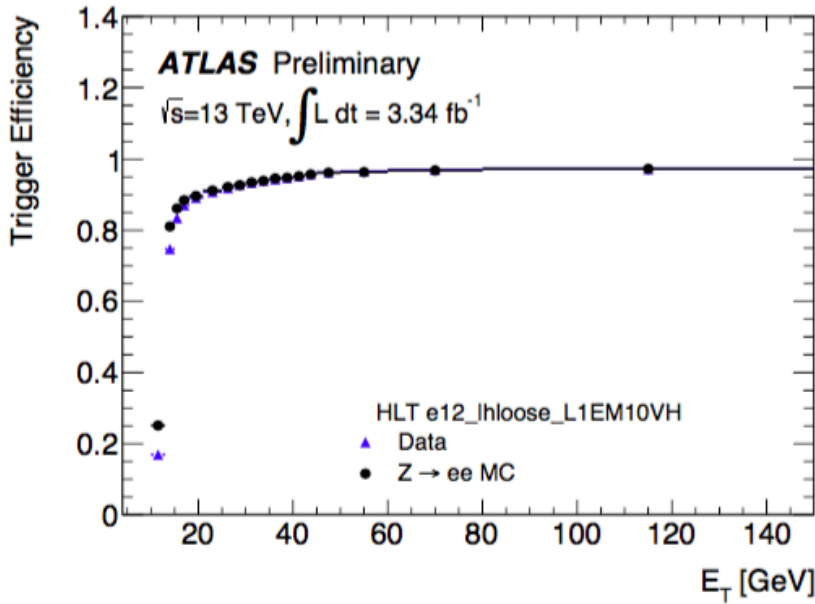


Figure 39: Trigger efficiencies as a function of  $E_T$  for data and MC. Efficiencies are given for offline selected loose electrons.



1233

1234 OBJECT RECONSTRUCTION IN THE ATLAS DETECTOR

---

1235 Object reconstruction is the computationally intensive process of interpreting  
1236 the signals from the approximately 100 million read-out channels of  
1237 the ATLAS detector into a collection of particles and jets, the objects with  
1238 which physics analysis can be performed. This process is complicated, and  
1239 requires dedicated working groups in the ATLAS experiment that optimi-  
1240 ze the understanding of each type of object. These groups must all col-  
1241 laborate to provide a full picture of the events in the detector. For each  
1242 object type, candidate objects are reconstructed, and then an identification  
1243 step is performed, which chooses which candidates will be used at the  
1244 analysis level, based on a series of quality requirements.

## 1245 5.1 ELECTRONS

1246 Electrons are reconstructed through a combination of [ID](#) and calorimeter  
1247 measurements. They travel through the tracking system, leaving charge de-  
1248 posits in each layer, then are absorbed by the electromagnetic calorimeter.  
1249 These two measurements work in conjunction to deliver high resolution  
1250 measurements of electron momentum from low- $p_T$ , where track curvature  
1251 gives the most reliable measure of the electron’s energy, to high- $p_T$ , where  
1252 the tracks are almost perfectly straight, but the calorimeter can still pro-  
1253 vide a reliable measurement.

1254 In the central region ( $|\eta| < 2.47$ ) of the ATLAS detector, electron recon-  
1255 struction begins with the identification of energy deposits in the electro-  
1256 magnetic calorimeter. The calorimeter clusters are seeded by sliding longi-  
1257 tudinal windows, which are measured in units of 0.025 in  $\eta$  and  $\phi$ .  $3 \times 5$   
1258 unit windows are used, which require at least 2.5 GeV in the window to  
1259 form a seed [53].

1260 These clusters are matched to [ID](#) tracks by extrapolating each track to the  
1261 middle layer of the calorimeter and identifying nearby clusters. If there are  
1262 multiple tracks associated with a given cluster, tracks with silicon hits are  
1263 preferentially chosen, and then the track with the smallest  $\Delta R$  to the center  
1264 of the cluster is selected. If a matching track is found, it is used to deter-  
1265 mine the likely direction of bremsstrahlung radiation in the calorimeter,  
1266 and maximum distance to match a track to a cluster is expanded in the  $\phi$   
1267 direction to account for this radiation. If no track is found, the cluster is  
1268 rejected.

1269 The calorimeter clusters are then rebuilt in larger windows,  $3 \times 7$  in the  
1270 barrel and  $5 \times 5$  in the end-caps. An estimate of the energy is made by sum-  
1271 ming the measured calorimeter energy with estimates of the energy lost  
1272 before the electron reached the calorimeter, energy outside of the cluster  
1273 window, and energy not fully deposited in the calorimeter. These estimates

1274 are made with parametrized functions determined from a combination of  
 1275 MC and measurements of energy loss determined with the presampler.

1276 The momentum of a central electron is determined through a combina-  
 1277 tion of the calorimeter and track measurements of the electron, while its  $\eta$   
 1278 and  $\phi$  are taken from the track at its vertex.

1279 In the forward region, where no tracking is available, electron energy is  
 1280 determined more roughly. Calorimeter cells are formed into variable-sized  
 1281 clusters in regions of significant energy deposition, and the center of the  
 1282 cluster is used to determine angular coordinates of the electron. However,  
 1283 because these electrons have worse resolution in both their position and  
 1284 energy, they are often rejected by analyses that depend on well-measured  
 1285 objects.

1286 These reconstructed electron candidates' quality are then assessed based  
 1287 on an algorithm that uses multivariate analysis to assign a likelihood that  
 1288 a candidate is a true electron based on input from just under twenty differ-  
 1289 ent variables. These include track quality, hadronic leakage, cluster shape,  
 1290 and transition radiation, incorporating information from as many subde-  
 1291 tectors as possible in its determination of the candidate's quality. Each  
 1292 variable is assigned a probability distribution function for true electrons  
 1293 and background processes, and they are collectively used to provide a  
 1294 *likelihood* value which can be cut on.

1295 Three levels of identification, Loose, Medium, and Tight, are defined with  
 1296 different likelihood cuts, with electron candidates passing tighter identifi-  
 1297 cation levels always a subset of looser electrons. Figure 40 gives the effi-  
 1298 ciencies at each of these working points both for true electrons and for  
 1299 hadrons, which can be misidentified as electrons. Tighter working points  
 1300 have worse efficiencies, but lower misidentification rates for hadrons as  
 1301 well as photons.

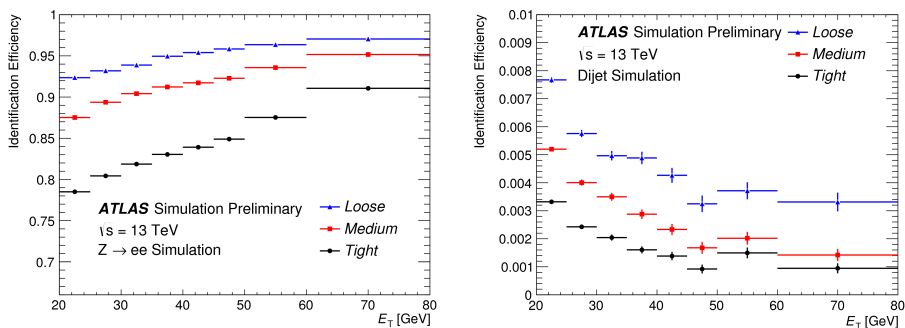


Figure 40: Identification efficiencies from MC samples for Loose, Medium, and Tight working points. Left is the efficiency for identification of true electrons taken from  $Z \rightarrow ee$  MC, and right is the efficiency for misidentification of jets as electrons taken from dijet MC [54].

1302 MC efficiencies can be compared to efficiencies measured in data using  
 1303 the tag-and-probe method, to obtain a *scale factor*, a correction factor ap-  
 1304 plied to MC to better emulate the rates at which electrons are reconstructed  
 1305 and identified in data. Figure 41 shows a comparison of the combined re-

1306 construction and identification efficiencies in data and MC, with the result-  
 1307 ing scalefactors also displayed as the ratio.

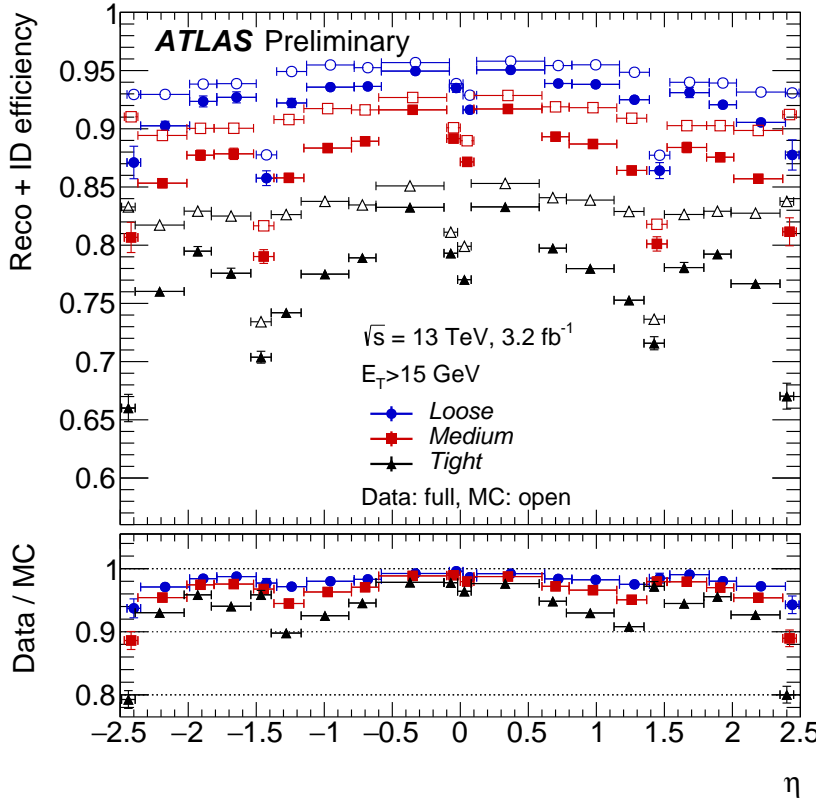


Figure 41: Combined electron reconstruction and identification efficiencies measured as a function of  $\eta$  for data (using the tag-and-probe method on  $Z \rightarrow ee$  events) and  $Z \rightarrow ee$  MC. Distributions include all electrons with  $E_T > 15$  GeV. [54].

1308 Electrons can also have *isolation* requirements, cuts on nearby calorime-  
 1309 ter activity or tracks. Isolation variables are primarily used to reject non-  
 1310 prompt leptons, leptons which aren't produced by the initial hard scatter-  
 1311 ing of the  $p - p$  collision. These can be produced by heavy flavor hadron  
 1312 decays and converted photons, as well as misidentified hadrons. Cuts are  
 1313 made on the amount of nearby calorimetric energy and sum of the  $p_T$  of  
 1314 any nearby tracks relative to the electron's energy, forming a series of work-  
 1315 ing points. Fixed cut working points, which specify the relative fraction to  
 1316 cut on, can be used, but efficiency targeted working points are more pop-  
 1317 ular. These include Tight and Loose working points, which operate at 95  
 1318 and 98% efficiency respectively, and working points that target higher ef-  
 1319 ficiencies at higher electron  $p_T$ , Gradient and GradientLoose. These work-  
 1320 ing points each have 99% efficiency for electrons with  $p_T > 60$  GeV, but 90  
 1321 and 95% efficiencies at 25 GeV.

## 1322 5.2 PHOTONS

1323 The reconstruction of photons is performed in parallel to electron recon-  
 1324 struction. Seed clustering is performed, and tracks are matched to these  
 1325 clusters, as in the case of the electron reconstruction described in [Sec-  
 1326 tion 5.1](#).

1327 Photons can be converted to electron-positron pairs in the [ID](#), leaving  
 1328 a pair of tracks, or they can pass through without conversion, leaving no  
 1329 tracks behind. As a consequence, calorimeter clusters resulting from pho-  
 1330 tons can have no tracks associated with them, two tracks, or one track, in  
 1331 the case that one of the conversion tracks is not reconstructed. The recon-  
 1332 struction software attempts to identify all these scenarios and differentiate  
 1333 these clusters from electron and hadron deposits [55].

1334 Two-track clusters are required to consist of two oppositely charged  
 1335 tracks that emerge from a conversion vertex running parallel to one an-  
 1336 other. A likelihood that these tracks are from electrons is determined using  
 1337 the high threshold hits in the [TRT](#), and quality requirements are made on  
 1338 the tracks using this likelihood. For tracks with silicon hits, a loose like-  
 1339 lihood requirement of 10% is made, while tracks without silicon hits are  
 1340 required to have at least 80% likelihood. The tracks are then fit to deter-  
 1341 mine the conversion vertex, and quality cuts are made, such as requiring  
 1342 that conversion vertices within the silicon volume correspond to tracks  
 1343 with silicon hits.

1344 Single track clusters occur most often from conversions in the outermost  
 1345 layers of the [ID](#), and are more difficult to reconstruct. Tracks are typically  
 1346 lost because an electron or positron resulting from the conversion has a  $p_T$   
 1347 too low to be reconstructed, or because the two tracks are so close together  
 1348 that they're identified as a single track. The single track is required to have  
 1349 at least a 95% electron likelihood from [TRT](#) hits, and must not have a hit in  
 1350 the innermost layer of the pixel detector. The conversion vertex is defined  
 1351 as the first hit of the single track.

1352 The tracks associated with these conversion vertices are extrapolated to  
 1353 the calorimeter and matched to cluster, except in the case that there are two  
 1354 tracks that differ substantially in their  $p_T$  measurements, in which case the  
 1355 position of the conversion vertex is used for extrapolation to the calorime-  
 1356 ter, assuming a straight-line trajectory. If multiple vertices are matched to  
 1357 a single cluster, preference is given to vertices with double tracks, silicon  
 1358 hits, and finally to tracks closest to the interaction point.

1359 Any cluster with neither a conversion vertex or a track associated with  
 1360 it is identified as an unconverted photon. Clusters associated with both  
 1361 electrons and photons are assigned to one or the other based on their  
 1362 properties. Clusters are preferentially identified as photons in the case that  
 1363 they are matched to a conversion vertex in which at least one track is  
 1364 associated with both the vertex and the cluster, or if the associated tracks  
 1365 have a  $p_T$  smaller than the cluster's  $p_T$ .  $E/p$ , the ratio of the cluster and  
 1366 track energy measurements, can also be used to differentiate electrons and

1367 photons. Electron candidates are instead reconstructed as photons if they  
 1368 have  $E/p > 10$  or if the track matched to the electron has  $p_T$  below 2 GeV.

1369 Photon energy is determined in a  $3 \times 5$  ( $3 \times 7$ ) window for unconverted  
 1370 (converted) photons in the barrel, where the window is expanded to com-  
 1371 pensate for the increased spread of energy from the conversion products.  
 1372 In the endcap, the  $5 \times 5$  window is used in all cases. Like the electrons,  
 1373 the calibration of the photon's energy accounts for energy loss before the  
 1374 calorimeter, as well as energy deposited outside the cell and beyond the  
 1375 electromagnetic calorimeter.

1376 Photon identification is performed in the range  $|\eta| < 2.37$  using a se-  
 1377 ries of cuts on the shape of the shower in the electromagnetic calorime-  
 1378 ter, as well as the amount of additional energy deposited in the hadronic  
 1379 calorimeter. Photons in the the so called *crack* region of the calorime-  
 1380 ter ( $1.37 < |\eta| < 1.52$ ), where a discontinuity prevents accurate assess-  
 1381 ment of photon energy, are rejected. The photon identification has only  
 1382 one working point, called **Tight**, which has an identification efficiency  
 1383 of 53–64% (47–61%) for unconverted (converted) photons with  $E_T = 10$   
 1384 GeV and 88–92% (96–98%) for photons with  $E_T \geq 100$  GeV [56]. Effici-  
 1385 cies as a function of  $p_T$  measured in the 2016 data and compared to **MC**  
 1386 can be seen in Figure 42.

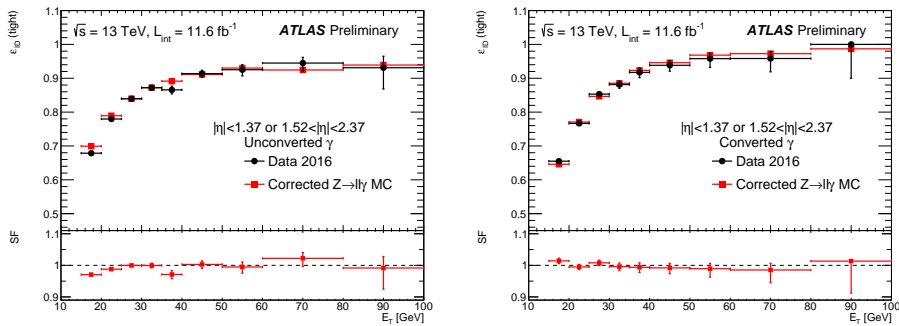


Figure 42: Comparison of Tight identification efficiency measurements from data and  $Z \rightarrow \ell\ell\gamma$  MC for unconverted (left) and converted (right) photons, with an inclusive  $\eta$  selection. The bottom of each figure shows the ratio of data and MC efficiencies. [57].

1387 Photon isolation, like electron isolation, can be determined as the com-  
 1388 bination of nearby calorimeter deposits and tracks. Fixed cuts on the iso-  
 1389 lation as a fraction of photon energy is typically used. A working point  
 1390 called **FixedCutTight** reconstructs the amount of calorimeter energy (ex-  
 1391 cluding that of the photon) in a cone of  $\Delta R = 0.4$  around the photon and  
 1392 the amount of energy from the sum of track  $p_T$  in a cone of  $\Delta R = 0.2$ ,  
 1393 including only tracks associated with the primary vertex. Defined relative  
 1394 to the photon's  $p_T$ , this working point includes photons with calorimetric  
 1395 isolation less than  $0.022 p_T + 2.45$  GeV and track isolation less than  $0.05 p_T$   
 1396 [58].

## 1397 5.3 MUONS

1398 Muon reconstruction is performed independently in the **ID** and the **MS**,  
 1399 then the two measurements are combined when consistent tracks are found  
 1400 in each system [59]. The **ID** reconstruction is performed using the tracking  
 1401 mechanism over the  $|\eta| < 2.5$  range. As with electrons, hits in the layers  
 1402 of the **ID** are fit to tracks, a process described in more detail in [Chapter 6](#).

1403 The **MS** track reconstruction is performed in the  $|\eta| < 2.7$  range and  
 1404 begins with a search in each muon chamber for patterns of hits consistent  
 1405 with a track, called *segments*. The **MDT** chamber hits are fit to a straight line,  
 1406 and nearby **RPC** and **TGC** chambers provide the coordinate orthogonal to  
 1407 the magnetic curvature for these hits. Segments are also built in the **CSC**,  
 1408 where they are required to be loosely consistent with a track originating  
 1409 from the interaction point.

1410 These segments are then fit together, starting from the middle layers  
 1411 of the **MS**, with track quality requirements on the resulting combinations  
 1412 based on the  $\chi^2$  of the fits. Tracks must have at least two segments, except  
 1413 in the transition region between the barrel and endcap, where a single high  
 1414 quality segment can qualify as a track. Segments are allowed to be shared  
 1415 between multiple tracks in the initial reconstruction, but after the combi-  
 1416 nation, tracks with shared segments and low quality fits are removed.

1417 These **MS** tracks are then combined with measurements from other parts  
 1418 of the ATLAS detector. The best quality muons are combined muons,  
 1419 which have **ID** and **MS** tracks associated to them, the hits of which are re-fit  
 1420 to form a combined track. **MS** hits can be added or removed at this stage  
 1421 based on their consistency with the new track. Other types of muons exist,  
 1422 including extrapolated muons, which have only **MS** tracks that are con-  
 1423 sistent with the interaction point, calorimeter-tagged muons, which com-  
 1424 bine an **ID** track with a calorimeter deposit consistent with a muon, and  
 1425 segment-tagged muons, which combine an **ID** track with a segment in the  
 1426 **MS**. Muons with shared **ID** tracks are not allowed, with preference given  
 1427 to combined muons, then calorimeter-tagged muons, and lastly segment-  
 1428 tagged muons.

1429 There are four muon identification working points for muons: **Loose**,  
 1430 **Medium**, **Tight**, and **High- $p_T$** . These working points all have different effi-  
 1431 ciencies for the identification of muons, balanced against the mis-identification  
 1432 of hadrons. One of the key variables for their discrimination is  $q/p$  signif-  
 1433 icance, which quantifies the consistency between the **ID** and **MS** mea-  
 1434 surements of momentum. The  $\chi^2$  of the combined fit is also an important  
 1435 discriminator.

1436 The **Loose**, **Medium**, and **Tight** efficiencies are inclusive, with all **Tight**  
 1437 muons passing the **Medium** requirements, and **Medium** muons passing the  
 1438 **Loose** requirements. The **Loose** requirement includes all types of recon-  
 1439 structed muons, but allows muons without **MS** tracks only in the  $\eta < 0.1$   
 1440 range where there is a gap in the **MS** coverage to accomodate cabling  
 1441 for the calorimeter system. The **Medium** working point includes only com-  
 1442 bined and extrapolated muons, and is the default for most ATLAS analy-

ses. Extrapolated muons are allowed only outside the **ID** tracking system ( $|\eta| > 2.5$ ), a region often excluded by analyses because of the decreased efficiency and larger  $p_T$  resolution of these muons. For the combined muons, at least three hits in at least two **MDT** layers are required (except in the  $\eta < 0.1$  region) and a  $q/p$  significance cut is made to reduce backgrounds. Even with the reduced requirements at low  $\eta$ , there is a drop in efficiency in this region, as shown in Figure 43. The Tight working point additionally cuts on  $\chi^2$  and makes further requirements on the consistency between **ID** and **MS**  $p_T$  measurements.

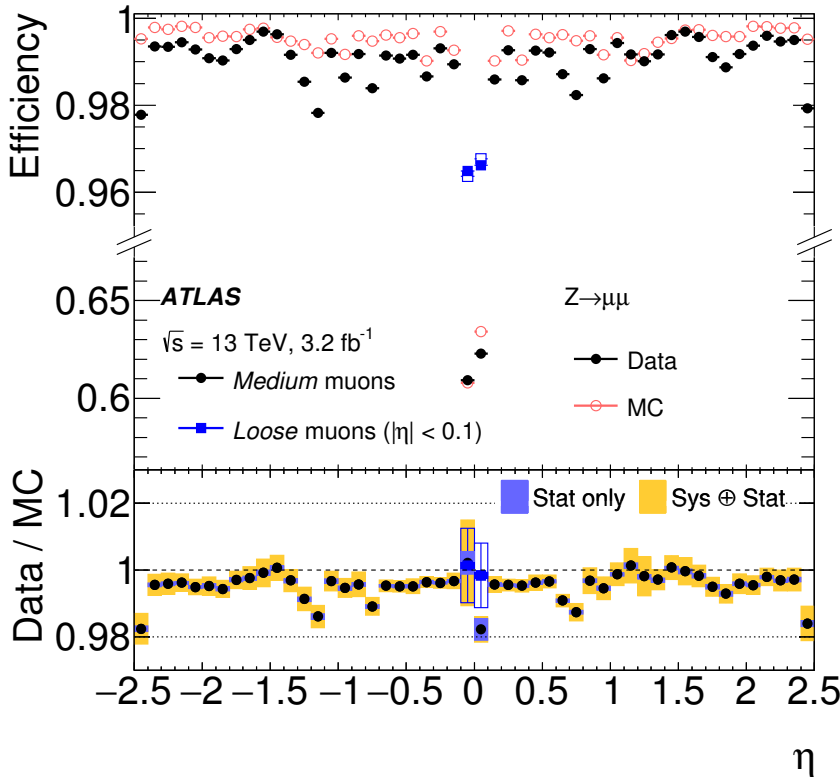


Figure 43: Muon reconstruction efficiency for the Medium and (for small  $|\eta|$ ) Loose working points measured with  $Z \rightarrow \mu\mu$  events in data using the tag-and-probe method and in MC as a function of  $\eta$ . The ratio between the two is shown at the bottom. [59]

The High- $p_T$  working point is designed to minimize the resolution for high- $p_T$  muons, at the cost of lower efficiencies. Muons passing the High- $p_T$  requirements must have at least three **MDT** hits in three layers, which decreases efficiency but gives greatly improved  $p_T$  resolution. In addition, some regions of the **MS** with poor alignment are vetoed to cut down on mismeasurement. Compared to the default working point these muons have much lower efficiency: 78% (90%) for High- $p_T$  muons compared to 96% (96%) for Medium in the  $p_T$  range of 4-20 GeV (20-100 GeV). The efficiency as a function of  $\eta$  for this working point can be seen in Figure 44, where the efficiency loss due to the of vetoing of some chambers is especially apparent. Mismodeling of the alignment and the specificity of the

1463 momentum resolution cuts cause a large discrepancy between data and  
1464 MC efficiencies, resulting in scale factors that differ from unity by as much  
1465 as 10%.

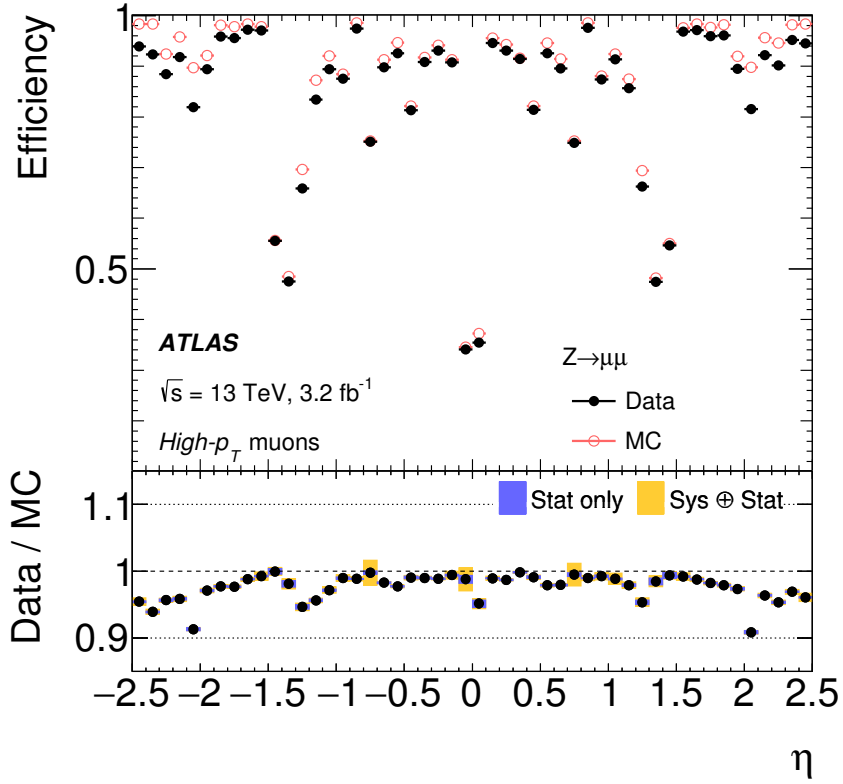


Figure 44: Muon reconstruction efficiency for the High- $p_T$  working point measured with  $Z \rightarrow \mu\mu$  events in data using the tag-and-probe method and in MC as a function of  $\eta$ . The ratio between the two is shown at the bottom. [59]

1466 The most common isolation selection for muons is designed in the same  
1467 way as the electron isolation, and also called GradientLoose. It is con-  
1468 structed such that muons with  $p_T$  of 25 GeV have an efficiency of 95%, and  
1469 muons with  $p_T$  of 60 GeV have an efficiency of 99%.

#### 1470 5.4 JETS

1471 Jets are the most complicated objects to reconstruct in the ATLAS detector  
1472 because each jet is an assembly of many hadronic particles. In contrast to a  
1473 lepton, whose reconstructed energy can easily be compared to its true en-  
1474 ergy from simulation, even a jet's true energy is ambiguous, and is depen-  
1475 dent on the choice of the jet's definition. The standard jet reconstruction  
1476 algorithm used in the ATLAS experiment is called anti- $k_t$  [60].

1477 This algorithm begins with clusters in the calorimeter defined by topo-  
1478 logically connected cells with energy deposits significantly higher than  
1479 the noise background. These clusters can be defined in multiple ways, but

1480 there are two collections used most commonly for analysis. One uses cluster energies calibrated for electromagnetic showers ([EM](#)), and another uses  
 1481 clusters calibrated to hadronic showers. The second uses a method called  
 1482 Local Cluster Weighting ([LCW](#)), which first determines the extent to which  
 1483 the cluster is electromagnetic or hadronic based on the energy density and  
 1484 the shower depth, then applies a calibration accordingly for each cluster.  
 1485

1486 To reconstruct jets, a set of clusters is chosen and the anti- $k_t$  algorithm  
 1487 is then applied, beginning with the highest energy cluster and grouping it  
 1488 with nearby clusters according to the distance measure

$$d_{ij} = \min(k_{ti}^{-2}, k_{tj}^{-2}) \frac{\Delta_{ij}^2}{R^2} \quad (32)$$

1489 where  $R$  is the algorithm's radius parameter, typically set to 0.4,  $\Delta$  gives  
 1490 the angular separation of the two clusters, and  $k_t$  is the transverse mo-  
 1491 mentum associated with the cluster. The jet is defined by clusters grouped  
 1492 within the cone radius, then the axis of the jet is reassessed. This process  
 1493 is iterated upon until a stable jet is produced. The inverse dependence on  
 1494 the  $k_t$  of the cluster produces jets with energetic cores and softer edges,  
 1495 which matches the expectation from a hadronic shower. In addition it is  
 1496 infrared and collinear safe, with neither soft emission or collinear particles  
 1497 altering the reconstruction of the jet.

1498 A series of calibrations are then applied to these jets. The first is to cor-  
 1499 rect for additional hadronic energy due to pile-up. [Figure 45](#) demonstrates  
 1500 the impact of pile-up on the energy density of an event, and this overall  
 1501 change in energy density can affect the amount of stray energy associated  
 1502 with reconstructed jets. To remove this dependence, a correction is taken  
 1503 from [MC](#) and parametrized in terms  $p_T$ ,  $\eta$ , and the number of primary ver-  
 1504 tices in the event, as well as the average number of vertices, which makes  
 1505 correction for out-of-time pile-up possible. Next, jets are corrected to have  
 1506 their origin at the primary vertex instead of the center of the ATLAS de-  
 1507 tector. After that, the jets are corrected based on  $\eta$  dependent Jet Energy  
 1508 Scale ([JES](#)) factors derived from [MC](#). [Figure 46](#) shows the energy response,  
 1509 the inverse of these factors, for [EM](#) jets. Lastly, an observed bias in the  $\eta$   
 1510 measurement of jets is accounted for.

1511 In addition to correcting for additional energy due to pile-up, it is neces-  
 1512 sary to reject reconstructed jets that come from pile-up vertices. To accom-  
 1513 plish this, a multivariate algorithm called [JVT](#) was created which builds  
 1514 upon an older method, [JVF](#) [62]. The original method vetoed jets by sum-  
 1515 ming the total  $p_T$  of associated tracks and assessing the fraction of that  $p_T$   
 1516 that came from tracks associated with the event's primary vertex. This frac-  
 1517 tion decreases with higher pile-up, making the construction of an explicit  
 1518 cut difficult in varying pile-up conditions. [JVT](#) improved on the method  
 1519 by producing a pile-up corrected [JVF](#)-like variable and including it in the  
 1520 inputs of the tagger with other variables measuring the fraction of jet en-  
 1521 ergy that can be associated with the primary vertex. [Figure 47](#) shows the  
 1522 efficiency and fake rate for the two methods, demonstrating [JVT](#)'s superior  
 1523 stability across events with different numbers of pile-up vertices.

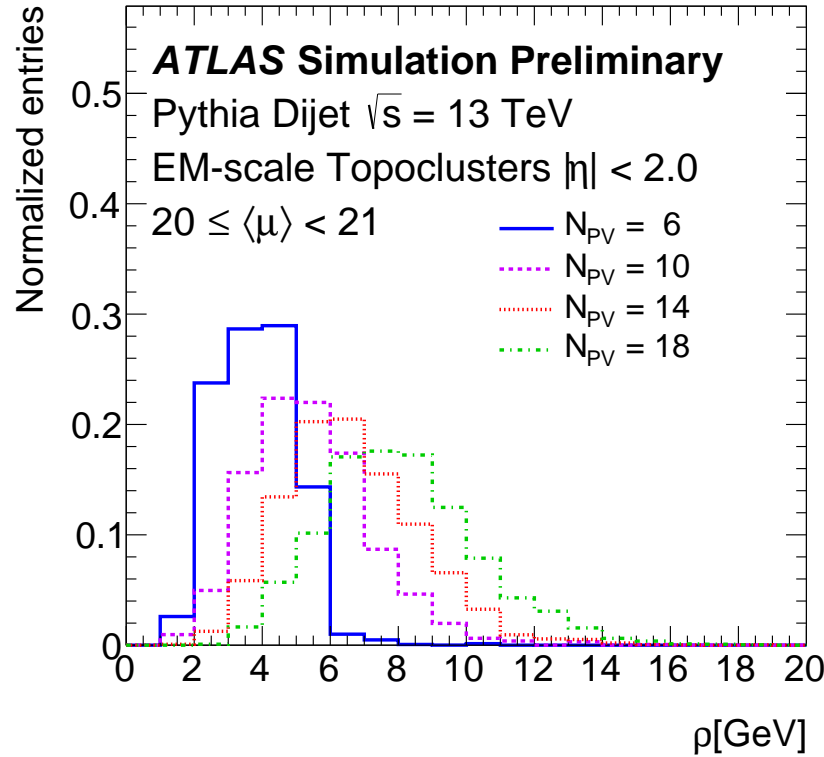


Figure 45: Distribution of event  $p_T$  density,  $\rho$ , taken from MC dijets for different numbers of primary vertices. [61]

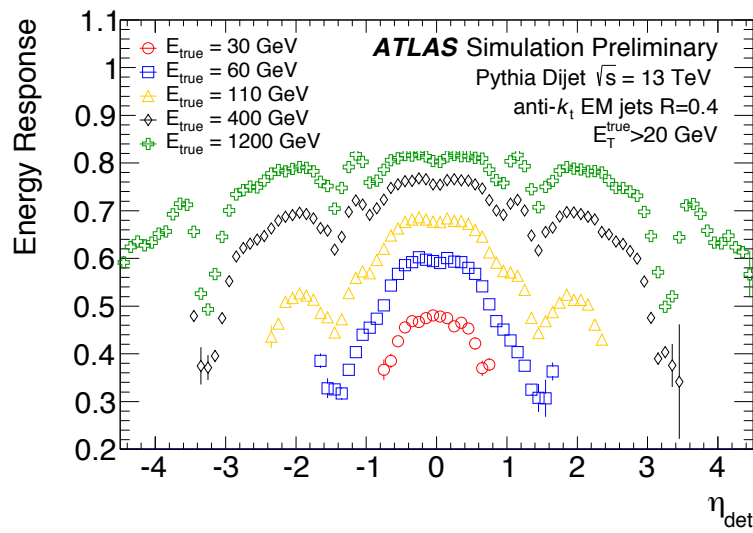


Figure 46: Energy response as a function of energy and  $\eta$  for EM jets in dijet MC. [61]

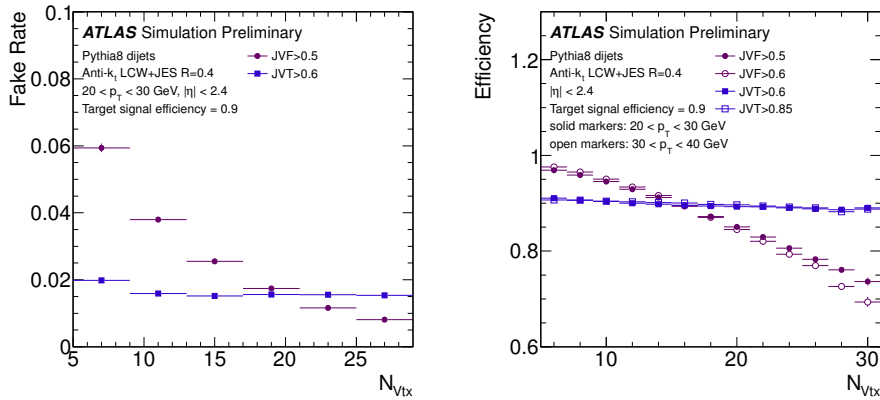


Figure 47: Dijet MC distributions of the number of pile-up jets passing the JVT and JVf cuts (left) and the efficiency for jets from the primary vertex (right) as a function of number of primary vertices in the event [62].

It is possible to differentiate jets resulting from  $b$ -hadron decays from other jets due to the non-negligible lifetimes of the hadrons. Many BSM processes preferentially produce  $b$  quarks, as does any process involving top quarks, so this identification can be useful for targeting specific decays in many analyses. Multivariate techniques are used to identify secondary vertices using the ID [63]. In ATLAS, separate algorithms are used to identify jets with tracks with significantly non-zero impact parameters, tracks that reconstruct a secondary vertex, and tracks that can be identified with a chain of vertices beginning with the primary vertex. This information is fed into a boosted decision tree called MV2c20, which outputs a discriminant shown in Figure 48. Using this discriminant, a working point is chosen such that  $b$ -jets can be identified with a 70% efficiency, with misidentification rates at around 12% for  $c$ -jets and 0.2% for light-flavor jets.

### 5.5 OVERLAP REMOVAL

Because most of these reconstruction methods are run independently, it is common for energy deposits and tracks to be shared between jets and particles of different types. To account for this, a process called Overlap Removal (OR) is used, which iteratively removes overlapping objects. The process is performed at the *baseline* level, a set of loose selections on objects which are later further refined to create the *signal* objects used in analysis. Each analysis defines these levels according to its needs; the specific requirements made for the analysis described in Part iv are outlined in Chapter 8.

The first step in the OR process is to remove reconstructed jets that appear to be due to calorimetric deposits from an electron. To accomplish this, any baseline jet within  $\Delta R = 0.2$  from a baseline electron is removed. A caveat is added due to the frequent production of leptons in the decay of heavy-flavor jets; if the jet is  $b$ -tagged, the electron will be removed instead. After these electrons and jets have been removed, a new search is

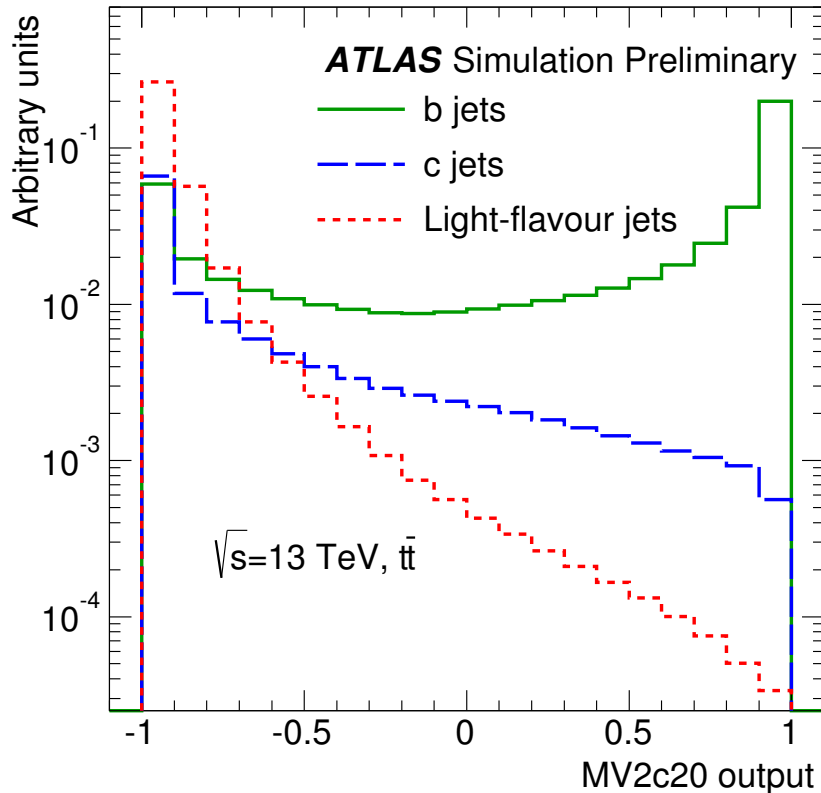


Figure 48: Distribution of MV2c20 output for  $b$ -jets,  $c$ -jets, and light-flavor jets in  $t\bar{t}$  MC [63].

1553 done for jets and electrons within  $\Delta R = 0.4$  of one another. In this iteration,  
 1554 the electron is removed, again to reduce backgrounds from heavy-flavor  
 1555 decays.

1556 Next, the muon-jet OR is applied, which is very similar to that of the  
 1557 electron. Any jet within  $\Delta R = 0.2$  of a muon is removed, unless the jet is  
 1558  $b$ -tagged, in which case the muon is removed due to the likelihood that it  
 1559 resulted due to a heavy-flavor decay. The muon-jet OR then differs from the  
 1560 electron's in that a  $p_T$ -based  $\Delta R$  cut is used in the last step. Muons within  
 1561  $\Delta R < \min(0.04 + (10 \text{ GeV})/p_T, 0.4)$  of a jet are removed, with the shrink-  
 1562 ing cone for high- $p_T$  muons designed to improve efficiency for energetic  
 1563 muons that produce significant calorimeter deposits, while still rejecting  
 1564 the heavy-flavor muons that are typically lower  $p_T$ .

1565 The next step is to remove electrons resulting from muon bremsstrahlung.  
 1566 Any remaining electron within  $\Delta R = 0.1$  of a muon is removed from the  
 1567 event.

1568 Lastly, overlap between photons and both jets and electrons is consid-  
 1569 ered. Baseline photons within  $\Delta R = 0.4$  of an electron are removed, as are  
 1570 jets within  $\Delta R = 0.4$  of a remaining photon.

## 1571 5.6 MISSING TRANSVERSE MOMENTUM

1572 Missing transverse momentum ( $\mathbf{p}_T^{\text{miss}}$ , with magnitude  $E_T^{\text{miss}}$ ), is the neg-  
 1573 ative vector sum of  $p_T$  measured in an event. Because colliding parti-  
 1574 cles have no initial transverse momentum, the true value of this quan-  
 1575 tity should be zero unless a particle escapes the detector without being  
 1576 measured, as neutrinos do. In practice, the reconstructed  $E_T^{\text{miss}}$  can also be  
 1577 non-zero due to mismeasurement.  $E_T^{\text{miss}}$  reconstruction is perhaps the most  
 1578 complex because it depends on all other object reconstructions performed  
 1579 in the ATLAS detector.

1580  $E_T^{\text{miss}}$  components are calculated independently for each type of base-  
 1581 line object reconstructed, as well as for a soft term, which accounts for  
 1582 low- $p_T$  radiation [64]. This component comprises the energy observed by  
 1583 the ATLAS detector but not associated with a baseline object, and can be  
 1584 calculated based either based on calorimeter or track measurements. While  
 1585 the Calorimeter Soft Term (CST) is very sensitive to pile-up, the Track Soft  
 1586 Term (TST) is much more robust, as it can exclude tracks emanating from  
 1587 pile-up vertices. Tracks associated with any reconstructed object are also  
 1588 removed. Figure 49 shows the TST resolution's dependence on number of  
 1589 primary vertices, which is considerably more stable than CST. Because of  
 1590 this improved performance, using TST to reconstruct  $E_T^{\text{miss}}$  is now the stan-  
 1591 dard for ATLAS analyses.

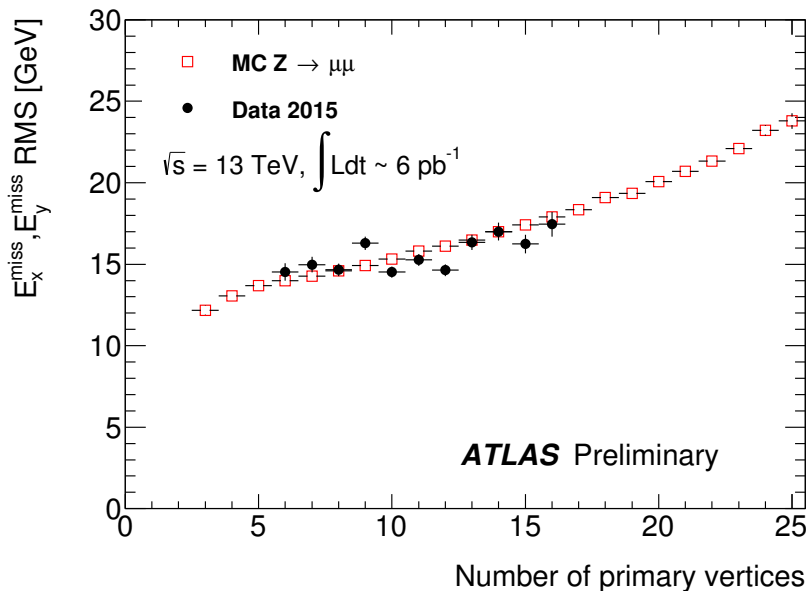


Figure 49: Distributions of the resolution of the  $x$  and  $y$  components of TST  $E_T^{\text{miss}}$  in  $Z \rightarrow \mu\mu$  events in data and MC [65].

1592 Figure 50 shows the the  $E_T^{\text{miss}}$  resulting from muons, jets, and the soft  
 1593 term in  $Z \rightarrow \mu\mu$  events. These events very rarely have any true  $E_T^{\text{miss}}$ , so  
 1594 these distributions primarily demonstrate how mismeasurement of vari-  
 1595 ous objects contributes to the  $E_T^{\text{miss}}$  term. Though the soft term falls off  
 1596 very quickly, rarely producing events with more than 50 GeV of  $E_T^{\text{miss}}$ , both

- 1597 the jet and muon distributions have longer tails, producing more events  
1598 with higher  $E_T^{\text{miss}}$ .  
1599 The jet and muon distributions both have significant high tails, while  
1600 the soft term falls off much more quickly.

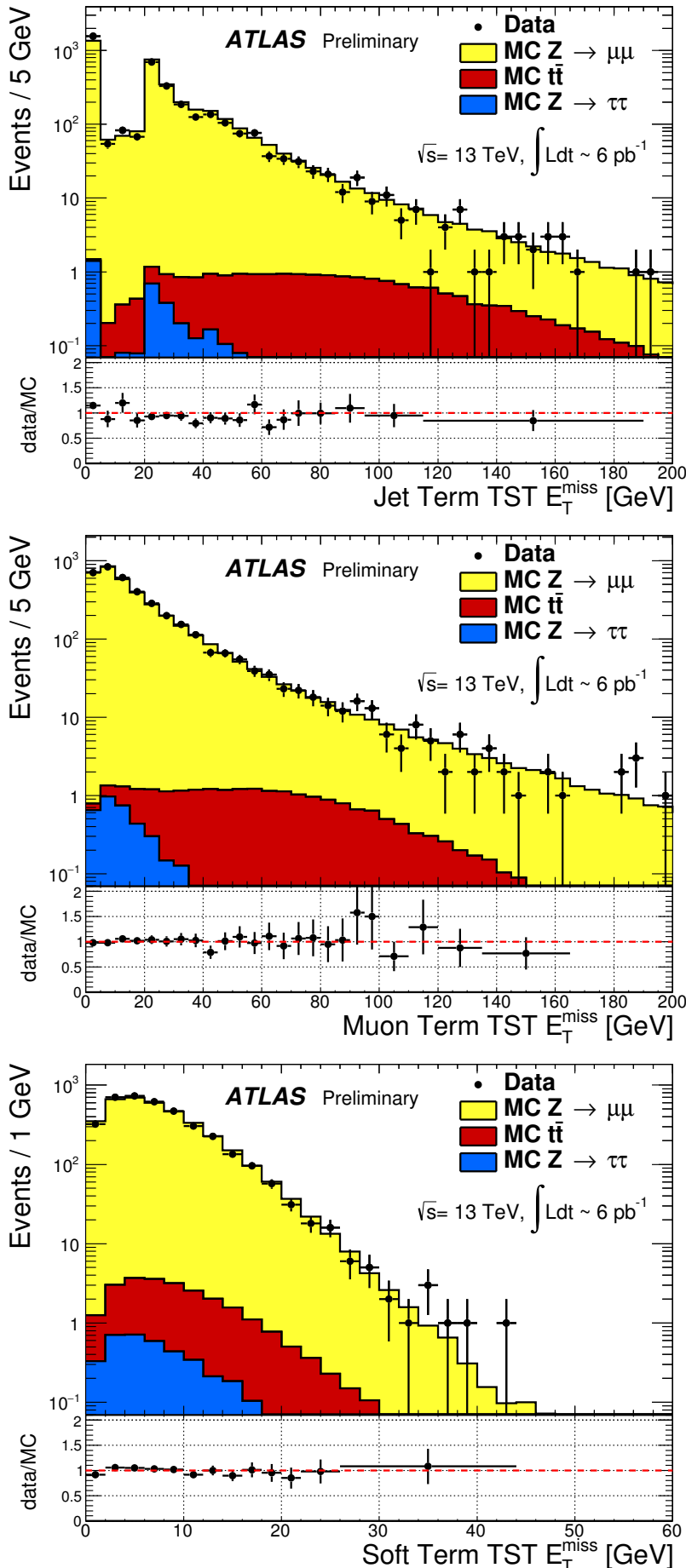


Figure 50: Distributions of the jet term (top left), muon term (top right), and TST (bottom)  $E_T^{\text{miss}}$  in  $Z \rightarrow \mu\mu$  events in data and MC. In the jet term distribution, the feature at zero is due to events with no jets, and the spike at 20 GeV corresponds to the minimum jet  $p_T$  considered for the analysis [65].



1601

## 1602 APPLICATION OF A NEURAL NETWORK TO PIXEL 1603 CLUSTERING

### 1604 6.1 CLUSTERING IN THE PIXEL DETECTOR

1605 Creating tracks from individual hits in the Inner Detector is one of most  
 1606 computationally challenging parts of the reconstruction of ATLAS events.  
 1607 Each event typically contains thousands of hits in the pixel detector alone,  
 1608 which must be combined into one coherent picture of which particles tra-  
 1609 versed the detector, and how they moved and lost energy as they traveled.  
 1610 A typical particle deposits charge in several pixels per layer, forming a se-  
 1611 ries of clusters which can be connected together to form a track. This track  
 1612 can in turn be used to measure the charge, momentum, and trajectory of  
 1613 the particle.

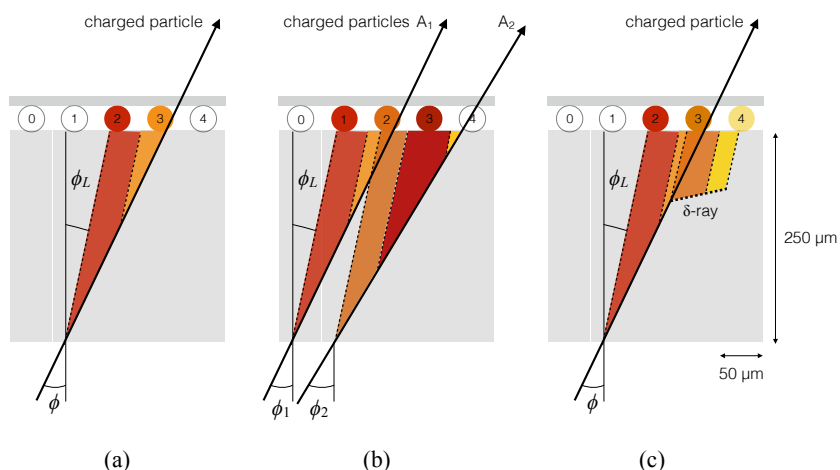


Figure 51: A few possible types of clusters in the Pixel Detector. (a) shows a single particle passing through a layer of the detector, (b) shows two particles passing through the detector, creating a single merged cluster, and (c) shows a single particle emitting a  $\delta$ -ray as it passes through the detector [66].

1614 The process of going from clusters to track is relatively simple in an  
 1615 isolated environment in which one particle travels cleanly through all the  
 1616 layers, but can be complicated by multiple close-by tracks and by a single  
 1617 particle's emission of low energy particles, called  $\delta$ -rays. In these cases, it  
 1618 can be hard to tell how many particles were involved in creating a clus-  
 1619 ter, and where exactly each of those particles passed through the layer. A  
 1620 few examples of particle interactions with the pixel sensor can be seen in  
[Figure 51](#).

1622 Clusters are initially made by a process called Connected Component  
 1623 Analysis ([CCA](#)). In this process, pixels in a given layer are grouped together  
 1624 if they share any edge or corner. The position of the resulting cluster is  
 1625 defined by local  $x$  and  $y$  coordinates, which describe its position and size  
 1626 within the pixel module on which it appears. Determining the position  
 1627 of the particle that formed that cluster is less straightforward, and has  
 1628 recently been updated from a charge interpolation method to a method  
 1629 using a [NN](#).

1630 6.1.1 Charge Interpolation Method

1631 A typical cluster contains a few pixel hits spanning in the  $x$  and  $y$  direc-  
 1632 tions, each with its own measurement of charge deposition, or [ToT](#). In the  
 1633 charge interpolation method, these individual hits are combined to make  
 1634 one estimation of the position a single particle which passed through them,  
 1635 using the following equation:

$$x_{cluster} = x_{center} + \Delta_x(\phi, N_{row}) \cdot \left[ \Omega_x - \frac{1}{2} \right] \quad (33)$$

$$x_{cluster} = x_{center} + \Delta_x(\phi, N_{row}) \cdot \left[ \Omega_x - \frac{1}{2} \right] \quad (34)$$

1636 where  $\Omega_{x(y)}$  is defined by

$$\Omega_{x(y)} = \frac{q_{last\ row(col)}}{q_{first\ row(col)} + q_{last\ row(col)}} \quad (35)$$

1637 and  $q$  represents the [ToT](#) of a given pixel, and  $\Delta_{x(y)}$  is a function derived  
 1638 from either data or [MC](#) and produces an output related to the projected  
 1639 length of the particles track on the pixel sensor and is measured as a func-  
 1640 tion of  $\phi$ , the incident angle of a particle on the sensor, and  $N_{row(col)}$ , the  
 1641 number of pixels in the  $x$  and  $y$  direction.

1642 In a simple case, such as (a) of [Figure 51](#), this method works quite effec-  
 1643 tively. However, in cases like (b), it has no ability distinguish two-particle  
 1644 from one-particle clusters, and can only assign a cluster center between the  
 1645 two particles' locations, despite that intermediate pixel having the lowest  
 1646 [ToT](#). Furthermore, because this method can't differentiate two-particle clus-  
 1647 ters, the tracking software can't use that information to preferentially al-  
 1648 low multiple tracks to share two-particle clusters. Allowing tracks to share  
 1649 clusters indiscriminately in dense track environments creates fake tracks  
 1650 from the many possible cluster combinations, so this cannot be broadly  
 1651 permitted. In cases like (c), the  $\delta$ -ray will bias the measurement of the  
 1652 particle's position in whichever direction it is emitted.

1653 6.1.2 Improving Measurement with Neural Networks

1654 To address these problems, a series of [NNs](#) were created [66]. The first esti-  
 1655 mates the number of particles in a given cluster, the second estimates their

1656 positions within the cluster, and the third assesses the uncertainty of the  
 1657 position measurement. They are referred to, respectively, as the “Number”,  
 1658 “Position”, and “Error” NNs.

1659 These NNs are taken from the AGILEPack library [67], and trained using  
 1660 simulated ATLAS MC. Each NN is given the following inputs:

- 1661 • a  $7 \times 7$  grid of cluster ToT information<sup>1</sup>
- 1662 • a 7-element vector containing the  $y$ -size of the pixels in the grid<sup>2</sup>
- 1663 • the layer of the pixel detector that the cluster was observed in
- 1664 • a variable indicating whether the cluster is located in the barrel or  
 1665 endcap
- 1666 •  $\theta$  and  $\phi$  variables projecting the incident angles of the particle on the  
 1667 sensor<sup>3</sup>
- 1668 • the pixel module’s  $\eta$  index, a label assigned to each module that  
 1669 differentiates modules based on their  $\eta$  position

1670 After the Number NN predicts a number of particles associated with the  
 1671 cluster, required to be between 1 and 3, the same inputs are fed to one of  
 1672 three Position NNs based on the determined number of particles, which  
 1673 then outputs the  $x$  and  $y$  positions of each of the particles. Then, the same  
 1674 inputs combined with the output of the Position NN are fed into one of  
 1675 three Error NNs (also distinguished by number of particles), which outputs  
 1676 an uncertainty for each of the position predictions made. An example of  
 1677 the output of this process can be seen in Figure 52, where the improved  
 1678 position resolution from the ability to identify a multi-particle cluster is  
 1679 evident.

1680 The particle location predictions from the NNs are then handed to the  
 1681 tracking software, which now can use these multiple particle position es-  
 1682 timations as independent hits to be fit. As a result, tracks in dense envi-  
 1683 ronments have fewer clusters shared between multiple tracks, and their  
 1684 trajectories are known to a greater degree of precision.

## 1685 6.2 IMPACT OF THE NEURAL NETWORK

1686 The NN was first applied to 7 TeV data, where it improved position res-  
 1687 olution for particles in small and large clusters. Figure 53 shows the im-  
 1688 provement from the addition of the NN in  $x$  resolution in different cluster

---

<sup>1</sup> Clusters spanning more than seven pixels in either direction are rare, but when they occur they are rejected, and the original charge interpolation estimate of a single particle’s position is kept.

<sup>2</sup> The pixel detector contains some long pixels at the edges of modules, and this is intended to help the NN identify these cases.

<sup>3</sup> If the NN is applied before tracking is performed, these angles project to the nominal interaction point, and if tracking has already been performed, the angles are taken from the track fit to the cluster.

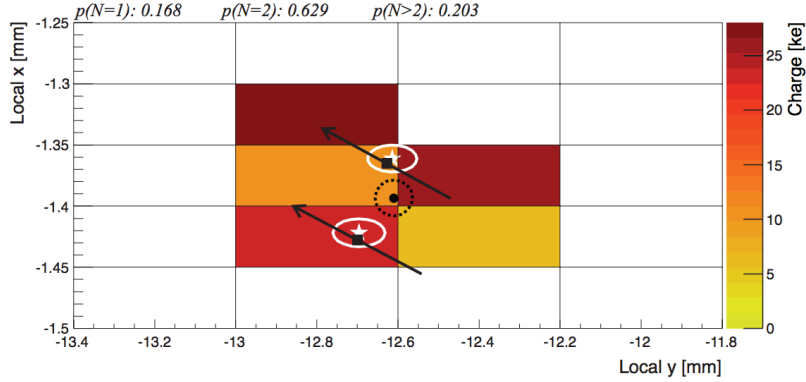


Figure 52: One example of a two-particle cluster and its truth information compared with the output of the NNs. The boxes represent pixels, with a color scale indicating ToT. At top, the  $p(N = i)$  values give the output of the Number NN, the probabilities that the cluster contains 1, 2, and 3 particles. Given the highest probability is for  $N = 2$ , the other NNs predict the position and errors of the two particles (in white). The black arrows and squares represent the truth information from the cluster, and the black dot and dotted line show the position measurement for the un-split cluster [66].

1689 sizes. The improvement from charge interpolation clustering is particu-  
 1690 larly evident in the 4-pixel case, where the double peaked structure of the  
 1691 interpolation method has been completely removed with the NN.

### 1692 6.2.1 The Neural Network in 13 TeV Data

1693 In Run 2, the tracking algorithm is first run on the CCA clusters with posi-  
 1694 tions determined via charge interpolation, where it constructs tracks with  
 1695 loose quality requirements. In this step, the tracking algorithm allows  
 1696 shared clusters, clusters used in multiple track fits [68]. The NN is then  
 1697 used to identify which clusters are likely to have had multiple particles  
 1698 pass through them, and to estimate the positions of those particles. In the  
 1699 case that the cluster is determined to have resulted only from one particle,  
 1700 tracks that share that cluster are penalized. In general, tracks with more  
 1701 than two shared clusters are rejected.

1702 Because the NN is trained only with MC simulations, any mismodeling of  
 1703 the way charge is deposited in the ATLAS detector could cause the NN to  
 1704 perform in an unexpected way when applied to data. The potential impact  
 1705 of this mismodeling was investigated with 13 TeV MC [69]. The goal of  
 1706 these studies was to determine which variables the NN's predictions were  
 1707 most sensitive to, and whether it was likely that these variables could be  
 1708 mismodeled enough to produce unexpected results in data.

1709 One example of a variable capable of significantly altering the NN out-  
 1710 puts was the overall charge scale. To study its impact, the ToT of all pixels  
 1711 in a cluster were scaled up and down, and the resulting outputs of the  
 1712 NN were compared, as shown in Figure 54. In this case, the likelihood to

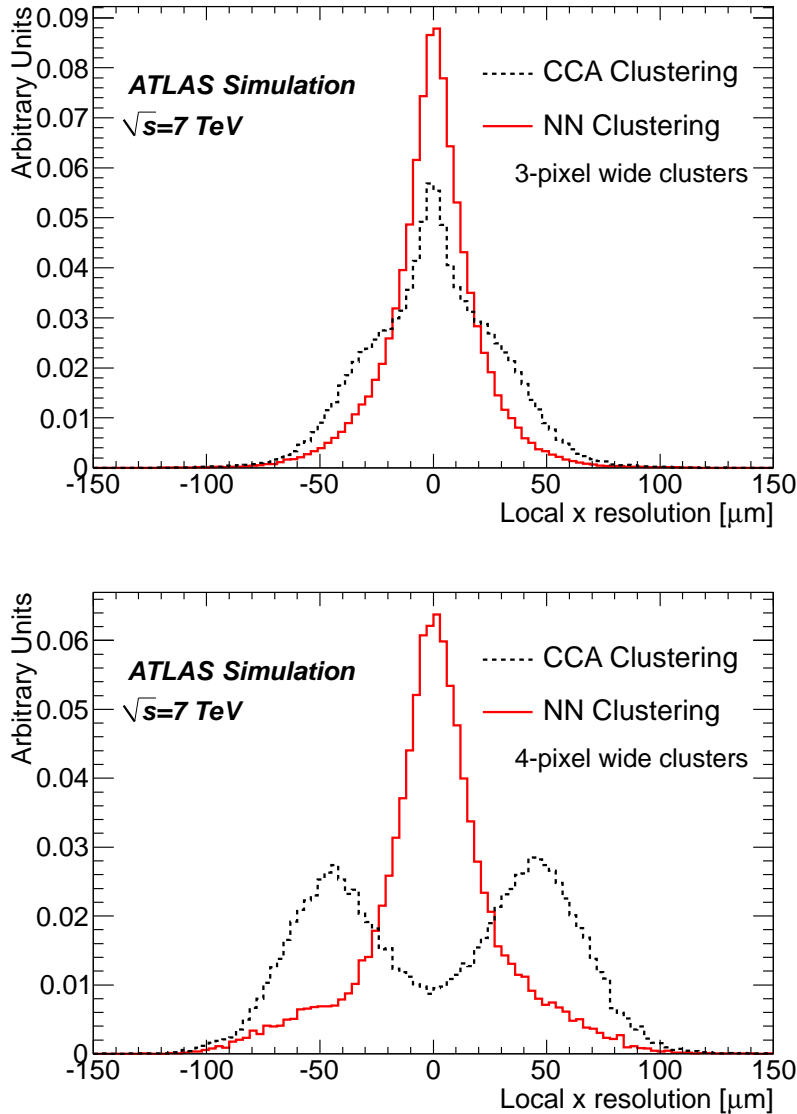


Figure 53:  $x$  resolutions for clusters with 3 (top) and 4 (bottom) pixels in the  $x$  direction in 7 TeV data for CCA (using only charge interpolation to determine position) and NN clustering taken from MC [66].

misidentify multi-particle clusters and single particle clusters depended significantly on this scaling. However, experts on the simulation of this scale agree that it's unlikely to be mismodeled by more than 10%, so very extreme effects from a difference between data and MC are unlikely. Overall, it was found that variations on the cluster charge produced a significant impact on predictions, while all other variations, such as incidence angle variation and spatial smearing of charge, had a minimal effect.

In addition to studies on the impact of alterations of individual simulation variables, studies directly comparing the NN output in data and MC were performed. Figure 55 shows a comparison of how often the NN identifies different types of clusters in data and MC. Each figure is made using by selecting pairs of collimated tracks that share a common cluster on a given

layer, then calculating the fraction of those clusters that are determined by the **NN** to be single or multi-particle clusters. This fraction is plotted as a function of the distance between the two tracks in the cluster's layer. Very good agreement is seen between the two samples, demonstrating that the **MC**-trained **NN** performs similarly on both **MC** and data.

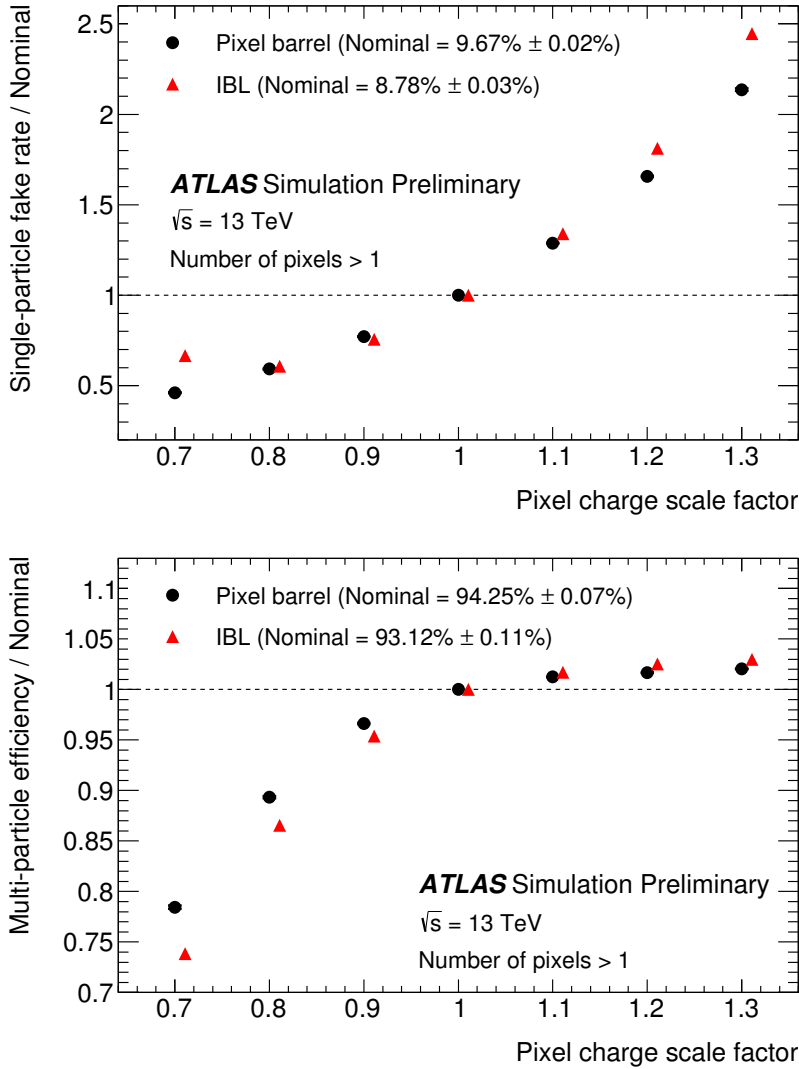


Figure 54: Performance of the pixel neural network used to identify clusters created by multiple charged particles, as a function of constant coherent scaling of the charge in each pixel in the cluster. The top figure shows the rate at which the neural network wrongly identifies clusters with one generated particle as clusters with multiple particles. The bottom figure shows the rate at which the neural network correctly identifies clusters generated by multiple particles as such.

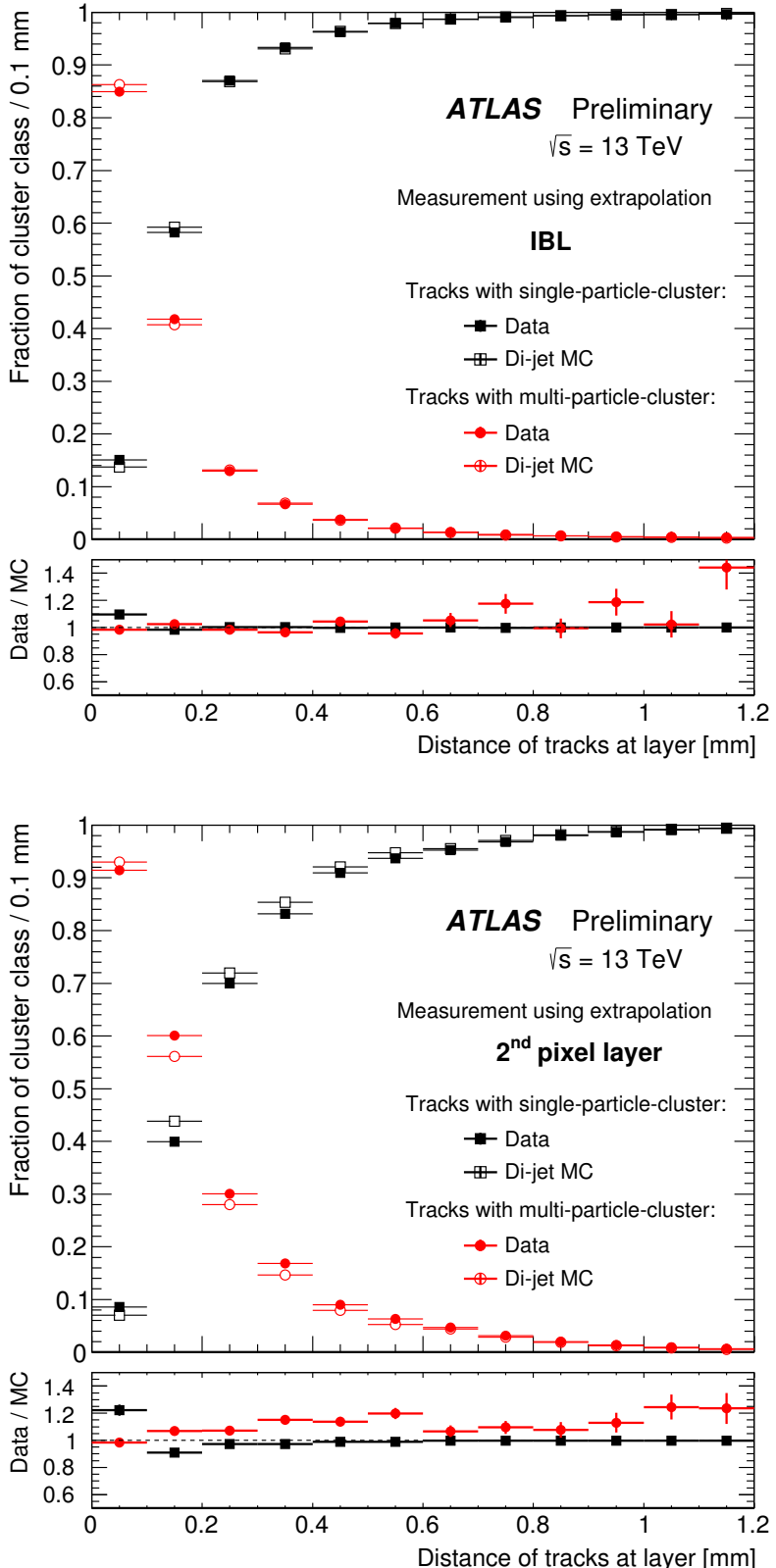


Figure 55: Fraction of cluster classes as a function of the distance between tracks for IBL (top) and 2nd pixel layer (bottom).

1730

## Part IV

1731

### SEARCHING FOR SUPERSYMMETRY

1732

This section describes an analysis of the ATLAS data carried out by the author and her analysis team. The analysis was performed on events from  $p - p$  collisions provided by the LHC at  $\sqrt{s}=13$  TeV. It searches for events like those described in [Section 2.2.3](#), which contain a Z boson decaying to leptons, jets, and missing transverse energy. The selection of a signal region in which to search for these events, background estimates, systematic uncertainty estimates, results, and interpretations are all discussed.

1733

1734

1735

1736

1737

1738

1739

1740



1741

## 1742 BACKGROUND PROCESSES

1743 This analysis is fundamentally a search for Supersymmetry ([SUSY](#)) in events  
 1744 with two leptons whose invariant mass is consistent with a Z boson. Ad-  
 1745 ditional event selections are made to reduce Standard Model ([SM](#)) pro-  
 1746 cesses relative to potential [SUSY](#) processes, defined by simplified models  
 1747 discussed in [Section 2.2.3](#). [SUSY](#) events typically have large amounts of  
 1748  $E_T^{\text{miss}}$ ,  $H_T$  (the scalar sum of the  $p_T$  of all jets and the leading two leptons  
 1749 in an event), and many jets. All of these features can help isolate these  
 1750 events from backgrounds. To understand what cuts would optimize the  
 1751 sensitivity of the search, it is essential to first understand what these [SM](#)  
 1752 backgrounds are.

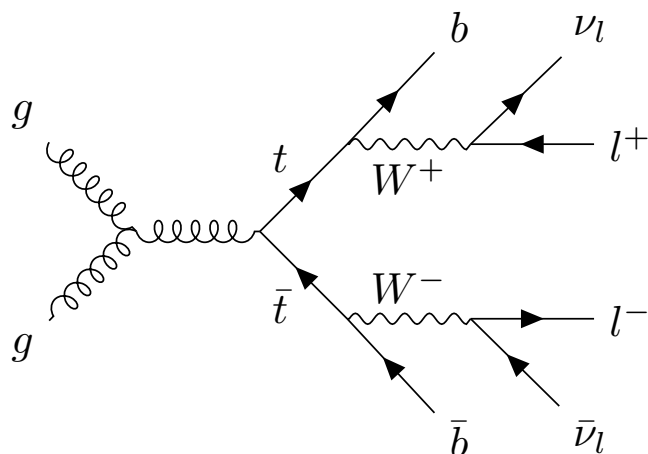


Figure 56: An example Feynman diagram of  $t\bar{t}$  production and decay.

1753 TOP-ANTITOP ( $t\bar{t}$ ) production is the largest background for this search.  
 1754 [Figure 56](#) shows an example of this process, which results in many jets, lep-  
 1755 tons, and neutrinos, which are seen in the detector as  $E_T^{\text{miss}}$ . Thus,  $t\bar{t}$  events  
 1756 naturally have high  $E_T^{\text{miss}}$  and  $H_T$ , jets, and leptons from two different W  
 1757 boson decays, which may coincidentally form an invariant mass consistent  
 1758 with a Z boson. These events are very difficult to separate from potential  
 1759 signals, though keeping the mass window small and requiring  $E_T^{\text{miss}}$  and  
 1760  $H_T$  above the typical values for  $t\bar{t}$  events helps reduce this background.

1761 DIBOSON ( $VV$ ) production is the next leading background. These events  
 1762 can contain real Z bosons and will peak on-Z like a signal. In addition, in  
 1763 events like [Figure 57](#), an additional W boson can decay to another lepton  
 1764 and a neutrino, providing  $E_T^{\text{miss}}$ . The pictured process can occur with asso-  
 1765 ciated jets, but at reduced rates, so adding a jet requirement to the signal  
 1766 region helps reduce these events. If the W boson in this diagram instead

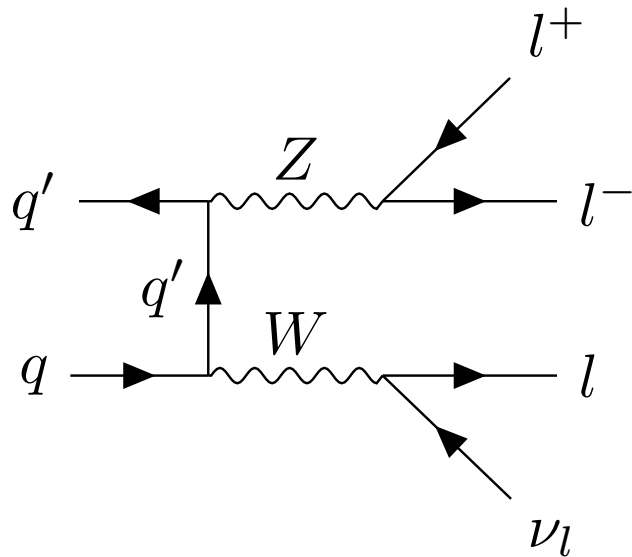


Figure 57: An example Feynman diagram of the production and decay of a  $WZ$  event.

1767 decayed to two jets, there would be no true  $E_T^{\text{miss}}$  from a neutrino, so a  
1768  $E_T^{\text{miss}}$  cut in conjunction with a jet cut is very effective in reducing the total  
1769 diboson background. A veto on a third lepton could also be used to reduce  
1770 this background, but, depending on the signal model considered, this veto  
1771 can also decrease signal acceptance, so it is not used in this analysis.

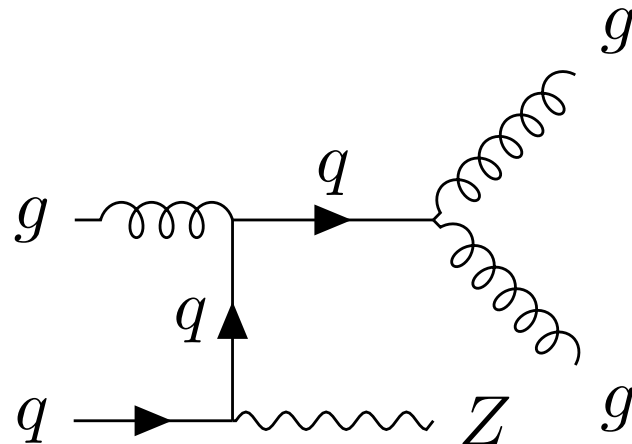


Figure 58: An example Feynman diagram of the production and decay of a  $Z/\gamma^* + \text{jets}$  event.

1772  $Z/\gamma^* + \text{JETS}$  processes are very common but, as shown in Figure 58,  
1773 don't produce any true  $E_T^{\text{miss}}$ . A high  $H_T$  cut helps reduce this background,  
1774 but this process often occurs with associated jets, producing many events  
1775 with large amounts of hadronic activity.  $E_T^{\text{miss}}$  is the most powerful variable  
1776 to reduce this background, because though events with mismeasured jets

1777 or leptons can fake  $E_T^{\text{miss}}$ , mismeasurements drastic enough to produce  
 1778 hundreds of GeV of  $E_T^{\text{miss}}$  are rare.

1779 Other processes can contribute to the Standard Model background at  
 1780 lower rates. Processes similar to  $Z/\gamma^* + \text{jets}$  but with a W boson instead of  
 1781 a Z have real  $E_T^{\text{miss}}$  from leptonic W decays, but only one lepton. However,  
 1782 a fake or non-prompt lepton can cause these events to look very similar to  
 1783 simulated signals. Additionally, there are rare processes such as  $t\bar{t}$  produc-  
 1784 tion in association with bosons that will also be difficult to separate from  
 1785 signal processes.

1786 **7.1 DATA AND MONTE CARLO SAMPLES**

1787 This analysis uses data collected by the ATLAS detector from  $p - p$  colli-  
 1788 sions at a center-of-mass energy of 13 TeV in 2015 and 2016, corresponding  
 1789 to a total luminosity of  $14.7 \text{ fb}^{-1}$ . The data collected using a combination  
 1790 of unprescaled single and dilepton triggers, discussed in greater detail in  
 1791 [Chapter 9](#). In addition, photon events are collected for use in a control  
 1792 region using both prescaled and unprescaled triggers, with the lowest trig-  
 1793 ger threshold at 20 GeV.

1794 MC samples are generated for each background process that appears  
 1795 in the signal and validation regions. [Table 2](#) details the method used to  
 1796 produce each sample, and more information can be found in [Section 2.3](#).  
 1797 These simulated background events, in conjunction with the simulated  
 1798 signal discussed in [Section 2.2.3](#), are used to determine approximate sensi-  
 1799 tivities of the search and optimize signal regions and amount of data used.  
 1800 The background MC also provides a valuable cross-check for many of the  
 1801 data-driven background estimates discussed in [Chapter 10](#), and in some  
 1802 cases, provides the primary estimate of the background.

Table 2: Simulated background event samples used in this analysis with the corresponding matrix element and parton shower generators, cross-section order in  $\alpha_s$  used to normalise the event yield, underlying-event tune and PDF set.

Physics process	Generator	Parton Shower	Cross section	Tune	PDF set
$t\bar{t} + W$ and $t\bar{t} + Z$ [70, 71]	MG5_AMC@NLO	Pythia 8.186	NLO [72, 73]	A14	NNPDF23LO
$t\bar{t} + WW$ [70]	MG5_AMC@NLO	Pythia 8.186	LO [38]	A14	NNPDF23LO
$t\bar{t}$ [74]	PowHEG Box v2 r3026	Pythia 6.428	NNLO+NNLL [75, 76]	PERUGIA2012	NULO CT10
Single-top ( $Wt$ ) [74]	PowHEG Box v2 r2856	Pythia 6.428	Approx. NNLO [77]	PERUGIA2012	NULO CT10
$WW$ , $WZ$ and $ZZ$ [78]	SHERPA 2.1.1	SHERPA 2.1.1	NLO [79, 80]	SHERPA default	NULO CT10
$Z/\gamma^*(\rightarrow \ell\ell) + \text{jets}$ [81]	SHERPA 2.1.1	SHERPA 2.1.1	NNLO [82, 83]	SHERPA default	NULO CT10
$\gamma + \text{jets}$	SHERPA 2.1.1	SHERPA 2.1.1	LO [42]	SHERPA default	NULO CT10
$V(=W, Z)\gamma$ signal	SHERPA 2.1.1	SHERPA 2.1.1	LO [42]	SHERPA default	NULO CT10
	MG5_AMC@NLO	Pythia 8.186	NULO	A14	NNPDF23LO

1803

## 1804 OBJECT IDENTIFICATION AND SELECTION

1805 This section describes the identification and selection of objects in the  
 1806 events of this analysis. Objects are first required to pass *baseline* selections,  
 1807 which are used for Overlap Removal ([OR](#)) and the calculation of  $E_T^{\text{miss}}$ ,  
 1808 then have tighter *signal* selections applied, which define the objects consid-  
 1809 ered in the final analysis of events. Definitions are presented for electrons,  
 1810 muons, and jets, which are all required in the Signal Region ([SR](#)) of the  
 1811 analysis, as well as photons, which are used in background estimation.  
 1812 This section refers to quality definitions described in [Chapter 5](#).

## 1813 8.1 ELECTRONS

1814 Electrons are reconstructed using the Egamma algorithm discussed in [Sec-](#)  
 1815 [tion 5.1](#). All electrons are required to be within  $|\eta| < 2.47$ , to ensure that all  
 1816 tracks are consistently within the tracking capability of the [ID](#). Baseline lep-  
 1817 tons are required to have  $p_T > 10 \text{ GeV}$  and pass the [LHLoose](#) quality stan-  
 1818 dard. Signal leptons are further required to be of [LHMedium](#) quality with  
 1819 [GradientLoose](#) isolation, and must have  $p_T > 25 \text{ GeV}$ . Additional cuts on  
 1820 impact parameter are made for electrons with the goal of identifying only  
 1821 electrons coming from the primary vertex of the event, the vertex with the  
 1822 highest associated  $p_T$ . These requirements, and all the other requirements  
 1823 made on the electrons can be seen in [Table 3](#).

Cut	Value/description
Baseline Electron	
Acceptance	$p_T > 10 \text{ GeV},  \eta^{\text{clust}}  < 2.47$
Quality	<a href="#">Loose</a>
Signal Electron	
Acceptance	$p_T > 25 \text{ GeV},  \eta^{\text{clust}}  < 2.47$
Quality	<a href="#">Medium</a>
Isolation	<a href="#">GradientLoose</a>
Impact parameter	$ z_0 \sin \theta  < 0.5 \text{ mm}$ $ d_0 / \sigma_{d_0}  < 5$

Table 3: Summary of the electron selection criteria. The signal selection require-  
 ments are applied on top of the baseline selection.

1824 With these requirements, the ATLAS detector is 95% efficient at identify-  
 1825 ing electrons with  $p_T > 25 \text{ GeV}$ , which rises to 99% at  $p_T > 60 \text{ GeV}$ [[84](#)]. Scale  
 1826 factors are applied to correct [MC](#) to match data efficiencies. These efficien-

1827 cies are measured as a function of  $p_T$  and  $\eta$ , and include both electron  
 1828 identification efficiencies and trigger efficiencies.

1829 **8.2 MUONS**

1830 Muons are reconstructed according to the process discussed in [Section 5.3](#).  
 1831 Baseline muons are required to have  $p_T > 10$  GeV and  $|\eta| < 2.5$ , including  
 1832 muons that can be tracked both by the [ID](#) and the [MS](#), and must pass a  
 1833 Medium quality cut. Signal muons are additionally required to have  $p_T >$   
 1834 25 GeV, and to have [GradientLoose](#) isolation. As with the electrons, quality  
 1835 cuts are made to ensure that the muon is consistent with coming from  
 1836 a decay from the event's primary vertex. Additionally, the muon must  
 1837 not be flagged [isBadMuon](#), which reduces the number of events with very  
 1838 inconsistent [ID](#) and [MS](#) tracks. The full set of requirements can be seen in  
 1839 [Table 4](#).

Cut	Value/description
Baseline Muon	
Acceptance	$p_T > 10$ GeV, $ \eta  < 2.5$
Quality	Medium
Signal Muon	
Acceptance	$p_T > 25$ GeV, $ \eta  < 2.5$
Quality	Medium
Isolation	<a href="#">GradientLoose</a>
Impact parameter	$ z_0 \sin \theta  < 0.5$ mm $ d_0/\sigma_{d_0}  < 3$
isBadMuon	MCP <a href="#">isBadMuon</a> Flag

Table 4: Summary of the muon selection criteria. The signal selection requirements are applied on top of the baseline selection.

1840 Muons with  $p_T > 25$  GeV are identified with a 95% efficiency, which  
 1841 rises to 99% for muons with  $p_T > 80$  GeV[85]. Including trigger and iso-  
 1842 lation requirements, these efficiencies drop to about 80% for muons with  
 1843  $p_T > 25$  GeV and 90% for muons with  $p_T > 200$  GeV. This drop is largely  
 1844 the consequence of incomplete  $\eta$  coverage of the [RPCs](#), discussed in [Sec-](#)  
 1845 [tion 5.3](#). Scalefactors to correct the [MC](#) identification efficiencies according  
 1846 to data are used.

1847 **8.3 JETS**

1848 Jets are reconstructed according to [Section 5.4](#), with baseline jets using the  
 1849 [AntiKt4EMTopo](#) algorithm, with a minimum  $p_T$  of 20 GeV and  $|\eta| < 2.8$ .  
 1850 Signal jets increase this  $p_T$  requirement to 40 GeV and decrease their ac-

1851 ceptance to  $|\eta| < 2.5$ . JVT requirements are enforced to reduce the number  
1852 of jets from pile-up. The full set of requirements can be seen in [Table 5](#).

Cut	Value/description
Baseline jet	
Collection	AntiKt4EMTopo
Acceptance	$p_T > 20 \text{ GeV}$ , $ \eta  < 2.8$
Signal jet	
Acceptance	$p_T > 30 \text{ GeV}$ , $ \eta  < 2.5$
JVT	$ \text{JVT}  > 0.59$ for jets with $p_T < 60 \text{ GeV}$ and $ \eta  < 2.4$
Signal $b$ -jet	
$b$ -tagger Algorithm	MV2c20
Efficiency	77 %
Acceptance	$p_T > 30 \text{ GeV}$ , $ \eta  < 2.5$
JVT	$ \text{JVT}  > 0.59$ for jets with $p_T < 60 \text{ GeV}$ and $ \eta  < 2.4$

Table 5: Summary of the jet and  $b$ -jet selection criteria. The signal selection requirements are applied on top of the baseline requirements.

1853 Though no  $b$ -jets are required in the SR of this analysis, some Control  
1854 Regions (CRs) use  $b$ -enhanced and  $b$ -vetoed regions to determine the im-  
1855 pact of heavy flavor. These  $b$ -jets are identified using the MV2c20 algorithm  
1856 at a 77% efficient working point, and are only identified for  $|\eta| < 2.5$ .

## 1857 8.4 PHOTONS

1858 Photons are used to estimate the  $Z/\gamma^* + \text{jets}$  background in this analy-  
1859 sis, and they are reconstructed according to [Section 5.2](#). Baseline and sig-  
1860 nal photons are nearly identical. Each must pass a tight selection with  
1861 FixedCutTight isolation and have  $p_T > 25 \text{ GeV}$  as well as  $|\eta| < 2.37$ . Sig-  
1862 nal photons with  $1.37 < |\eta| < 1.6$  are rejected due to an discontinuity  
1863 in the calorimeter which results in very large energy resolutions in this  
1864 region. The full selection requirements can be seen in [Table 6](#).

Cut	Value/description
Baseline Photon	
Acceptance	$p_T > 25 \text{ GeV},  \eta  < 2.37$
Quality	tight
Signal Photon	
Acceptance	$p_T > 25 \text{ GeV},  \eta  < 2.37$ rejecting $1.37 <  \eta  < 1.6$
Quality	tight
Isolation	FixedCutTight

Table 6: Summary of the photon selection criteria.

1865

1866 EVENT SELECTION

---

1867 The goal of this analysis is to identify events resembling [Figure 14](#) in col-  
 1868 lisions in the ATLAS detector. In order to do this, a Signal Region ([SR](#)) is  
 1869 defined with the goal of maximizing the identification efficiency of signal-  
 1870 like events while minimizing [SM](#) backgrounds. However, because this anal-  
 1871 ysis reinvestigates an excess of events seen in Run 1 with the ATLAS de-  
 1872 tector, the signal region was frozen and could not be reoptimized for the  
 1873 new, higher energy data in Run 2. The [SR](#), called *SRZ*, was predetermined,  
 1874 including events with two opposite-sign, same-flavor leptons that recon-  
 1875 struct a mass,  $m_{\ell\ell}$ , close to that of the Z boson, with the additional require-  
 1876 ment of two jets,  $E_T^{\text{miss}} > 225 \text{ GeV}$ , and  $H_T$  of at least 600 GeV. Additionally,  
 1877 a cut on  $\Delta\phi(\text{jet}_{12}, p_T^{\text{miss}})$  was made in order to reduce the number of events  
 1878 with high  $E_T^{\text{miss}}$  due to mismeasurement of one of the leading two jets.

1879 Though this [SR](#) was fixed, the methods used to estimate its expected [SM](#)  
 1880 backgrounds were not. A set of Control Regions ([CRs](#)) and Validation Re-  
 1881 gions ([VRs](#)) were chosen to make these estimations possible. [CRs](#) are regions  
 1882 in which the collected data can be used to make an estimate of an expected  
 1883 background in the [SR](#), while [VRs](#) are used to confirm the efficacy of these  
 1884 methods. Both [CRs](#) and [VRs](#) are designed to minimize contamination from  
 1885 the [BSM](#) process being searched for. This is desirable because signal con-  
 1886 tamination in a [CR](#) can lead to an overestimate of the [SM](#) background in  
 1887 the [SR](#), disguising a genuine signal as background. Contamination in a [VR](#),  
 1888 where background estimates are being validated, can make it appear that  
 1889 the [SM](#) background is not well described by an estimate, causing analyzers  
 1890 to adjust the method to account for the difference, and again, disguising  
 1891 the effect of the same signal in the [SR](#).

1892 The strategy for estimating the [FS](#) backgrounds, for example, depends  
 1893 on a series of [CRs](#) and [VRs](#) depicted in [Figure 59](#). One estimate, the fla-  
 1894 vor symmetry method, takes data from CR-FS, a different-flavor region with  
 1895 slightly wider  $m_{\ell\ell}$  bounds than the [SR](#), and uses these events to predict  
 1896 the contribution of flavor symmetric processes to SRZ. An independent  
 1897 method called a sideband fit uses a control region CRT to measure the  
 1898 flavor symmetric events outside of the Z mass window, and uses [MC](#) to  
 1899 extrapolate inside the Z mass window to SRZ. Then, both methods are  
 1900 validated at lower  $E_T^{\text{miss}}$  with an otherwise identical series of regions, with  
 1901 VRS corresponding to SRZ, VRT corresponding to CRT, and VR-FS corre-  
 1902 sponding to CR-FS.

1903 Each background estimation requires its own set of these regions, and  
 1904 the full list of regions used in this analysis can be seen in [Table 7](#). In ad-  
 1905 dition to the Flavor Symmetric ([FS](#)) regions described above, there is one  
 1906 more [CR](#), CR- $\gamma$ , which is a photon region used to predict the number of  
 1907  $Z/\gamma^* + \text{jets}$  events, a process described in [Section 10.2](#). Additional [VRs](#),

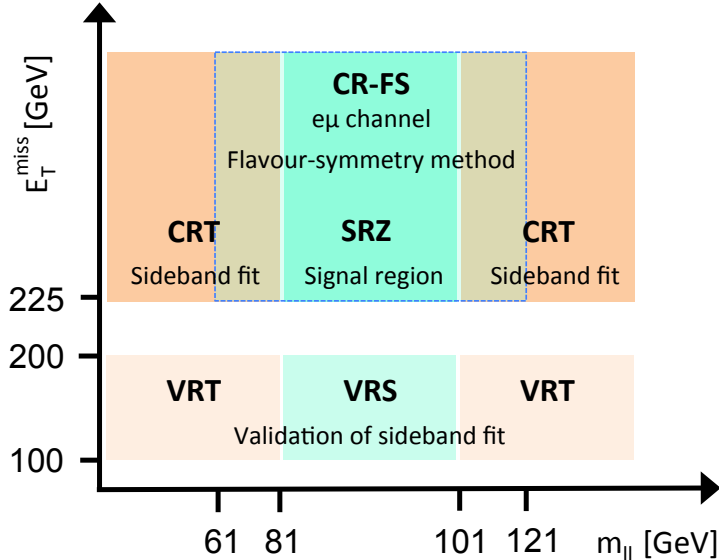


Figure 59: Schematic diagrams of the control, validation and signal regions for the on-shell  $Z$  (top) and edge (bottom) searches. For the on-shell  $Z$  search the various regions are shown in the  $m_{\ell\ell} - E_T^{\text{miss}}$  plane, whereas in the case of the edge search the signal and validation regions are depicted in the  $H_T - E_T^{\text{miss}}$  plane.

1908 VR-ZZ, VR-WZ, and VR- $\bar{3}L$ , are introduced in order to validate the back-  
 1909 grounds taken directly from MC. There are several additional regions used,  
 1910 for example, in the estimation of the fakes and  $Z/\gamma^* + \text{jets}$  backgrounds,  
 1911 that are defined in their respective sections.

## 1912 9.1 TRIGGER STRATEGY

1913 In order to collect data for the analysis, triggers must be chosen that pro-  
 1914 vide good efficiency in each of the SR, VR, and CRs. This analysis primarily  
 1915 depends on triggers on leptons, which are required in nearly every region.  
 1916 To simplify the application of trigger scalefactors, which correct MC yields  
 1917 for a given trigger to match the data efficiencies, events are broken down  
 1918 into a series of kinematic ranges, each with a designated trigger. These  
 1919 regions can be seen in Table 8.

1920 In kinematic regions where single lepton triggers are fully efficient, they  
 1921 are preferentially used. In lower- $p_T$  ranges, dilepton triggers are used, tar-  
 1922 geting either  $ee$ ,  $\mu\mu$ , or  $e\mu$  events. Electron triggers are selected over muon  
 1923 triggers when possible because they have higher efficiencies in most cases.

1924 In CR- $\gamma$ , there are no leptons, so an alternate trigger strategy must be  
 1925 used. Section 10.2.1 describes this triggering scheme, which includes a  
 1926 combination of prescaled and unprescaled photon triggers to allow for the  
 1927 collection of low- $p_T \gamma + \text{jets}$  events.

Table 7: Overview of all signal, control and validation regions used in the on-shell Z search. More details are given in the text. The flavour combination of the dilepton pair is denoted as either “SF” for same-flavour or “DF” for different flavour. All regions require at least two leptons, unless otherwise indicated. In the case of CR $\gamma$ , VR-WZ, VR-ZZ, and VR-3L the number of leptons, rather than a specific flavour configuration, is indicated. The main requirements that distinguish the control and validation regions from the signal region are indicated in bold. Most of the kinematic quantities used to define these regions are discussed in the text. The quantity  $m_T(\ell_3, E_T^{\text{miss}})$  indicates the transverse mass formed by the  $E_T^{\text{miss}}$  and the lepton which is not assigned to either of the Z-decay leptons.

On-shell Z regions	$E_T^{\text{miss}}$ [GeV]	$H_T$ [GeV]	$n_{\text{jets}}$	$m_{\ell\ell}$ [GeV]	SF/DF	$\Delta\phi(\text{jet}_{12}, p_T^{\text{miss}})$	$m_T(\ell_3, E_T^{\text{miss}})$ [GeV]	$n_{\text{b-jets}}$
Signal region								
SRZ	> 225	> 600	$\geq 2$	$81 < m_{\ell\ell} < 101$	SF	> 0.4	—	—
Control regions								
CRZ	< <b>60</b>	> 600	$\geq 2$	$81 < m_{\ell\ell} < 101$	SF	> 0.4	—	—
CR-FS	> 225	> 600	$\geq 2$	<b>61</b> < $m_{\ell\ell}$ < <b>121</b>	DF	> 0.4	—	—
CRT	> 225	> 600	$\geq 2$	> <b>40</b> , $m_{\ell\ell} \notin [81, 101]$	SF	> 0.4	—	—
CR $\gamma$	—	> 600	$\geq 2$	—	$0\ell, 1\gamma$	—	—	—
Validation regions								
VRZ	< <b>225</b>	> 600	$\geq 2$	$81 < m_{\ell\ell} < 101$	SF	> 0.4	—	—
VRT	<b>100–200</b>	> 600	$\geq 2$	> <b>40</b> , $m_{\ell\ell} \notin [81, 101]$	SF	> 0.4	—	—
VRS	<b>100–200</b>	> 600	$\geq 2$	$81 < m_{\ell\ell} < 101$	SF	> 0.4	—	—
VR-FS	<b>100–200</b>	> 600	$\geq 2$	<b>61</b> < $m_{\ell\ell}$ < <b>121</b>	DF	> 0.4	—	—
VR-WZ	<b>100–200</b>	—	—	—	<b>3</b> $\ell$	—	< 100	0
VR-ZZ	< 100	—	—	—	<b>4</b> $\ell$	—	—	0
VR-3L	<b>60–100</b>	> 200	$\geq 2$	$81 < m_{\ell\ell} < 101$	<b>3</b> $\ell$	> 0.4	—	—

Lepton $p_T$	Trigger in 2015	Trigger in 2016
Di-electron channel		
$p_T(e_1) > 65 \text{ GeV}$	HLT_e60_lhmedium	HLT_e60_lhmedium_nod0
$p_T(e_1) \leq 65 \text{ GeV}$	HLT_2e17_lhloose	HLT_2e17_lhvloose_nod0
Di-muon channel		
$p_T(\mu_1) > 52.5 \text{ GeV}$	HLT_mu50	HLT_mu50
$p_T(\mu_1) \leq 52.5 \text{ GeV}$	HLT_mu24_mu8noL1	HLT_2mu14_nomucomb
Electron-muon channel		
$p_T(e) > 65 \text{ GeV}$	HLT_e60_lhmedium	HLT_e60_lhmedium_nod0
$p_T(e) \leq 65 \text{ GeV}$ and $p_T(\mu) > 52.5 \text{ GeV}$	HLT_mu50	HLT_mu50
$p_T(e) \leq 65 \text{ GeV}$ and $p_T(\mu) \leq 52.5 \text{ GeV}$ and $p_T(e) < p_T(\mu)$	HLT_e7_lhmedium_mu24	HLT_e7_lhmedium_nod0_mu24
$p_T(e) \leq 65 \text{ GeV}$ and $p_T(\mu) \leq 52.5 \text{ GeV}$ and $p_T(\mu) < p_T(e)$	HLT_e17_lhloose_mu14	HLT_e17_lhloose_nod0_mu14

Table 8: Lepton trigger requirements used for the analysis in different regions of lepton- $p_T$  phase space.

## 1928 9.2 SIGNAL EFFICIENCY AND CONTAMINATION

1929 Using the simplified models discussed in [Section 2.2.3](#), the contributions  
 1930 of potential signals in these regions can be studied. In the [SR](#), the goal  
 1931 is to include as much of the potential signal as possible, while excluding  
 1932 as much [SM](#) background as possible. [Figure 60](#) shows the acceptance and  
 1933 efficiency for the simplified models at different mass points. Acceptance  
 1934 is defined as the fraction of signal events that produce signatures that  
 1935 kinematically match the [SR](#), while the efficiency is the fraction of these  
 1936 events expected to be correctly identified by the ATLAS detector.

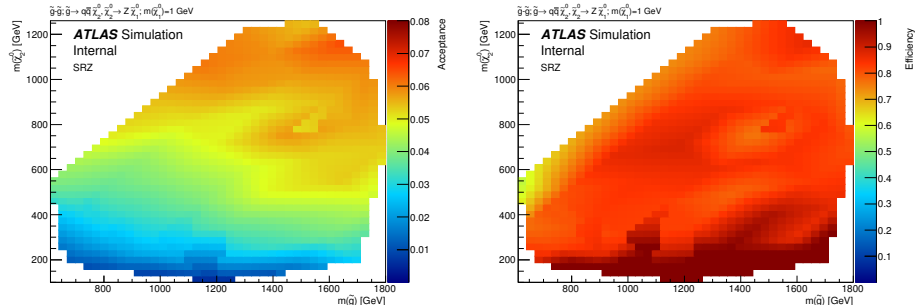


Figure 60: Signal region acceptance (left) and efficiency (right) in SRZ for the simplified model with gluino pair production with  $\tilde{\chi}_2^0$  decays to  $\tilde{\chi}_1^0$  and an on-shell Z boson with 1GeV neutralino LSP. Acceptance is calculated by applying the signal-region kinematic requirements to truth objects in [MC](#), which do not suffer from identification inefficiencies or measurement resolutions.

1937 A similar test is done for the main [CRs](#) and [VRs](#) which estimates their sus-  
 1938 ceptibility to signal contamination. Figures [61](#) and [62](#) show the fraction of  
 1939 events in these regions expected to come from signal for different points  
 1940 on the simplified model's mass grid. Contamination is highest in VRS, at

1941 low  $m_{\tilde{g}}$ . However, past analyses have already excluded most models with  
 1942  $m_{\tilde{g}} < 800$  GeV, so these regions are not important targets for this search  
 1943 [1].

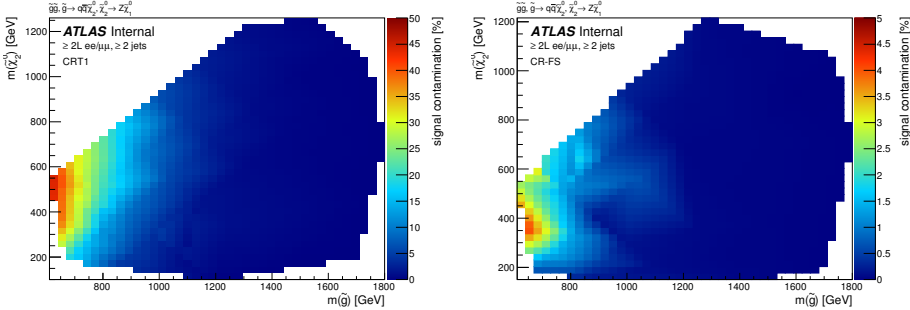


Figure 61: Expected signal contamination in CRT (left) and CR-FS (right) for the signal model with gluino pair production, where the gluinos decay to quarks and a neutralino, with the neutralino subsequently decaying to a Z boson and a 1GeV neutralino LSP.

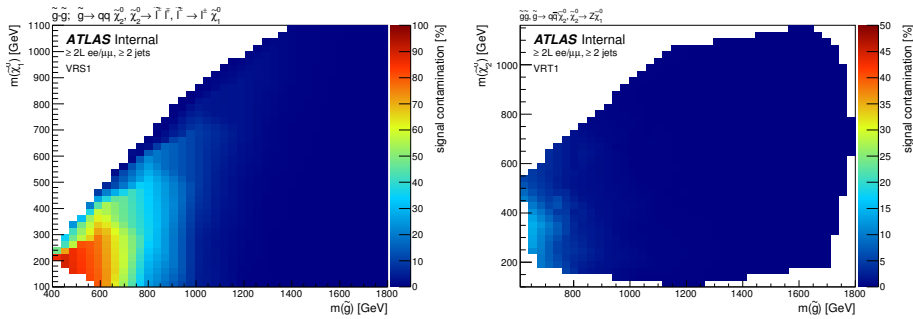


Figure 62: Expected signal contamination in VRS (left) and VRT (right) for the signal model with gluino pair production, where the gluinos decay to quarks and a neutralino, with the neutralino subsequently decaying to a Z boson and a 1GeV neutralino LSP.



1944  
1945 BACKGROUND ESTIMATION

---

1946 This analysis requires two leptons that reconstruct to a  $Z$  mass, jets,  $E_T^{\text{miss}}$ ,  
1947 and  $H_T$ . Any standard model processes that produce this signature will  
1948 appear as a background to the search. The most important task of the  
1949 analysis is to identify and estimate these backgrounds, so that any excess  
1950 of events appearing on top of the standard model background can be iden-  
1951 tified. The main backgrounds for this analysis are described in [Chapter 7](#).  
1952 The largest background is from flavor symmetric processes, with smaller  
1953 contributions coming from diboson processes,  $Z/\gamma^* + \text{jets}$ , rare top pro-  
1954 cesses, and fake and non-prompt leptons.

1955 10.1 FLAVOR SYMMETRIC PROCESSES

1956 Flavor Symmetric ([FS](#)) backgrounds include any processes that produce  
1957 pairs of leptons with uncorrelated flavor in the final state. In this analysis,  
1958 the largest contribution comes from  $t\bar{t}$ , with additional events from pro-  
1959 cesses like  $WW$  and  $Z \rightarrow \tau\tau$ . In these processes, each lepton comes from  
1960 a different decay. Unlike a  $Z \rightarrow \ell\ell$  decay then, these leptons' flavors are  
1961 completely independent.

1962 10.1.1 *Flavor Symmetry Method*

1963 As a consequence of the independence of the lepton flavors, any [FS](#) process  
1964 should produce  $ee$ ,  $\mu\mu$ , and  $e\mu$  events in a 1:1:2 ratio. This ratio is taken  
1965 advantage of in the flavor symmetry method by measuring  $e\mu$  events in  
1966 data and using them to predict the contribution of these processes in the  
1967  $ee$  and  $\mu\mu$  channels. [1]

1968 To estimate the number of events in SRZ, a control region called CR-FS is  
1969 used. Both regions are defined in [Table 7](#). CR-FS is very similar to SRZ with  
1970 two changes: it requires different-flavor leptons instead of the same-flavor  
1971 leptons required by SRZ, and the  $m_{\ell\ell}$  range it covers has been expanded  
1972 by a factor of three, now ranging from 61 to 121 GeV. The expansion of the  
1973  $m_{\ell\ell}$  window is done to increase the number of events in the control region,  
1974 thus lowering the statistical uncertainty of the prediction<sup>1</sup>.

1975 This control region is expected to be about 95% pure in [FS](#) processes,  
1976 with most of the remaining events coming from fake or non-prompt lep-

---

<sup>1</sup> Though this statistical uncertainty is no longer dominant for the analysis, the method was developed for a smaller dataset for which this expansion dramatically decreased the total uncertainty on the background prediction. [86] Because of previous excesses seen, the signal region was not reoptimized for the larger dataset used in this search, but in future iterations of this analysis, the signal region will likely have tighter cuts, making this decreased statistical uncertainty significant once again.

tons. The **FS** portion is made up primarily of  $t\bar{t}$  ( $\sim 80\%$ ), with additional contributions from  $Wt$  ( $\sim 10\%$ ),  $WW$  ( $\sim 10\%$ ), and  $< 1\% Z \rightarrow \tau\tau$ .

After the number of data events are measured in CR-FS, correction factors are applied to account for trigger efficiencies, selection efficiencies, the  $m_{\ell\ell}$  expansion, and the purity of the control region. Combining these factors, the estimate for number of events in the  $ee$  and  $\mu\mu$  channels is as follows:

$$N_{ee}^{\text{est}} = \frac{1}{2} \cdot f_{\text{FS}} \cdot f_{Z\text{-mass}} \cdot \sum_{N_{e\mu}^{\text{data}}} k_e(p_T^\mu, \eta^\mu) \cdot \alpha(p_T^{\ell_1}, \eta^{\ell_1}), \quad (36)$$

$$N_{\mu\mu}^{\text{est}} = \frac{1}{2} \cdot f_{\text{FS}} \cdot f_{Z\text{-mass}} \cdot \sum_{N_{\mu\mu}^{\text{data}}} k_\mu(p_T^e, \eta^e) \cdot \alpha(p_T^{\ell_1}, \eta^{\ell_1}), \quad (37)$$

where  $N_{e\mu}^{\text{data}}$  is the number of data events observed in CR-FS,  $f_{\text{FS}}$  is the **FS** purity in CR-FS,  $f_{Z\text{-mass}}$  is the fraction of events in the widened  $m_{\ell\ell}$  range expected to be in the on- $Z$  range (taken from  $t\bar{t}$  MC),  $k_e(p_T, \eta)$  and  $k_\mu(p_T, \eta)$  are relative selection efficiencies for electrons and muons, calculated in bins of  $p_T$  and  $\eta$  of the lepton to be replaced, and  $\alpha(p_T, \eta)$  accounts for the different trigger efficiencies for events in each channel, binned based on the kinematics of the leading lepton. These  $k$  and  $\alpha$  factors are calculated from data in an inclusive on- $Z$  selection ( $81 < m_{\ell\ell}/\text{GeV} < 101$ ,  $\geq 2$  jets), according to:

$$k_e(p_T, \eta) = \sqrt{\frac{N_{ee}^{\text{meas}}}{N_{\mu\mu}^{\text{meas}}}} \quad (38)$$

$$k_\mu(p_T, \eta) = \sqrt{\frac{N_{\mu\mu}^{\text{meas}}}{N_{ee}^{\text{meas}}}} \quad (39)$$

$$\alpha(p_T, \eta) = \frac{\sqrt{\epsilon_{ee}^{\text{trig}}(p_T, \eta) \times \epsilon_{\mu\mu}^{\text{trig}}(p_T, \eta)}}{\epsilon_{e\mu}^{\text{trig}}(p_T, \eta)} \quad (40)$$

where  $\epsilon_{ee/\mu\mu}^{\text{trig}}$  is the trigger efficiency<sup>2</sup> and  $N_{ee/\mu\mu}^{\text{meas}}$  is the number of  $ee/\mu\mu$  events in the inclusive on- $Z$  region described above. Here  $k_e(p_T, \eta) = 1/k_\mu(p_T, \eta)$ , and this  $k$  factor is calculated separately for leading and sub-leading leptons, and the appropriate  $k$  value is selected based on which of the leptons is to be replaced.

Electron, muon, and trigger efficiencies are all quite close to one, and as a consequence, these correction factors are typically within 10% of unity, except in the region  $|\eta| < 0.1$  where, because of the lack of coverage of the muon spectrometer, they are up to 50% from unity.

<sup>2</sup> This efficiency is defined by taking all events in the inclusive on- $Z$  selection mentioned above and determining the fraction that passes the relevant trigger requirement defined by [Table 8](#). Because the offline selection made on these events already has some trigger dependence, this calculation of efficiency could be slightly biased. This effect is considered in [Section 11.1.1](#), and the uncertainty applied to the estimate as a result is described.

Region	$ee$ prediction	$\mu\mu$ prediction	combined prediction
SRZ	$16.50 \pm 2.11$	$16.67 \pm 2.04$	$33.16 \pm 3.94$
VRS	$49.70 \pm 4.61$	$49.60 \pm 4.56$	$99.31 \pm 8.47$

Table 9: Yields in signal and validation regions for the flavor symmetric background. Errors include statistical uncertainty, uncertainty from MC closure, uncertainty from the  $k$  and  $\alpha$  factors, uncertainty due to deriving triggers efficiencies from a DAOD, and uncertainty on the MC shape used to correct for the  $m_{\ell\ell}$  expansion.

2002     The estimate is corrected for contamination of non-**FS** backgrounds in  
 2003    CR-**FS**. A scaling factor is determined by subtracting these backgrounds  
 2004    from the number of  $e\mu$  events measured in CR-**FS**, then determining the  
 2005    fraction of the original data events that this pure-**FS** number represents.  
 2006    The estimate for the non-**FS** backgrounds is taken from **MC** for all processes  
 2007    except fakes, which are predicted from data using the matrix method de-  
 2008    scribed in [Section 10.3](#).

2009     A prediction is made both for the signal region, SRZ, and the lower- $E_T^{\text{miss}}$   
 2010    validation region, VRS. This process is performed separately for the two  
 2011    data taking periods, 2015 and 2016, because of the changing triggers and  
 2012    conditions. The results are then summed together, as shown in [Table 9](#).  
 2013    The uncertainties in this table are discussed in [Section 11.1.1](#).

#### 2014    10.1.2 Sideband Fit Method

2015     As a crosscheck to the flavor symmetry method, a **MC**-based method is  
 2016    used. This method is called a *sideband fit*, and it begins with a **MC** estimate  
 2017    of the signal region across an  $m_{\ell\ell}$  range that includes all values above 40  
 2018    GeV. This region, excluding the on-Z range that makes up the **SR**, is used  
 2019    as a control region, defined as CRT in [Table 7](#).

2020     The total data yield is measured in CRT, and the **MC** is fit to match this  
 2021    yield with one normalization factor which scales the overall  $t\bar{t}$  background.  
 2022    As mentioned in the previous section,  $t\bar{t}$  is the dominant **FS** background,  
 2023    making up about 80% of the total events. All other backgrounds contribut-  
 2024    ing to this control region are constrained by their uncertainties, which are  
 2025    used as nuisance parameters in the fit. The normalization factor from this  
 2026    fit is then applied to the  $t\bar{t}$  **MC** yield in the **SR**, and combined with the **MC**  
 2027    predictions of the other **FS** processes in the **SR** to give a final estimate of  
 2028    this background. The results of the fit can be seen in [Table 10](#).

2029     The method is repeated in VRS to validate the method. The normal-  
 2030    ization factors, listed in [Table 11](#), are significantly different for the two  
 2031    regions. This is expected because there is a known problem in which the  
 2032     $t\bar{t}$  **MC** over-predicts the high- $E_T^{\text{miss}}$  tail. This effect can be seen in a data-**MC**  
 2033    comparison in [Figure 63](#). This is likely due to a mismodeling of the top  
 2034    quark  $p_T$  distribution, which does not match the spectrum seen in data [87,

## BACKGROUND ESTIMATION

channel	$ee/\mu\mu$ CRT	$ee/\mu\mu$ SRZ	$ee$ SRZ	$ee/\mu\mu$ SRZ
Observed events	273	60	35	25
Fitted bkg events	$272.76 \pm 16.88$	$49.33 \pm 8.04$	$27.09 \pm 4.73$	$22.70 \pm 3.80$
Fitted flavour symmetry events	$236.96 \pm 21.66$	$28.96 \pm 7.47$	$16.41 \pm 4.33$	$12.55 \pm 3.29$
Fitted $WZ/ZZ$ events	$4.03 \pm 1.13$	$14.27 \pm 4.45$	$7.81 \pm 2.45$	$6.46 \pm 2.07$
Fitted SHERPA $Z/\gamma^*$ + jets events	$1.95 \pm 0.14$	$0.00 \pm 0.00$	$0.00 \pm 0.00$	$0.00 \pm 0.00$
Data-driven $Z/\gamma^*$ + jets ( $\gamma$ + jets) events	$0.00 \pm 0.00$	$3.10 \pm 2.25$	$1.02^{+1.25}_{-1.02}$	$2.08 \pm 1.38$
Fitted rare top events	$4.04 \pm 1.04$	$2.90 \pm 0.76$	$1.39 \pm 0.38$	$1.50 \pm 0.40$
Data-driven fake lepton events	$25.78 \pm 14.26$	$0.10^{+0.18}_{-0.10}$	$0.46 \pm 0.45$	$0.10 \pm 0.01$
MC exp. SM events	366.71	61.01	33.73	27.74
MC exp. flavour symmetry events	331.32	40.72	23.09	17.63
MC exp. $WZ/ZZ$ events	4.02	14.20	7.77	6.43
MC exp. SHERPA $Z/\gamma^*$ + jets events	1.94	0.00	0.00	0.00
Data-driven exp. $Z/\gamma^*$ + jets ( $\gamma$ + jets) events	0.00	3.10	1.02	2.08
MC exp. rare top events	4.04	2.89	1.39	1.50
Data-driven exp. fake lepton events	25.39	0.10	0.46	0.10

Table 10: Background fit results from the sideband fit method. The  $t\bar{t}$  MC's normalization is taken as a free parameter in the fit to data in CRT, then that normalization factor is applied in SRZ. The results are shown here both divided between the  $ee$  and  $\mu\mu$  channels and summed together. All other backgrounds are taken from MC in CRT, while in SRZ, the  $Z/\gamma^*$  + jets contribution is taken from the  $\gamma$  + jets method. The uncertainties quoted include both statistical and systematic components.

2035 88]. However, this method corrects for this mismodeling by performing fits  
 2036 in regions very kinematically similar to the signal region.

Fit region	$t\bar{t}$ normalization
CRT	$0.64 \pm 0.18$
VRT	$0.80 \pm 0.09$

Table 11: Summary of the  $t\bar{t}$  normalization factors calculated by the sideband fit to CRT and VRT for the 2015+2016 data.

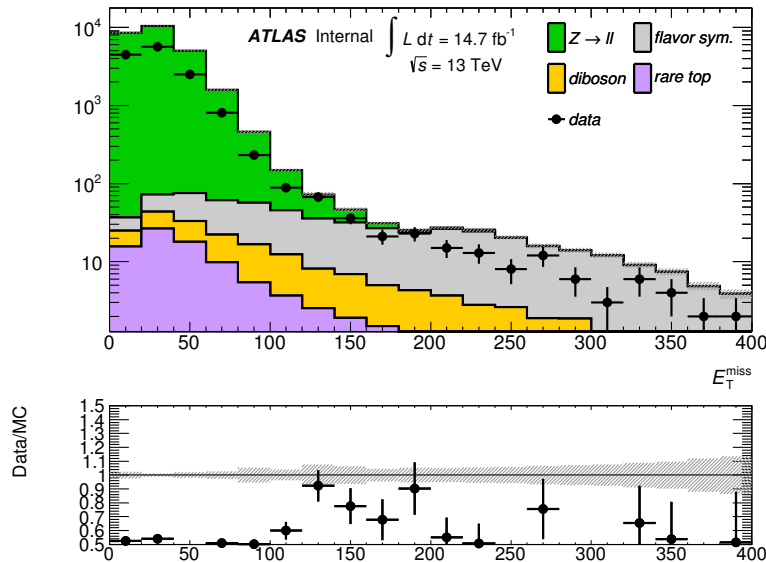


Figure 63: Comparison of data and MC in a selection like SRZ, without the  $E_T^{\text{miss}}$  cut.

2037 This method is extremely effective as a crosscheck because it uses a com-  
 2038 pletely independent dataset from the flavor symmetry method, and the  
 2039 two methods have very little overlap in dependence on MC. They produce  
 2040 consistent results in both SRZ and VRS, as shown in Table 12.

## 2041 10.2 $Z/\gamma^*$ + JETS BACKGROUND

2042 The  $Z/\gamma^*$  + jets background is mainly produced by a process called Drell-  
 2043 Yan in which annihilating quark/anti-quark pairs produce a  $Z$  boson or  
 2044 a virtual photon. These bosons then decay to two leptons, which, in the  
 2045 case of the  $Z$  boson, naturally appear in the  $Z$ -mass window. The bo-  
 2046 son typically recoils off a hadronic system, which can satisfy the jet and  
 2047  $H_T$  requirement in SRZ. However, this process rarely produces real  $E_T^{\text{miss}}$   
 2048 (though occasionally neutrinos do appear in its hadronic decays), so most  
 2049 events with large amounts of  $E_T^{\text{miss}}$  are the result of extreme mismeasure-  
 2050 ment. Because SRZ cuts on the very high  $E_T^{\text{miss}}$  tails of a  $Z$  distribution, a  
 2051 small change in the assumptions about jet resolution or energy scale in MC

Region	Flavour-symmetry	Sideband fit
SRZ	$33 \pm 4$	$29 \pm 7$
VR-S	$99 \pm 8$	$92 \pm 25$

Table 12: Comparison of FS background predictions from the nominal method, the flavor symmetry method, and the cross-check, the sideband fit method. Uncertainties include statistical and systematic uncertainties in both cases.

2052 can drastically change the prediction, and a low  $Z/\gamma^* + \text{jets}$  prediction  
 2053 can result in a signal-like peak appearing in the final result.

2054 Because of this volatility in the MC prediction in these high  $E_T^{\text{miss}}$  tails, a  
 2055 data-driven method is used to estimate this background. The method uses  
 2056  $\gamma + \text{jets}$  events which, like the  $Z/\gamma^* + \text{jets}$  events, contain one boson recoil-  
 2057 ing against a hadronic system. These  $\gamma + \text{jets}$  events are then corrected for  
 2058 the kinematic differences between  $\gamma$  and  $Z$ s [33, 89]. The sample of  $\gamma + \text{jets}$   
 2059 events is taken from CR- $\gamma$ , defined in Table 7. This region is similar to the  
 2060 SRZ selection without the  $E_T^{\text{miss}}$  requirement, but it vetoes events with lep-  
 2061 tons and requires at least one photon. Additionally, the  $\Delta\phi(\text{jet}_{12}, p_T^{\text{miss}})$  cut  
 2062 in SRZ, which is designed to reduce the background from mismeasured  
 2063 jets, is removed for this region because of its unpredictability at very low  
 2064 values of  $E_T^{\text{miss}}$ , when the angle of the  $E_T^{\text{miss}}$  is much less meaningful.

2065 Despite their similarities, there are many theoretical differences between  
 2066  $\gamma$  and  $Z$  events. The massive  $Z$  boson recoils differently against a jet system  
 2067 than the massless photon. Another consequence of its masslessness is that  
 2068 photons cannot appear in decays with no jets because such a decay would  
 2069 always violate conservation of energy in some frame. As a consequence,  
 2070 many kinematic variables have different shapes between the two samples.  
 2071 Figure 64 shows a MC comparison of boson  $p_T$  between  $\gamma$  and  $Z$  events,  
 2072 demonstrating the shape differences between the two processes.

2073 The most significant experimental difference between  $Z$  and  $\gamma$  events  
 2074 is that  $Z$  bosons rapidly decay, in the case of this analysis, to two leptons,  
 2075 which are then be observed by the ATLAS detector. In contrast, the photon  
 2076 is stable, and can be directly detected by ATLAS. This means that the re-  
 2077 constructed  $Z$  boson and the directly observed photon have very different  
 2078 energy resolutions, which can result in different amounts of  $E_T^{\text{miss}}$  in the  
 2079 two events.

2080 Ultimately, the goal of this method is to predict the  $E_T^{\text{miss}}$  distribution of  
 2081 the  $Z+\text{jets}$  background. These differences between  $Z+\text{jet}$  and  $\gamma+\text{jet}$  events  
 2082 can be broken down into two categories: differences which affect the jet  
 2083 energy and measurement, and differences which affect the boson energy  
 2084 and measurement. The differences in the hadronic system are simpler, and  
 2085 mostly consist of different numbers and energies of jets between the two  
 2086 samples, which can be accounted for via reweighting in a variable that's  
 2087 representative of the total energy scale of the event. The differences in the

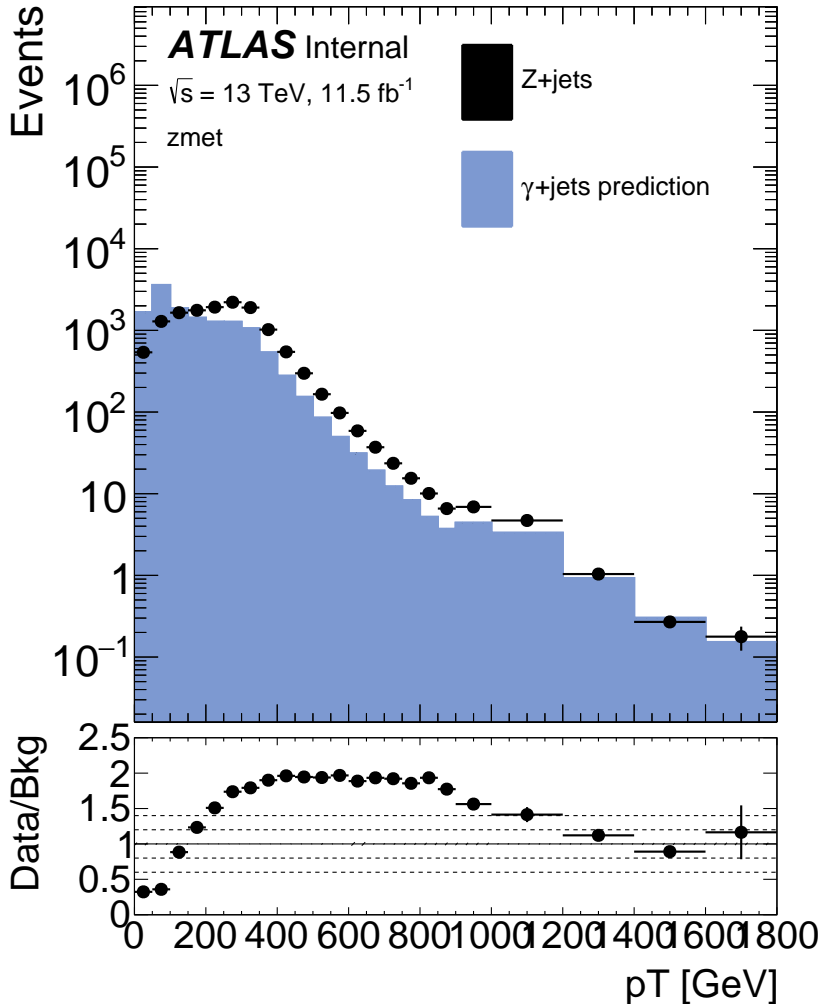


Figure 64: MC comparison of boson  $p_T$  in a selection of photon and  $Z \rightarrow \ell\ell$  events with  $H_T > 600$  GeV.

2088    bosons are more complex, and require the application of smearing func-  
 2089    tions based on the different observed objects. Together these corrections  
 2090    allow for complete modeling of the  $Z/\gamma^* + \text{jets}$   $E_T^{\text{miss}}$  spectrum with  $\gamma+\text{jet}$   
 2091    events.

2092    10.2.1 *Photon and Z Event Selection*

2093    The baseline photon events come from an inclusive CR with no  $E_T^{\text{miss}}$  cut,  
 2094    a lepton veto, and the requirement of at least one photon, which is called  
 2095    CR- $\gamma$  and defined in Table 7<sup>3</sup>. This selection is very pure in  $\gamma+\text{jet}$  events,  
 2096    but some  $V\gamma$  events are also included, which can include real  $E_T^{\text{miss}}$ . These  
 2097    backgrounds are subtracted off at the end off the estimation procedure.

---

<sup>3</sup> This region includes an  $H_T$  cut, which requires the translation of photon  $p_T$  into an equivalent di-lepton  $p_T$  scalar sum. This process is described in Section 10.2.4.

2098 The triggering scheme for these events is more complicated than in other  
 2099 regions because the lowest unprescaled photon trigger requires a photon  
 2100  $p_T$  of at least 120 (140) GeV in 2015 (2016) datataking, but the method re-  
 2101 quires events with much lower  $p_T$  to predict the full  $Z$ -boson  $p_T$  spectrum.  
 2102 To accomplish this, the lower- $p_T$  photons are broken down into small  $p_T$   
 2103 ranges with a different prescaled trigger required in each range, listed in  
 2104 [Table 13](#). The events in each selection are then weighted by the prescale  
 2105 value of the trigger used to reconstruct a smooth  $p_T$  spectrum.

$p_T$ Range [GeV]	Trigger Name
2015 Data-Taking	
$37 < p_T < 45$	HLT_g35_loose_L1EM15
$45 < p_T < 50$	HLT_g40_loose_L1EM15
$50 < p_T < 55$	HLT_g45_loose_L1EM15
$55 < p_T < 125$	HLT_g50_loose_L1EM15
$p_T > 125$	HLT_g120_loose_L1EM15
2016 Data-Taking	
$25 < p_T < 30$	HLT_g20_loose_L1EM12
$30 < p_T < 40$	HLT_g25_loose_L1EM12
$40 < p_T < 45$	HLT_g35_loose_L1EM12
$45 < p_T < 50$	HLT_g40_loose_L1EM12
$50 < p_T < 55$	HLT_g45_loose_L1EM12
$55 < p_T < 65$	HLT_g50_loose_L1EM12
$65 < p_T < 75$	HLT_g60_loose_L1EM12
$75 < p_T < 85$	HLT_g70_loose_L1EM12
$85 < p_T < 105$	HLT_g80_loose_L1EM12
$105 < p_T < 145$	HLT_g100_loose_L1EM12
$p_T > 145$	HLT_g140_loose_L1EM12

Table 13: List of triggers used to collect photon events in 2015 and 2016 data-taking.

2106 These  $\gamma$  events can then be compared to baseline  $Z \rightarrow \ell\ell$  events with  
 2107 a similar selection. These events have the same dilepton requirements as  
 2108 SRZ, without the  $m_{\ell\ell}$  cut. They also have no  $E_T^{\text{miss}}$  cut, but like the photons,  
 2109 are required to have  $H_T > 600$  GeV as in SRZ.

### 2110 10.2.2 Smearing of Photon Events

2111 While  $Z$ +jet events are measured as a pair of leptons recoiling against  
 2112 a hadronic system,  $\gamma$ +jet events are measured only as one object recoil-  
 2113 ing against jets. In addition, detector resolution is different for electrons,

muons, and photons. The impact of these differences must be corrected for in  $\gamma+\text{jet}$  events in order for them to accurately predict the  $E_{\text{T}}^{\text{miss}}$  distribution of the  $Z$ s. Luckily, in most cases, the resolution of the photon's  $p_{\text{T}}$  is better than the  $Z$  boson's, so the photon events can be smeared to emulate the  $Z$ s.

To isolate mismeasurement of boson  $p_{\text{T}}$ , this method uses  $E_{T,\parallel}^{\text{miss}}$ , the  $E_{\text{T}}^{\text{miss}}$  projection on an axis defined by the momentum of the boson. Figure 65 shows the  $E_{T,\parallel}^{\text{miss}}$  distribution in MC for the two samples, and demonstrates the discrepancies between them. The core of the photon distribution is somewhat similar to the  $Z \rightarrow ee$  distribution because, in the high- $p_{\text{T}}$  limit, measurements of both photons and electrons are primarily taken from the electromagnetic calorimeter and should have similar resolutions. For muons, which rely only on tracks to determine  $p_{\text{T}}$ , the resolution becomes very large at high  $p_{\text{T}}$  values where the tracks are nearly straight. As a consequence, the resolutions for photon and  $Z \rightarrow \mu\mu$  events are very different.

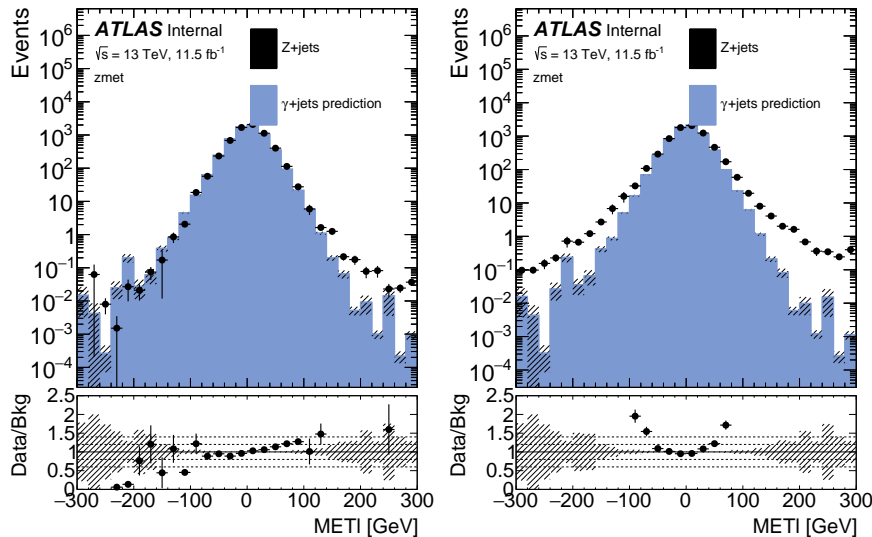


Figure 65:  $E_{T,\parallel}^{\text{miss}}$  distributions in MC for  $Z+\text{jets}$   $ee$  (left) and  $\mu\mu$  (right) channels compared to  $\gamma + \text{jets}$  in an inclusive region with  $H_{\text{T}} > 600$  GeV.

A function to smear photon events is derived from the deconvolution of the photon and lepton response functions, taken from 1-jet CRs with no  $H_{\text{T}}$  cut, which are otherwise identical to the baseline  $Z$  and  $\gamma$  selections. This region is chosen because it is orthogonal to the SR, so the resolution can be obtained from data as well as MC. In these regions, events are binned in boson  $p_{\text{T}}$ , and in each bin, a  $E_{T,\parallel}^{\text{miss}}$  distribution is made. The smearing function is derived for each bin via the deconvolution of the  $Z/\gamma^* + \text{jets}$  and  $\gamma + \text{jets}$  distributions.

Next, for each photon event, the smearing function matching the event's photon  $p_{\text{T}}$  is sampled, yielding a smearing factor  $\Delta p_{\text{T}}$ . The photon's  $p_{\text{T}}$  is then adjusted according to

$$p_{\text{T}}^{\gamma'} = p_{\text{T}}^{\gamma} + \Delta p_{\text{T}} \quad (41)$$

2140 and the corresponding change in  $E_T^{\text{miss}}$  is made,

$$E_{T,\parallel}^{\text{miss}'} = E_{T,\parallel}^{\text{miss}} - \Delta p_T. \quad (42)$$

2141 The nominal smearing function is taken from MC in order to remove con-  
 2142 tamination from other backgrounds, and the resulting  $E_{T,\parallel}^{\text{miss}}$  distributions  
 2143 can be seen in Figure 66. Though there is a small amount of oversmearing  
 2144 in the negative tail, the improvement in agreement between the distribu-  
 2145 tions is clear.

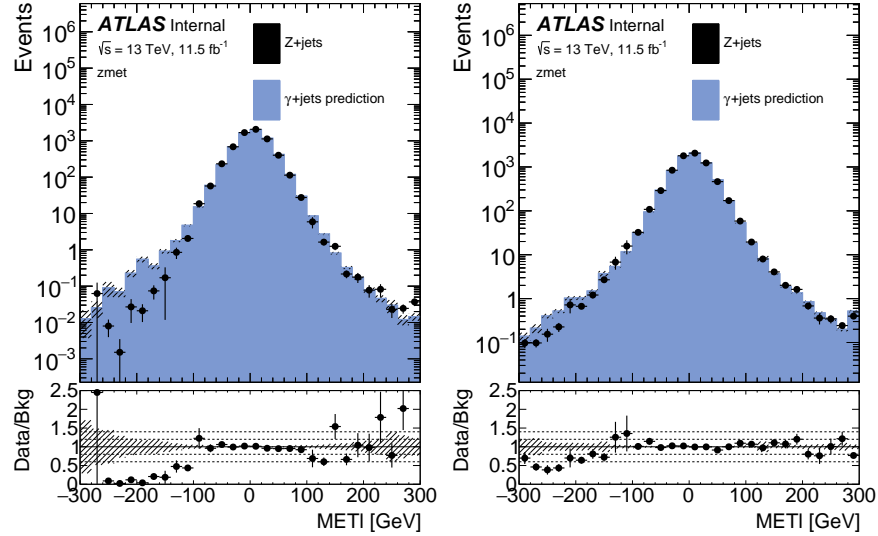


Figure 66:  $E_{T,\parallel}^{\text{miss}}$  distributions in MC for Z+jets ee (left) and  $\mu\mu$  (right) channels compared to  $\gamma + \text{jets}$  in an inclusive region with  $H_T > 600 \text{ GeV}$  after the smearing procedure has been performed. These distributions have also been  $p_T$  reweighted, as described in Section 10.2.3.

### 2146 10.2.3 $p_T$ Reweighting of Photon Events

2147 Next, the photon events are reweighted to match the boson  $p_T$  of the Z  
 2148 events. This is accomplished by making histograms of boson  $p_T$  for  $\gamma$  and  
 2149 Z events, similar to that in Figure 64, and with binning identical to that  
 2150 used in Section 10.2.2. Photons are binned based on their smeared  $p_T$  deter-  
 2151 mined in the previous step. A reweighting factor  $f(p_T)$  is then calculated  
 2152 in each bin, according to

$$f(x) = \frac{N_{Z/\gamma^*+\text{jets}}(x)}{N_{\gamma+\text{jets}}(x)} \quad (43)$$

2153 in MC, and in data according to

$$f(x) = \frac{N_{\text{data}}(x) - N_{t\bar{t}}(x) - N_{VV}(x)}{N_{\gamma+\text{jets data}}(x)} \quad (44)$$

where the contamination from other backgrounds is taken from MC and subtracted from the  $Z$  selection. The resulting reweighting factors can be seen in Figure 67 and are calculated independently for  $ee$  and  $\mu\mu$  events.

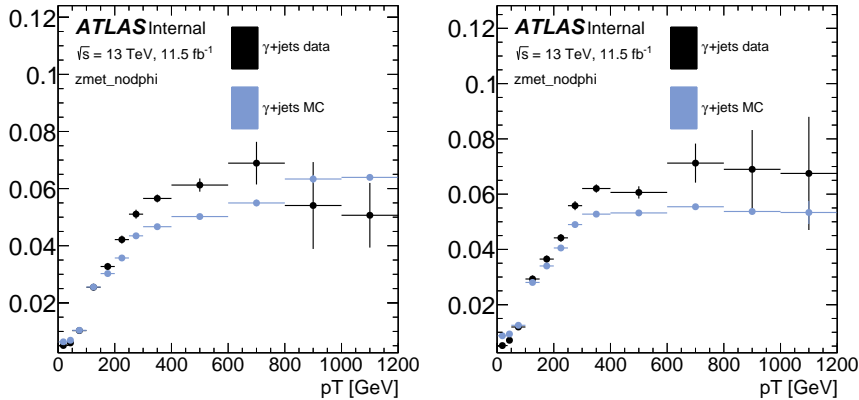


Figure 67: Photon reweighting factors for the  $ee$  (left) and  $\mu\mu$  (right) channels derived from data and MC.

This reweighting, though it is performed on the boson  $p_T$ , primarily serves to produce more similar jet distributions between the  $\gamma$  and  $Z$  samples. Because, excluding  $E_T^{\text{miss}}$  contributions, the boson  $p_T$  must match the energy of the jet system off which it recoils, these two variables are closely tied. Once the two samples have similar amounts of hadronic energy, the  $E_T^{\text{miss}}$  contribution from mismeasurement of jet energy should also be similar.

Together, the boson smearing and  $p_T$  reweighting produce a  $E_T^{\text{miss}}$  spectrum in the modified photon events that closely match that of the  $Z$  events. Figures 68 and 69 show the comparison of the  $E_T^{\text{miss}}$  distributions before any alteration, with only  $p_T$  reweighting, and after the smearing and reweighting, demonstrating the impact of each step. Once the  $E_T^{\text{miss}}$  distribution is well described, the  $\Delta\phi(\text{jet}_{12}, p_T^{\text{miss}})$  can be applied.

#### 10.2.4 Determining $H_T$ and $m_{\ell\ell}$

One complication thus far ignored is that CR- $\gamma$  has no leptons, but some quantities that define the SR require them, namely  $H_T$  (which includes the  $p_T$  of the two leading leptons) and  $m_{\ell\ell}$ . Both of these variables are determined by creating histograms binned in the boson  $p_T$  and sampling.

In the case of  $H_T$ , distributions of the scalar sum of the  $p_T$  of the leading leptons are made for each  $Z$   $p_T$  bin. A sampled value from the distribution is then added to the  $H_T$  of the jets in a photon event to produce the final estimate. This sampling is done before any reweighting is performed because the  $H_T$  is needed to make the preselection for the reweighting process. However, the smearing is performed inclusively in  $H_T$ , so this procedure can be performed using the smeared photon  $p_T$  to choose the distribution to sample.

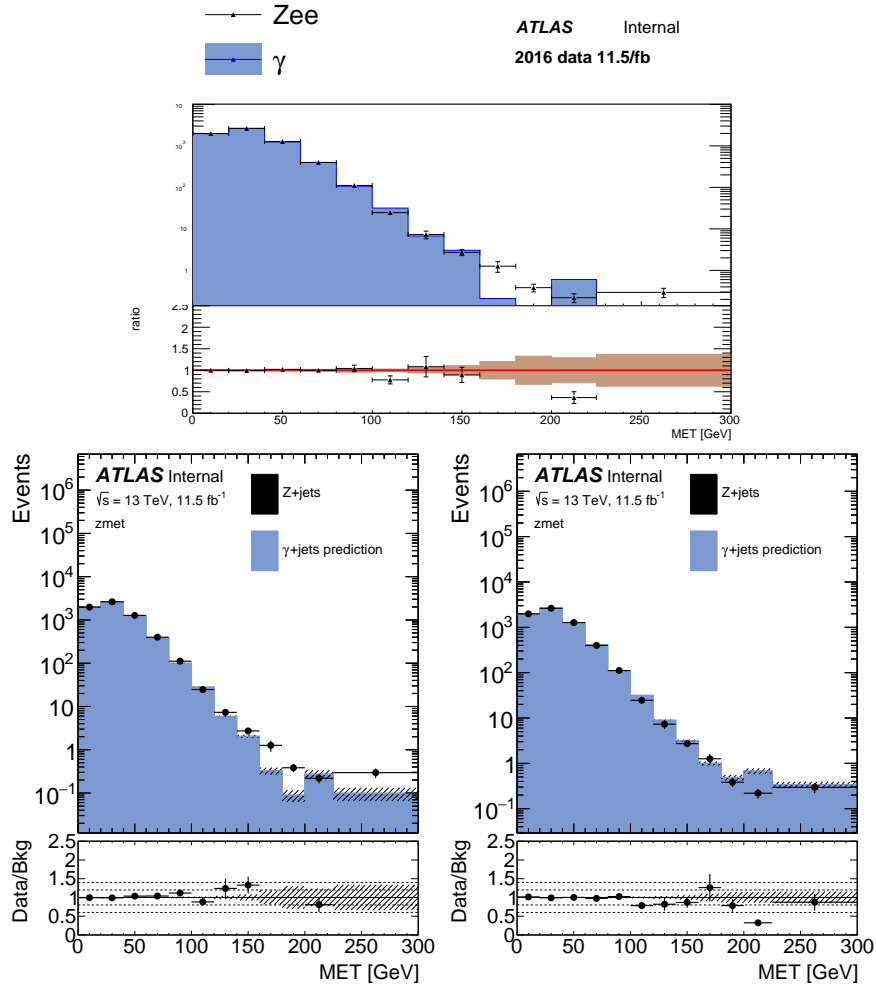


Figure 68:  $E_T^{\text{miss}}$  distribution comparing MC distributions of photon and Z events before any smearing is applied (top), with only  $p_T$  reweighting applied (bottom left), and after  $p_T$  reweighting and smearing have both been applied (bottom right) in the  $ee$  channel of 2016 data.

2183     The  $m_{\ell\ell}$  determination is done after both the smearing and reweighting,  
2184     and is tied closely to the smearing step. Mismeasurements in lepton  $p_T$   
2185     can create  $E_T^{\text{miss}}$  in a  $Z/\gamma^* + \text{jets}$  event, but the same event is likely to mi-  
2186     grate off the  $Z$   $m_{\ell\ell}$  window due to the mismeasured lepton. Thus it is very  
2187     important that the two effects be carefully correlated in the manipulated  
2188     photon events. To achieve this, MC Z events from the 1-jet CR described in  
2189     Section 10.2.2 are used to make two-dimensional distributions of  $m_{\ell\ell}$  as  
2190     a function of the difference between reconstructed and true Z  $p_T$  for the  
2191      $ee$  and  $\mu\mu$  channels. A photon event then uses the  $\Delta p_T$  assigned to it dur-  
2192     ing the smearing process to index the distribution, and an  $m_{\ell\ell}$  value is  
2193     sampled from the corresponding bin <sup>4</sup>

<sup>4</sup> Ideally this  $\Delta p_T$  would also include the difference between the true and reconstructed  $p_T$  of the photon events, but this information is of course not accessible in data. Luckily, in the events in the final SR this value is typically negligible compared to the  $\Delta p_T$  from smearing, so the impact is small.

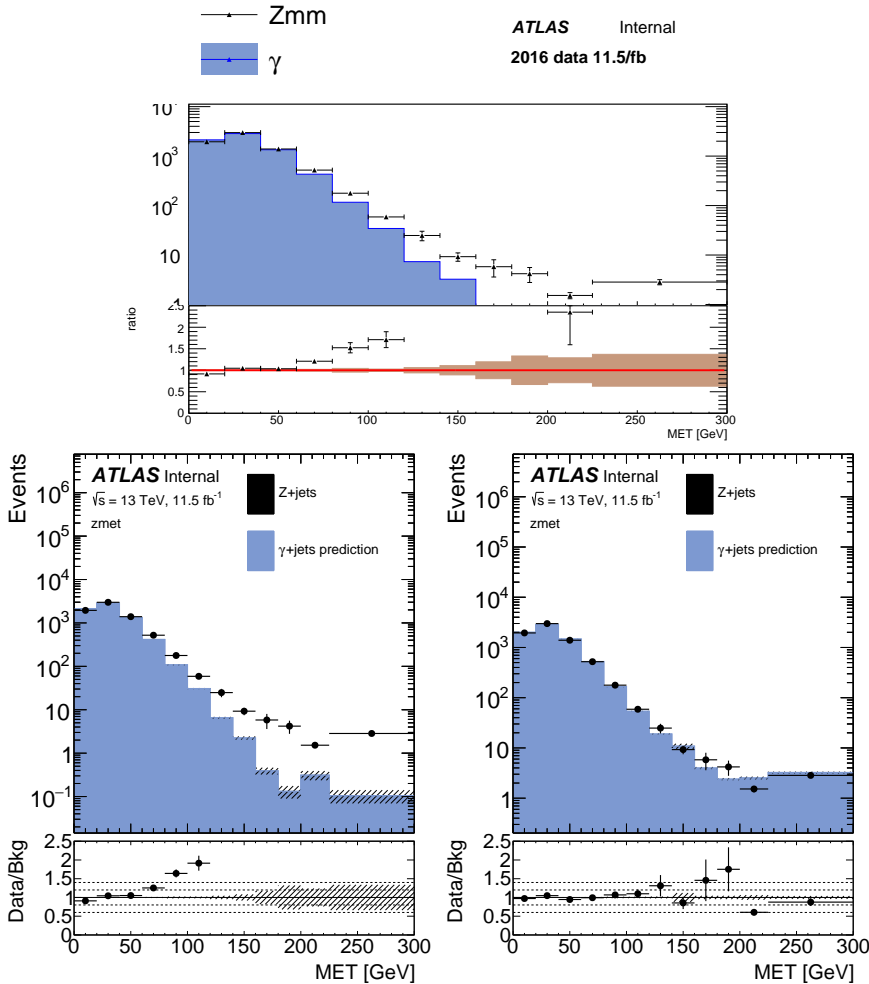


Figure 69:  $E_T^{\text{miss}}$  distribution comparing MC distributions of photon and Z events before any smearing is applied (top), with only  $p_T$  reweighting applied (bottom left), and after  $p_T$  reweighting and smearing have both been applied (bottom right) in the  $\mu\mu$  channel of 2016 data.

To test the soundness of this procedure, it is repeated purely in MC, and the results of the MC prediction and the data prediction are compared to the  $m_{\ell\ell}$  distribution in  $Z/\gamma^* + \text{jets}$  MC in Figure 70. After the  $m_{\ell\ell}$  distribution has been emulated, a cut requiring that the photon events be “on the Z mass peak” can be required.

#### 10.2.5 Subtraction of $V\gamma$ Events

At high  $E_T^{\text{miss}}$ , where the signal region lies, contamination of CR- $\gamma$  with  $V\gamma$  events becomes significant, as shown in Figure 71. These events must be subtracted from the  $\gamma + \text{jets}$  prediction because, once the photons are corrected to approximate Zs, they essentially provide a (not very accurate) prediction of diboson events, which are already accounted for in another background estimate.

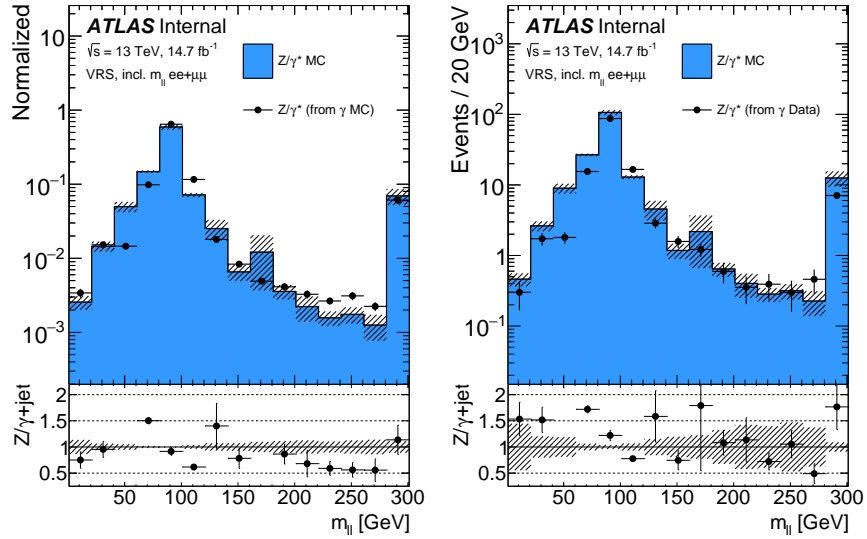


Figure 70:  $Z/\gamma^*$  + jets MC  $m_{\ell\ell}$  distribution compared to the prediction from  $\gamma$  + jets method performed on MC (left) and the prediction from  $\gamma$  + jets method performed on data (right).

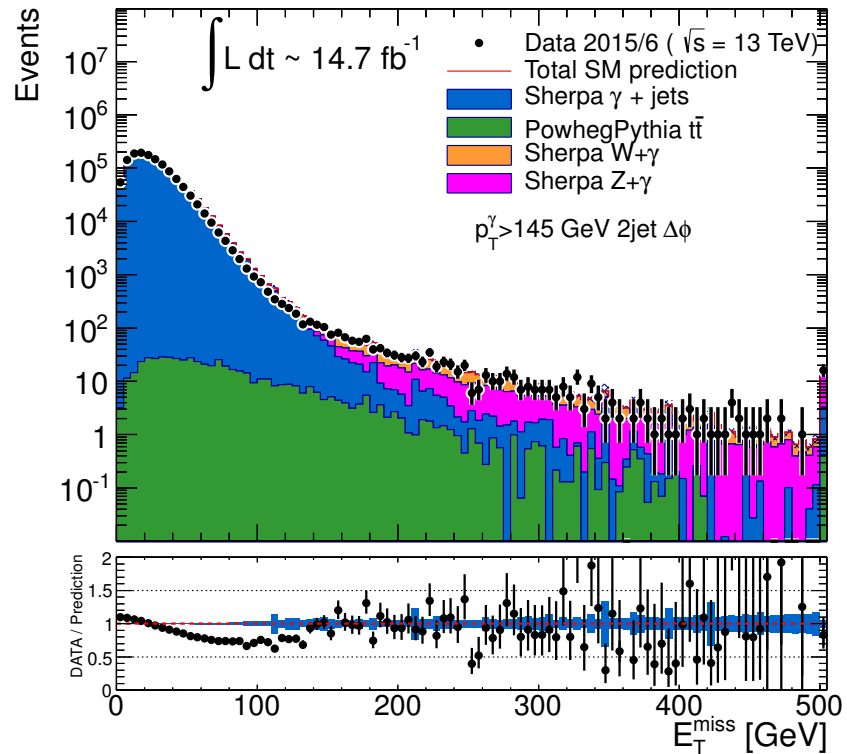
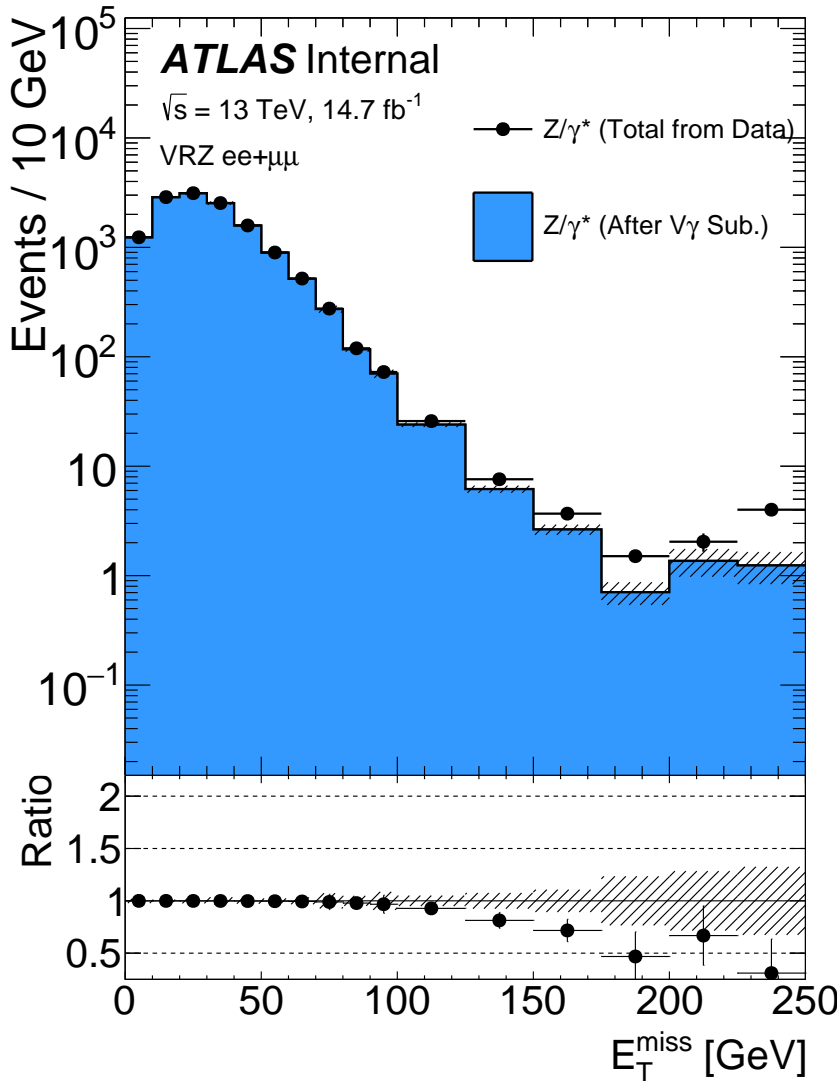


Figure 71: Comparison of data and MC in CR- $\gamma$  without any  $H_T$  cut, including the contributions from various  $V\gamma$  processes.

2206 This subtraction accomplished by performing the  $\gamma$  + jets method on  $V\gamma$   
 2207 MC to approximate these backgrounds' contribution to the final  $E_T^{\text{miss}}$  dis-  
 2208 tribution. This contribution is then subtracted from the  $\gamma$  + jets prediction,

the impact of which can be seen in [Figure 72](#). As expected, the impact is greatest at high  $E_T^{\text{miss}}$  where these backgrounds are most significant.



[Figure 72](#): Total  $\gamma + \text{jets}$  data prediction in SRZ (excluding the  $E_T^{\text{miss}}$  cut) and the prediction after the  $V\gamma$  subtraction.

#### 10.2.6 Validation in Data

The  $\gamma + \text{jets}$  jets method is validated in a region called VRZ, defined in [Table 7](#), which is similar to SRZ, but with an inverted  $E_T^{\text{miss}}$  cut. [Figure 73](#) shows the low- $E_T^{\text{miss}}$  portion of this VR where the  $Z/\gamma^* + \text{jets}$  background is dominant. Here, the three data-driven background estimates, as well as the remaining MC backgrounds are stacked and compared to the data yield in this region, demonstrating excellent agreement across a wide  $E_T^{\text{miss}}$  range.

An additional check can be made in VRZ by removing the  $\Delta\phi(\text{jet}_{12}, \mathbf{p}_T^{\text{miss}})$  intended to suppress the  $Z/\gamma^* + \text{jets}$  background from jet mismeasurement.

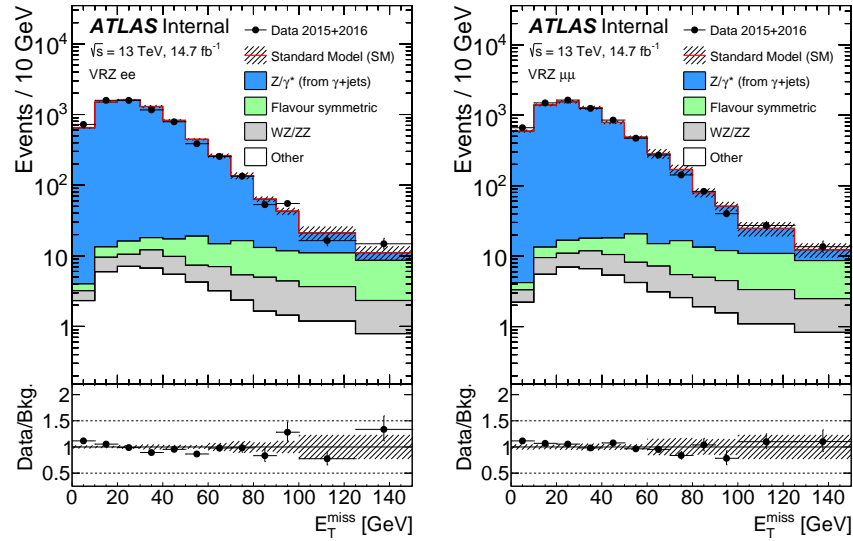


Figure 73:  $E_T^{\text{miss}}$  distribution in VRZ  $ee$  (left) and  $\mu\mu$  (right) with total data yield compared to the sum of the prediction from the  $\gamma + \text{jets}$  method, the prediction from the flavor symmetry method, the prediction from the fake background estimation (included under “other”), and the remaining backgrounds taken from MC.

2221 Figure 74 shows the distribution of this variable in VRZ, and demonstrates  
 2222 that, even at low values where the  $Z/\gamma^* + \text{jets}$  background is dominant,  
 2223 the  $\gamma + \text{jets}$  method models it accurately.

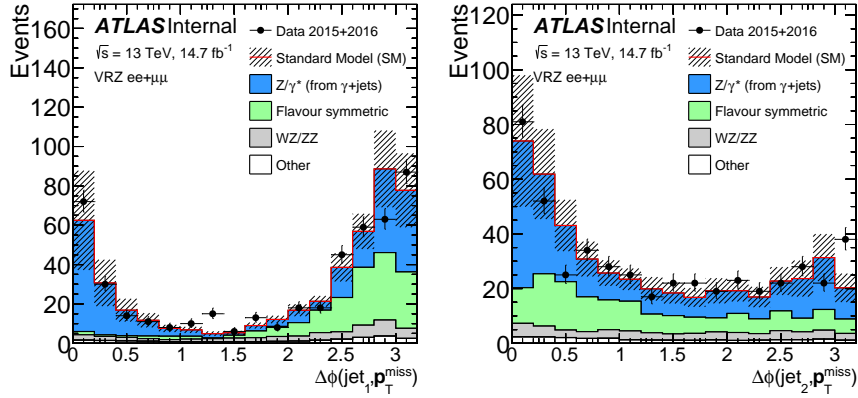


Figure 74:  $\Delta\phi(\text{jet}, p_T^{\text{miss}})$  distribution for the leading jet (left) and the subleading jet (right). The comparison is performed in VRZ with the cut on  $\Delta\phi(\text{jet}_{12}, p_T^{\text{miss}})$  removed. The total data yield is compared to the sum of the prediction from the  $\gamma + \text{jets}$  method, the prediction from the flavor symmetry method, the prediction from the fake background estimation (included under “other”), and the remaining backgrounds taken from MC.

## 2224 10.3 FAKE AND NON-PROMPT LEPTONS

2225 The *fakes* background consists of processes that produce only one lepton,  
 2226 but whose events are otherwise kinematically similar to the [SR](#). These pro-  
 2227 cesses include semileptonic  $t\bar{t}$ ,  $W$ -jets, and single top processes. Though  
 2228 these processes typically only produce one lepton, they can be recon-  
 2229 structed with two leptons due to a hadron being misidentified as a lepton  
 2230 or due to a real non-prompt lepton resulting from photon conversions or  
 2231  $B$ -hadron decays. As with the  $Z/\gamma^* + \text{jets}$  background, it is very difficult  
 2232 to predict with [MC](#) because the flaws in reconstruction are typically less  
 2233 well described by the models used in [MC](#) production than the successes.  
 2234 Nonetheless, a rough estimate can be made of this background by using  
 2235 [MC](#), which indicates that the number of fake events in SRZ is consistent  
 2236 with zero.

2237 Despite the small predicted contribution in the [SR](#), a data-driven method  
 2238 called the *matrix method* is employed to estimate these fake events [90]. This  
 2239 method is also used to estimate the fakes contribution to other control and  
 2240 validation regions where their impact is more significant.

2241 In the matrix method, the quality requirements for signal leptons are  
 2242 loosened to give a selection of baseline leptons (see [Table 3](#) and [Table 4](#)),  
 2243 which consist of a higher fraction of fake leptons. In each [CR](#), [VR](#), or [SR](#), the  
 2244 remaining kinematic selections are made on the baseline leptons, and the  
 2245 number of leptons in the region which pass the signal lepton requirements  
 2246 ( $N_{\text{pass}}$ ) and the number which fail ( $N_{\text{fail}}$ ) are measured. For a 1-lepton  
 2247 selection, these quantities can be used to predict the number of fake events  
 2248 that pass the selection according to:

$$N_{\text{pass}}^{\text{fake}} = \frac{N_{\text{fail}} - (1/\epsilon^{\text{real}} - 1) \times N_{\text{pass}}}{1/\epsilon^{\text{fake}} - 1/\epsilon^{\text{real}}}. \quad (45)$$

2249 The efficiencies  $\epsilon^{\text{real}}$  and  $\epsilon^{\text{fake}}$  give the relative identification efficiency  
 2250 from baseline to signal for genuine, prompt leptons and fake and non-  
 2251 prompt leptons, respectively. For a 2-lepton selection, the principle is the  
 2252 same, but the equation is more complicated, requiring a four-by-four ma-  
 2253 trix to account for possible combinations of real and fake leptons.

2254 To calculate  $\epsilon^{\text{real}}$ , the tag-and-probe method is performed a selection of  
 2255  $Z \rightarrow \ell\ell$  data events, CR-real, described in [Table 14](#). In this method, one *tag*  
 2256 lepton passing a signal selection is required, as is another *probe* lepton pass-  
 2257 ing a baseline requirement. Distributions in  $m_{\ell\ell}$  for events with a tag and  
 2258 a passing probe and events with a tag and a failing probe are produced  
 2259 and fit, and the efficiency is computed using the ratio acquired from the  
 2260 fit. A comparison of data and [MC](#) in CR-real can be seen in [Figure 75](#).

2261 The fake efficiency,  $\epsilon^{\text{fake}}$ , is determined using the tag-and-probe method  
 2262 in CR-fake, also described in [Table 14](#). This region is different from all  
 2263 other regions considered in this analysis because it requires same-sign lep-  
 2264 tons. Very few processes genuinely produce two same-sign leptons, so this  
 2265 region is enhanced in fake leptons. An upper limit on  $E_{\text{T}}^{\text{miss}}$  is placed on

Fakes regions	$E_T^{\text{miss}}$ [GeV]	$H_T$ [GeV]	$n_{\text{jets}}$	$m_{\ell\ell}$ [GeV]	SF/DF	OS/SS	$n_{\ell}$
CR-real	–	$> 200$	$\geq 2$	<b>81–101</b>	$2\ell$ SF	OS	2
CR-fake	$< 125$	–	–	$> 12$	$2\ell$ SF/DF	SS	$\geq 2$

Table 14: Control regions used to measure efficiencies of real and fake leptons. The flavour combination of the dilepton pair is denoted as either “SF” for same-flavour or “DF” for different flavour. The charge combination of the leading lepton pairs are given as “SS” for same-sign or “OS” for opposite-sign.

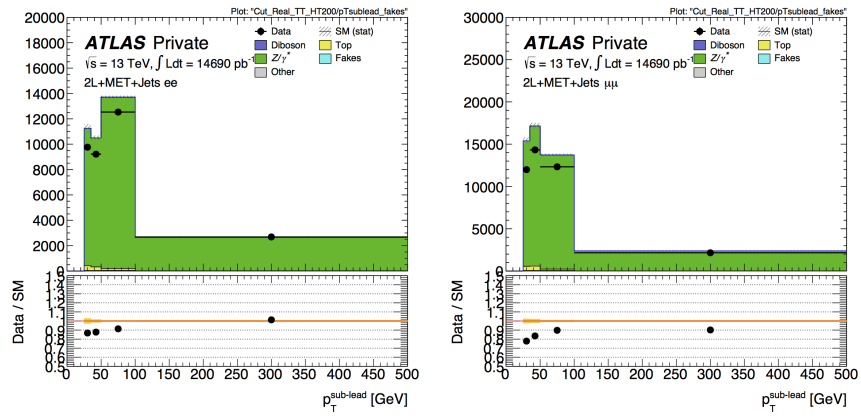


Figure 75: Sub-leading lepton  $p_T$  for  $ee$  (left) and  $\mu\mu$  (right) events in the tight-tight region used to measure the real-lepton efficiency for 2016.

2266 CR-fake to limit the possible contamination from BSM processes. According  
 2267 to MC, real, prompt leptons make up about 7% (11%) of the baseline  
 2268 electron (muon) sample and about 10% (61%) of the signal electron (muon)  
 2269 sample in this region. These real lepton backgrounds are subtracted from  
 2270 the CR-fake yields when calculating the efficiencies. Figure 76 shows a  
 2271 comparison of data and MC in this region.

2272 This method is validated in a fakes-rich validation region with a same-  
 2273 sign lepton requirement,  $E_T^{\text{miss}} \geq 50\text{GeV}$ ,  $\geq 2$  jets, and a veto on  $m_{\ell\ell}$  on  
 2274 the Z-mass peak for same flavor channels. The results of this validation  
 2275 can be seen in Figure 77. With the systematic uncertainties, discussed in  
 2276 Section 11.1.3, the prediction agrees well with the data across a wide range  
 2277 of  $m_{\ell\ell}$  values.

#### 2278 10.4 DIBOSON AND RARE TOP PROCESSES

2279 The remaining backgrounds are diboson processes (excluding WW, which  
 2280 is included in the FS background) and rare top processes. Dibosons events

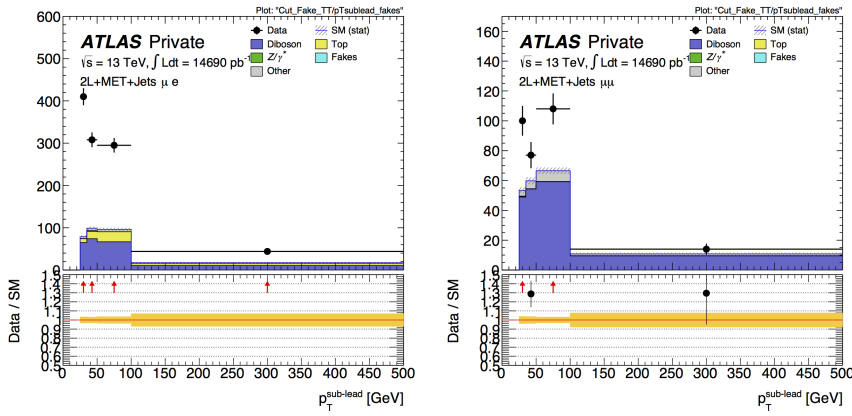


Figure 76: Sub-leading lepton  $p_T$  for  $\mu e$  (left) and  $\mu \mu$  (right) events in the tight-tight region used to measure the fake-lepton efficiency for 2016.

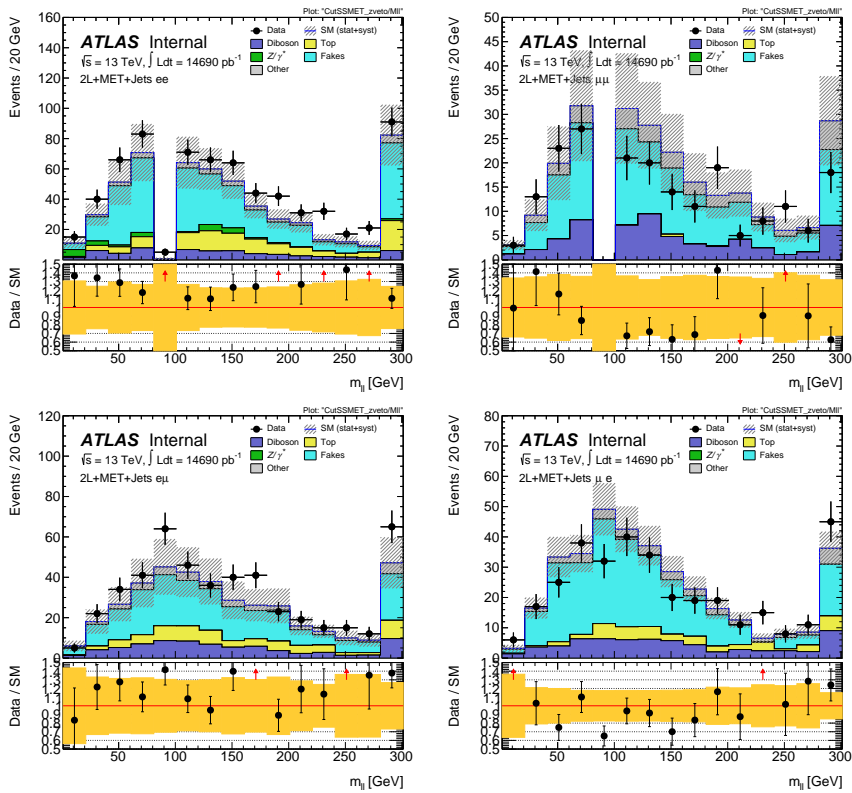


Figure 77: Same sign validation regions in the  $ee$  (top left),  $\mu\mu$  (top right),  $e\mu$  (bottom left) and  $\mu e$  (bottom right) channels combining 2015+2016 data. Uncertainty bands include both statistical and systematic uncertainties.

make up about 30% of the events in SRZ, while rare top process contributions are much smaller. Both are taken directly from MC, with validation regions to confirm the accuracy of the prediction. These regions are described in Table 7, and target different parts of these backgrounds. VR-ZZ is a four-lepton selection designed to select a very pure sample of ZZ events. VR-WZ requires three leptons and makes specific cuts on  $m_T$ , the

transverse mass, and  $E_T^{\text{miss}}$  in order to select mostly  $WZ \rightarrow ll\nu\nu$  events. VR-3L is similar to VR-S, but loosens the  $H_T$  and  $E_T^{\text{miss}}$  cuts and requires at least three leptons. This region is designed to target any  $\geq 3$ -lepton process in a region as kinematically close to SRZ as possible while still maintaining enough events to validate. The makeups of these multilepton validation regions, as well as VRS, are shown in [Table 15](#).

	VR-S	VR-WZ	VR-ZZ	VR-3L
Observed events	236	698	132	32
Total expected background	$224 \pm 41$	$613 \pm 66$	$139 \pm 25$	$35 \pm 10$
Flavour-symmetric	$99 \pm 8$	-	-	-
WZ/ZZ events	$27 \pm 13$	$573 \pm 66$	$139 \pm 25$	$25 \pm 10$
Rare top events	$11 \pm 3$	$14 \pm 3$	$0.44 \pm 0.11$	$9.1 \pm 2.3$
$Z/\gamma^* + \text{jets}$ events	$84 \pm 37$	-	-	-
Fake lepton events	$4 \pm 4$	$26 \pm 6$	-	$0.6 \pm 0.3$

[Table 15](#): Yields in validation regions. In VRS, data-driven background estimates are used for  $Z/\gamma^* + \text{jets}$ , fakes, and [FS](#) processes. All other backgrounds are taken from [MC](#), including all backgrounds in the multi-lepton [VRS](#). Uncertainties include statistical and systematic components.

To confirm that the kinematics are well modeled in the diboson validation regions, distributions of boson mass and  $p_T$  are shown in [MC](#) and data. Figures [78](#) and [79](#) show these distributions for VR-WZ, and [Figure 80](#) shows these distributions for VR-ZZ.

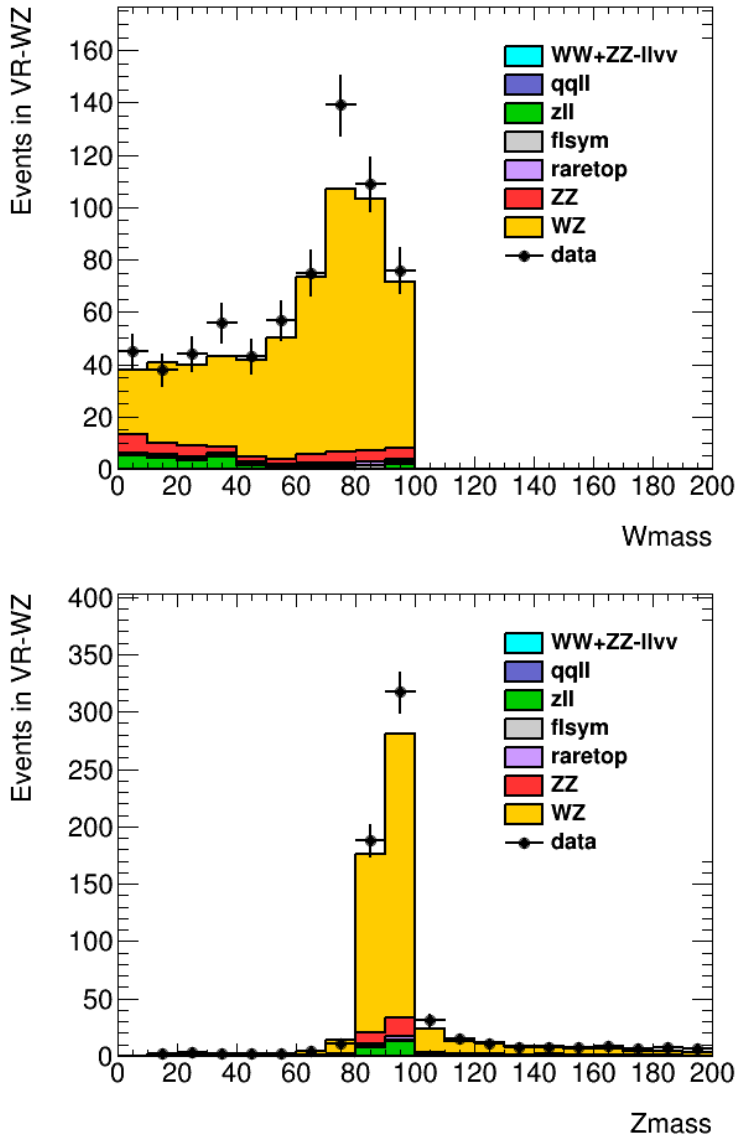


Figure 78: Distribtuions of data and MC in VR-WZ. Reconstructed transverse mass of the  $W$  (top) and mass of the  $Z$  (bottom).

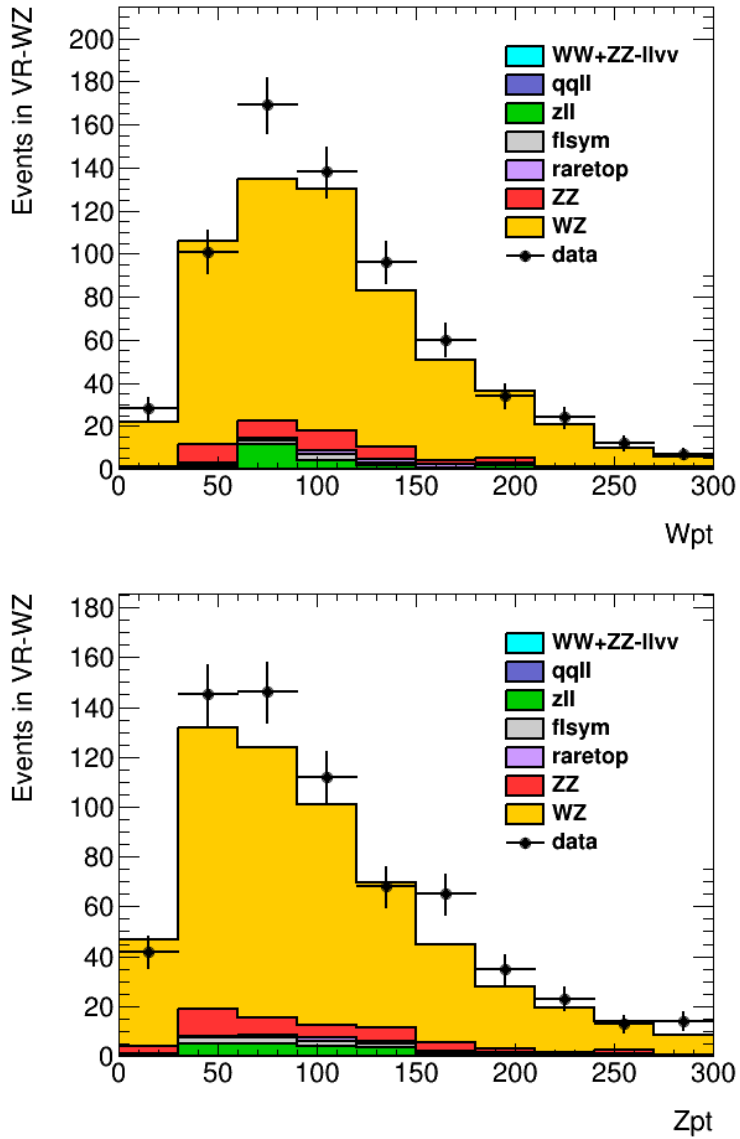


Figure 79: Distributions of data and MC in VR-WZ.  $p_T$  of the  $W$  (top) and  $Z$  (bottom).

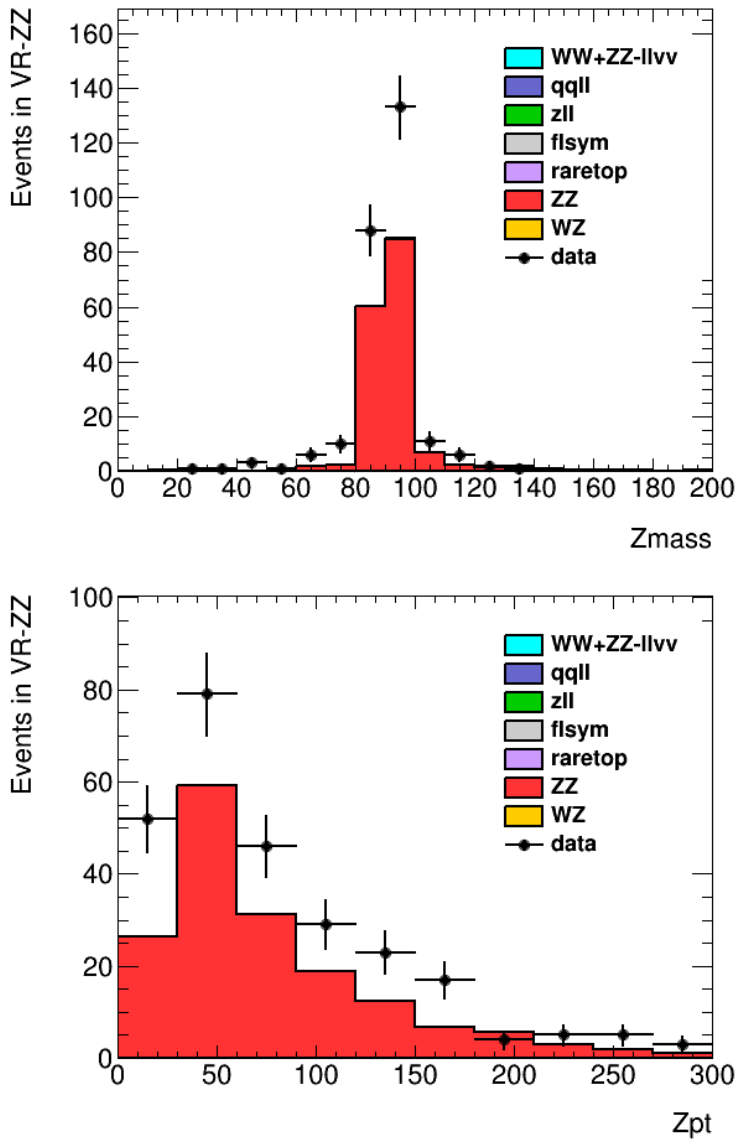


Figure 8o: Distributions in VR-WZ. On the top, mass of the Z bosons in the event, and on the bottom,  $p_T$  of the Z bosons.



2297

## 2298 SYSTEMATIC UNCERTAINTIES

## 2299 11.1 UNCERTAINTIES ON DATA-DRIVEN BACKGROUNDS

2300 11.1.1 *Uncertainties on the Flavor Symmetry Method*

2301 The flavor symmetry method is a data driven method that makes its esti-  
 2302 mate primarily on based events populating an [SR-like CR](#) in the different-  
 2303 flavor channel. The statistical uncertainty on these events makes up the  
 2304 dominant uncertainty on the method. To reduce this uncertainty, the  $m_{\ell\ell}$  range  
 2305 on the [CR](#) is expanded, approximately tripling the number of events in [CR-](#)  
 2306 [FS](#). The statistical uncertainty is reduced by this expansion, though it is  
 2307 still significantly higher than any of the other systematic uncertainties on  
 2308 this method, as seen in [Table 16](#). Also included in the statistical uncertainty  
 2309 column is the uncertainty on the number of non-[FS](#) events in [CR-FS](#), which  
 2310 is used to scale the prediction to account for contamination in the [CR](#).

Reg.	Ch.	Pred.	Uncertainties					
			stat. clos.	MC and $\alpha$	k and $\alpha$	dAOD usage	$m_{\ell\ell}$ shape	total
SRZ	$ee$	16.50	1.82	0.88	0.53	0.12	0.22	2.11
	$\mu\mu$	16.67	1.83	0.79	0.33	0.11	0.23	2.04
	$ee+\mu\mu$	33.16	3.66	1.07	0.86	0.23	0.45	3.94
VRS	$ee$	49.70	3.21	2.34	2.20	0.34	0.75	4.61
	$\mu\mu$	49.60	3.14	2.88	1.40	0.31	0.75	4.56
	$ee+\mu\mu$	99.31	6.34	4.00	3.60	0.65	1.49	8.47

Table 16: Uncertainties in the on-Z signal and validation regions. Nominal predictions are given with statistical uncertainty (including uncertainty from subtracted backgrounds), MC Closure uncertainty, uncertainty on the prediction from varying  $k$  and  $\alpha$  by their statistical uncertainties, comparing the efficiencies from AODs to that of DAOs, and on the  $m_{\ell\ell}$  widening, which includes MC statistics and a data/MC comparison in a loosened region.

2311 The next largest contribution to the uncertainty comes from [MC](#) closure  
 2312 tests, which are used to determine how effective the method is in its predic-  
 2313 tion. If, for example, using weights derived from an inclusive selection at  
 2314 high  $E_T^{\text{miss}}$  lead to a bias, the closure test would indicate that and an appro-  
 2315 priate uncertainty could be placed on the estimate based on the difference  
 2316 between the [MC](#) prediction and the prediction from the flavor symmetry  
 2317 method.

2318 In this test, the entire FS procedure is performed on  $t\bar{t}$  MC, including a  
 2319 recalculation of weighting factors  $\alpha$  and  $k$ . The prediction from  $e\mu$  events  
 2320 in MC is compared to the MC  $ee$  and  $\mu\mu$  events, as seen in Figure 81. The dif-  
 2321 ference between the two predictions is then summed in quadrature with  
 2322 the statistical uncertainty on each prediction to give the total closure un-  
 2323 certainty seen in Table 16. In these closure tests, all predictions agree within  
 2324 the statistical uncertainty, so the largest contributor to the resulting error  
 2325 is MC statistics.

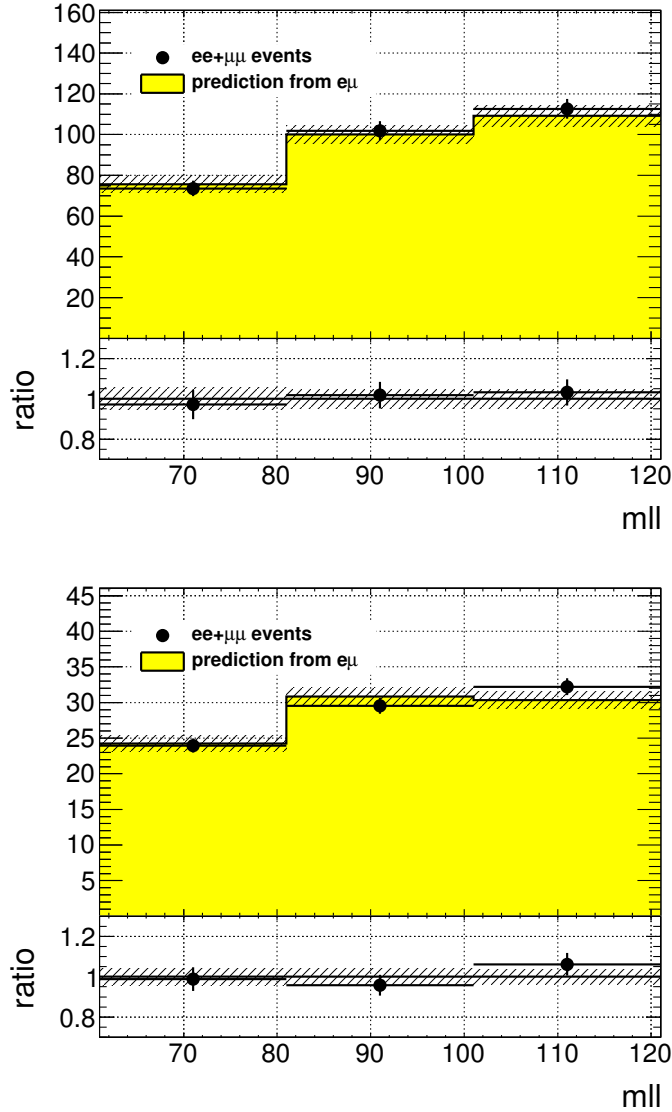


Figure 81: MC closure plots of VRS (top) and SRZ (bottom). The number of events from MC (black points) is compared to the number of events predicted from the flavor symmetry method (yellow histogram). The comparison is performed before the expanded  $m_{ll}$  window is used to predict the on-Z bin, but because the shape is taken from the same MC, the result is identical.

2326 A small uncertainty is added based on the statistical uncertainty on the  
 2327  $k$  and  $\alpha$  factors derived from data. These factors are measured in many dif-  
 2328 ferent bins (see, for example, the different measurements of  $k$  in Figure 82),  
 2329 and as a consequence, some bins can have very large statistical uncertain-  
 2330 ties. To assess the uncertainty on the total estimate, each measurement  
 2331 of these factors is varied by its uncertainty in order to produce the max-  
 2332 imum and minimum possible prediction. The differences with respect to  
 2333 the nominal prediction are used to create a symmetrized error, which is  
 2334 included in Table 16.

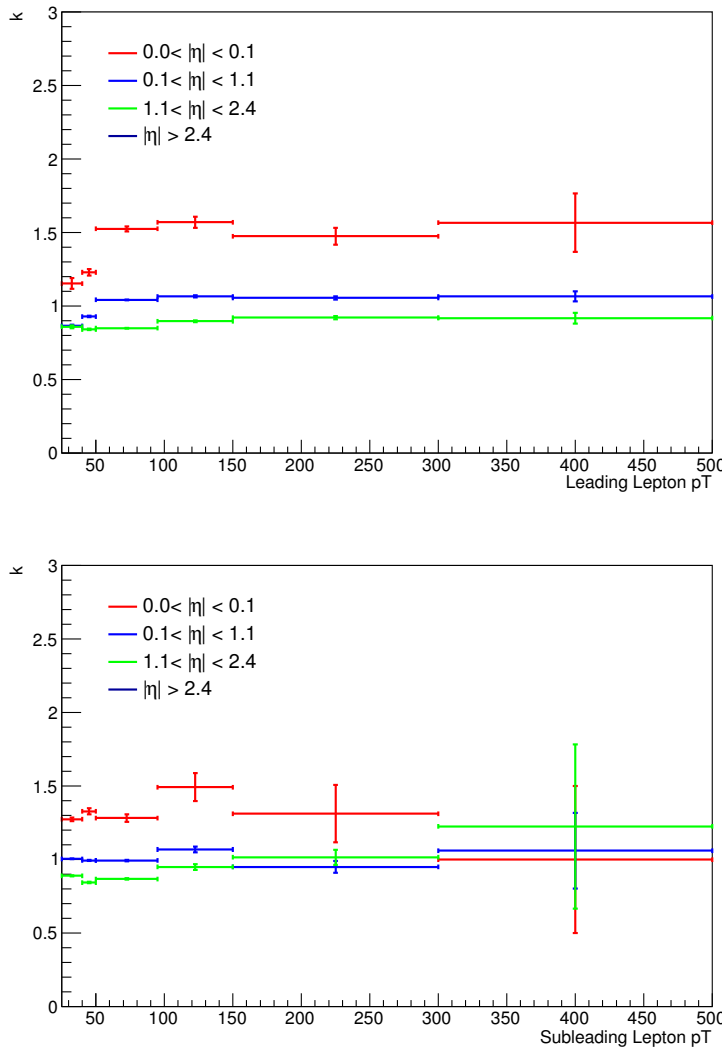


Figure 82: Measurements of  $k$ , the ratio of electron to muon events, in bins of  $p_T$  and  $\eta$ . On the top is the measurements indexed by the leading lepton, while the measurements indexed by the subleading lepton are on the bottom. These efficiencies are for the 2016 dataset.

2335 The next uncertainty considers a potential bias in the way the  $\alpha$  factors  
 2336 are calculated. Because they are derived from data, there is already trig-  
 2337 ger dependence in data collection; only events passing a trigger are stored.

Additional trigger dependence is created by the data format used for analysis. ATLAS data and MC are stored in a format called Analysis Object Data (AOD), but smaller, slimmer versions of these datasets, called derived AODs (dAODs) are used for analysis. These dAODs are designed with specific analyses in mind, filtering on the triggers and objects required by the analyses. As a consequence, in the dAOD used in this analysis, there are explicit requirements that lepton or  $E_T^{\text{miss}}$  triggers are passed in order for events to be included.

As a consequence, the trigger efficiencies  $\epsilon^{\text{trig}}$  used in Equation 40 to define  $\alpha$  do not consider all possible data events. The  $\epsilon^{\text{trig}}$  factor is calculated for each trigger using events passing the kinematic selection for that trigger, outlined in Section 9.1. The efficiency factor is then measured according to the equation

$$\epsilon^{\text{trig}} = \frac{N_{\text{trig}}}{N_{\text{all}}} \quad (46)$$

where  $N_{\text{trig}}$  is the number of events passing the trigger in the kinematic selection and  $N_{\text{all}}$  is all events in the selection. The latter measurement is the one subject to this bias, as it contains only the events that pass at least one trigger required for inclusion in the dAOD. As a consequence of these missing events, the  $\epsilon^{\text{trig}}$  values will be artificially high. However, because the ratio of trigger efficiencies for the different channels is the only quantity needed for this analysis, the missing events will only bias the prediction if the different channels are differently impacted by the trigger preselection.

Calculating the flavor symmetry method's dependence on these biases requires the use of MC. With a generated MC sample, there is no trigger dependence, so an unskimmed sample can be compared to a typical skimmed MC dAOD to identify the effect of the skimming. Figure 83 shows a comparison of the  $\alpha$  factors calculated for different bins in  $E_T^{\text{miss}}$  from the nominal source, data, as well as these two MC sources. A  $E_T^{\text{miss}}$  dependence would be the most likely bias between the two MC-derived  $\alpha$  factors because  $E_T^{\text{miss}}$  triggers are the only triggers besides lepton triggers that will allow an event to be accepted into the dAOD used by this analysis. Though there is some difference between the data-derived  $\alpha$  and those taken from MC, it is clear from this plot that there is very little dependence on the choice of an unskimmed or skimmed sample. The calculation of the uncertainty is performed by repeating the flavor symmetric method in MC with each of the two  $\alpha$  factors and using the difference between the estimates as a symmetric error.

The last uncertainty relates to the main MC dependence of the method - the  $m_{\ell\ell}$  shape of the FS background. A correction factor is taken from MC in order to account for the  $m_{\ell\ell}$  widening, and the accuracy of that factor must be checked. Its shape is compared to that of data in region similar to VR-FS, but with an  $H_T$  cut lowered to 300 GeV to increase statistics. The difference between the fraction of events on the Z-mass peak in data and MC in this region is taken as a systematic uncertainty. To confirm that using

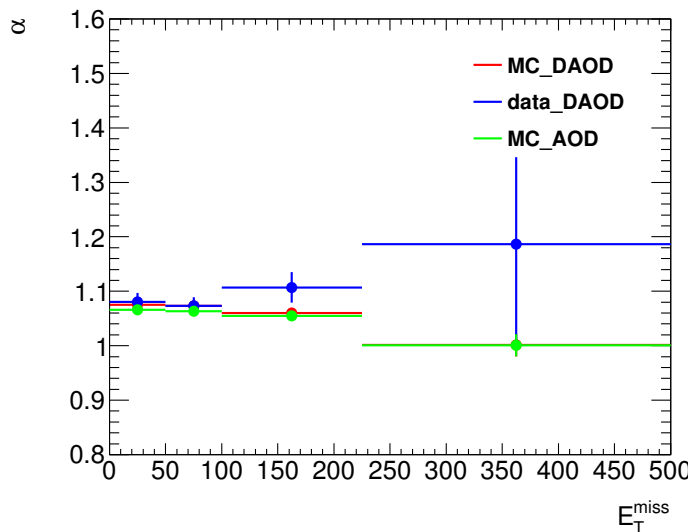


Figure 83:  $\alpha$ , the trigger efficiency ratio, calculated as a function of  $E_T^{\text{miss}}$  from three different sources: data (blue), the usual skimmed  $t\bar{t}$  MC (red), and an unskimmed  $t\bar{t}$  MC (green).

2382 this lowered  $H_T$  cut still gives a valid answer, the fractions are compared  
 2383 as a function of  $H_T$  in Figure 84. In these plots, especially in the higher-  
 2384 statistics 2016 plot, it is clear both that the data and MC agree very well  
 2385 and that there is no strong  $H_T$  dependence.

2386 All the uncertainties are calculated independently for the two datasets,  
 2387 then added together. Statistical uncertainties, including the MC closure sta-  
 2388 tistical uncertainties and the  $k$  and  $\alpha$  uncertainties, are added in quadrature  
 2389 between the two years. Uncertainties that are more likely to be correlated,  
 2390 such as the difference between the two estimates in MC closure and the  
 2391 dependence on using a dAOD to calculate trigger efficiencies, are added  
 2392 linearly. The total uncertainty is about 12% of the nominal prediction in  
 2393 SRZ and about 9% in VRS.

### 2394 11.1.2 Uncertainties on the $\gamma + \text{jets}$ Method

2395 One of the largest sources of uncertainty on the  $\gamma + \text{jets}$  method is derived  
 2396 by comparing the results from reweighting in different variables. Though  
 2397 boson  $p_T$  is used as the nominal reweighting variable, the differences in  
 2398 the kinematics of  $\gamma$  and Z events also impact number of jets,  $H_T$ , and  $E_T$   
 2399 (which includes the mass of the boson). The  $\gamma + \text{jets}$  method is repeated  
 2400 using each of these variables to reweight, and their  $E_T^{\text{miss}}$  distributions are  
 2401 shown in Figure 85. The maximum difference from the nominal prediction  
 2402 is symmetrized and used as an uncertainty on the method.

2403 Another uncertainty is applied to estimate the validity of using MC in a  
 2404 1-jet CR to determine the smearing functions. Smearing functions are made  
 2405 using data from the same 1-jet region and using MC in a  $\geq 2$ -jet region  
 2406 otherwise identical to the 1-jet CR. These distributions are also shown in  
 2407 Figure 85, and like the alternate reweighting distributions, are used to find

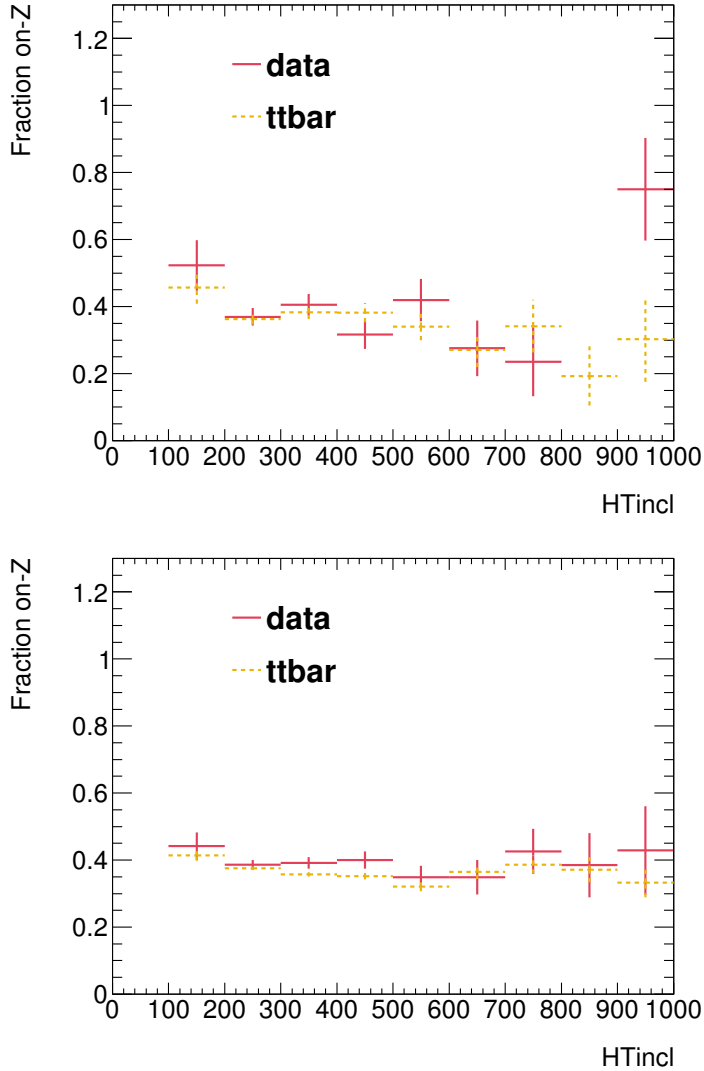


Figure 84: Plots of the fraction of on-Z events with a VR-FS-like selection as a function of  $H_T$ . The top figure shows 2015 data and MC while the bottom figure shows the same for 2016.

2408 a maximum difference from the nominal prediction which is translated  
2409 into a symmetric error.

2410 As in the flavor symmetric method, the full procedure is carried out on  
2411 MC in order to test MC closure, including a recalculation of any weights  
2412 that are typically derived from data. The resulting comparison between  
2413  $Z/\gamma^* + \text{jets}$  MC and the  $\gamma + \text{jets}$  method performed on MC can be seen  
2414 in Figure 86. The final non-closure uncertainty is taken from VRS, where  
2415 larger numbers of events give a clearer picture of the success of the method  
2416 than in SRZ. In this region, the statistical uncertainty on the prediction is  
2417 compared to the non-closure, and the larger of the two is used as the final  
2418 uncertainty.

2419 The uncertainty on the  $V\gamma$  contamination in CR- $\gamma$  is also considered.  
2420 An uncertainty on the MC prediction is made based on comparison of data

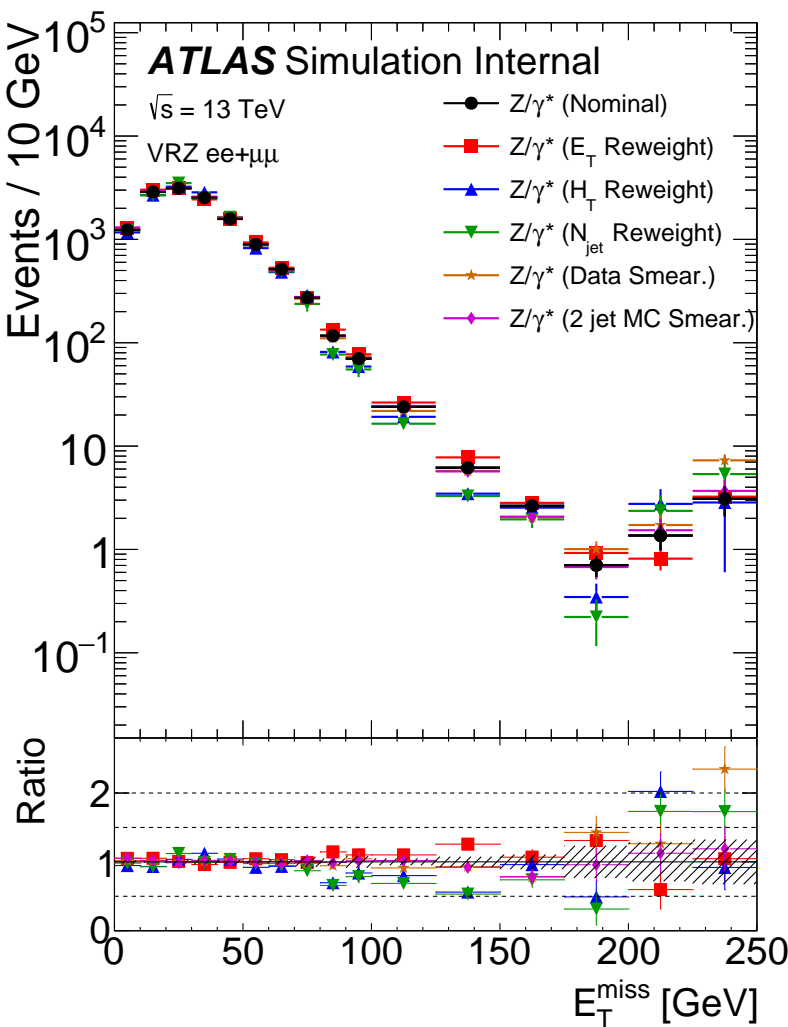


Figure 85:  $E_T^{\text{miss}}$  distributions for  $\gamma + \text{jets}$  predictions using different reweighting variables, as well as distributions with the nominal reweighting but with smearing functions taken from data and from MC in a  $\geq 2$ -jet region.

and MC in a  $W + \text{jets}$  VR, shown in Figure 87. This VR is similar to CR- $\gamma$ , but instead of vetoing events with leptons, requires at least one well-isolated lepton with a  $p_T$  over 25 GeV. At  $E_T^{\text{miss}}$  values over 100 GeV, region is about 90% pure in  $W\gamma$  processes. The MC agrees well with data in this region, even at very high  $E_T^{\text{miss}}$ , so an uncertainty of 16% based primarily on statistical uncertainty in this VR is placed on the  $V\gamma$  MC. This uncertainty is propagated to the final result through the subtraction procedure.

An uncertainty on the  $m_{\ell\ell}$  shape is determined using MC closure as well. The comparison of  $m_{\ell\ell}$  shapes in  $Z/\gamma^* + \text{jets}$  MC and the  $\gamma + \text{jets}$  method applied to MC is shown in Figure 70. As with the main MC closure test, the maximum of the statistical uncertainty and the non-closure is taken as the final uncertainty on this background.

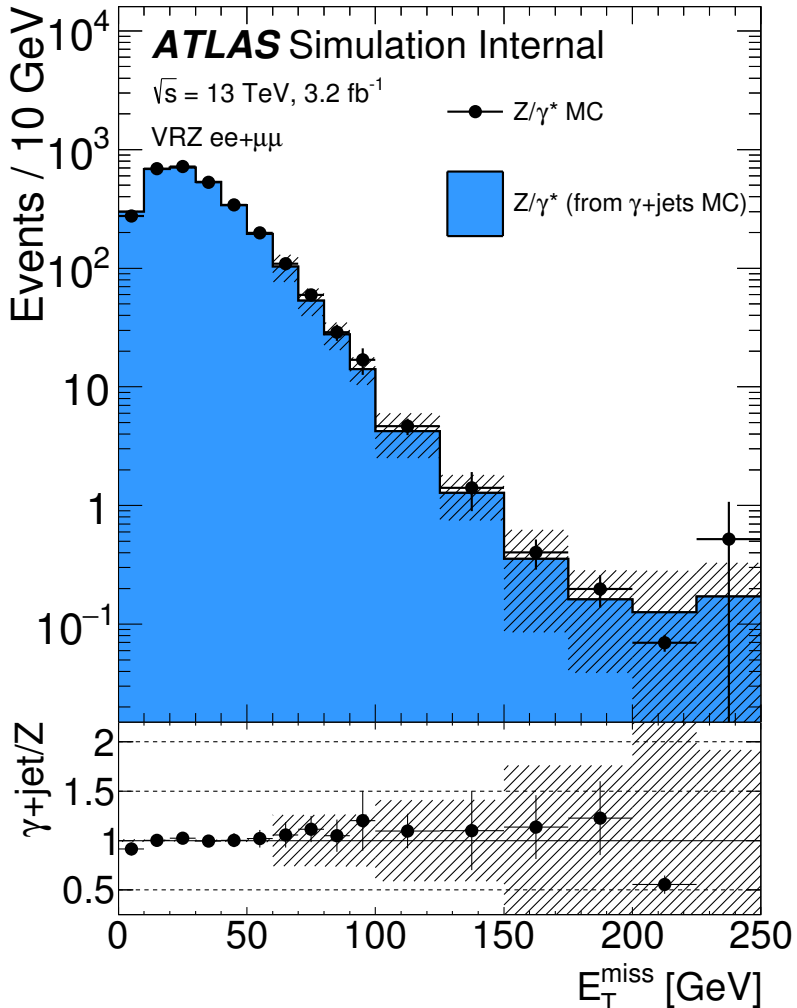


Figure 86: MC closure of the  $\gamma + \text{jets}$  method as a function of  $E_T^{\text{miss}}$  comparing the MC prediction of the Z background with the  $\gamma + \text{jets}$  MC. The uncertainty band includes both statistical and reweighting uncertainties.

2433 One last uncertainty based on the statistical uncertainty on the number  
 2434 of  $\gamma + \text{jets}$  data events used for this method is also included. The full  
 2435 breakdown of uncertainty in SRZ can be seen in Table 17.

#### 2436 11.1.3 Uncertainties on the Fakes Background

2437 Systematic uncertainties on the fakes background are derived from a se-  
 2438 ries of variations on the nominal method. Variations include scaling the  
 2439 real and fake efficiencies up and down by their statistical uncertainties,  
 2440 scaling the prompt lepton contamination in CR-fake up and down by 20%,  
 2441 and by requiring and vetoing  $b$ -tagged jets in CR-fake to determine the  
 2442 dependence on heavy flavor. Statistical uncertainties can also be large in  
 2443 regions with small numbers of events in the baseline selection, such  
 2444 as SRZ. In other regions, the  $b$ -tagging dependence provides the largest

Ch.	Pred.	Uncertainties (%)						
		$V\gamma$ sub.	MC clos.	$m_{\ell\ell}$ shape	re- weight	smear	stat.	total
$ee$	1.02	53.0	21.0	19.0	100.0	65.0	56.0	145.0
$\mu\mu$	2.08	27.0	14.0	23.0	30.0	59.0	40.0	86.0
$ee+\mu\mu$	3.1	36.0	16.0	22.0	43.0	60.0	33.0	92.0

Table 17: Uncertainty breakdown for the  $\gamma + \text{jets}$  method in SRZ. Uncertainties considered are the impact of MC uncertainty on  $V\gamma$  backgrounds, MC closure, uncertainty on  $m_{\ell\ell}$  shape (also determined via MC closure), reweighting uncertainties, smearing uncertainties, and statistical uncertainty on the  $\gamma + \text{jets}$  events used in the method.

uncertainty. The full breakdown of uncertainties for the most important regions are listed in Table 18.

Variation	SRZ	CRT	CRFS	VRFS	VRS	VRT
Nominal	$0.10 \pm 1.61$	$25.39 \pm 5.35$	$3.73 \pm 2.19$	$10.53 \pm 3.56$	$3.64 \pm 3.20$	$80.06 \pm 9.80$
EL F Up	0.15	30.23	3.96	10.93	3.56	92.46
EL F Down	0.06	21.80	3.52	10.18	3.54	70.07
EL R Up	0.25	26.17	3.92	11.10	4.13	82.57
EL R Down	-0.07	24.51	3.52	9.92	3.10	77.24
MU F Up	-0.20	32.48	4.77	16.41	5.25	86.48
MU F Down	0.29	20.17	2.91	7.04	2.87	70.12
MU R Up	0.13	25.67	3.78	10.66	3.81	81.18
MU R Down	0.05	25.04	3.67	10.38	3.44	78.72
Total Sys	+0.26 -0.35	+8.64 -6.39	+1.08 -0.87	+5.92 -3.56	+1.70 -0.97	+14.24 -14.42
Total Sys (%)	+261.05 -354.72	+34.01 -25.19	+29.05 -23.23	+56.22 -33.85	+46.57 -26.60	+17.78 -18.02
Real Cont. Up	0.23	20.97	3.06	8.08	3.15	68.79
Real Cont. Down	-0.01	29.67	4.38	12.95	4.16	90.23
b-jet	0.31	40.44	5.28	8.98	5.63	120.50
no b-jet	0.16	23.44	3.08	11.38	3.97	70.55
Total Sys	+0.25 -0.11	+15.65 -4.83	+1.69 -0.93	+2.56 -2.90	+2.09 -0.49	+41.71 -14.74
Total Sys (%)	+260.46 -109.06	+61.66 -19.02	+45.30 -24.85	+24.32 -27.58	+57.31 -13.35	+52.10 -18.42

Table 18: Systematic uncertainties on the fake-lepton background for on-Z regions for 2015+2016 yields. The nominal yield includes statistical uncertainty from the baseline selection in a given region. The following rows indicate the results of varying the real and fake lepton efficiencies up and down by their statistical uncertainty. Real cont. gives an uncertainty on the contamination of real leptons in the fake lepton efficiency. b-jet and no b-jet indicate the impact of requiring or vetoing b-tagged jets in the regions used to measure the fake efficiency.

## 11.2 THEORETICAL AND EXPERIMENTAL UNCERTAINTIES

Experimental uncertainties cover any detector effect or LHC condition that may not be modeled precisely correctly in MC. For each uncertainty, a standard prescription from the ATLAS experiment is followed. Uncertainties are included on the following parameters:

- Luminosity (2.9%) [91, 92]
- Jet energy scale [61]
- Jet energy resolution [61]
- Jet vertex tagging
- Heavy flavor tagging
- $E_T^{\text{miss}}$  soft term [64]
- $e/\mu$  momentum scale
- $e/\mu$  trigger, reconstruction, and identification efficiencies
- Pile-up

These uncertainties are applied to all MC samples used in the analysis. This includes signal models, diboson and rare top samples for the nominal estimate, and all backgrounds taken from MC in the sideband fit.

Theoretical uncertainties include cross-section uncertainties, scale uncertainties, and PDF uncertainties. For the diboson samples, the scale uncertainties, given in Table 19 are calculated by varying each scale up and down by a factor of two. These are combined with a 6% cross-section uncertainty and a generator uncertainty obtained by comparing PowHEG and SHERPA MC yields in a given region. This generator uncertainty, shown in Table 20, is dominant in most regions. Rare top processes are given a 13% PDF and scale variation uncertainty [38] and a 22% cross section uncertainty [71–73].

Signal models have both the central value and uncertainty on cross-sections taken from an envelope of predictions using different scales and PDF sets [93]. The signal processes are calculated at Next-to-Leading-Logarithmic Accuracy (NLO+NLL); they are initially calculated at NLO in the strong coupling constant, with additional terms from next-to-leading-logarithmic resummation of soft gluon emission [94–98].

### 11.3 IMPACT OF UNCERTAINTIES ON THE SIGNAL REGION

The breakdown of each major uncertainty’s contribution to the total uncertainty in SRZ is shown in Table 21. The dominant uncertainty is the diboson generator uncertainty, followed by the statistical uncertainty from the FS background. Uncertainties smaller than 1% are not shown in the table.

$VV \rightarrow ll\nu\nu$ Samples							
	SRZ	VRS	CRT	VRT	VRWZ	VRZZ	VR <sub>3</sub> L
resummation	0.07	0.03	0.01	0.02	0.00	0.00	0.00
renormalization	0.13	0.17	0.16	0.22	0.00	0.00	0.00
factorization	0.01	0.01	0.01	0.03	0.00	0.00	0.00
total	0.15	0.17	0.16	0.22	0.00	0.00	0.00
$WZ \rightarrow lll\nu$ Samples							
	SRZ	VRS	CRT	VRT	VRWZ	VRZZ	VR <sub>3</sub> L
resummation	0.07	0.05	0.13	0.08	0.02	0.00	0.01
renormalization	0.26	0.20	0.28	0.21	0.07	0.00	0.18
factorization	0.04	0.04	0.02	0.06	0.01	0.00	0.02
total	0.28	0.21	0.31	0.23	0.07	0.00	0.18
$ZZ \rightarrow llll$ Samples							
	SRZ	VRS	CRT	VRT	VRWZ	VRZZ	VR <sub>3</sub> L
resummation	0.27	1.07	0.01	0.01	0.06	0.01	0.53
renormalization	0.28	0.26	0.30	0.60	0.07	0.04	0.14
factorization	0.27	0.25	0.30	0.58	0.13	0.02	0.16
total	0.48	1.13	0.43	0.84	0.16	0.05	0.57

Table 19: Fractional uncertainties of dibosons in signal and validation regions from Sherpa scale variations.

Region	Sherpa Events/fb <sup>-1</sup>	Sherpa Events	Powheg Events/fb <sup>-1</sup>	Powheg Events	% Difference
WZ Samples					
SRZ+VRZ	5.219	76.722	3.286	48.300	37.046
CRT+VRT	1.060	15.583	0.742	10.913	29.970
WW/ZZ Samples					
SRZ+VRZ	1.921	28.244	0.685	10.070	71.424
CRT+VRT	6.281	92.332	3.142	46.188	55.474

Table 20: Comparison of yields in on-Z and off-Z regions in Sherpa and Powheg diboson MC at 14.7 fb<sup>-1</sup>.

Source	Relative systematic uncertainty [%]
SRZ	
Total systematic uncertainty	17
WZ/ZZ generator uncertainty	13
Flavour symmetry (statistical)	7
WZ/ZZ scale uncertainty	6
$Z/\gamma^* + \text{jets}$ (systematic)	4
Flavour symmetry (systematic)	3
$Z/\gamma^* + \text{jets}$ (statistical)	2
Fake-leptons	1

Table 21: Overview of the dominant sources of systematic uncertainty on the total background estimate in the signal regions. The values shown are relative to the total background estimate, shown in %.

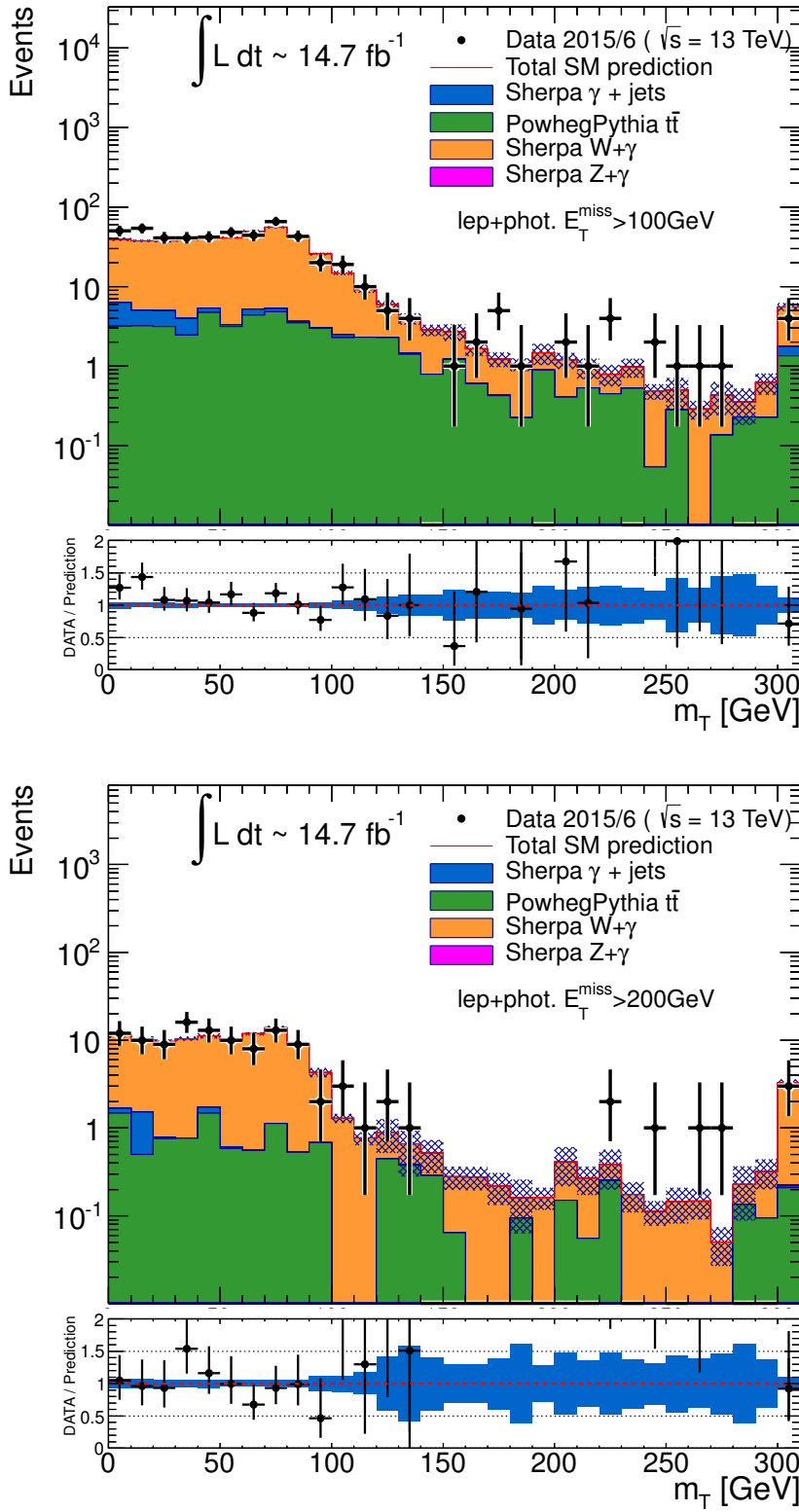


Figure 87: Distributions of  $m_T(\ell, E_T^{\text{miss}})$ , the transverse mass of the lepton and the  $E_T^{\text{miss}}$  in a VR designed to target  $W\gamma$  processes. Top is the distribution with a  $E_T^{\text{miss}}$  cut at 100 GeV, and bottom is the same distribution with a  $E_T^{\text{miss}}$  cut of 200 GeV.



2485

## 2486 RESULTS

2487 The results of the search can be seen in [Table 22](#), which displays the ex-  
 2488 pected and observed numbers of events in SRZ, both divided by channel  
 2489 and inclusively. The predictions and uncertainties for each background are  
 2490 shown, though many of these uncertainties are correlated between back-  
 2491 grounds, so the final uncertainty does not correspond to a simple addition  
 2492 in quadrature of each error. A total of sixty events are observed, with  $53.5 \pm 9.3$   
 2493 events expected. [Figure 88](#) shows the expected and observed results  
 2494 visually for the SR as well as three VRs, all designed to verify the accuracy  
 2495 of the backgrounds taken from MC. Excellent agreement is seen in all cases,  
 2496 with the largest deviation at about  $1\sigma$ .

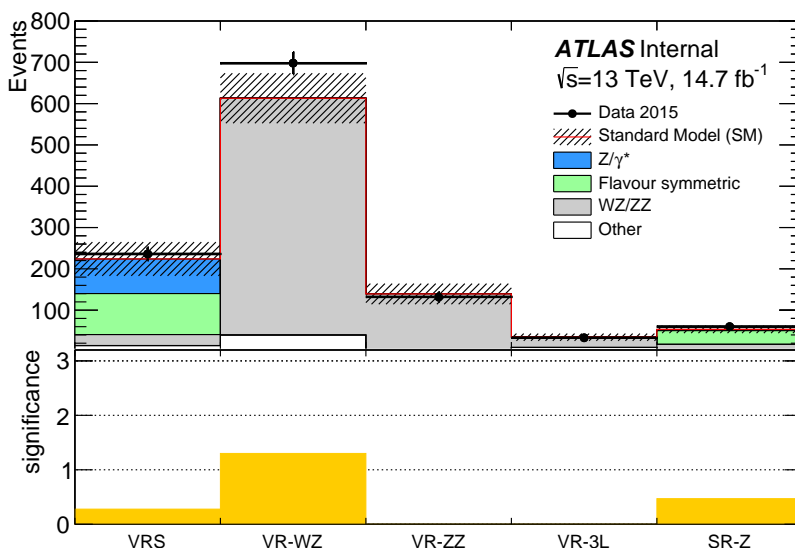


Figure 88: Comparison of background predictions and data yields in four validation regions, as well as the signal region. Definitions of all regions can be found in [Table 7](#), with both rare top and fake backgrounds grouped together under the “other” label. The uncertainty band includes all statistical and systematic uncertainties. Below is a panel of the one-sided statistical significances of the deviations between the predicted and observed quantities for each region.

2497 [Table 22](#) also shows several statistical interpretations of the results. The  
 2498 discovery  $p$ -value for zero signal strength, which gives the probability that  
 2499 the observed events are compatible with a SM-only hypothesis, is given as  
 2500  $0.32$ . The significance is listed as  $0.47\sigma$ , which is a reinterpretation of the  $p$ -  
 2501 value into a gaussian significance. This  $p$ -value is one-sided; when the data  
 2502 yield is less than expected the  $p$ -value is set to  $0.5$ , and the significance is  
 2503 set to  $0$ .  $S^{95}$ , the upper limit on the number of signal events that could be

Table 22: Number of events expected and observed in the  $ee$ ,  $\mu\mu$ , and combined channels. Expected predictions include all systematic and statistical uncertainties discussed in Chapter 11. Also shown is the discovery  $p$ -value for zero signal strength ( $p(s = 0)$ ) [99], Gaussian significance, 95% CL observed and expected upper limits on the number of signal events ( $S^{95}$ ), and the corresponding observed upper limit on the visible cross section ( $\langle \epsilon\sigma \rangle_{\text{obs}}^{95}$ ).

	SRZ	SRZ $ee$	SRZ $\mu\mu$
Observed events			
	60	35	25
Total expected background events	$53.5 \pm 9.3$	$27.1 \pm 5.1$	$26.8 \pm 4.4$
Flavour-symmetric ( $t\bar{t}$ , $Wt$ , $WW$ and $Z \rightarrow \tau\tau$ ) events	$33.2 \pm 3.9$	$16.5 \pm 2.1$	$16.7 \pm 2.0$
$Z/\gamma^*$ + jets events	$3.1 \pm 2.8$	$1.0^{+1.3}_{-1.0}$	$2.1 \pm 1.4$
$WZ/ZZ$ events	$14.2 \pm 7.7$	$7.8 \pm 4.3$	$6.4 \pm 3.5$
Rare top events	$2.9 \pm 0.8$	$1.4 \pm 0.4$	$1.5 \pm 0.4$
Fake-lepton events	$0.1^{+0.8}_{-0.1}$	$0.5^{+0.7}_{-0.5}$	$0^{+0.2}_{-0.2}$
$p(s = 0)$	0.32	0.15	0.5
Significance ( $\sigma$ )	0.47	1.00	0
Observed (Expected) $S^{95}$	$28.2 (24.5^{+8.9}_{-6.7})$	$22.0 (15.8^{+6.5}_{-4.5})$	$12.9 (14.0^{+5.7}_{-3.9})$
$\langle \epsilon\sigma \rangle_{\text{obs}}^{95}$ [fb]	1.9	1.5	0.88

in the SR at a 95% CL, is determined both for the expected and observed number of events. This limit is also reinterpreted based on the integrated luminosity used in the search to produce an upper limit on the visible cross-section of signal events,  $\langle\epsilon\sigma\rangle_{\text{obs}}^{95}$ .

The predictions in SRZ, combined with the MC shapes, are used to produce plots in a broader  $m_{\ell\ell}$  range, seen in Figure 89. These plots are useful demonstrations of efficacy of the background estimation methods, showing the well-modeled  $Z/\gamma^* + \text{jets}$  shape in the same-flavor region, and in the different-flavor region, demonstrating that there are no extreme fluctuations within the region used to predict the flavor symmetric background.

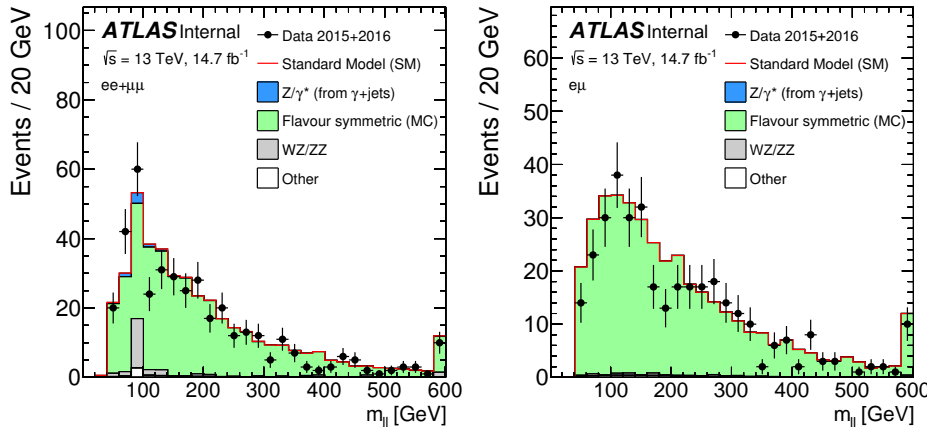


Figure 89: Comparisons as a function of  $m_{\ell\ell}$  of background predictions with observed data in an SRZ-like region, with the  $m_{\ell\ell}$  cut removed. Left is the same-flavor channel, where all background shapes are taken from MC and scaled to their SRZ predictions, except for the  $Z/\gamma^* + \text{jets}$  background, which is taken entirely from the data-driven background. Right is the different-flavor channel, in which the backgrounds are taken directly from MC, except for  $t\bar{t}$ , which is scaled to match the total data yield.

Focusing in on the SR itself, comparisons of background predictions, observed events, and signal models can be made as a function of key variables for the analysis. Figure 90 shows several of these. The first two figures focus on the features of the SR events' leading leptons; they give the mass and  $p_T$  of a hypothetical parent particle reconstructed from the leptons. In the case of events with a real Z boson, these variables simply give that boson's mass at  $p_T$ . The next two figures show distributions in the two most important variables used to differentiate signal from background,  $E_T^{\text{miss}}$  and  $H_T$ . In this analysis, where the frozen SR resulted in cuts on these quantities that are lower than those that would be chosen based on a new optimization, these plots show that, even in more sensitive regions, no large excess above the SM background is seen. The last pair of figures relates to the jets in the event, showing the total number of jets and the total number of  $b$ -jets in the SR events. The  $b$ -jet quantity is not explicitly cut on in the analysis because the fraction of  $b$ -jets produced is extremely model dependent. However, an excess at high  $b$ -jet

2530 multiplicity would suggest a BSM process. In each of these distributions,  
 2531 the observed distributions match the background predictions very well,  
 2532 and no evidence for any of the superimposed signal models is seen.

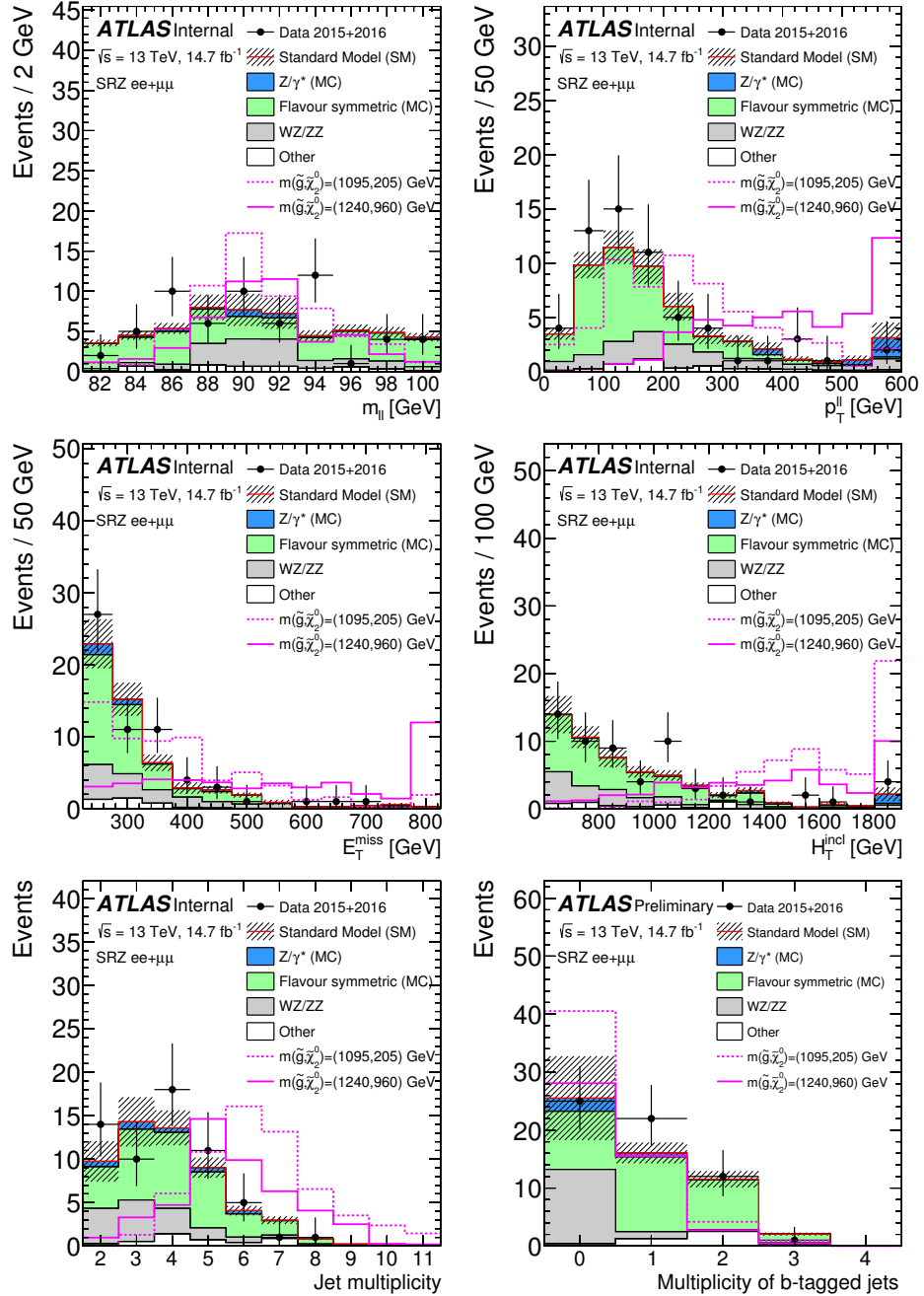


Figure 90: Distributions of observed data, background predictions, and simulated signals are shown in SRZ as a function of  $m_{\ell\ell}$ ,  $p_T^{\ell\ell}$ ,  $E_T^{\text{miss}}$ ,  $H_T$ , number of jets, and number of  $b$ -jets. The two example signals have  $(m(\tilde{g}), m(\tilde{\chi}_2^0)) = (1095, 205) \text{ GeV}$ . All background shapes are taken from MC, and in the case of flavor symmetric and  $Z/\gamma^* + \text{jets}$  backgrounds, their yields are scaled to match the data-driven predictions. Uncertainties include statistical and systematic components.

2533 Comparisons of the observed and expected yield are also made as a  
2534 function of  $\Delta\phi(\text{jet}_{12}, p_T^{\text{miss}})$ , shown in Figure 91. Here, results are shown  
2535 in a region similar to SRZ with the cut on this variable removed, showing  
2536 the efficacy of the background prediction in a region enhanced in  $Z/\gamma^* +$   
2537 jets events. Again, excellent agreement is seen between the background  
2538 prediction and observed data.

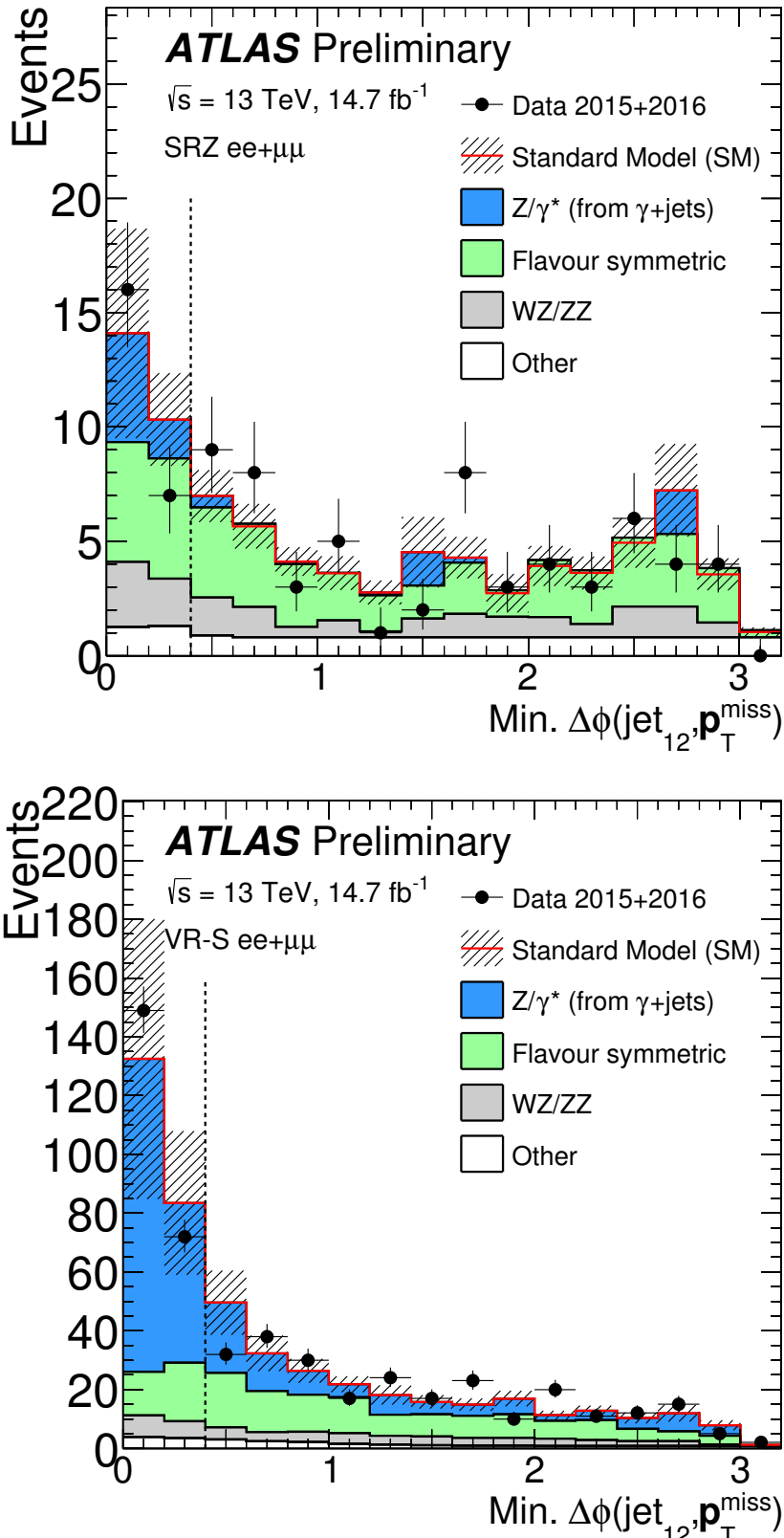


Figure 91: Comparisons as a function of  $\Delta\phi(\text{jet}_{12}, \mathbf{p}_T^{\text{miss}})$  of background predictions with observed data in an SRZ-like (left) and VRS-like (right) region, with the  $\Delta\phi(\text{jet}_{12}, \mathbf{p}_T^{\text{miss}})$  cut removed. All background shapes are taken from MC and scaled to their SRZ predictions, except for the Z/ $\gamma^*$  + jets background, which is taken entirely from the data-driven background.

2539

2540 INTERPRETATIONS

---

2541 Using the simplified models discussed in [Section 2.2.3](#), these results can be  
 2542 interpreted into exclusions of theories based on the masses of the particles  
 2543 involved. Of course, these exclusions include all the assumptions of the  
 2544 models used, so they shouldn't be interpreted to mean that no theory  
 2545 with a given set of particle masses can possibly exist, but they do provide  
 2546 a helpful guideline for targeting future searches and comparing results  
 2547 from different analyses.

2548 Limits are determined using a program called HistFitter [99], designed  
 2549 within the ATLAS experiment, which builds upon the capabilities of ROOT  
 2550 [100], RooStats [101], and HistFactory [102] to combine the uncertainties  
 2551 of the various background predictions, including their correlations, and  
 2552 produce cross-section limits at 95% CL using the  $CL_S$  prescription [103,  
 2553 104]. In this prescription, a likelihood is constructed based on the expected  
 2554 signal and background contributions to the SR. Nuisance parameters are  
 2555 created based on the statistical and systematic uncertainties for each data-  
 2556 driven background, as well as for each systematic applied to the MC-driven  
 2557 background estimates. The fit uses Gaussian models for nuisance param-  
 2558 eters for all signal and background uncertainties, except for the statistical  
 2559 uncertainty on data- and MC-driven background estimates, which are in-  
 2560 terpreted as Poissonian. Experimental uncertainties are considered fully  
 2561 correlated across the signal and background MC-based estimates.

2562 A fit is performed, leaving a signal strength parameter ( $\mu$ ) free, to max-  
 2563 imize the likelihood, and subsequent fits are preformed to at discrete  $\mu$   
 2564 values to determine the relative likelihood of each value. Using this rela-  
 2565 tive likelihood, the probability of a background-only hypothesis,  $p_b$ , can be  
 2566 determined by setting  $\mu = 0$ , as well as the probability of a signal + back-  
 2567 ground hypothesis  $p_{s+b}$  with any non-zero signal strength, but nominally  
 2568 with  $\mu = 1$ . The confidence limit is constructed as a ratio

$$CL_S = \frac{p_{s+b}}{1 - p_b}. \quad (47)$$

2569 Then, if  $CL_S$  falls below 5%, the signal + background hypothesis can be  
 2570 excluded at 95%. Expected exclusion limits are constructed by assuming  
 2571 the observed data precisely matches the prediction, and  $1\sigma$  uncertainty  
 2572 bands are formed by varying the nuisance parameters away from their fit-  
 2573 ted values to produce a change in the likelihood. The observed limit uses  
 2574 the actual observation of data in the SR to set exclusion limits, so any excess  
 2575 above the expected background will result in worse limits than expected,  
 2576 and any deficit will result in better limits. This exclusion is typically dis-  
 2577 played with error bands that represent a  $1\sigma$  variation in the cross-section  
 2578 of the signal models.

The simplified model discussed in Section 2.2.3, in which pair-produced gluinos decay via a  $\tilde{\chi}_2^0$  to jets, a Z boson, and a  $\tilde{\chi}_1^0$  LSP, is produced in two grids, which differ by their choice of the LSP mass. The first grid assumes a light LSP, fixing its mass to 1 GeV for all mass points, and is shown as a function of  $\tilde{g}$  and  $\tilde{\chi}_2^0$ . The second grid is defined as a function of  $\tilde{g}$  and  $\tilde{\chi}_1^0$ , and its varying LSP mass is defined relative to the  $\tilde{\chi}_2^0$  mass by  $m(\tilde{\chi}_1^0) = m(\tilde{\chi}_2^0) - 100$  GeV. Figure 92 shows the first of these grids, along with exclusions on a similar simplified model, which replaces the gluinos with squarks and uses the same mass scheme. The exclusion contours on the second grid is shown in Figure 93, as a function of  $m(\tilde{g})$  and  $m(\tilde{\chi}_1^0)$ .

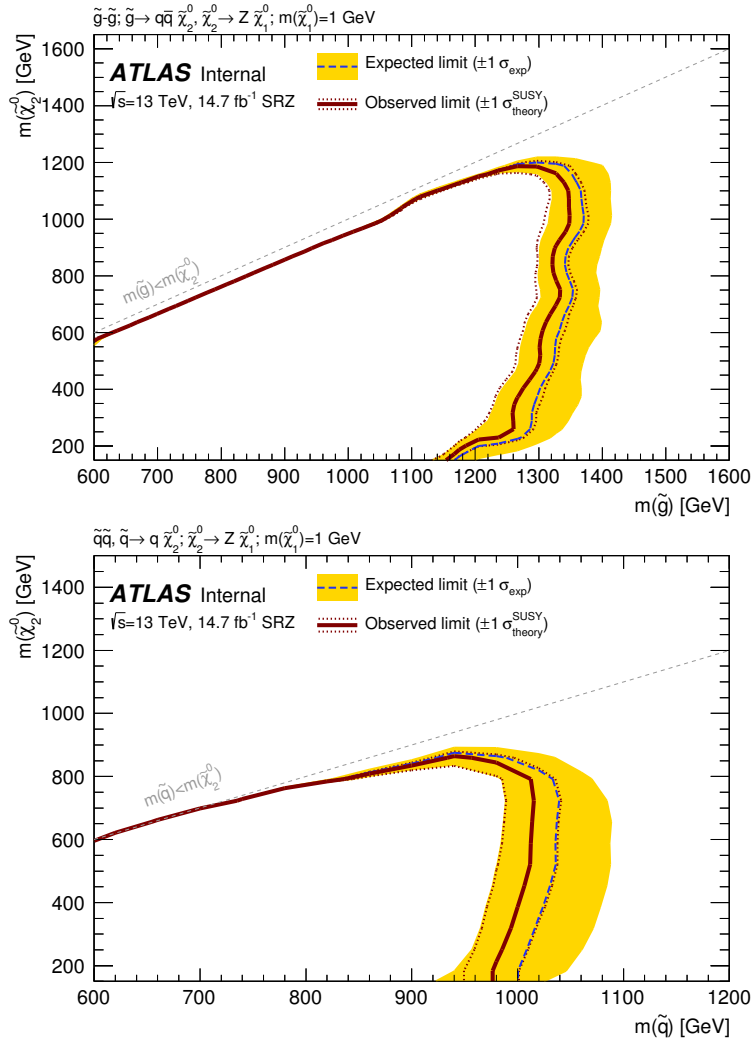


Figure 92: Expected and observed exclusion contours derived from the results in SRZ for the (top)  $\tilde{g}-\tilde{\chi}_2^0$  on-shell grid and (bottom)  $\tilde{q}-\tilde{\chi}_2^0$  on-shell grid. The dashed blue line indicates the expected limits at 95% CL and the yellow band shows the  $1\sigma$  variation of the expected limit as a consequence of the uncertainties in the background prediction and the experimental uncertainties in the signal ( $\pm 1\sigma_{\text{exp}}$ ). The observed limits are shown by the solid red line, with the dotted red lines indicating the variation resulting from changing the signal cross section within its uncertainty ( $\pm 1\sigma_{\text{theory}}^{\text{SUSY}}$ ).

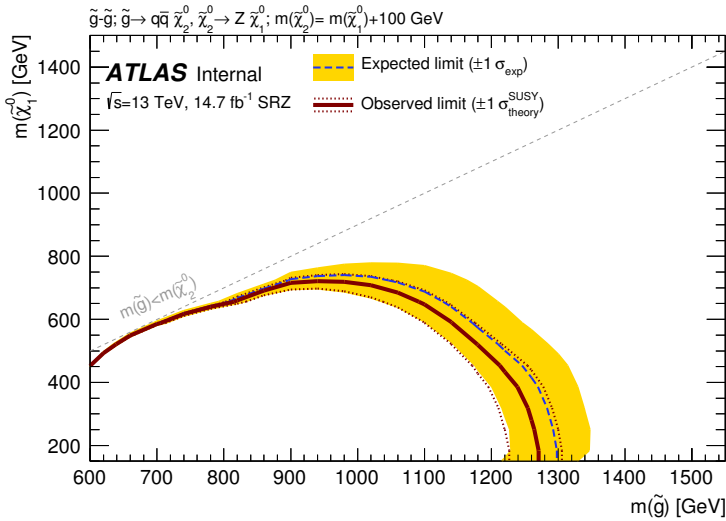


Figure 93: Expected and observed exclusion contours derived from the results in SRZ for the  $\tilde{g}-\tilde{\chi}_1^0$  on-shell grid. The dashed blue line indicates the expected limits at 95% CL and the yellow band shows the  $1\sigma$  variation of the expected limit as a consequence of the uncertainties in the background prediction and the experimental uncertainties in the signal ( $\pm 1\sigma_{\text{exp}}$ ). The observed limits are shown by the solid red line, with the dotted red lines indicating the variation resulting from changing the signal cross section within its uncertainty ( $\pm 1\sigma_{\text{theory}}^{\text{SUSY}}$ ).

2589 In general, the observed exclusions are slightly weaker than the expected  
 2590 exclusions, due to a very small excess of events observed in SRZ. The  
 2591 observed lower limit on  $m(\tilde{g})$  is about 1.3 TeV for models with  $m(\tilde{\chi}_2^0) = 500$   
 2592 GeV for the  $\tilde{g}-\tilde{\chi}_2^0$  grid. These improve significantly on the previous ATLAS  
 2593 exclusion, which used different models for interpretation, but placed a  
 2594 lower limit on  $m(\tilde{g})$  at around 900 GeV for similar  $m(\tilde{\chi}_2^0)$ .



2595

## Part V

2596

### CONCLUSIONS

2597



2598

2599 CONCLUSIONS AND OUTLOOK

2600 After a series of moderate excesses observed by the ATLAS experiment  
 2601 in events with a Z boson, jets, and  $E_T^{\text{miss}}$ , this analysis performed on 14.7  
 2602  $\text{fb}^{-1}$  of 13 TeV data sees excellent agreement between observations and  
 2603 the background expectation. The resulting exclusion pushes the gluino  
 2604 mass lower limit beyond 1 TeV, putting further constraints on possible  
 2605 SUSY models. Along with the many other searches for SUSY, this exclusion  
 2606 limits the phase space available for natural SUSY models. However, SUSY is  
 2607 adaptable; new theories stretching those bounds are continually proposed  
 2608 as tighter experimental constraints are set, and there are always small gaps  
 2609 in the exclusions where sparticles could hide.

2610 ATLAS's dataset for 2016 includes 36  $\text{fb}^{-1}$ , more than twice the lumi-  
 2611 nosity included in this search. Because no excess was seen in this analysis,  
 2612 the next search in this channel will be able to re-optimize its signal re-  
 2613 gions for this larger dataset. In fact, because the signal region has been  
 2614 frozen since the 8 TeV search, this analysis's signal region hasn't ever been  
 2615 re-optimized for the increased energy of the LHC's collisions. A new sig-  
 2616 nal region that increases  $E_T^{\text{miss}}$  and  $H_T$  requirements will allow for better  
 2617 sensitivity to SUSY processes.

2618 In addition, the current signal region, in which 60 events were observed  
 2619 with 14.7  $\text{fb}^{-1}$ , will be populated enough to be subdivided based on event  
 2620 features. The current search is agnostic to the number of  $b$ -jets in the event,  
 2621 for example, but there are now enough events to separate this signal region  
 2622 into complementary  $b$ -tagged and  $b$ -vetoed regions, allowing analyzers to  
 2623 independently target models which produce  $b$ -jets and those that don't,  
 2624 and in the latter case, to dramatically reduce the  $t\bar{t}$  background. Signal  
 2625 regions can also be binned in other model-dependent features, like number  
 2626 of jets, and the  $E_T^{\text{miss}}$  and  $H_T$  requirements can be increased independently,  
 2627 targeting different event topologies.

2628 The LHC will continue to run through 2018 with a possible increase to  
 2629  $\sqrt{s} = 14 \text{ TeV}$ , and will shut down for upgrades until 2021. Three more  
 2630 years of data-taking at 14 TeV will follow, with approximately twice the  
 2631 current luminosity, referred to as Run 3. After that, the LHC will shut down  
 2632 again to prepare for the High Luminosity Large Hadron Collider (HL-LHC),  
 2633 which will begin data-taking in 2026 at a luminosity approximately five  
 2634 times the current rate. This run will result in roughly  $3000 \text{ fb}^{-1}$ , which  
 2635 will allow for dramatically better sensitivity in SUSY searches. An example  
 2636 can be seen in Figure 94, which shows the potential exclusions on a simple  
 2637 gluino pair-production model with decays via squarks to a LSP, for the  
 2638 approximate luminosities of Run 3 and the HL-LHC.

2639 Searches like this one will surely be repeated with higher and higher  
 2640 luminosities, the analyses increasing both in sensitivity and in complexity.

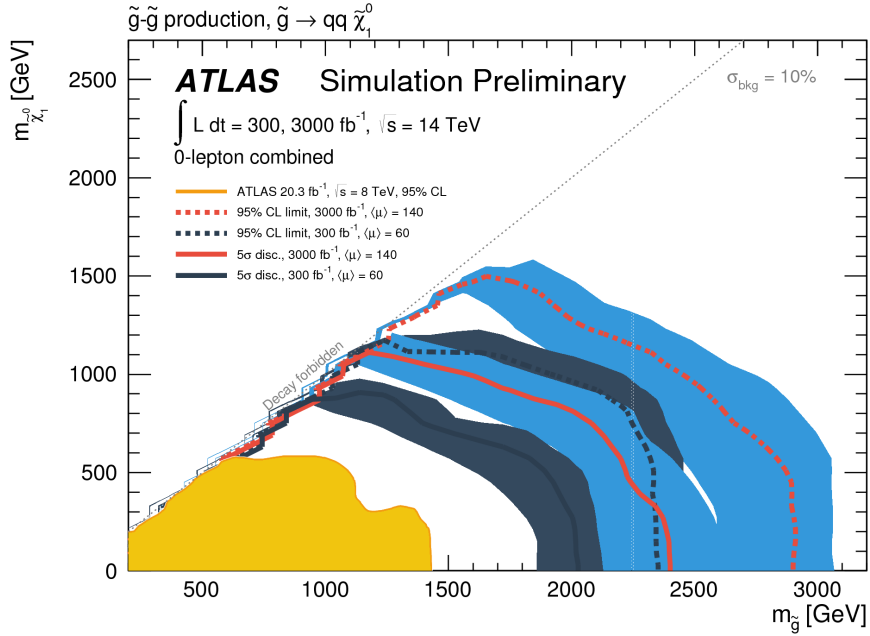


Figure 94: Expected 95% CL exclusion contours (dashed) and  $5\sigma$  discovery contours (solid) for  $L_{int} = 300^{-1}$  (black) and  $3000^{-1}$  (red) for gluino pair-production, with  $1\sigma$  bands representing the uncertainty on the production cross-section. Superimposed is the observed 8 TeV exclusion for similar models. [105]

2641 Whether or not they uncover any hints of physics beyond the Standard  
2642 Model remains to be seen.

## BIBLIOGRAPHY

---

- [1] ATLAS Collaboration. “Search for supersymmetry in events containing a same-flavour opposite-sign dilepton pair, jets, and large missing transverse momentum in  $\sqrt{s} = 8$  TeV  $pp$  collisions with the ATLAS detector.” In: *Eur. Phys. J. C* 75 (2015), p. 318. doi: [10.1140/epjc/s10052-015-3518-2](https://doi.org/10.1140/epjc/s10052-015-3518-2). arXiv: [1503.03290 \[hep-ex\]](https://arxiv.org/abs/1503.03290).
- [2] ATLAS Collaboration. *A search for supersymmetry in events containing a leptonically decaying Z boson, jets and missing transverse momentum in  $\sqrt{s} = 13$  TeV  $pp$  collisions with the ATLAS detector.* ATLAS-CONF-2015-082. 2015. URL: <http://cdsweb.cern.ch/record/2114854>.
- [3] C. P. Burgess and G. D. Moore. *The standard model: A primer.* Cambridge University Press, 2006. ISBN: 9780511254857, 9781107404267, 9780521860369.
- [4] S. L. Glashow. “Partial Symmetries of Weak Interactions.” In: *Nucl. Phys.* 22 (1961), pp. 579–588. doi: [10.1016/0029-5582\(61\)90469-2](https://doi.org/10.1016/0029-5582(61)90469-2).
- [5] Abdus Salam. “Renormalizability of Gauge Theories.” In: *Phys. Rev.* 127 (1 1962), pp. 331–334. doi: [10.1103/PhysRev.127.331](https://doi.org/10.1103/PhysRev.127.331). URL: <http://link.aps.org/doi/10.1103/PhysRev.127.331>.
- [6] Steven Weinberg. “A Model of Leptons.” In: *Phys. Rev. Lett.* 19 (21 1967), pp. 1264–1266. doi: [10.1103/PhysRevLett.19.1264](https://doi.org/10.1103/PhysRevLett.19.1264). URL: <http://link.aps.org/doi/10.1103/PhysRevLett.19.1264>.
- [7] D. Galbraith. *The Standard Model of the Standard Model.* 1997. URL: <http://davidgalbraith.org/portfolio/ux-standard-model-of-the-standard-model/>.
- [8] David J Griffiths. *Introduction to elementary particles; 2nd rev. version.* Physics textbook. New York, NY: Wiley, 2008. URL: <https://cds.cern.ch/record/111880>.
- [9] P. Hut and K. A. Olive. “A cosmological upper limit on the mass of heavy neutrinos.” In: *Physics Letters B* 87 (Oct. 1979), pp. 144–146. doi: [10.1016/0370-2693\(79\)90039-X](https://doi.org/10.1016/0370-2693(79)90039-X).
- [10] Huang, Qing-Guo, Wang, Ke, and Wang, Sai. “Constraints on the neutrino mass and mass hierarchy from cosmological observations.” In: *Eur. Phys. J. C* 76.9 (2016), p. 489. doi: [10.1140/epjc/s10052-016-4334-z](https://doi.org/10.1140/epjc/s10052-016-4334-z). URL: <http://dx.doi.org/10.1140/epjc/s10052-016-4334-z>.
- [11] The MEG Collaboration. “Search for the Lepton Flavour Violating Decay  $\mu^+ \rightarrow e^+ \gamma$  with the Full Dataset of the MEG Experiment.” In: (2016). eprint: [arXiv:1605.05081](https://arxiv.org/abs/1605.05081).
- [12] LHCb collaboration. “Observation of  $J/\Psi p$  resonances consistent with pentaquark states in  $\Lambda_b^0 \rightarrow J/\Psi K^- p$  decays.” In: (2015). doi: [10.1103/PhysRevLett.115.072001](https://doi.org/10.1103/PhysRevLett.115.072001). eprint: [arXiv:1507.03414](https://arxiv.org/abs/1507.03414).

- [13] K. A. Olive et al. “Review of Particle Physics.” In: *Chin. Phys. C* 38 (2014), p. 090001. doi: [10.1088/1674-1137/38/9/090001](https://doi.org/10.1088/1674-1137/38/9/090001).
- [14] Johan Messchendorp. “Physics with Charmonium – A few recent highlights of BESIII.” In: *PoS Bormio2013* (2013), p. 043. arXiv: [1306.6611 \[hep-ex\]](https://arxiv.org/abs/1306.6611).
- [15] A. D. Martin, W. J. Stirling, R. S. Thorne, and G. Watt. “Parton distributions for the LHC.” In: (2009). doi: [10.1140/epjc/s10052-009-1072-5](https://doi.org/10.1140/epjc/s10052-009-1072-5). eprint: [arXiv:0901.0002](https://arxiv.org/abs/0901.0002).
- [16] W.J. Stirling. *proton-(anti)proton cross sections*. 2013. URL: <http://www.hep.ph.ic.ac.uk/~wstirlin/plots/plots.html>.
- [17] F. Zwicky. “Die Rotverschiebung von extragalaktischen Nebeln.” In: *Helvetica Physica Acta* 6 (1933), 110–127.
- [18] Douglas Clowe, Marusa Bradac, Anthony H. Gonzalez, Maxim Markevitch, Scott W. Randall, Christine Jones, and Dennis Zaritsky. “A direct empirical proof of the existence of dark matter.” In: (2006). doi: [10.1086/508162](https://doi.org/10.1086/508162). eprint: [arXiv:astro-ph/0608407](https://arxiv.org/abs/astro-ph/0608407).
- [19] G. Hinshaw et al. “Five-Year Wilkinson Microwave Anisotropy Probe (WMAP) Observations: Data Processing, Sky Maps, and Basic Results.” In: (2008). doi: [10.1088/0067-0049/180/2/225](https://doi.org/10.1088/0067-0049/180/2/225). eprint: [arXiv:0803.0732](https://arxiv.org/abs/0803.0732).
- [20] T. S. van Albada, J. N. Bahcall, K. Begeman, and R. Sancisi. “Distribution of dark matter in the spiral galaxy NGC 3198.” In: *The Astrophysical Journal* 295 (Aug. 1985), pp. 305–313. doi: [10.1086/163375](https://doi.org/10.1086/163375).
- [21] M. Gell-Mann. *THE EIGHTFOLD WAY: A THEORY OF STRONG INTERACTION SYMMETRY*. 1961. doi: [10.2172/4008239](https://doi.org/10.2172/4008239). URL: <http://www.osti.gov/scitech/servlets/purl/4008239>.
- [22] J. Wess and B. Zumino. “Supergauge transformations in four dimensions.” In: *Nuclear Physics B* 70.1 (1974), pp. 39–50. ISSN: 0550-3213. doi: [http://dx.doi.org/10.1016/0550-3213\(74\)90355-1](http://dx.doi.org/10.1016/0550-3213(74)90355-1). URL: <http://www.sciencedirect.com/science/article/pii/0550321374903551>.
- [23] J.-L. Gervais and B. Sakita. “Field theory interpretation of supergauges in dual models.” In: *Nuclear Physics B* 34 (1971), pp. 632–639. doi: [10.1016/0550-3213\(71\)90351-8](https://doi.org/10.1016/0550-3213(71)90351-8).
- [24] P. Ramond. “Dual Theory for Free Fermions.” In: *Physical Review D* 3 (1971), pp. 2415–2418. doi: [10.1103/PhysRevD.3.2415](https://doi.org/10.1103/PhysRevD.3.2415).
- [25] Stephen P. Martin. “A Supersymmetry primer.” In: (1997). [Adv. Ser. Direct. High Energy Phys. 18, 1 (1998)]. doi: [10.1142/9789812839657\\_0001](https://doi.org/10.1142/9789812839657_0001), [10.1142/9789814307505\\_0001](https://doi.org/10.1142/9789814307505_0001). arXiv: [hep-ph/9709356 \[hep-ph\]](https://arxiv.org/abs/hep-ph/9709356).
- [26] Craig J Copi, David N. Schramm, and Michael S. Turner. “Big-Bang Nucleosynthesis and the Baryon Density of the Universe.” In: (1994). doi: [10.1126/science.7809624](https://doi.org/10.1126/science.7809624). eprint: [arXiv:astro-ph/9407006](https://arxiv.org/abs/astro-ph/9407006).

- [27] NobelPrize.org. *The Nobel Prize in Physics 2004 - Popular Information*. 2016. URL: [https://www.nobelprize.org/nobel\\_prizes/physics/laureates/2004/popular.html](https://www.nobelprize.org/nobel_prizes/physics/laureates/2004/popular.html).
- [28] ATLAS Collaboration. “Dark matter interpretations of ATLAS searches for the electroweak production of supersymmetric particles in  $\sqrt{s} = 8$  TeV proton-proton collisions.” In: (2016). doi: [10.1007/JHEP09\(2016\)175](https://doi.org/10.1007/JHEP09(2016)175). eprint: [arXiv:1608.00872](https://arxiv.org/abs/1608.00872).
- [29] The ATLAS collaboration. “Further searches for squarks and gluinos in final states with jets and missing transverse momentum at  $\sqrt{s} = 13$  TeV with the ATLAS detector.” In: (2016).
- [30] W. Beenakker, S. Brensing, M. Krämer, A. Kulesza, E. Laenen, L. Motyka, and I. Niessen. “Squark and gluino hadroproduction.” In: (2011). doi: [10.1142/S0217751X11053560](https://doi.org/10.1142/S0217751X11053560). eprint: [arXiv:1105.1110](https://arxiv.org/abs/1105.1110).
- [31] ATLAS Collaboration. *ATLAS SUSY Searches - 95% CL Lower Limits*. <https://atlas.web.cern.ch/Atlas/GROUPS/PHYSICS/CombinedSummaryPlots/SUSY/ATLASsl> 2016.
- [32] Wim Beenakker, Christoph Borschensky, Michael Krämer, Anna Kulesza, and Eric Laenen. *NNLL-fast: predictions for coloured supersymmetric particle production at the LHC with threshold and Coulomb resummation*. 2016. eprint: [arXiv:1607.07741](https://arxiv.org/abs/1607.07741).
- [33] CMS Collaboration. “Search for physics beyond the standard model in events with a Z boson, jets, and missing transverse energy in  $pp$  collisions at  $\sqrt{s} = 7$  TeV.” In: *Phys. Lett. B* 716 (2012), pp. 260–284. doi: [10.1016/j.physletb.2012.08.026](https://doi.org/10.1016/j.physletb.2012.08.026). arXiv: [1204.3774 \[hep-ex\]](https://arxiv.org/abs/1204.3774).
- [34] CMS Collaboration. “Search for physics beyond the standard model in events with two leptons, jets, and missing transverse momentum in  $pp$  collisions at  $\sqrt{s} = 8$  TeV.” In: *JHEP* 04 (2015), p. 124. doi: [10.1007/JHEP04\(2015\)124](https://doi.org/10.1007/JHEP04(2015)124). arXiv: [1502.06031 \[hep-ex\]](https://arxiv.org/abs/1502.06031).
- [35] *Search for new physics in final states with two opposite-sign same-flavor leptons, jets and missing transverse momentum in pp collisions at sqrt(s)=13 TeV*. Tech. rep. CMS-PAS-SUS-15-011. Geneva: CERN, 2015. URL: <https://cds.cern.ch/record/2114811>.
- [36] Richard D. Ball et al. “Parton distributions with LHC data.” In: *Nucl. Phys.* B867 (2013), pp. 244–289. doi: [10.1016/j.nuclphysb.2012.10.003](https://doi.org/10.1016/j.nuclphysb.2012.10.003). arXiv: [1207.1303 \[hep-ph\]](https://arxiv.org/abs/1207.1303).
- [37] Hung-Liang Lai et al. “New parton distributions for collider physics.” In: *Phys. Rev. D* 82 (2010), p. 074024. doi: [10.1103/PhysRevD.82.074024](https://doi.org/10.1103/PhysRevD.82.074024). arXiv: [1007.2241 \[hep-ph\]](https://arxiv.org/abs/1007.2241).
- [38] J. Alwall, R. Frederix, S. Frixione, V. Hirschi, F. Maltoni, O. Matelaer, H. S. Shao, T. Stelzer, P. Torrielli, and M. Zaro. “The automated computation of tree-level and next-to-leading order differential cross sections, and their matching to parton shower simula-

- tions.” In: *JHEP* 07 (2014), p. 079. doi: [10.1007/JHEP07\(2014\)079](https://doi.org/10.1007/JHEP07(2014)079). arXiv: [1405.0301 \[hep-ph\]](https://arxiv.org/abs/1405.0301).
- [39] P. Nason. “A new method for combining NLO QCD with shower Monte Carlo algorithms.” In: *JHEP* 0411 (2004), p. 040. arXiv: [hep-ph/0409146 \[hep-ph\]](https://arxiv.org/abs/hep-ph/0409146).
- [40] S. Frixione, P. Nason, and C. Oleari. “Matching NLO QCD computations with parton shower simulations: the POWHEG method.” In: *JHEP* 0711 (2007), p. 070. arXiv: [0709.2092 \[hep-ph\]](https://arxiv.org/abs/0709.2092).
- [41] S. Alioli, P. Nason, C. Oleari, and E. Re. “A general framework for implementing NLO calculations in shower Monte Carlo programs: the POWHEG BOX.” In: *JHEP* 1006 (2010), p. 043. arXiv: [1002.2581 \[hep-ph\]](https://arxiv.org/abs/1002.2581).
- [42] T. Gleisberg et al. “Event generation with Sherpa 1.1.” In: *JHEP* 0902 (2009), p. 007. arXiv: [0811.4622 \[hep-ph\]](https://arxiv.org/abs/0811.4622).
- [43] T. Sjöstrand, S. Mrenna, and P. Skands. “PYTHIA 6.4 Physics and Manual.” In: *JHEP* 0605 (2006), p. 026. doi: [10.1088/1126-6708/2006/05/026](https://doi.org/10.1088/1126-6708/2006/05/026). arXiv: [hep-ph/0603175 \[hep-ph\]](https://arxiv.org/abs/hep-ph/0603175).
- [44] S. Agostinelli et al. “GEANT4: A simulation toolkit.” In: *Nucl. Instrum. Meth. A* 506 (2003), pp. 250–303. doi: [10.1016/S0168-9002\(03\)01368-8](https://doi.org/10.1016/S0168-9002(03)01368-8).
- [45] Morad Aaboud et al. “A measurement of material in the ATLAS tracker using secondary hadronic interactions in 7 TeV pp collisions.” In: (2016). arXiv: [1609.04305 \[hep-ex\]](https://arxiv.org/abs/1609.04305).
- [46] Lyndon Evans and Philip Bryant. “LHC Machine.” In: *Journal of Instrumentation* 3.08 (2008), So8001. URL: <http://stacks.iop.org/1748-0221/3/i=08/a=S08001>.
- [47] *LEP design report*. Copies shelved as reports in LEP, PS and SPS libraries. Geneva: CERN, 1984. URL: <https://cds.cern.ch/record/102083>.
- [48] ATLAS Collaboration. “The ATLAS Experiment at the CERN Large Hadron Collider.” In: *JINST* 3 (2008), So8003. doi: [10.1088/1748-0221/3/08/S08003](https://doi.org/10.1088/1748-0221/3/08/S08003).
- [49] The CMS Collaboration. “The CMS experiment at the CERN LHC.” In: *Journal of Instrumentation* 3.08 (2008), So8004. URL: <http://stacks.iop.org/1748-0221/3/i=08/a=S08004>.
- [50] The LHCb Collaboration. “The LHCb Detector at the LHC.” In: *Journal of Instrumentation* 3.08 (2008), So8005. URL: <http://stacks.iop.org/1748-0221/3/i=08/a=S08005>.
- [51] The ALICE Collaboration. “The ALICE experiment at the CERN LHC.” In: *Journal of Instrumentation* 3.08 (2008), So8002. URL: <http://stacks.iop.org/1748-0221/3/i=08/a=S08002>.
- [52] ATLAS Collaboration. *2015 start-up trigger menu and initial performance assessment of the ATLAS trigger using Run-2 data*. ATL-DAQ-PUB-2016-001. 2016. URL: [http://cds.cern.ch/record/2136007](https://cds.cern.ch/record/2136007).

- [53] “Electron performance measurements with the ATLAS detector using the 2010 LHC proton-proton collision data.” In: *Eur. Phys. J. C* 72 (2012), p. 1909. doi: [10.1140/epjc/s10052-012-1909-1](https://doi.org/10.1140/epjc/s10052-012-1909-1). arXiv: [1110.3174 \[hep-ex\]](https://arxiv.org/abs/1110.3174).
- [54] *Electron efficiency measurements with the ATLAS detector using the 2015 LHC proton-proton collision data.* Tech. rep. ATLAS-CONF-2016-024. Geneva: CERN, 2016. URL: <http://cds.cern.ch/record/2157687>.
- [55] ATLAS Collaboration. *Measurement of the photon identification efficiencies with the ATLAS detector using LHC Run-1 data.* 2016. eprint: [arXiv:1606.01813](https://arxiv.org/abs/1606.01813).
- [56] *Photon identification in 2015 ATLAS data.* Tech. rep. ATL-PHYS-PUB-2016-014. Geneva: CERN, 2016. URL: <https://cds.cern.ch/record/2203125>.
- [57] *Photon Identification Efficiencies using 2016 Data with radiative Z boson decays.* Tech. rep. EGAM-2016-003. Geneva: CERN, 2016. URL: <https://atlas.web.cern.ch/Atlas/GROUPS/PHYSICS/PLLOTS/EGAM-2016-003/index.html>.
- [58] *Official Isolation Working Points.* Geneva, 2016. URL: <https://twiki.cern.ch/twiki/bin/view/AtlasProtected/IsolationSelectionTool#Photons>.
- [59] ATLAS Collaboration. “Muon reconstruction performance of the ATLAS detector in proton–proton collision data at  $\sqrt{s}=13$  TeV.” In: (2016). doi: [10.1140/epjc/s10052-016-4120-y](https://doi.org/10.1140/epjc/s10052-016-4120-y). eprint: [arXiv:1603.05598](https://arxiv.org/abs/1603.05598).
- [60] Matteo Cacciari, Gavin P. Salam, and Gregory Soyez. “The Anti-k(t) jet clustering algorithm.” In: *JHEP* 0804 (2008), p. 063. doi: [10.1088/1126-6708/2008/04/063](https://doi.org/10.1088/1126-6708/2008/04/063). arXiv: [0802.1189 \[hep-ph\]](https://arxiv.org/abs/0802.1189).
- [61] ATLAS Collaboration. *Jet Calibration and Systematic Uncertainties for Jets Reconstructed in the ATLAS Detector at  $\sqrt{s} = 13$  TeV.* ATL-PHYS-PUB-2015-015. 2015. URL: <http://cds.cern.ch/record/2037613>.
- [62] ATLAS Collaboration. *Tagging and suppression of pileup jets with the ATLAS detector.* ATLAS-CONF-2014-018. 2014. URL: <http://cds.cern.ch/record/1700870>.
- [63] ATLAS Collaboration. *Expected performance of the ATLAS b-tagging in Run-2.* ATL-PHYS-PUB-2015-022. 2015. URL: <http://cdsweb.cern.ch/record/2037697>.
- [64] ATLAS Collaboration. *Expected performance of missing transverse momentum reconstruction for the ATLAS detector at  $\sqrt{s} = 13$  TeV.* ATL-PHYS-PUB-2015-023. 2015. URL: <http://cds.cern.ch/record/2037700>.
- [65] ATLAS Collaboration. *Performance of missing transverse momentum reconstruction for the ATLAS detector in the first proton-proton collisions at  $\sqrt{s} = 13$  TeV.* ATL-PHYS-PUB-2015-027. 2015. URL: <http://cds.cern.ch/record/2037904>.

- [66] ATLAS Collaboration. “A neural network clustering algorithm for the ATLAS silicon pixel detector.” In: *JINST* 9 (2014), P09009. doi: [10.1088/1748-0221/9/09/P09009](https://doi.org/10.1088/1748-0221/9/09/P09009). arXiv: [1406.7690 \[hep-ex\]](https://arxiv.org/abs/1406.7690).
- [67] Luke de Oliveira. *AGILEPack: Algorithms for Generalized Inference, Learning, and Extraction*. 2016. URL: <http://lukedeo.github.io/AGILEPack/>.
- [68] ATLAS Collaboration. *Measurement of performance of the pixel neural network clustering algorithm of the ATLAS experiment at  $\sqrt{s} = 13$  TeV*. ATL-PHYS-PUB-2015-044. 2015. URL: <http://cdsweb.cern.ch/record/2054921>.
- [69] ATLAS Collaboration. *Robustness of the Artificial Neural Network Clustering Algorithm of the ATLAS experiment*. ATL-PHYS-PUB-2015-052. 2015. URL: <http://cdsweb.cern.ch/record/2116350>.
- [70] ATLAS Collaboration. *Modelling of the  $t\bar{t}H$  and  $t\bar{t}V$  ( $V = W, Z$ ) processes for  $\sqrt{s} = 13$  TeV ATLAS analyses*. ATL-PHYS-PUB-2016-005. 2016. URL: <http://cds.cern.ch/record/2120826>.
- [71] M. V. Garzelli, A. Kardos, C. G. Papadopoulos, and Z. Trocsanyi. “ $t\bar{t}W^{+-}$  and  $t\bar{t}Z$  Hadroproduction at NLO accuracy in QCD with Parton Shower and Hadronization effects.” In: *JHEP* 11 (2012), p. 056. doi: [10.1007/JHEP11\(2012\)056](https://doi.org/10.1007/JHEP11(2012)056). arXiv: [1208.2665 \[hep-ph\]](https://arxiv.org/abs/1208.2665).
- [72] J. M. Campbell and R. K. Ellis. “ $t\bar{t}W$  production and decay at NLO.” In: *JHEP* 1207 (2012), p. 052. arXiv: [1204.5678 \[hep-ph\]](https://arxiv.org/abs/1204.5678).
- [73] A. Lazopoulos, T. McElmurry, K. Melnikov, and F. Petriello. “Next-to-leading order QCD corrections to  $t\bar{t}Z$  production at the LHC.” In: *Phys. Lett. B* 666 (2008), p. 62. arXiv: [0804.2220 \[hep-ph\]](https://arxiv.org/abs/0804.2220).
- [74] ATLAS Collaboration. *Simulation of top quark production for the ATLAS experiment at  $\sqrt{s} = 13$  TeV*. ATL-PHYS-PUB-2016-004. 2016. URL: <http://cds.cern.ch/record/2120417>.
- [75] M. Czakon, P. Fiedler, and A. Mitov. “Total Top-Quark Pair-Production Cross Section at Hadron Colliders Through  $O(\alpha_s^4)$ .” In: *Phys. Rev. Lett.* 110 (2013), p. 252004. arXiv: [1303.6254 \[hep-ph\]](https://arxiv.org/abs/1303.6254).
- [76] M. Czakon and A. Mitov. “Top++: A Program for the Calculation of the Top-Pair Cross-Section at Hadron Colliders.” In: *Comput. Phys. Commun.* 185 (2014), p. 2930. doi: [10.1016/j.cpc.2014.06.021](https://doi.org/10.1016/j.cpc.2014.06.021). arXiv: [1112.5675 \[hep-ph\]](https://arxiv.org/abs/1112.5675).
- [77] N. Kidonakis. “Two-loop soft anomalous dimensions for single top quark associated production with a  $W^-$  or  $H^-$ .” In: *Phys. Rev. D* 82 (2010), p. 054018. doi: [10.1103/PhysRevD.82.054018](https://doi.org/10.1103/PhysRevD.82.054018). arXiv: [1005.4451 \[hep-ph\]](https://arxiv.org/abs/1005.4451).
- [78] ATLAS Collaboration. *Multi-Boson Simulation for 13 TeV ATLAS Analyses*. ATL-PHYS-PUB-2016-002. 2016. URL: <http://cds.cern.ch/record/2119986>.

- [79] J. M. Campbell and R. K. Ellis. “An update on vector boson pair production at hadron colliders.” In: *Phys. Rev. D* 60 (1999), p. 113006. arXiv: [hep-ph/9905386 \[hep-ph\]](#).
- [80] J. M. Campbell, R. K. Ellis, and C. Williams. “Vector boson pair production at the LHC.” In: *JHEP* 1107 (2011), p. 018. arXiv: [1105.0020 \[hep-ph\]](#).
- [81] ATLAS Collaboration. *Monte Carlo Generators for the Production of a W or Z/ $\gamma^*$  Boson in Association with Jets at ATLAS in Run 2*. ATL-PHYS-PUB-2016-003. 2016. URL: <http://cds.cern.ch/record/2120133>.
- [82] S. Catani, L. Cieri, G. Ferrera, D. de Florian, and M. Grazzini. “Vector boson production at hadron colliders: a fully exclusive QCD calculation at NNLO.” In: *Phys. Rev. Lett.* 103 (2009), p. 082001. arXiv: [0903.2120 \[hep-ph\]](#).
- [83] S. Catani and M. Grazzini. “An NNLO subtraction formalism in hadron collisions and its application to Higgs boson production at the LHC.” In: *Phys. Rev. Lett.* 98 (2007), p. 222002. arXiv: [hep-ph/0703012 \[hep-ph\]](#).
- [84] ATLAS Collaboration. *Electron efficiency measurements with the ATLAS detector using the 2012 LHC proton–proton collision data*. ATLAS-CONF-2014-032. 2014. URL: <http://cdsweb.cern.ch/record/1706245>.
- [85] ATLAS Collaboration. “Muon reconstruction performance of the ATLAS detector in proton–proton collision data at  $\sqrt{s} = 13$  TeV.” In: *Eur. Phys. J. C* 76 (2016), p. 292. DOI: [10.1140/epjc/s10052-016-4120-y](https://doi.org/10.1140/epjc/s10052-016-4120-y). arXiv: [1603.05598 \[hep-ex\]](#).
- [86] ATLAS Collaboration. *Search for supersymmetry in final states with jets, missing transverse momentum and a Z boson at  $\sqrt{s} = 8$  TeV with the ATLAS detector*. ATLAS-CONF-2012-152. 2012. URL: <http://cds.cern.ch/record/1493491>.
- [87] ATLAS Collaboration. “Measurement of the differential cross-section of highly boosted top quarks as a function of their transverse momentum in  $\sqrt{s} = 8$  TeV proton-proton collisions using the ATLAS detector.” In: *Phys. Rev. D* 93.3 (2016), p. 032009. DOI: [10.1103/PhysRevD.93.032009](https://doi.org/10.1103/PhysRevD.93.032009). arXiv: [1510.03818 \[hep-ex\]](#).
- [88] CMS Collaboration. “Measurement of the integrated and differential t-tbar production cross sections for high-pt top quarks in pp collisions at  $\sqrt{s} = 8$  TeV.” In: *Phys. Rev. D* (2016). Submitted. arXiv: [1605.00116 \[hep-ex\]](#).
- [89] ATLAS Collaboration. *Search for physics beyond the Standard Model in events with a Z boson and large missing transverse momentum using  $\sqrt{s} = 7$  TeV pp collisions from the LHC with the ATLAS detector*. ATLAS-CONF-2012-046. 2012. URL: <http://cdsweb.cern.ch/record/1448222>.

- [90] ATLAS Collaboration. “Search for squarks and gluinos in events with isolated leptons, jets and missing transverse momentum at  $\sqrt{s} = 8$  TeV with the ATLAS detector.” In: *JHEP* 1504 (2015), p. 116. doi: [10.1007/JHEP04\(2015\)116](https://doi.org/10.1007/JHEP04(2015)116). arXiv: [1501.03555 \[hep-ex\]](https://arxiv.org/abs/1501.03555).
- [91] ATLAS Collaboration. “Improved luminosity determination in pp collisions at  $\sqrt{s} = 7$  TeV using the ATLAS detector at the LHC.” In: *Eur. Phys. J. C* 73 (2013), p. 2518. doi: [10.1140/epjc/s10052-013-2518-3](https://doi.org/10.1140/epjc/s10052-013-2518-3). arXiv: [1302.4393 \[hep-ex\]](https://arxiv.org/abs/1302.4393).
- [92] ATLAS Collaboration. “Luminosity determination in pp collisions at  $\sqrt{s} = 8$  TeV using the ATLAS detector at the LHC.” In: *to be submitted to Eur. Phys. J. C* ().
- [93] Michael Kramer et al. *Supersymmetry production cross sections in pp collisions at  $\sqrt{s} = 7$  TeV*. 2012. arXiv: [1206.2892 \[hep-ph\]](https://arxiv.org/abs/1206.2892).
- [94] W. Beenakker, R. Höpker, M. Spira, and P.M. Zerwas. “Squark and gluino production at hadron colliders.” In: *Nucl. Phys. B* 492 (1997), pp. 51–103. doi: [10.1016/S0550-3213\(97\)00084-9](https://doi.org/10.1016/S0550-3213(97)00084-9). arXiv: [hep-ph/9610490 \[hep-ph\]](https://arxiv.org/abs/hep-ph/9610490).
- [95] A. Kulesza and L. Motyka. “Threshold resummation for squark-antisquark and gluino-pair production at the LHC.” In: *Phys. Rev. Lett.* 102 (2009), p. 111802. doi: [10.1103/PhysRevLett.102.111802](https://doi.org/10.1103/PhysRevLett.102.111802). arXiv: [0807.2405 \[hep-ph\]](https://arxiv.org/abs/0807.2405).
- [96] A. Kulesza and L. Motyka. “Soft gluon resummation for the production of gluino-gluino and squark-antisquark pairs at the LHC.” In: *Phys. Rev. D* 80 (2009), p. 095004. doi: [10.1103/PhysRevD.80.095004](https://doi.org/10.1103/PhysRevD.80.095004). arXiv: [0905.4749 \[hep-ph\]](https://arxiv.org/abs/0905.4749).
- [97] W. Beenakker et al. “Soft-gluon resummation for squark and gluino hadroproduction.” In: *JHEP* 0912 (2009), p. 041. doi: [10.1088/1126-6708/2009/12/041](https://doi.org/10.1088/1126-6708/2009/12/041). arXiv: [0909.4418 \[hep-ph\]](https://arxiv.org/abs/0909.4418).
- [98] W. Beenakker et al. “Squark and gluino hadroproduction.” In: *Int. J. Mod. Phys. A* 26 (2011), pp. 2637–2664. doi: [10.1142/S0217751X11053560](https://doi.org/10.1142/S0217751X11053560). arXiv: [1105.1110 \[hep-ph\]](https://arxiv.org/abs/1105.1110).
- [99] M. Baak et al. “HistFitter software framework for statistical data analysis.” In: *Eur. Phys. J. C* 75 (2014), p. 153. doi: [10.1140/epjc/s10052-015-3327-7](https://doi.org/10.1140/epjc/s10052-015-3327-7). arXiv: [1410.1280 \[hep-ex\]](https://arxiv.org/abs/1410.1280).
- [100] Rene Brun and Fons Rademakers. “ROOT — An object oriented data analysis framework.” In: *Nuclear Instruments and Methods in Physics Research Section A: Accelerators, Spectrometers, Detectors and Associated Equipment* 389.1 (1997), pp. 81 –86. issn: 0168-9002. doi: [http://dx.doi.org/10.1016/S0168-9002\(97\)00048-X](http://dx.doi.org/10.1016/S0168-9002(97)00048-X). URL: <http://www.sciencedirect.com/science/article/pii/S016890029700048X>.
- [101] Lorenzo Moneta, Kevin Belasco, Kyle Cranmer, Sven Kreiss, Alfonso Lazzaro, Danilo Piparo, Gregory Schott, Wouter Verkerke, and Matthias Wolf. *The RooStats Project*. 2010. eprint: [arXiv:1009.1003](https://arxiv.org/abs/1009.1003).

- [102] Kyle Cranmer, George Lewis, Lorenzo Moneta, Akira Shibata, and Wouter Verkerke. "HistFactory: A tool for creating statistical models for use with RooFit and RooStats." In: (2012).
- [103] Glen Cowan, Kyle Cranmer, Eilam Gross, and Ofer Vitells. "Asymptotic formulae for likelihood-based tests of new physics." In: *Eur. Phys. J. C* 71 (2011), p. 1554. DOI: [10.1140/epjc/s10052-011-1554-0](https://doi.org/10.1140/epjc/s10052-011-1554-0). arXiv: [1007.1727 \[physics.data-an\]](https://arxiv.org/abs/1007.1727).
- [104] A. Read. "Presentation of search results: the CLs technique." In: *Journal of Physics G: Nucl. Part. Phys.* 28 (2002), pp. 2693–2704. DOI: [10.1088/0954-3899/28/10/313](https://doi.org/10.1088/0954-3899/28/10/313).
- [105] *Prospects for a search for direct pair production of top squarks in scenarios with compressed mass spectra at the high luminosity LHC with the ATLAS Detector*. Tech. rep. ATL-PHYS-PUB-2016-022. Geneva: CERN, 2016. URL: <https://cds.cern.ch/record/2220904>.